MODELLING DATA STORAGE IN NANO–ISLAND MAGNETIC MATERIALS

A thesis submitted to the University of Manchester
for the degree of Doctor of Philosophy
in the Faculty of Engineering and Physical Sciences

2011

Josephat Kalezhi
School of Computer Science

Contents

Final word count: 52390

List of Tables

List of Figures

Abstract

Data storage in current hard disk drives is limited by three factors. These are thermal stability of recorded data, the ability to store data, and the ability to read back the stored data. An attempt to alleviate one factor can affect others. This ultimately limits magnetic recording densities that can be achieved using traditional forms of data storage. In order to advance magnetic recording and postpone these inhibiting factors, new approaches are required. One approach is recording on Bit Patterned Media (BPM) where the medium is patterned into nanometer-sized magnetic islands where each stores a binary digit.

This thesis presents a statistical model of write errors in BPM composed of single domain islands. The model includes thermal activation in a calculation of write errors without resorting to time consuming micromagnetic simulations of huge populations of islands. The model incorporates distributions of position, magnetic and geometric properties of islands. In order to study the impact of island geometry variations on the recording performance of BPM systems, the magnetometric demagnetising factors for a truncated elliptic cone, a generalised geometry that reasonably describe most proposed island shapes, were derived analytically. The inclusion of thermal activation was enabled by an analytic derivation of the energy barrier for a single domain island. The energy barrier is used in a calculation of transition rates that enable the calculation of error rates. The model has been used to study write-error performance of BPM systems having distributions of position, geometric and magnetic property variations. Results showed that island intrinsic anisotropy and position variations have a larger impact on write-error performance than geometric variations.

The model was also used to study thermally activated Adjacent Track Erasure (ATE) for a specific write head. The write head had a rectangular main pole of 13 by 40 nm (cross-track $\times$ down-track) with pole trailing shield gap of 5 nm and pole side shield gap of 10 nm. The distance from the pole to the top surface of the medium was 5 nm, the medium was 10 nm thick and there was a 2 nm interlayer between the soft underlayer (SUL) and the medium, making a total SUL to pole spacing of 17 nm. The results showed that ATE would be a major problem and that cross-track head field gradients need to be more tightly controlled than down-track. With the write head used, recording at 1 $\mathrm{Tb/in^2}$ would be possible on single domain islands.

Declaration

No portion of the work referred to in this thesis has been submitted in support of an application for another degree or qualification of this or any other university or other institute of learning.

Copyright

i. The author of this thesis (including any appendices and/or schedules to this thesis) owns certain copyright or related rights in it (the "Copyright") and s/he has given The University of Manchester certain rights to use such Copyright, including for administrative purposes.

ii. Copies of this thesis, either in full or in extracts and whether in hard or electronic copy, may be made only in accordance with the Copyright, Designs and Patents Act 1988 (as amended) and regulations issued under it or, where appropriate, in accordance with licensing agreements which the University has from time to time. This page must form part of any such copies made.

iii. The ownership of certain Copyright, patents, designs, trade marks and other intellectual property (the "Intellectual Property") and any reproductions of copyright works in the thesis, for example graphs and tables ("Reproductions"), which may be described in this thesis, may not be owned by the author and may be owned by third parties. Such Intellectual Property and Reproductions cannot and must not be made available for use without the prior written permission of the owner(s) of the relevant Intellectual Property and/or Reproductions.

iv. Further information on the conditions under which disclosure, publication and commercialisation of this thesis, the Copyright and any Intellectual Property and/or Reproductions described in it may take place is available in the University IP Policy (see `http://www.campus.manchester.ac.uk/medialibrary/policies/intellectual-property.pdf`), in any relevant Thesis restriction declarations deposited in the University Library, The University Library's regulations (see `http://www.manchester.ac.uk/library/aboutus/regulations`) and in The University's policy on presentation of Theses

Acknowledgements

I would like to express my sincere gratitude to my supervisor, Prof Jim Miles, for his invaluable guidance and help during the course of my research and useful discussions during writing of this thesis.
I would also like to thank my family for their continued support and encouragement during the difficult times of my studies.
My sincere thanks also goes to my advisor, Dr Paul Nutter as well as Dr Branson Belle and to all those who gave suggestions during writing of this thesis and supported me in any respect during this project.

Chapter 1

Introduction

This chapter introduces a brief historical perspective of magnetic recording, highlights notable developments since the discovery and discusses the challenges that prevent further developments using traditional forms of recording. Alternative forms of recording that have the potential to overcome the barriers and further the development of recording are introduced. This is followed by the aims and objectives. The research contributions are stated and a thesis outline is provided.

1.1 Magnetic recording: historical perspective

Magnetic recording was discovered by Valdemar Poulsen in 1898 and since then has played an important role in audio, video and computer development (Daniel *et al.*, 1998, p. 15). In 1956, the first magnetic hard disk drive known as RAMAC, an acronym for Random Access Method of Accounting and Control, was built by IBM which had a total capacity of 5 Mega Bytes (MB) at a magnetic recording density of 2 kbit/in^2 (Moser *et al.*, 2002). The magnetic recording density is measured in terms of the number of bits stored per unit area of the disk surface and is thus referred to as areal density in the literature. The RAMAC had a total of 50 disks, each being 24 inch in diameter (Wood and Takano, 2006) as shown in Figure 1.1. The areal density is an important quantity in that its growth rate is a measure of rate of advance of the technology (Wood *et al.*, 2007).

From the year RAMAC was built, economic factors arising from the growth in demand for information storage systems in a number of applications has prompted the need to reduce the cost per bit and improve the performance of hard disk drives (O'Grady and Laidler, 1999). Research in magnetic recording in order to

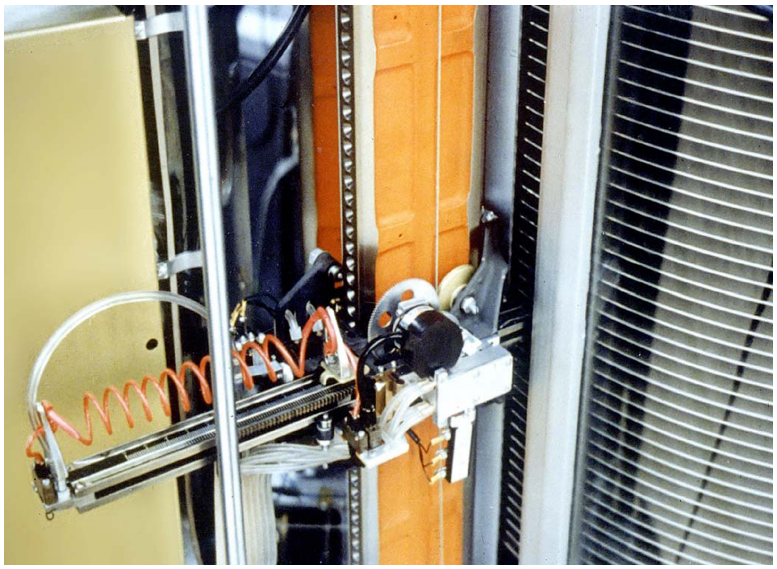

Figure 1.1: Photograph of the first disk drive in 1956 (RAMAC) showing the head positioning mechanism and the disk stack (Hoagland, 2005). The gap visible between the disks is around 1 centimetre.

fulfil these demands has led to areal densities increasing rapidly over the years (Moser *et al.*, 2002) as shown in Figure 1.2. This has led to hard disk drives that are small, light and powerful in comparison to RAMAC. Magnetic recording technology is now ubiquitous and can be found in applications such as laptops, digital television, personal video recorders and iPods.

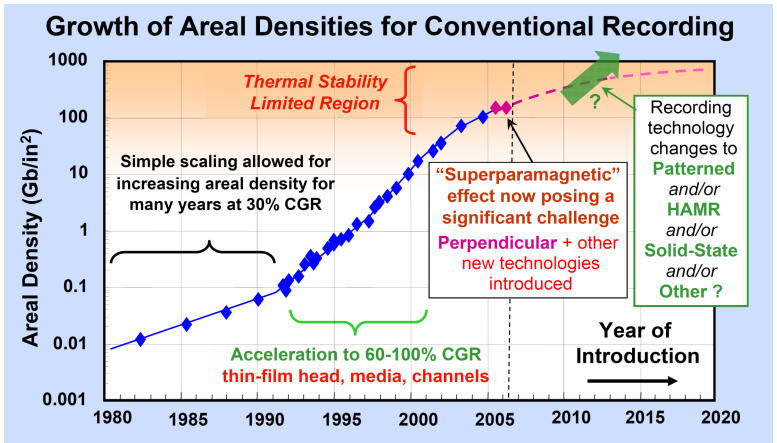

Figure 1.2: The number of bits stored per unit area of disk surface (areal density) for products from 1980 to 2006 (Wood and Takano, 2006).

1.2 Developments in magnetic recording

The earliest traditional form of magnetic recording in hard disk drives was longitudinal recording (see section 2.3) where the recorded information is represented by magnetisation patterns in the plane of a disk. In order to increase recording densities, a scaling approach where all relevant physical dimensions of the system are scaled in the same proportion (Mallinson, 1996) was applied. Apart from the scaling approach, new materials and better sensors have also led to an increase in recording densities (see Figure 1.2). In longitudinal recording, the demagnetising fields between regions of opposite magnetisation produce a destabilising effect that prevents higher recording densities from being attained.

Perpendicular recording (see section 2.4) was introduced in 2006 and is the current technology used in hard disk drives where the recorded information is represented by magnetisation patterns oriented perpendicular to the disk surface (Iwasaki, 1980). The application of the traditional scaling approach has become limited by thermal stability, write-ability and signal to ratio (SNR) requirements (see section 2.5) which affect each other. These competing effects will probably limit the areal density up to around 1 Tb/in^2 (Kryder and Gustafson, 2005; Richter, 2007; Wood *et al.*, 2002; Wood, 2000).

A number of approaches have been proposed in an effort to extend recording densities beyond the capabilities of conventional approaches. One of the promising approaches is recording on Bit Patterned Media (BPM) which provides thermal stability (Weller and Moser, 1999; Hughes, 2000) and is the focus of this research. In BPM (see section 2.6.1), the medium is patterned into nanometer-sized magnetic islands where each stores one bit.

Other approaches involve supplying additional sources of energy to assist the write head to write on higher anisotropy media. Such methods are referred to as Energy Assisted Magnetic Recording (EAMR). This can be done by either heating the medium as done in Heat Assisted Magnetic Recording (HAMR) (Ruigrok *et al.*, 2000; Moser *et al.*, 2002) or by the addition of a radio frequency magnetic field which occurs in Microwave Assisted Magnetic Recording (MAMR) (Zhu *et al.*, 2008). There are challenges associated with these approaches despite being capable of extending areal densities, and these are discussed in section 2.6.2.

In addition to BPM and EAMR, there is an alternative approach called Two-Dimensional Magnetic Recording (TDMR) which instead uses advanced signal processing applied to conventional media to extend recording densities (Wood

et al., 2009) and thus avoids the challenges associated with BPM, HAMR or MAMR. This is further explained in section 2.7.

The three approaches, BPM, EAMR and TDMR represent attempts to increase recording densities by improvements to media, heads and signal processing respectively. Historically all of these have improved in parallel and it is likely that all three approaches will contribute.

Islands in BPM tend to vary in geometry, position and magnetic properties due to tolerances introduced during fabrication and it is thought that these will cause write errors in BPM (Richter *et al.*, 2006b). Although BPM samples of credible densities have been made, a number of problems remain, one of which is to predict the timing margin available for synchronising the write head switching position with respect to the target island in order to achieve a required Bit Error Rate (BER) (Richter *et al.*, 2006b). Understanding of this requirement will inform media designers of the key parameters in media design, and will enable the design parameters of servo systems to be determined.

1.3 Research Aims and Objectives

It has been established that the distribution of island position, geometric and magnetic parameters give rise to errors when writing data (Richter *et al.*, 2006a,b). For BPM to be adopted, there should be low errors rates (around 10^{-6} to 10^{-4}) during writing. In addition, the probability of flipping the magnetisation of the recorded bit due to random thermal events should be low.

A number of models have been proposed to study the impact of distributions of island properties on the recording performance of BPM (see section 3.4). The original statistical model proposed by Richter *et al.* (2006b) is extremely efficient and can be used to study data storage errors due to incorrect write head timing relative to the intended island to be written and errors arising from distribution of switching fields. However, some assumptions introduced in some aspects of the derivation underestimate the major contributions of write errors.

Other models rely on micromagnetic simulations such as those proposed by Schabes (2008); Livshitz *et al.* (2009a,b); Greaves *et al.* (2010). Despite being accurate, such models are inherently very time consuming owing to the nature of micromagnetic simulations.

In order to achieve low error rates during data storage, simulations of very

large numbers of islands would be required. This is not practical using normal micromagnetic simulation models whereas Richter's model (Richter *et al.*, 2006b) is very simple but limited. Therefore an efficient but realistic model that captures the essential features of data storage and that avoids the assumptions of previous models without resorting to micromagnetic simulation of huge populations of islands is desired.

Due to the unpredictable nature of the fabrication process, practical islands tend to vary in size, shape, spacing and magnetic properties. It is these variations that are thought to be sources of data storage errors in BPM (Richter *et al.*, 2006a,b).

During data storage, the write head traverses over islands and attempts to write data on a target island as shown in Figure 1.3. As the head attempts to

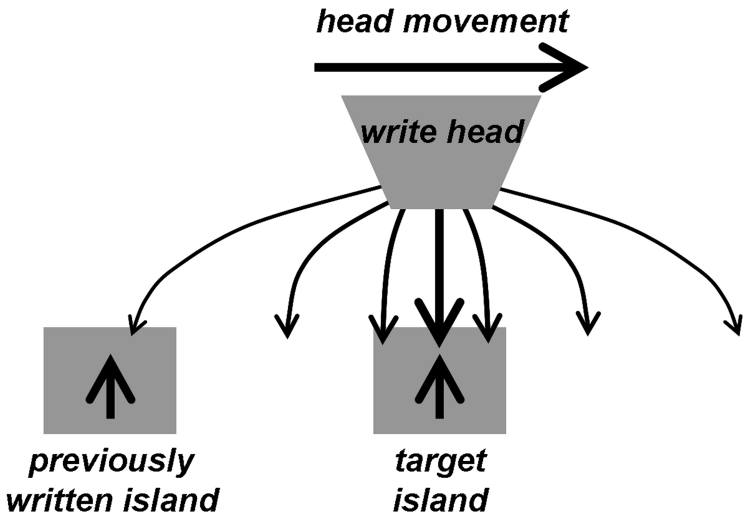

Figure 1.3: Write head traversing islands as it attempts to write a target island.

write the current (target) island, the field strays over neighbouring islands. There is a possibility that the target island may fail to be written. This can occur if its switching field (anisotropy) is higher than the average. This can also happen because of island position variations or the head is not at the right position. In addition to this, there is a risk that the previously written island shown in Figure 1.3 or islands on adjacent tracks could be overwritten. This can occur if the switching field (anisotropy) is lower than the average. This can also happen thermally, by random excitation in the presence of a destabilising field. The previously written island or islands on adjacent tracks could be overwritten because of island position variations or the head not being at the right position. Since

data storage errors are inevitable, it is important to understand how accurately the write head needs to be positioned in order to keep errors acceptable.

The aim of this research is to study the effect of variations of island position, geometry and magnetic properties on data storage errors. This should provide a model that can predict the timing margin available at a given BER for a specified head field.

The statistical write model will be based upon efficient but realistic calculations of data storage on single islands that can be developed into a statistical model. Since islands are not all identical, the first task involves studying the dependence of switching field on island geometric properties (shape or size).

This is to be followed by a calculation of the probability of thermally activated writing of an island with a given switching field in an arbitrary vector head field. An approach to incorporate distributions of island properties in a calculation of switching probabilities is to be devised. Having obtained switching probabilities, the write-window is to be determined. The write-window is the region within which the head must switch field direction in order to write the target island and only the target island with an acceptable error rate. The last task involves calculating total errors, which arise not only from the write head failing to correctly write data along the main track but also arising from accidentally overwriting islands on adjacent tracks.

1.4 Research contributions

An analytic method of computing magnetometric demagnetising factors for truncated elliptic cones that reasonably describe proposed island shapes has been devised. This led to a derivation of an analytic model for switching fields for islands having this geometry. The model predictions were in excellent agreement with micromagnetic simulation results for island sizes of interest. The study revealed that the switching fields of islands in BPM vary less with island size but somewhat more with island ellipticity and sidewall angle. The analytic model suggested that islands with a non 1:1 Bit Aspect Ratio (BAR > 1) may worsen write errors on adjacent tracks, and that cylindrical islands might therefore be optimal. The model was extended to predict switching fields for non-uniform applied fields and the results were in excellent agreement with micromagnetic simulations.

An analytic expression for the energy barrier of a single domain uniaxial particle for magnetisation rotation confined to a plane at any applied field angle was derived. A method to compute the energy barrier for Exchange Coupled Composite (ECC) media in a two-spin approximation that does not rely on switching fields was also developed. The results also showed that ECC islands can be designed to switch at a similar field to single domain islands but retain a significant energy barrier in the presence of an external field. The energy barrier is used in a calculation of transition rates and this led to a derivation of the switching probability that takes into account thermal activation at a given head position. This eventually developed into an accurate and computationally efficient error model for down-track write errors.

A method of incorporating distributions of island position, magnetic and geometric parameters was devised. The model showed that island geometric (size or shape) property variations have less impact on write errors than island position or anisotropy variations.

This was followed by a method of calculating off-track errors that arise when the head is not perfectly aligned on-track. Studies of Adjacent Track Erasure (ATE) showed that ATE would be a major problem and that cross-track head field gradients need to be more tightly controlled than down-track. With the write head used, recording at 1 Tb/in^2 would be possible on single domain islands.

1.5 Thesis outline

Chapter 2 reviews the past and current approaches of magnetic recording followed by limitations that arise in the search to further advance magnetic recording. Promising approaches to delay the onset of these limitations in order to extend areal densities, notably Bit Patterned Media (BPM), are discussed.
Chapter 3 provides a review of current models of magnetic recording in detail followed by a discussion of models relevant to BPM. Limitations of these models are discussed which form the basis of the development of a new model for data storage in BPM.
Chapter 4 presents the development of a statistical model of BPM. A method to compute the demagnetising factors of truncated elliptic cones, a generalised geometry that describe proposed island geometries is devised. The dependence of switching fields on island geometry and various applied field orientations in

uniform fields is studied using the model. The switching of islands in non uniform fields is also presented. In the study of switching fields, the model results are validated against micromagnetic simulations.

Chapter 5 continues the development of the statistical write model. An analytic expression for the energy barrier of a single domain uniaxial particle for magnetisation rotation confined to a plane is derived. Following this is a derivation of the probability of thermally activated switching during the data storage process. The calculation of switching probability uses the derived energy barrier expression. A method of incorporating distributions of island properties in a calculation of the switching probability is presented. This is followed by a method to include magnetostatic interactions. Finally, an extension to two layer island structures is discussed.

Chapter 6 presents one-dimensional simulation results using a write head whose field distribution varies only in one dimension. The problem of synchronising the write head switching position with the island to be written in order to achieve a given required Bit Error Rate (BER) is studied. A write-window analysis which enables a quantitative study of write head synchronisation is presented. Distributions of island properties and their impact on the write-window are also presented. The chapter concludes by comparing model predictions with other models.

Chapter 7 presents two-dimensional simulation results, where in addition to studying on-track errors, errors arising from overwriting islands on adjacent tracks for repeated writings on the main track are presented. Finally, two-dimensional maps of BER are presented.

Chapter 8 reports the main findings of the research project and possible directions for future work.

Chapter 2

Magnetic recording: limitations and proposed solutions

2.1 Introduction

This chapter provides an overview of magnetic recording. To begin with, the principle of magnetic recording is described. This is followed by a description of traditional and current forms of magnetic recording. Following this is a discussion of limitations of these forms of recording in further extending recording densities. The chapter then outlines some alternative approaches that can be used to further extend magnetic recording densities.

2.2 Principle of magnetic recording

In order to perform magnetic recording, a recording medium and a recording head are required (Richter, 1999). The recording medium consists of a substrate that contains magnetic particles whereas the recording head is an electromagnet that produces a magnetic field that is driven by a current coded with information to be recorded. During the recording process, the head moves relative to the medium and the magnetic fields produced magnetise the particles in the medium leading to the storage of data. During the replay process, as the head traverses the medium, the flux from the medium entering the head leads to a read-back signal. The data is then read back using electromagnetic induction where the rate of change of flux entering the head manifests itself as an induced voltage.

Figure 2.1 shows a schematic of the magnetic recording process. The diagram

shows the head that moves relative to the medium and the magnetisation patterns left by the head. The medium in this case is magnetised along the film plane which is referred to as longitudinal recording (see section 2.3). At higher

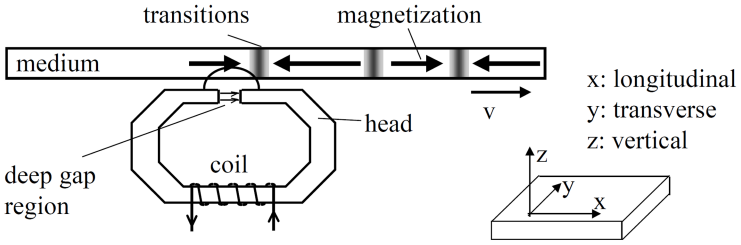

Figure 2.1: Longitudinal magnetic recording schematic (Richter, 1999). The head produces magnetic fields that magnetise the particles in the medium.

recording densities, inductive read-back does not provide the necessary sensitivity and thus current hard disk drives use *magnetoresistive* (MR) heads to read back the data (Richter, 1999). Magnetoresistive materials have a unique property of changing their resistance in the presence of a magnetic field. The drop in voltage across them is used as a basis to detect flux. Thus MR materials detect magnetic flux and not flux change which makes the read-back process independent of the head velocity relative to the medium (Richter, 1999). Various types of MR devices have been used including Giant Magnetoresistive (GMR) and Tunneling Magnetoresistive (TMR) devices.

2.3 Longitudinal magnetic recording

Longitudinal magnetic recording has been the form of storage used in hard disk drives until 2006 (Wood *et al.*, 2007). In this form of storage, the magnetisation of the recorded bit which represents the recorded information lies in plane of the recording media as shown in Figure 2.2. This is because the magnetic anisotropy of the particles creates a fictitious field referred to as the anisotropy field that in this case is directed along the plane thereby aligning the magnetisation in plane. The system comprises a recording head with two elements, one for reading and the other for writing data. The purpose of the inductive write element is to record data which in this case refers to magnetisation patterns in the plane of the disk. As the head moves, the magnetic fields produced magnetise the medium

appropriately leading to the storage of data. A region separating opposite magnetisation patterns is called a *transition*. The presence or absence of a transition represents a binary digit (bit) that is either a 0 or 1.

Identical successive bits give rise to regions that are continuously magnetised in the same direction. Where data values change from 1 to 0 or 0 to 1 the magnetisation directions of the two regions are opposite with a narrow transition region between them in which the magnetisation varies along the track direction. The track direction is defined by the write head as it moves and magnetises the medium. To maximise the amount of data that can be stored and to enable the data clock to be recovered, the input (or user) data is encoded in an electronic system before being magnetically written so that the data is effectively stored as the presence or absence of transitions. The read element reads back the information by measuring the stray field arising from the transitions between regions of opposite magnetisation.

The arrangement of demagnetising fields produces a destabilising effect on the written magnetisation as shown in Figure 2.3 (White, 2000). The demagnetising fields not only broaden the transitions, which is not desirable at higher recording densities but also make the magnetisation less stable in that the fields act to oppose the direction of magnetisation. In order for the magnetisation to reverse its direction an amount of energy is required. This is referred to as the *energy barrier* that prevents spontaneous reversal. The demagnetising fields reduce the energy barrier and increase the probability that random thermal fluctuations will cause data to be lost. This shows that longitudinal recording is not favourable in attaining higher recording densities. According to Wood and Takano (2006) and as shown in Figure 1.2, products using longitudinal recording can have magnetic recording densities up to 100 Gbits/in^2.

2.4 Perpendicular magnetic recording

Perpendicular magnetic recording was introduced into the hard disk drive in 2006 (Wood *et al.*, 2007). Figure 2.4 shows a schematic of perpendicular magnetic recording. In this form of recording, the magnetisation is aligned perpendicular to the plane of the medium (Iwasaki, 1980). The system also comprises a recording head with two elements, one for reading and the other for writing data. The purpose of the inductive write element is to record the magnetisation which in

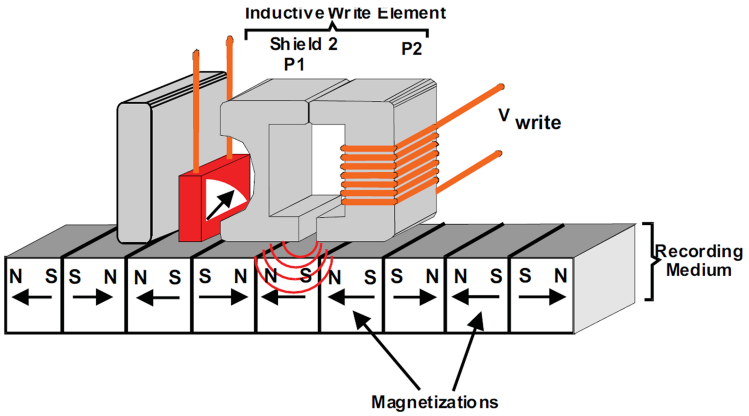

Figure 2.2: Longitudinal magnetic recording schematic (Wood *et al.*, 2007). The magnetisation of the recorded bit lies in plane of the recording medium.

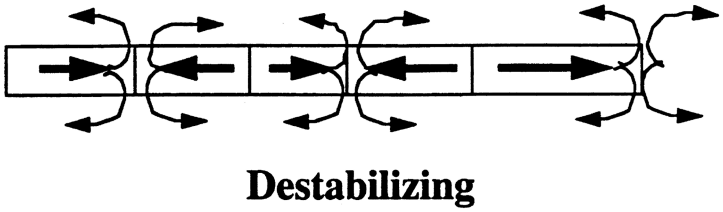

Figure 2.3: Destabilising effect in longitudinal magnetic recording (White, 2000). Thick arrows represent the magnetisation whereas fine arrows represent demagnetising fields.

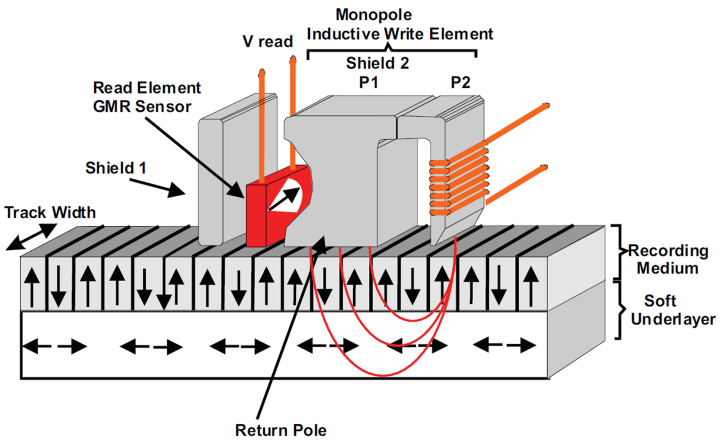

Figure 2.4: Perpendicular magnetic recording schematic (Wood *et al.*, 2007). The magnetisation of the recorded bit lies in a plane perpendicular to the disk surface.

this case is in a plane perpendicular to the disk surface. Similar to longitudinal recording, the read element reads back the information by measuring the stray field arising from the magnetised regions. The soft underlayer ensures that the flux from the write pole is concentrated within a region between the pole tip and the soft underlayer (Wood *et al.*, 2007). The recording layer lies in this region where the flux is intense. In this case, higher head fields can be experienced by the medium which makes it possible to write high coercivity media. In addition, the soft underlayer serves to strengthen the read-back signal and thus reduces the interference from adjacent tracks. This arises from the imaging effect of the soft underlayer.

Perpendicular magnetic recording alleviates the thermal stability problem encountered in longitudinal magnetic recording. It was mentioned in section 2.3 that in longitudinal recording, the demagnetising fields cause the magnetisation to be less stable. Consider a regular 010101... data pattern as shown in Figure 2.5. At the centre of the transition, the magnetisation is an antisymmetric function and thus the field produced by the material to the right exactly cancels that from the left and the demagnetising field, H_d, vanishes at the transition centre. At low density in SI units $H_d = -M_r$ where M_r is the magnetisation at the bit centre. As the density increases each bit becomes shorter in length until the finite gradient $\mathrm{d}H_d/\mathrm{d}x$ results in a peak value of H_d that is less than M_r and the destabilising effect of H_d is reduced. As density is further increased the peak demagnetising field reduces further and perpendicular recording becomes more stable.

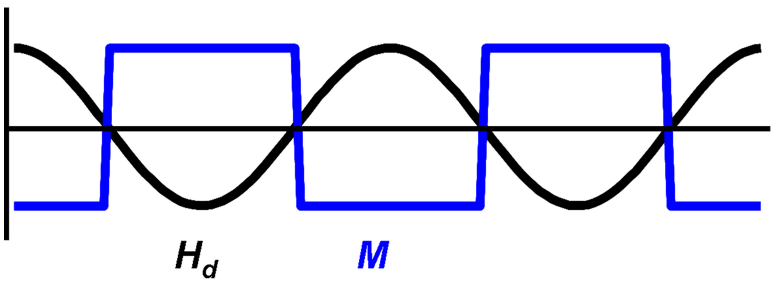

Figure 2.5: Less destabilising effect in perpendicular magnetic recording. Shown are the perpendicular components of the magnetisation (M) and demagnetising field (H_d).

In addition, the grains can be made larger by increasing their vertical dimension and reducing the in-plane dimension which enhances thermal stability (White, 2000). This arrangement favours attaining higher recording densities. A

study by Bertram and Williams (2000) showed that perpendicular recording has $4-5:1$ density advantage over longitudinal recording. As shown in Figure 1.2, perpendicular magnetic recording was introduced in a regime where thermal stability was already limited and the areal density growth was slowing down, thus a search to further increase areal densities implied maintaining thermal stability, but doing so introduced other problems. These are discussed in the next section.

2.5 Conventional magnetic recording limitations

The growth in magnetic recording densities in conventional recording as shown in Figure 1.2 has been achieved through scaling the recording process. According to Mallinson (1996), scaling implies changing all relevant physical dimensions in the same proportion. The reduction in bit size, in particular, has led to small grain sizes since a sufficient number of grains is required in a bit to maintain a satisfactory *Signal to Noise Ratio* (SNR). Apart from the scaling approach, new materials and better sensors have also led to an increase in recording densities (see Figure 1.2).

Towards the end of the 1990s it was known that the traditional scaling approach would reach a fundamental limit as small magnetic grains of the recording medium became thermally unstable (Richter, 1999). This eventually results in the loss of stored data. Such grains are said to be *superparamagnetic* in that their behaviour is similar to paramagnets. Paramagnets have no net magnetic moment in the absence of an applied field and their moment is proportional to the applied field. In a paramagnet if the field is instantly switched off it takes some time for the magnetisation to relax back to zero. The superparamagnetic limit affects both longitudinal and perpendicular recording.

The magnetic energy stored in a grain is K_1V where K_1 represents the magnetic anisotropy energy density (see section 3.3) and V is the volume of the grain. It requires an energy K_1V to reverse the grain and when the thermal energy k_BT, where k_B is the Boltzmann constant and T is the absolute temperature, becomes comparable to K_1V it may spontaneously reverse. This leads to *thermal decay* and ultimately superparamagnetism.

One way to avoid superparamagnetism is to use grains having high values of K_1. This not only guarantees thermal stability but also increases the anisotropy field, H_K, a fictitious field that aligns the magnetisation along the easy axes.

Since the field required to reverse the magnetisation is proportional to H_K, a higher write head field is required. However, head fields are dependent upon the head materials, the largest of which is 2.4 Tesla, obtained from *cobalt–iron* (CoFe) material (Richter, 2007). Thus, it is observed that there are limitations on *write–ability*. From this explanation, it is seen that an attempt to overcome one undesirable effect affects other constraints. These three competing effects (*SNR*, *thermal stability*, *write–ability*) are collectively referred to as *trilemma* in the literature (Richter, 2007). Because of these, conventional perpendicular magnetic recording is expected to be limited to an areal density of 1 $\mathrm{Tb/in^2}$ (Kryder and Gustafson, 2005; Richter, 2007; Wood *et al.*, 2002; Wood, 2000).

2.5.1 Exchange Coupled Composite (ECC) media

Exchange Coupled Composite (ECC) systems or exchange systems were originally used in bulk permanent magnets (Kneller and Hawig, 1991) and in thin films (Fullerton *et al.*, 1998) to optimise the energy product. The idea of ECC media or exchange coupled media was introduced in magnetic recording by Suess *et al.* (2005) and independently by Victora and Shen (2005) which theoretically makes it possible to extend magnetic recording densities beyond the original predicted onset of superparamagnetism (Albrecht *et al.*, 2009). An ECC type medium consists of a soft magnetic layer exchange coupled to a hard magnetic layer. A demonstration of the capability of ECC type media for recording purposes was carried out by Wang *et al.* (2005). The study reported that the write-ability of the medium could be improved while thermal stability is retained and that the switching field is less sensitive to angle dispersion in comparison to perpendicular media.

A simple ECC type medium has two layers exchange coupled to each other at the interface. Figure 2.6 shows a two layer island model. The magnetic moment of the low anisotropy layer (soft) rotates easily in an applied field. The moment of the high anisotropy layer (hard) does not rotate easily in an applied field. The high anisotropy layer ensures that the moments in the hard layer are aligned to the anisotropy in the absence of an applied field. This ensures that the probability of flipping the moments due to random thermal events is very low in the absence of an applied field which leads to thermal stability. The interlayer exchange coupling ensures that the moments in the hard and soft layers are coupled to each other and that the reversed top layer helps the bottom layer to switch. This implies

that a lower field than required to switch the hard layer causes the magnetisation in the lower layer to start reversing and thus in addition to the external field there is an exchange field.

The magnetisation reversal process in such a structure is incoherent which can lead to lower switching fields compared to single layer structures but having a high thermal stability. These collective features, when optimised, can lead to a system that supports higher recording densities. In this way, thermal stability can be achieved and the write-ability problem addressed. However, this approach is likely to encounter a limit at further higher recording densities whereby new approaches will be required (Albrecht *et al.*, 2009).

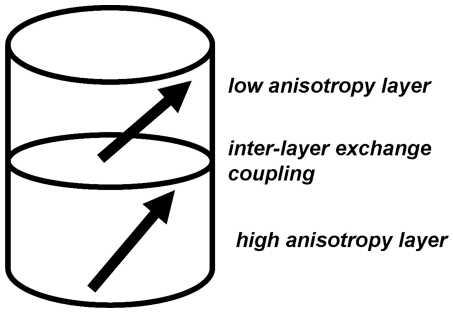

Figure 2.6: Two layer Exchange Coupled Composite (ECC) island model. The magnetisation in the low anisotropy layer rotates easily in an applied field. The high anisotropy layer provides thermal stability. The interlayer exchange coupling ensures that the reversed top layer helps the bottom layer to switch.

2.6 Approaches to extend magnetic recording densities beyond 1Tb/in^2

A number of approaches have been proposed to further extend recording densities beyond the capabilities of conventional magnetic recording. Outlined below are approaches that are likely to replace conventional magnetic recording.

2.6.1 Bit Patterned Media

Magnetic recording on Bit Patterned Media (BPM) is a promising approach to extend magnetic recording densities in that it provides thermal stability (Hughes, 1999, 2000; Weller and Moser, 1999) and consequently postpones the onset of

superparamagnetism (White *et al.*, 1997). In BPM, the medium is patterned into nanometer sized magnetic islands (see Figure 2.7) where each represents a binary digit (bit). These islands are not exchange coupled to each other, unlike grains in conventional media, but experience magnetostatic interactions from others. Figure 2.8 shows a schematic of recording on BPM. BPM has the potential to extend magnetic recording densities beyond 1 Tb/in^2 (Albrecht *et al.*, 2009).

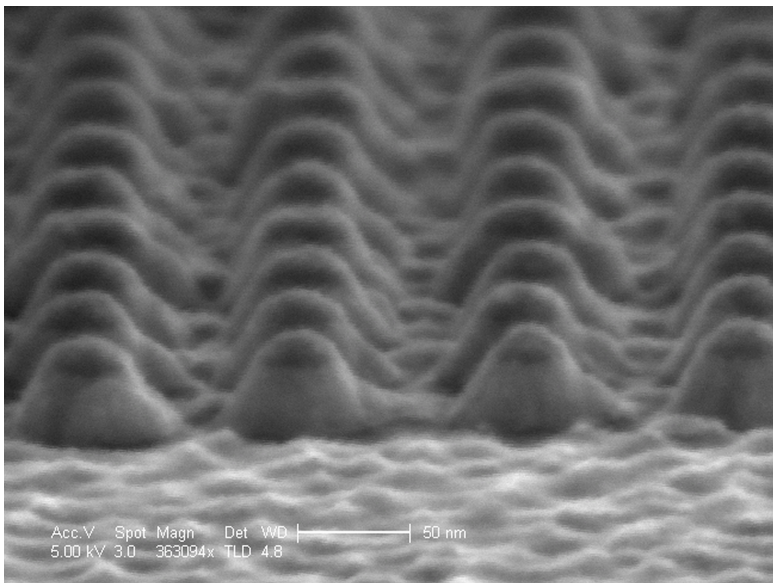

Figure 2.7: Scanning Electron Microscope (SEM) image of real islands (Belle *et al.*, 2008, 2007) where the lighter shaded material in the shape of truncated cones is magnetic. This shows that real islands are not identical but can vary in size and shape.

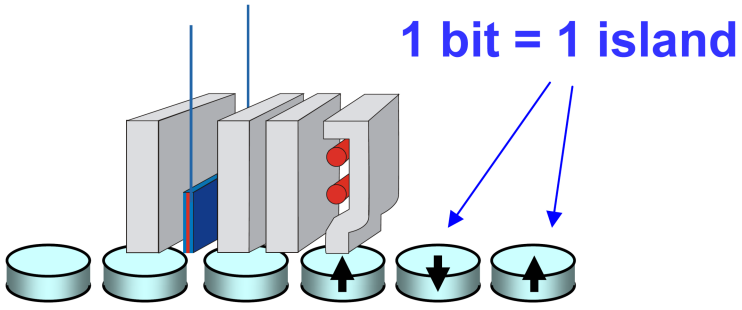

Figure 2.8: Recording on Bit Patterned Media schematic (Wood and Takano, 2006). Shown is the read head, write head and islands.

According to Albrecht *et al.* (2009) there are, in general, two approaches to

fabricate BPM. One approach involves patterning substrates before any magnetic media is deposited on them followed by deposition of the magnetic thin film on the pre-patterned substrates. This approach has an advantage in that there is no etching of the magnetic material and the optimisation of patterning and the recording media can be carried out independent of each other.

The other approach involves the deposition of magnetic media as a continuous thin film after which the film is patterned into discrete islands. The advantage of this approach is that it leaves no magnetic material between islands and that the overgrowth of islands is avoided since the film is grown on a flat substrate.

Recording on BPM differs to recording in conventional continuous granular media in a number of ways. The SNR in conventional recording depends on the transition jitter which is influenced by the size and distribution of the grains and the distribution in switching fields and write field gradients (Albrecht *et al.*, 2009). In BPM, the most likely source of media noise arises from patterning tolerances introduced during the fabrication process (Albrecht *et al.*, 2009). The other difference is that BPM recording requires synchronised writing where the write clock is synchronised with individual islands under the write head whereas this is not necessary in conventional recording (Albrecht *et al.*, 2009). Following are some of the potential benefits of BPM (Moser *et al.*, 2002; White *et al.*, 1997).

- The volume of an island is much larger than that of a grain usually used in conventional recording media, implying that the thermal stability is enhanced.
- The head fields required to write data on an island are not different from those used in conventional media, since the anisotropy is not affected.
- The arrays of islands could result in an acceptable SNR even for larger recording densities.
- The transition and track edge noise are reduced.
- The *tracking* process is simplified.

Despite the potential benefits, there are challenges that arise in BPM. One major challenge is related to fabrication. The use of *electron beam lithography* (EBL) which provides the high resolution required to produce small islands is expensive and time consuming (Moser *et al.*, 2002; Albrecht *et al.*, 2009). To

resolve this problem, according to Albrecht *et al.* (2009), a likely route will involve creating a master pattern by electron beam lithography and self assembly and then copying this pattern to disks using *nanoimprint lithography* (Chou *et al.*, 1996). Apart from the fabrication problem, another important challenge is the difficulty in synchronising the write head current waveform on a nanoscale to individual islands as the head traverses over islands (Moser *et al.*, 2002, 2007; White *et al.*, 1997).

Due to the unpredictable nature of the fabrication process, the islands do not follow a strict pattern and tend to vary in size, shape, spacing and magnetic properties. It is thought that these will cause write errors in BPM (Richter *et al.*, 2006b). As pointed out by Thomson *et al.* (2006), the switching field distribution originates from distributions of anisotropy, magnetisation, exchange, magnetostatic interactions and island geometry.

A study of the areal density potential of BPM was carried out by Richter *et al.* (2006a,b). According to their analysis, the recording performance of BPM will be dominated by *written-in errors* which arise from statistical variations in magnetic properties, geometric properties and positions of islands. Written-in errors or hard errors occur when the write head fails to write data on an intended island or writes it onto the wrong island. Five sources of noise that worsen the system performance and contribute to the *read-back medium* SNR are variations in island spacing, size, shape, thickness and saturation magnetisation (Richter *et al.*, 2006a,b). They concluded that recording on BPM at recording densities beyond 1 Tb/in^2 is possible but requires tight distributions in magnetic properties and positions of islands.

An analysis by Richter *et al.* (2006a,b) also pointed out that to attain even higher recording densities, BPM composed of more advanced islands each of which contains several layers exchange coupled to each other will be required. Such media are referred to as Exchange Coupled Composite BPM or ECC BPM.

Moser *et al.* (2007) studied the dependence of written-in errors in BPM on the off-track position of the write head using a static write/read tester. Their study illustrated the importance of on-track head alignment and, in particular, the relationship between error rates and write head off-track position.

At extremely higher recording densities, BPM might likely be combined with energy-assisted magnetic recording, also referred to as second-generation BP recording (Schabes, 2008). This approach to recording is explained in the next

section.

2.6.2 Energy Assisted Magnetic Recording

The idea of Energy Assisted Magnetic Recording (EAMR) is to assist the head to write higher anisotropy media that otherwise would not been possible using the available head fields. This can be done by either heating the medium or by the addition of a microwave frequency magnetic field.

2.6.2.1 Heat Assisted Magnetic Recording

One form of EAMR is Heat Assisted Magnetic Recording (HAMR). In HAMR, the reduction in the magnetic anisotropy of the medium with increased temperature is exploited (Ruigrok *et al.*, 2000; Moser *et al.*, 2002). Figure 2.9 shows a schematic of a HAMR system. A recording medium having a very high magnetic anisotropy

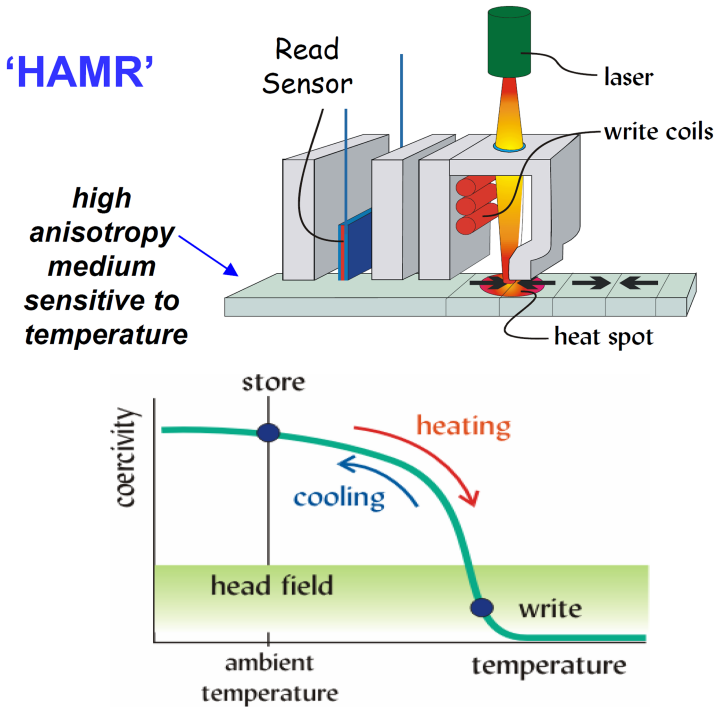

Figure 2.9: Heat Assisted Magnetic Recording schematic (Wood and Takano, 2006).

is temporarily heated using a laser during the write process resulting in a medium with lower anisotropy. In this way, the switching field, which is the value of the field required to switch the magnetic state of the medium, is significantly reduced

and the write head field becomes sufficient to reverse the magnetisation. After heating, the medium is quickly cooled back to ambient temperature to complete the write process. Since very high values of magnetic anisotropy can be used, this guarantees improved thermal stability.

Despite this being a promising approach, there are a number of practical challenges to be addressed. During the write process, the medium temperature can rise by about 300 K or higher, which implies an effective thermal management system would be required since repeated heating could lead to deformation of the head and the medium (Pan and Bogy, 2009). The heated spot must also be no wider than the track, which is substantially below the wavelength of light.

2.6.2.2 Microwave Assisted Magnetic Recording

According to Zhu *et al.* (2008), Microwave Assisted Magnetic Recording (MAMR) is another mechanism that enables the write head to write higher anisotropy media using fields significantly below the media coercivity. Their study revealed that an applied field as low as one-third of the media coercivity could be sufficient to reverse the magnetisation under certain applied field angles.

In this form of recording, a pulsed magnetic field is applied in a direction opposite the initial magnetisation direction. In addition to this, a localised ac field at microwave frequencies is applied in a direction perpendicular to the initial magnetisation direction. The ac field enables the magnetisation to increase the precessional angle and thus precesses towards the other equilibrium magnetisation position. This mechanism enables a pulsed field to switch magnetisation at a field significantly lower than the medium coercivity due to the absorption of energy from the ac field (Zhu *et al.*, 2008). Figure 2.10 shows a schematic of the fields and the magnetisation trajectory in MAMR. To achieve the lowest switching field, the frequency of the transverse ac field should match the ferromagnetic resonant frequency (FMR) of the media.

There is a threshold pulse duration for reversal to occur if the energy absorption rate exceeds the damping rate. For pulse durations below the threshold it is not possible to switch the magnetisation (Zhu *et al.*, 2008). For completeness, an oscillator to generate the necessary localised microwave frequency magnetic field was also proposed. However, there is a technical challenge in producing a component that generates an efficient ac field and furthermore, the anticipated gain in recording density using MAMR would not be sufficient to reach 10 $\mathrm{Tb/in^2}$

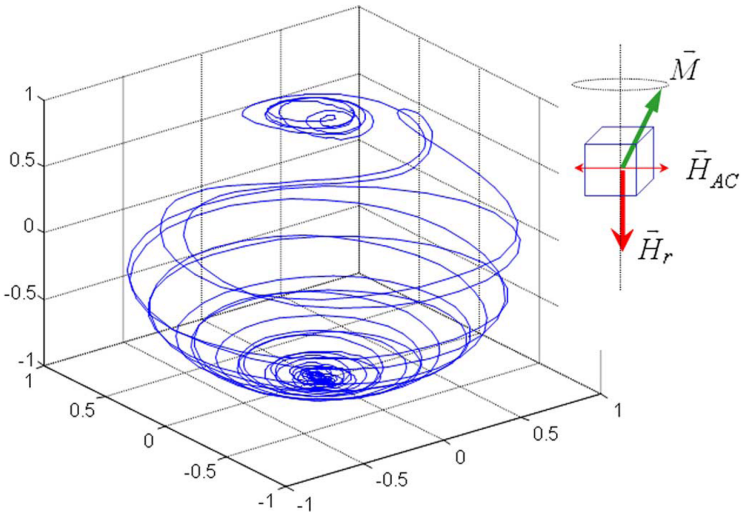

Figure 2.10: Microwave Assisted Magnetic Recording principle: magnetisation trajectory and applied fields (Zhu *et al.*, 2008).

according to Shiroishi *et al.* (2009). There is another problem that the frequency has to accurately match the FMR frequency, which depends on the anisotropy field. The anisotropy field varies in practical media and thus some grains/islands might not switch. Winkler *et al.* (2009) proposed a multi-layer system where each layer had different anisotropy field and frequency so that separate layers can be written selectively.

2.7 Two-Dimensional Magnetic Recording

Two-Dimensional Magnetic Recording (TDMR) is an alternative approach which uses conventional media to extend recording densities and thus avoids the challenges associated with BPM, HAMR or MAMR.

In TDMR, radical methods for writing, read-back and signal processing are employed (Wood *et al.*, 2009). The writing is carried out through shingled write recording (SWR) where overlapping tracks are written sequentially by a wide write pole that has a side shield only along the track edge (Wood *et al.*, 2009; Shiroishi *et al.*, 2009). To perform a two dimensional read-back, sophisticated signal processing techniques that rely on the adjacent track waveforms are employed (Wood *et al.*, 2009). The ultimate goal of TDMR is one bit per grain which can yield recording densities of 10 Tb/in^2 (Wood *et al.*, 2009) and this limit can be

reached provided that the writing and read-back processes have a high resolution and low noise (Shiroishi *et al.*, 2009).

Advantages of shingled writing include the elimination of Adjacent Track Erasure (ATE), availability of high write field from larger write pole, sharp corner-edge fields (Shiroishi *et al.*, 2009). However, when a track is to be updated all preceding tracks should be initially recovered and rewritten which is a disadvantage of shingled writing.

2.8 Summary and Conclusions

This chapter has reviewed the traditional and current forms of magnetic recording. The scaling approach used to extend recording densities in the traditional forms of recording led to a discussion of three competing effects, referred to as the trilemma, which limit magnetic recording densities in these media. Some techniques to extend the limits have been reviewed.

In order to achieve recording densities beyond the capability of conventional media requires new approaches. This led to a discussion of promising approaches such as BPM, where the media is patterned into nanometer sized magnetic islands. The benefits and challenges of BPM have been discussed. Apart from BPM, energy assisted magnetic recording approaches such as HAMR and MAMR have been discussed including the challenges associated with them. To achieve even higher recording densities BPM is likely to be combined with energy assisted approaches. The chapter has also discussed TDMR, an approach that uses conventional recording media to further extend recording densities but using different means of writing, read-back and signal processing. BPM recording (BPMR), EAMR, TDMR effectively each address only one component of the system and one corner of the trilemma as shown in Figure 2.11. In reality all these will be used to some extent.

The next chapter covers current models of magnetic recording.

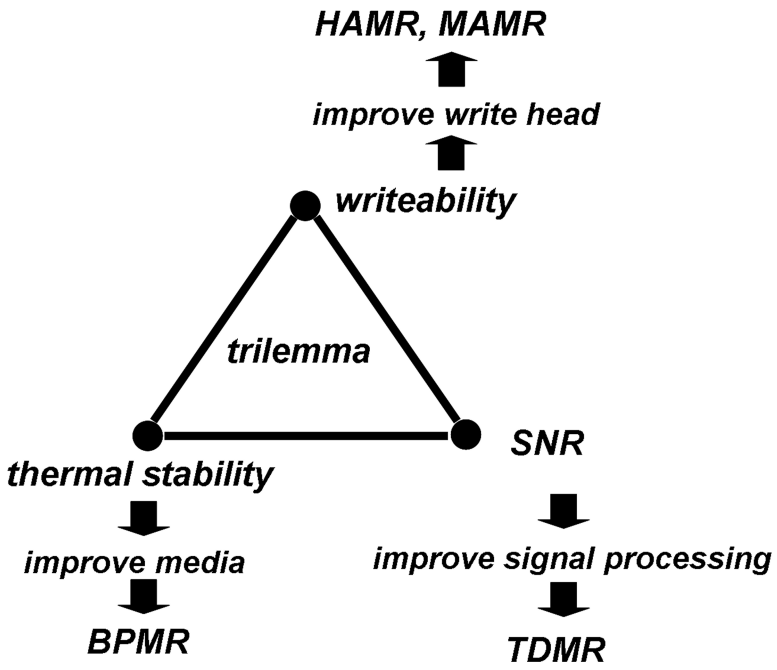

Figure 2.11: Trilemma of magnetic recording and possible solutions.

Chapter 3

Current models of magnetic recording

3.1 Introduction

This chapter presents current models of magnetic recording. To begin with, the Stoner–Wohlfarth model is presented. This is followed by a description of micromagnetic models where static and dynamic micromagnetics are considered. Thermal activation is also considered. The chapter then introduces models of magnetic recording in BPM.

3.2 Stoner–Wohlfarth model

The *Stoner–Wohlfarth* model (Stoner and Wohlfarth, 1948) is a simple but useful model that sufficiently explains the physics of single domain ferromagnetic particles in the presence of an applied field (Tannous and Gieraltowski, 2008). Stoner and Wohlfarth (1948) pointed out that ferromagnetic materials are composed of particles having distinct magnetic properties from the matrix surrounding them and for sufficiently small particles, the *exchange energy* (see section 3.3) ensures that the magnetic spins are held parallel to each other. This implies that the magnetisation is uniform inside a particle. Any space dependence of magnetisation costs a lot of energy and is thus not allowed for such small particles (Aharoni, 2000, p. 105) in which case the exchange energy is taken as a constant. The space dependence can be allowed for larger particles because the *magnetostatic energy*

contribution is not negligible and thus favours the creation of domains (see section 3.3). Such small particles are referred to as *single domain* particles and an assumption was made that they were well separated from each other and thus interactions between them were neglected (Stoner and Wohlfarth, 1948). These particles are now referred to as *Stoner–Wohlfarth* particles in the contemporary literature and they make reasonable representations of the islands in patterned media. Therefore, the study of their behaviour in an applied magnetic field is essential.

Stoner and Wohlfarth (1948) studied the problem of determining the equilibrium direction(s) of the magnetisation of a particle whose shape is described by an ellipsoid of revolution as shown in Figure 3.1 where an external magnetic field was applied at certain directions relative to the major axis of the ellipsoid. Only two energies were considered in the minimisation to determine the equilibrium magnetisation direction; the magnetostatic energy and the interaction with an applied field. Since the exchange energy is constant, it can be excluded from the energy minimisations.

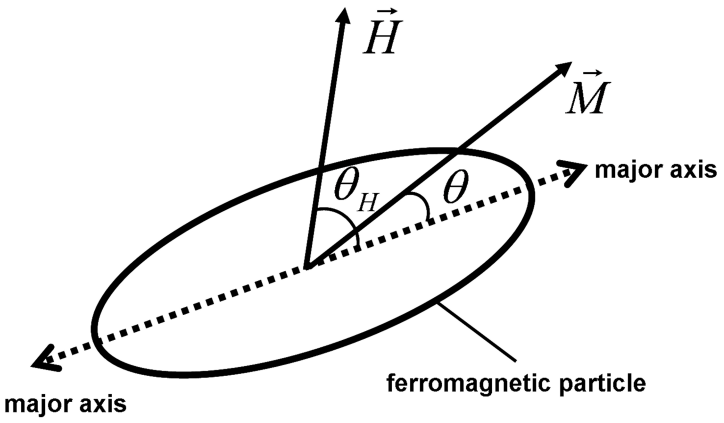

Figure 3.1: Ferromagnetic particle in the presence of an applied field.

In Figure 3.1, $\vec{H}$ represents the applied field, $\vec{M}$ the magnetisation, θ_H is the angle between the major axis and the field $\vec{H}$, θ is the angle between the magnetisation $\vec{M}$ and the major axis. The magnetostatic energy of a ferromagnetic particle is written in SI units as (Aharoni, 2000, p. 111)

$$E_{\mathrm{M}} = -(\mu_0/2) \int \vec{M} \cdot \vec{H}_d \mathrm{d}^3\vec{r} \tag{3.1}$$

where μ_0 is the permeability of free space, $\vec{M}$ is the magnetisation, $\vec{H}_d$ the self-demagnetising field and $\mathrm{d}^3\vec{r}$ is a volume element. The self-demagnetising field can be expressed as

$$\vec{H}_d = -\vec{N} \cdot \vec{M} \tag{3.2}$$

where $\vec{N}$ is the demagnetising factor tensor which depends on particle shape. For geometries described by an ellipsoid of revolution, the self-demagnetising field is uniform inside the body. After substituting equation (3.2), into equation (3.1) and assuming uniform magnetisation, the magnetostatic energy takes the form

$$\begin{aligned} E_{\mathrm{M}} &= (\mu_0/2)\vec{M} \cdot \left[\int \vec{N}\mathrm{d}^3\vec{r}\right] \cdot \vec{M} \\ &= (\mu_0/2)V\vec{M} \cdot \mathcal{N} \cdot \vec{M} \end{aligned} \tag{3.3}$$

where V is the particle volume and $\mathcal{N}$ is the volume average of the demagnetising factor tensor.

For realistic geometries, the self-demagnetising field is not guaranteed to be uniform and can vary with position within a uniformly magnetised particle. In this case, the volume average of the self-demagnetising field, equation (3.2), assuming uniform magnetisation is

$$\vec{\mathcal{H}}_d = -\mathcal{N} \cdot \vec{M} \tag{3.4}$$

where $\vec{\mathcal{H}}_d$ represents the volume averaged self-demagnetising field. The volume average of the demagnetising factor tensor, $\mathcal{N}$, is referred to as the *magnetometric* demagnetising factor tensor. For particle shapes described by an ellipsoid of revolution, the demagnetising factors and magnetometric demagnetising factors are the same.

For an ellipsoid of revolution, if equation (3.3) is expanded using cartesian coordinates, the resulting expression is

$$E_{\mathrm{M}} = \frac{\mu_0 V}{2}\left[N_{xx}M_x^2 + N_{yy}M_y^2 + N_{zz}M_z^2\right] \tag{3.5}$$

where N_{xx}, N_{yy} and N_{zz} are demagnetising factors, and M_x, M_y, M_z, the cartesian components of the magnetisation vector. The cross terms in the demagnetising factor tensor of an ellipsoid of revolution vanish whereas the non-vanishing demagnetising factors are constant and $N_{xx} = N_{yy}$ if the major axis is in the z

direction.

It is convenient to express the magnetisation components in spherical coordinates (see Figure 3.2)

$$M_x = M_s \sin\theta \cos\phi \quad M_y = M_s \sin\theta \sin\phi \quad M_z = M_s \cos\theta \tag{3.6}$$

where M_s is the saturation magnetisation, θ is the polar angle and ϕ is the azimuthal angle. Substituting equation (3.6) into equation (3.5), and noting that $N_{xx} = N_{yy}$, the result is

$$\begin{aligned} E_{\mathrm{M}} &= \frac{\mu_0 M_s^2}{2} \left[N_{xx} \cos^2\phi + N_{yy} \sin^2\phi - N_{zz} \right] V \sin^2\theta + \frac{\mu_0 M_s^2}{2} N_{zz} V \\ &= \frac{\mu_0 M_s^2}{2} \left[N_{xx} - N_{zz} \right] V \sin^2\theta + \frac{\mu_0 M_s^2}{2} N_{zz} V. \end{aligned} \tag{3.7}$$

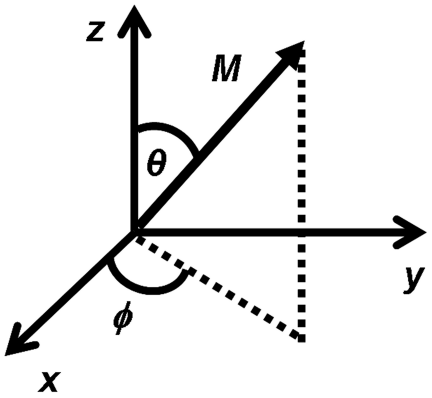

Figure 3.2: Spherical coordinates illustration.

Equation 3.7 has a form similar to that of crystalline anisotropy energy, $K_1 V \sin^2\theta$ (see section 3.3), except for the second term which is constant. This energy, equation (3.7), is also referred to as shape anisotropy energy because it depends on particle shape through demagnetising factors. The magnetisation in this case prefers to align along the major axis since $N_{xx} > N_{zz}$. According to equation 3.7, the shape anisotropy constant given by

$$K_{\mathrm{shape}} = \frac{\mu_0 M_s^2}{2} \left(N_{xx} - N_{zz} \right) \tag{3.8}$$

implies that $K \propto M_s^2$ where K is an anisotropy constant.

If the energy contribution due to an external field $\vec{H}$ (Zeeman energy) is included the total energy becomes

$$E = \frac{\mu_0 M_s^2}{2} \left[N_{xx} - N_{zz}\right] V \sin^2\theta + \frac{\mu_0 M_s^2}{2} N_{zz} V - \mu_0 V \vec{M} \cdot \vec{H}. \tag{3.9}$$

Expressing the magnetisation components in the Zeeman energy in spherical coordinates and ignoring the constant term, $\frac{\mu_0 M_s^2}{2} N_{zz} V$, which does not affect the behaviour of magnetisation, the total energy becomes

$$\begin{aligned} E = {} & \frac{\mu_0 M_s^2}{2} \left[N_{xx} - N_{zz}\right] V \sin^2\theta \\ & - \mu_0 M_s V H (\sin\theta_H \sin\theta \cos(\phi_H - \phi) + \cos\theta_H \cos\theta) \end{aligned} \tag{3.10}$$

where θ_H, ϕ_H are the applied field polar and azimuthal angles respectively.

It is convenient to work in dimensionless quantities and this can be achieved by dividing equation (3.10) by $\mu_0 M_s^2 \left[N_{xx} - N_{zz}\right] V$ throughout which leads to

$$\mathcal{E} = \frac{1}{2} \sin^2\theta - h \left[\sin\theta_H \sin\theta \cos(\phi_H - \phi) + \cos\theta_H \cos\theta\right] \tag{3.11}$$

where $\mathcal{E} = \frac{E}{\mu_0 M_s^2 [N_{xx} - N_{zz}] V}$, $h = \frac{H}{H_{K_{\text{shape}}}}$ and $H_{K_{\text{shape}}} = M_s \left(N_{xx} - N_{zz}\right)$.

Minimisation of equation (3.11) with respect to ϕ reveals that the magnetisation prefers to make an azimuthal angle $\phi = \phi_H$. In this case the total reduced energy simplifies to

$$\mathcal{E} = \frac{1}{2} \sin^2\theta - h \cos\left(\theta - \theta_H\right). \tag{3.12}$$

Given any h and θ_H, the magnetisation would prefer to make an angle, θ, with the major axis that minimises $\mathcal{E}$ where the first derivative vanishes, that is,

$$\frac{\partial \mathcal{E}}{\partial \theta} = \sin\theta \cos\theta - h \sin(\theta_H - \theta) = 0 \tag{3.13}$$

provided the angle, θ, corresponds to the minimum energy where

$$\frac{\partial^2 \mathcal{E}}{\partial \theta^2} = \cos^2\theta - \sin^2\theta + h \cos(\theta_H - \theta) > 0. \tag{3.14}$$

Equation (3.13) has more than one solution for any h, θ_H combination and there could be more than one minimum. To obtain a unique solution, as Aharoni (2000, p. 106) pointed out, it is essential to state and follow the history of the

value of h for each field angle θ_H. If a solution, θ, begins from a certain branch, it can only jump to another at a value of h provided there is no energy difference between the branches. This is the basis of *hysteresis*.

case 1: $\theta_H = 0$

For $\theta_H = 0$, the applied field is parallel to the major axis (see Figure 3.1). In this case the problem is trivial and a solution is sought for the following equations

$$\sin\theta\cos\theta + h\sin\theta = 0 \quad \text{provided} \quad \cos^2\theta - \sin^2\theta + h\cos\theta > 0. \tag{3.15}$$

One solution is $\cos\theta = -h$ (see Figure 3.3) provided $|h| < 1$, but when this is substituted in the second part of equation (3.15), this evaluates to

$$\cos^2\theta - \sin^2\theta + h\cos\theta = h^2 - 1. \tag{3.16}$$

It is evident that equation (3.16) is less than zero and according to the second derivative test, corresponds to an energy maximum.

Another solution is $\sin\theta = 0$ (see Figure 3.3) where the magnetisation is parallel to the major axis (see Figure 3.1) and when substituted in the second part of equation (3.14), this simplifies to

$$\cos^2\theta - \sin^2\theta + h\cos\theta = 1 + h\cos\theta. \tag{3.17}$$

Equation (3.17) can be greater than zero in which case the solution corresponds to a minimum.

Thus for $\sin\theta = 0$ and $1 + h\cos\theta > 0$, there are two possible solutions

$$\theta = 0 \quad \text{provided} \quad h > -1$$
$$\theta = \pi \quad \text{provided} \quad h < 1.$$

This implies that for $|h| < 1$, there are two solutions corresponding to the minimum which is either $\theta = 0$ or π. It is important at this stage to specify the field history in order to avoid the ambiguity. As an example, it is assumed that initially the applied field is large and positive, that is, $h > 1$, then reduced to zero and finally increased in the opposite direction.

In this case, it is clear that $\theta = 0$ is a solution until $h = -1$. At this value of h, $\frac{\partial^2 \mathcal{E}}{\partial \theta^2} = 0$, implying that the solution is no longer stable (the minimum vanishes) and a jump to $\theta = \pi$ becomes possible. According to this description, a hysteresis curve (a graph of magnetisation versus the applied field as shown in Figure 3.4) can be constructed. From this graph, the *switching field* (which is the field value required to switch the magnetisation direction from one orientation to another) can be obtained and corresponds to $h = -1$, which implies that $H_{\text{sw}} = -M_s\,(N_{xx} - N_{zz})$ in this case. H_{sw} is the actual value of the switching field.

case 2: $\theta_H \neq 0$

This is a non-trivial problem despite equation (3.13) looking simple as mentioned by several authors. (Stoner and Wohlfarth, 1948) stated

> *The general solution is not only very troublesome to derive, but also, when obtained, not adapted for numerical evaluation.*

Aharoni (2000, p. 107) mentioned that the problem should be solved numerically. It was also indicated by Tannous and Gieraltowski (2008) that for any general field angle, θ_H, equation 5.3 cannot be solved using an analytic approach.

An inverse interpolation approach was used by Stoner and Wohlfarth (1948) to solve the problem indirectly where the reduced field h was obtained from equation (3.13) at certain intervals of the angles $\theta_H - \theta$ for chosen values of θ_H.

Despite being a challenging task, an analytical expression for the solution to equation (3.13) was derived (see section 5.2).

Stoner and Wohlfarth (1948) also obtained an expression for the switching field for any field angle. This is obtained by solving the following two equations

$$\frac{\partial \mathcal{E}}{\partial \theta} = \sin\theta\cos\theta - h\sin(\theta_H - \theta) = 0 \tag{3.18}$$

$$\frac{\partial^2 \mathcal{E}}{\partial \theta^2} = \cos^2\theta - \sin^2\theta + h\cos(\theta_H - \theta) = 0. \tag{3.19}$$

If equation (3.18) is multiplied by $\sin\theta$ and equation (3.19) by $\cos\theta$ and the

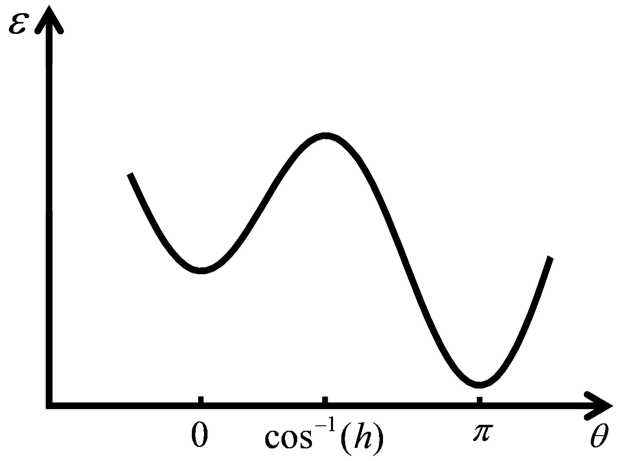

Figure 3.3: Energy landscape schematic for $\theta_H = 0$ in the presence of an applied field. Shown are two minima representing the directions preferred by the magnetisation and a maximum.

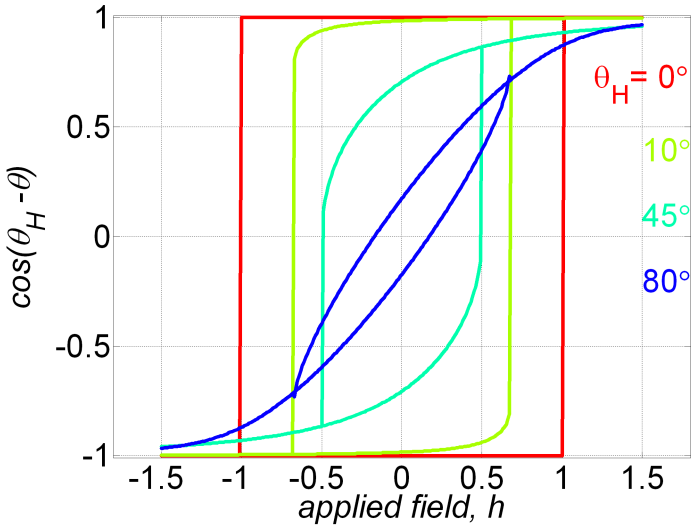

Figure 3.4: Hysteresis curves for various applied field angles. The vertical axis shows the component of magnetisation in the direction of applied field.

obtained expressions added, the result is

$$h\cos\theta_H = -\cos^3\theta. \tag{3.20}$$

Similarly, if equation (3.18) is multiplied by $\cos\theta$ and equation (3.19) by $\sin\theta$ and subtracting the obtained expressions, the result is

$$h\sin\theta_H = \sin^3\theta. \tag{3.21}$$

The parametric equation of the switching field given by equations (3.20) and (3.21) is referred to as the *Stoner–Wohlfarth* astroid. Figure 3.5 displays the astroid.

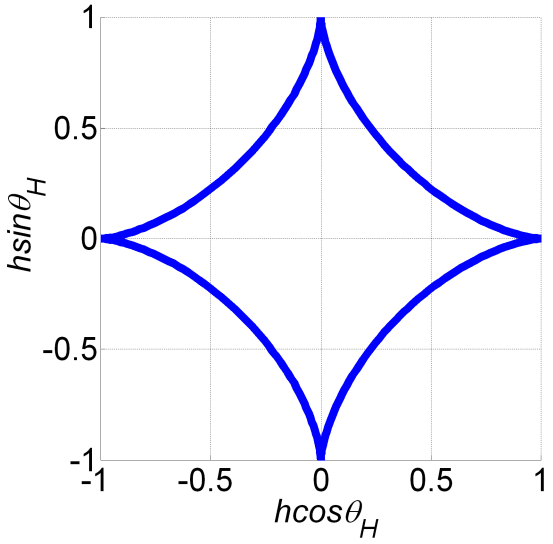

Figure 3.5: *Stoner–Wohlfarth* astroid.

If the magnetisation angle, θ, is eliminated in equations (3.20) and (3.21), the switching field in terms of the field angle is

$$h_{\text{sw}} = (\sin^{\frac{2}{3}}\theta_H + \cos^{\frac{2}{3}}\theta_H)^{-\frac{3}{2}} \quad \text{or} \quad H_{\text{sw}}(\theta_H) = H_{K_{\text{shape}}}(\sin^{\frac{2}{3}}\theta_H + \cos^{\frac{2}{3}}\theta_H)^{-\frac{3}{2}} \tag{3.22}$$

where $H_{K_{\text{shape}}} = M_s(N_{xx} - N_{zz})$. This is another expression for the *Stoner–Wohlfarth* astroid.

The write process for islands that follow coherent rotation involves comparing the head field to the switching field, equation (3.22). A successful write process occurs if the head field is greater than or equal to the switching field.

3.3 Micromagnetic models

The Stoner–Wohlfarth model describes the behaviour of non–interacting ellipsoidal single domain particles that reverse coherently whereby the magnetisation remains uniform throughout during the reversal. The assumption of coherent rotation and non–interacting ellipsoidal single domain particles does not hold in the general case. In BPM, the islands may not necessarily be ellipsoidal, could have shape variations, the reversal process may not be strictly coherent rotation, the applied field could be non–uniform and the magnetisation may have a spatial variation.

Micromagnetic models avoid the assumptions of the Stoner–Wohlfarth model in that the magnetisation can have a spatial variation inside the particle and apply to any shape. The only constraint is that the magnitude of the magnetisation vector, the saturation magnetisation, is fixed at any given temperature. Micromagnetics can be regarded as a continuum theory to describe the magnetisation processes in ferromagnets (Schrefl, 1999). As a continuum theory, it replaces the atomic spins by a continuous magnetisation vector that represents the atomic moment per unit volume. The magnetisation vector involves a length scale large enough to replace atomic moments yet small enough to understand the details of walls that separate domains (Schrefl, 1999).

Micromagnetism is a classical theory coined by Brown (1978) initially to study the details of domain walls that separate domains. The domain theory could not explain origins of domains and the properties of magnetic materials using the domain concept (Brown, 1962; Aharoni, 2000, p. 156). In the domain theory, the domain walls were considered a negligible part of space (Aharoni, 2000, p. 133).

In micromagnetics, the magnetic moment is treated as a classical vector and the total (Gibbs free) energy of a ferromagnetic body of any shape consists of four terms that compete in order to determine the equilibrium configuration of the magnetisation.

Exchange energy

This energy term arises from the quantum mechanical interactions among atomic spins (Schrefl, 1999). These interactions are short ranged and this energy prefers magnetic moments to be aligned parallel to each other. The exchange energy

between spins S_i and S_j (Aharoni, 2000, p. 121) can be expressed as

$$\mathcal{E}_{\text{ex}} = -\sum_{ij}{}' J_{ij}\vec{S}_i \cdot \vec{S}_j \tag{3.23}$$

where J_{ij} is the exchange integral. Since atomic exchange interactions are very short ranged, the exchange integral, J_{ij}, can be taken to be a constant, J, between the nearest neighbours and zero otherwise. In this case, the classical exchange energy is

$$\mathcal{E}_{\text{ex}} = -JS^2 \sum_{\text{neighbours}} \cos\phi_{ij} \tag{3.24}$$

where ϕ_{ij} represents the angle between spins $\vec{S}_i$ and $\vec{S}_j$.

The exchange forces are very strong implying that $|\phi_{ij}|$ is small and thus $\cos\phi_{ij} \approx 1 - \phi_{ij}^2$. The classical exchange energy then becomes

$$\begin{aligned}\mathcal{E}_{\text{ex}} &= -JS^2 \sum_{\text{neighbours}} (1 - \phi_{ij}^2) \\ &= -JS^2 \sum_{\text{neighbours}} 1 + JS^2 \sum_{\text{neighbours}} \phi_{ij}^2\end{aligned} \tag{3.25}$$

Now, since the first term represents the energy for all spins parallel, which is a constant, this term can be ignored because it does not affect the behaviour of the magnetisation. Therefore, the classical exchange energy becomes

$$\mathcal{E}_{\text{ex}} = JS^2 \sum_{\text{neighbours}} \phi_{ij}^2 \tag{3.26}$$

Figure 3.6 is useful in expressing angle ϕ_{ij} in terms of the magnetisation. Since the angles between spins are small, $\phi_{ij} \approx |\vec{m}_i - \vec{m}_j|$ where $\vec{m}$ represents a

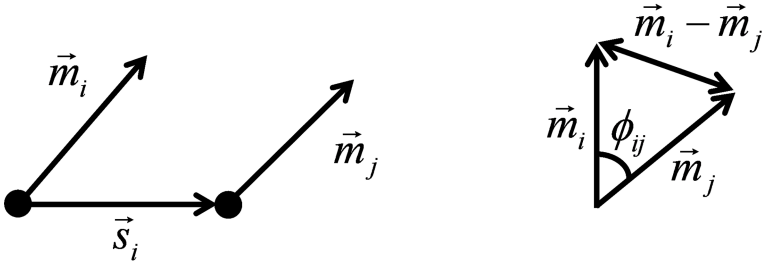

Figure 3.6: ϕ_{ij} in terms of $\vec{m}_i - \vec{m}_j$ (Aharoni, 2000, p. 134).

unit magnetisation vector. The first order Taylor expansion of ϕ_{ij} is $|\vec{m}_i - \vec{m}_j| = |(\vec{s}_i \cdot \nabla)\vec{m}|$ where $\vec{s}_i$ represents the position vector originating from lattice point i and terminating on point j.

With this approximation, the exchange energy, equation (3.26), becomes (Aharoni, 2000, p. 134)

$$\mathcal{E}_{\text{ex}} = JS^2 \sum_i \sum_{\vec{s}_i} |(\vec{s}_i \cdot \nabla)\vec{m}|^2. \tag{3.27}$$

The summation over $\vec{s}_i$ involves all position vectors from lattice point i to the nearest neighbours. For cubic crystals, if the summation is converted into an integral, the exchange energy becomes

$$\mathcal{E}_{\text{ex}} = \int w_{\text{e}} \mathrm{d}\tau \tag{3.28}$$

where $w_{\text{e}} = \frac{C}{2}[(\nabla m_x)^2 + (\nabla m_y)^2 + (\nabla m_z)^2]$ and $\mathrm{d}\tau$ is a volume element. $C = \frac{2JS^2}{a}c$ and a represents the unit cell length. The value of c is 1, 2 and 4 for simple, body centred, and face centred cubic respectively. In this localised spin model, magnetic moments are assumed to reside on atoms.

Magnetostatic energy

This energy term originates from long ranged classical interactions among magnetic dipoles (Aharoni, 2000, p. 109) and favours the existence of magnetic domains (Schrefl, 1999). Mathematically, the magnetostatic energy, $\mathcal{E}_{\text{M}}$, is

$$\mathcal{E}_{\text{M}} = -\int \frac{1}{2}\mu_0 \vec{M} \cdot \vec{H}' \mathrm{d}\tau \tag{3.29}$$

where $\vec{H}'$ is the demagnetising field and $\vec{M}$ is the magnetisation vector.

The demagnetising field can be obtained from the magnetic scalar potential U according to $\vec{H}' = -\nabla U$ (Aharoni, 2000, p. 125) where

$$U = \frac{1}{4\pi}\left(-\int \frac{\nabla' \cdot \vec{M}(\vec{r}')}{|\vec{r} - \vec{r}'|}\mathrm{d}\tau' + \int \frac{\vec{n} \cdot \vec{M}(\vec{r}')}{|\vec{r} - \vec{r}'|}\mathrm{d}S'\right). \tag{3.30}$$

The first integral in equation (3.30) is over the volume and the second over the surface of the bodies. The del operator, ∇', denotes the derivatives with respect to $\vec{r}'$, and $\vec{n}$ denotes the surface normal.

Equation (3.30) can be interpreted by considering magnetic charges where the

first term is the contribution to the potential due to a distribution of magnetic charges whose volume density is $-\nabla' \cdot \vec{M}(\vec{r}')$ and the second integral is the contribution due to magnetic charges whose surface density is $\vec{n} \cdot \vec{M}(\vec{r}')$. Since like charges repel, the volume charges, if there was nothing to hold them, would repel themselves until they become distributed within the surface of the ferromagnet (Aharoni, 2000, p. 126). The magnetostatic energy thus prefers to avoid volume charges hence favours the creation of a domain structure having surface charges. The same reasoning applies to surface charges in that they tend to distribute themselves over small areas in order to minimise the magnetic scalar potential.

Anisotropy energy

One of the most common forms of anisotropy is *crystalline anisotropy* or *magnetocrystalline anisotropy*. This form of anisotropy is caused by the spin–orbit interaction (Aharoni, 2000, p. 84). The crystal structure determines preferred orbital orientations. The spins therefore prefer to align along well-defined crystal axes through the spin–orbit interaction. This implies that there are certain directions where it is easier to magnetise a magnetic material. The energy term resulting from this is the magnetocrystalline anisotropy energy. In short, magnetocrystalline anisotropy energy arises from interactions between atomic spins and the crystal structure. This energy term prefers the magnetisation vector to be oriented along certain crystallographic directions (Schrefl, 1999).

Though the magnetocrystalline energy is normally smaller than the exchange energy, it determines the direction of the magnetisation (together with other forms of anisotropy if present), whereas the uniformity of the magnetisation is obtained from the exchange energy. The calculation of the spin–orbit interaction from first principles can be done but inaccuracies can arise and so anisotropy energy terms are usually expressed in power series expansions where the coefficients are obtained from experiments (Aharoni, 2000, p. 85).
There are two forms of crystalline anisotropy:

1. *Uniaxial anisotropy*
   Hexagonal crystals such as cobalt and all recording media possess this form of anisotropy since binary data (0 or 1) needs a two state system for storage. The uniaxial anisotropy energy density depends on the angle between the c–axis, which is [0001], and the magnetisation direction. According to experiment (Aharoni, 2000, p. 85), the energy density is symmetrical in the

basal plane, which is perpendicular to the c–axis, and is usually expressed as

$$w_u = K_1 \sin^2\theta + K_2 \sin^4\theta. \tag{3.31}$$

where K_1 and K_2 are constants which are obtained from experiments and depend on temperature. The expansion can be carried out to higher orders but the above expansion is sufficient for known ferromagnets (Aharoni, 2000, p. 86). The second term in equation (3.31) is normally smaller than the first and is often not included. However, $\frac{K_2}{K_1} \approx \frac{1}{4}$ for cobalt at room temperature according to Chikazumi (1994, p. 128) and Craik (1995, p. 90). For the majority of hexagonal crystals, the c–axis represents the easy axis and thus $K_1 > 0$.

For cobalt at room temperature, K_1 is positive and therefore w_u is a minimum when $\theta = 0$, in which case the magnetisation is parallel to the c–axis. If K_1 is negative, the magnetisation prefers to be perpendicular to the c–axis, which is along the basal plane. This happens in cobalt at approximately above 340 °C (Jakubovics, 1994, p. 56). According to Chikazumi (1994, p. 128) and Craik (1995, p. 90) for cobalt, $K_1 = 4.1 \times 10^5$ J/m^3 and $K_2 = 1.0 \times 10^5$ J/m^3 at room temperature.

2. *Cubic anisotropy*

   In cubic crystals, the x, y and z– axes or a combination define the crystallographic axes and thus the energy should be invariant when the axes are interchanged. The energy density is (Aharoni, 2000, p. 86).

$$w_c = K_1(m_x^2 m_y^2 + m_y^2 m_z^2 + m_z^2 m_x^2) + K_2 m_x^2 m_y^2 m_z^2 \tag{3.32}$$

   where $\vec{m}$ denotes the magnetisation whose magnitude is unity, K_1 and K_2 are constants which are obtained from experiments and depend on temperature. For cubic crystals, $K_1 > 0$ or $K_1 < 0$. The expansion can be carried out to higher orders but the above expansion is sufficient for known ferromagnets (Aharoni, 2000, p. 86).

   The energy density, $w_c = 0$ when the magnetisation is parallel to the cube edges, that is, the $< 100 >$ directions, for example $m_x = 1, m_y = m_z = 0$. $w_c = \frac{1}{3}K_1 + \frac{1}{27}K_2$ when the magnetisation is parallel to the $< 111 >$ directions, for example $m_x = m_y = m_z = \frac{1}{\sqrt{3}}$.

For $K_1 > 0$, w_c is a minimum when the magnetisation is parallel to the $< 100 >$ directions, in which case the easy axes are along the cube edges. This is the case for iron.

For $K_1 < 0$, w_c is a minimum when the magnetisation is parallel to the $< 111 >$ directions so that the easy axes are along the body diagonals. This is the case for nickel.

According to Chikazumi (1994, p. 128) for iron at room temperature, $K_1 = 4.8 \times 10^4$ J/m^3 and $K_2 = \pm 5.0 \times 10^3$ J/m^3 and for nickel at room temperature, $K_1 = -4.5 \times 10^3$ J/m^3 and $K_2 = 2.34 \times 10^5$ J/m^3. For $K_2 \gg K_1$, w_c is minimum when the magnetisation is parallel to the $< 100 >$ directions.

Mathematically, the anisotropy energy, $\mathcal{E}_\mathrm{a}$, is

$$\mathcal{E}_\mathrm{a} = \int w_a \mathrm{d}\tau \tag{3.33}$$

where w_a refers to either cubic or uniaxial anisotropy energy density.

Zeeman energy

The Zeeman energy originates from interactions between atomic spins and an external field. This energy term prefers the magnetisation vector to be aligned parallel to an external field. Expressed mathematically, the Zeeman energy, $\mathcal{E}_\mathrm{H}$, is

$$\mathcal{E}_\mathrm{H} = -\int \mu_0 \vec{M} \cdot \vec{H}_a \mathrm{d}\tau \tag{3.34}$$

where $\vec{H}_a$ is the external field and $\vec{M}$ is the magnetisation vector.

Total energy

The total energy is a sum of all energy terms

$$\begin{aligned} \mathcal{E}_\mathrm{tot} &= \mathcal{E}_\mathrm{ex} + \mathcal{E}_\mathrm{a} + \mathcal{E}_\mathrm{M} + \mathcal{E}_\mathrm{H} \\ &= \int \Big\{ \frac{C}{2} \big[(\nabla m_x)^2 + (\nabla m_y)^2 + (\nabla m_z)^2 \big] + w_\mathrm{a} \\ &\quad - \frac{1}{2} \mu_0 \vec{M} \cdot \vec{H}' - \mu_0 \vec{M} \cdot \vec{H}_a \Big\} \mathrm{d}\tau + \int w_\mathrm{s} \mathrm{d}S. \end{aligned} \tag{3.35}$$

Here w_s is the surface anisotropy energy density (Aharoni, 2000, p. 174) which arises because spins on the surface see different locality and thus the effect of the lattice is modified in the anisotropy.

3.3.1 Static micromagnetics

Static micromagnetics determines equilibrium configurations of the magnetisation in a ferromagnetic body by minimising the total energy, equation (3.35).

3.3.1.1 Brown's static equations

The minimisation of the total energy, equation (3.35), subject to the constraint, $|\vec{M}| = M_s(T)$, where $M_s(T)$ is the saturation magnetisation that depends on temperature, was rigorously carried out by Brown (1978). The resulting equations are referred to as *Brown static equations* and these are

$$\vec{m} \times \Big(\frac{C}{M_s} \nabla^2 \vec{m} + \mu_0 (\vec{H}_a + \vec{H}') - \frac{1}{M_s} \frac{\partial w_a}{\partial \vec{m}} \Big) = 0 \quad \text{within the body} \tag{3.36}$$

$$\vec{m} \times \Big(C \frac{\partial \vec{m}}{\partial n} + \frac{\partial w_s}{\partial \vec{m}} \Big) = 0 \quad \text{on the surface} \tag{3.37}$$

where $\vec{m} = \frac{\vec{M}}{M_s}$ represents the normalised magnetisation. The expression $\frac{C}{M_s} \nabla^2 \vec{m} + \mu_0 (\vec{H}_a + \vec{H}') - \frac{1}{M_s} \frac{\partial w_a}{\partial \vec{m}}$ in equation (3.36) represents the effective field, $\vec{H}_{\text{eff}}$. Equation (3.36) implies that the torque is zero throughout a ferromagnetic body when the magnetisation prefers to be aligned parallel to the effective field. Equation (3.37) represents boundary conditions.

3.3.2 Dynamic micromagnetics

Static micromagnetics reveals the equilibrium configuration of the magnetisation arising from the competition among the energy contributions described above. In fast switching, which is critical for magnetic recording, it is important to determine switching times. However, static micromagnetics does not reveal how the magnetisation evolves with time as the external field changes. Dynamic micromagnetics describes the time evolution of the magnetisation, making it possible to study switching times and how the reversal proceeds as time elapses.

3.3.2.1 Undamped motion

Before describing damped motion, a suitable starting point is to understand the motion of undamped and uncoupled magnetisation. In classical mechanics, the equation of motion of a rotating rigid body is

$$\frac{\mathrm{d}\vec{L}}{\mathrm{d}t} = \vec{T} \tag{3.38}$$

where $\vec{L}$ represents angular momentum and $\vec{T}$ the torque on that body. Equation (3.38) also holds in quantum mechanics where $\vec{L}$, the angular momentum operator, is replaced by the electron spin angular momentum operator, $\vec{S}$, (Gilbert, 2004). Thus the equation of motion for the spin becomes

$$\frac{\mathrm{d}\vec{S}}{\mathrm{d}t} = \vec{T}. \tag{3.39}$$

The relationship between the magnetic moment and spin angular momentum of an electron is

$$\vec{\mu} = -\gamma\vec{S} \tag{3.40}$$

where $\vec{\mu}$ is the magnetic moment, $\gamma = \frac{g|e|}{2m_e}$ is the gyromagnetic ratio of an electron spin, g is the Landé factor and e, m_e, the electron's charge and mass respectively.

A magnetic moment, $\vec{\mu}$, experiences a torque in a magnetic field given by

$$\vec{T} = \vec{\mu} \times \vec{H}. \tag{3.41}$$

Using $\vec{T}$ from equation (3.41) and $\vec{S}$ from equation (3.40), equation (3.39) becomes

$$-\frac{1}{\gamma}\frac{\mathrm{d}\vec{\mu}}{\mathrm{d}t} = \vec{\mu} \times \vec{H} \Rightarrow \frac{\mathrm{d}\vec{\mu}}{\mathrm{d}t} = -\gamma\vec{\mu} \times \vec{H}. \tag{3.42}$$

Equation (3.42) describes the motion of a magnetic moment in the presence of a magnetic field $\vec{H}$.

As Gilbert (2004) indicated, the magnetic field is not restricted to the external field but any torque can be due to an effective field $\vec{\mathcal{H}} = -\frac{\partial U(\vec{M})}{\partial \vec{M}}$ where $U(\vec{M})$ is the potential energy and $\vec{M}$ is the magnetisation vector. Using this definition,

the equation of motion for the magnetisation is

$$\frac{\mathrm{d}\vec{M}}{\mathrm{d}t} = -\gamma\vec{M} \times \vec{\mathcal{H}} \tag{3.43}$$

where the effective field is $\vec{\mathcal{H}} = \frac{C}{M_s}\nabla^2\vec{m} + \mu_0(\vec{H_a} + \vec{H'}) - \frac{1}{M_s}\frac{\partial w_a}{\partial \vec{m}}$ (Aharoni, 2000, p. 181). Equation (3.36) can be viewed as a special case of equation (3.43) if the magnetisation does not vary with time.

3.3.2.2 Damped motion

Equation (3.43) indicates that the magnetisation precession continues without end. However, from experiments, the changes in magnetisation decay in finite time, which is due to damping (Gilbert, 2004; Aharoni, 2000, p.181).

According to Gilbert (2004), in damping the energy from macroscopic motion of the local magnetisation is lost to microscopic thermal motion and this happens due to the coupling of magnetisation in spin waves to lattice vibrations and eddy currents. Other effects contributing to damping, according to Gilbert (2004), are polycrystalline structure, strains and crystal defects which include voids and interstitial atoms.

Gilbert (2004) pointed out that a quantitative description of the transfer process in order to understand complicated damping mechanisms is not easy to carry out and requires both theoretical calculations and experiments. He thus suggested a formulation of a phenomenological theory having parameters that determine the measure of rate of energy loss and a way of comparing experimental results with theoretical calculations.

Landau–Lifshitz equation of motion

An initial attempt to include damping was made by Landau and Lifshitz (1935). They added a damping term, $-\frac{\lambda}{M_s}\vec{M} \times (\vec{M} \times \vec{\mathcal{H}})$, to the effective field as shown in equation (3.44)

$$\frac{\mathrm{d}\vec{M}}{\mathrm{d}t} = -\gamma\vec{M} \times \vec{\mathcal{H}} - \frac{\lambda}{M_s}\vec{M} \times (\vec{M} \times \vec{\mathcal{H}}) \tag{3.44}$$

where λ is a phenomenological damping constant which is greater than zero. However, the Landau–Lifshitz damping term is only useful for small damping

but does not correctly describe large damping (Gilbert, 2004).

Landau–Lifshitz–Gilbert (LLG) equation of motion

Gilbert (2004) presented a reformulation of the phenomenological dynamic theory that takes into account large damping and agrees with a theory of damping in other physical systems.

As mentioned by Gilbert (2004), damping slows down macroscopic motion and thus converting the macroscopic kinetic and potential energy to kinetic energy of microscopic thermal motion (heat energy). The dynamic variable, in case of a ferromagnet is the magnetisation, $\vec{M}$, and the damping term is proportional to the velocity $\frac{\partial \vec{M}(\vec{r},t)}{\partial t}$. The damping of magnetisation motion converts the energy of macroscopic motion to that of microscopic thermal motion in spin waves or to other fields like eddy current or strain fields to which it is coupled, Gilbert (2004).

The damping term which he introduced is $-\eta \frac{\partial \vec{M}(\vec{r},t)}{\partial t}$ where η is a damping parameter that is dependent on the material.

To obtain the equation of motion, he first presented a Lagrangian formulation of the undamped magnetisation shown in equation (3.43). The Lagrangian form is

$$\frac{\mathrm{d}}{\mathrm{d}t}\frac{\delta \mathcal{L}[\vec{M}(\vec{r},t),\dot{\vec{M}}(\vec{r},t)]}{\delta \dot{\vec{M}}(\vec{r},t)} - \frac{\delta \mathcal{L}[\vec{M}(\vec{r},t),\dot{\vec{M}}(\vec{r},t)]}{\delta \vec{M}(\vec{r},t)} = 0 \tag{3.45}$$

where

$$\mathcal{L}[\vec{M}(\vec{r},t),\dot{\vec{M}}(\vec{r},t)] = T[\vec{M}(\vec{r},t),\dot{\vec{M}}(\vec{r},t)] - U[\vec{M}(\vec{r},t)]. \tag{3.46}$$

Here $\mathcal{L}$ represents the Lagrangian, T the kinetic energy, U the potential energy and $\dot{\vec{M}}(\vec{r},t) = \frac{\partial \vec{M}}{\partial t}$. Equation (3.45) can be extended to include the motion of damped magnetisation by introducing a dissipative force $\frac{\delta R[\dot{\vec{M}}(\vec{r},t)]}{\delta \dot{\vec{M}}(\vec{r},t)}$, as done by Gilbert (2004), so that it becomes

$$\frac{\mathrm{d}}{\mathrm{d}t}\frac{\delta \mathcal{L}[\vec{M}(\vec{r},t),\dot{\vec{M}}(\vec{r},t)]}{\delta \dot{\vec{M}}(\vec{r},t)} - \frac{\delta \mathcal{L}[\vec{M}(\vec{r},t),\dot{\vec{M}}(\vec{r},t)]}{\delta \vec{M}(\vec{r},t)} + \frac{\delta R[\dot{\vec{M}}(\vec{r},t)]}{\delta \dot{\vec{M}}(\vec{r},t)} = 0. \tag{3.47}$$

Here

$$R[\dot{\vec{M}}(\vec{r},t)] = \frac{\eta}{2}\int \dot{\vec{M}}(\vec{r},t)\cdot\dot{\vec{M}}(\vec{r},t)\mathrm{d}\vec{r} \tag{3.48}$$

is referred to as the Rayleigh dissipative functional.
In order to cater for non–uniform damping, Gilbert (2004) introduced the functional

$$R = \frac{1}{2}\sum_{i,j}\iint\Big[\frac{\partial\vec{M}_i(\vec{r},t)}{\partial t}\eta_{ij}(\vec{r},\vec{r}')\frac{\partial\vec{M}_j(\vec{r}',t)}{\partial t}\Big]\mathrm{d}\vec{r}\mathrm{d}\vec{r}'. \tag{3.49}$$

However, he emphasised that the calculation or measurement of the matrix $\eta_{ij}(\vec{r},\vec{r}')$ is not possible. He also indicated that for experiments conducted at low applied fields, η depends on domain structure which in turn depends on sample shape, size and the size of the applied field. In order to avoid these effects and measure a damping parameter that characterises the sample, it is necessary to apply a large magnetic field to a single domain sample. In this case, the rate of doing work against dissipative forces is

$$\frac{\mathrm{d}W}{\mathrm{d}t} = 2R[\dot{\vec{M}}] = \eta\int\dot{\vec{M}}(\vec{r},t)\cdot\dot{\vec{M}}(\vec{r},t)\mathrm{d}\vec{r}. \tag{3.50}$$

Using $\mathcal{L} = T - U$, $\frac{\delta U[\vec{M}]}{\delta\dot{\vec{M}}} = 0$ and $\frac{\delta R[\dot{\vec{M}}]}{\delta\dot{\vec{M}}} = \eta\dot{\vec{M}}$, the Lagrangian form, equation (3.47), becomes

$$\frac{\mathrm{d}}{\mathrm{d}t}\frac{\delta T[\vec{M},\dot{\vec{M}}]}{\delta\dot{\vec{M}}} - \frac{\delta T[\vec{M},\dot{\vec{M}}]}{\delta\vec{M}} + [-\vec{H}(\vec{r},t) + \eta\dot{\vec{M}}] = 0 \tag{3.51}$$

For $\eta = 0$, equation (3.51) reduces to the undamped case, equation (3.45), and should be equivalent to equation (3.43). The damping term in equation (3.51) appears as an additional field, referred to as a *damping field*. This should be added to the effective field. The Gilbert (2004) equation of motion with damping is thus

$$\frac{\partial\vec{M}(\vec{r},t)}{\partial t} = -\gamma\vec{M}(\vec{r},t)\times\Big[\vec{\mathcal{H}} - \eta\frac{\partial\vec{M}(\vec{r},t)}{\partial t}\Big]. \tag{3.52}$$

Equation (3.52) is equivalent to the Landau–Lifshitz form, equation (3.44).

In order to verify this, $\vec{M}\times$ is applied to both sides of equation (3.52).

$$\begin{aligned}\vec{M}\times\frac{\partial\vec{M}}{\partial t} &= -\gamma\vec{M}\times\Big[\vec{M}\times\big[\vec{\mathcal{H}}-\eta\frac{\partial\vec{M}}{\partial t}\big]\Big]\\ &= -\gamma\vec{M}\times\Big[\vec{M}\times\vec{\mathcal{H}}\Big]+\gamma\eta\vec{M}\times\Big[\vec{M}\times\frac{\partial\vec{M}}{\partial t}\Big].\end{aligned}\tag{3.53}$$

The second part of equation (3.53) can be simplified by observing that

$$\vec{M}\times\Big[\vec{M}\times\frac{\partial\vec{M}}{\partial t}\Big]=\vec{M}\Big[\vec{M}\cdot\frac{\partial\vec{M}}{\partial t}\Big]-\frac{\partial\vec{M}}{\partial t}\Big[\vec{M}\cdot\vec{M}\Big].\tag{3.54}$$

According to equation (3.52), $\vec{M}\cdot\frac{\partial\vec{M}}{\partial t}=0$. Therefore, equation (3.53) becomes

$$\vec{M}\times\frac{\partial\vec{M}}{\partial t}=-\gamma\vec{M}\times\Big[\vec{M}\times\vec{\mathcal{H}}\Big]-\gamma\eta M_s^2\frac{\partial\vec{M}}{\partial t}.\tag{3.55}$$

Expanding equation (3.52)

$$\frac{\partial\vec{M}}{\partial t}=-\gamma\vec{M}\times\vec{\mathcal{H}}+\gamma\eta\vec{M}\times\frac{\partial\vec{M}}{\partial t}.\tag{3.56}$$

Using $\vec{M}\times\frac{\partial\vec{M}}{\partial t}$ from equation (3.55), equation (3.56) becomes

$$\begin{aligned}\frac{\partial\vec{M}}{\partial t} &= -\gamma\vec{M}\times\vec{\mathcal{H}}-\gamma\eta\Big[\gamma\vec{M}\times\big[\vec{M}\times\vec{\mathcal{H}}\big]+\gamma\eta M_s^2\frac{\partial\vec{M}}{\partial t}\Big]\\ &= -\gamma\vec{M}\times\vec{\mathcal{H}}-\gamma^2\eta\vec{M}\times\big[\vec{M}\times\vec{\mathcal{H}}\big]-(\gamma\eta M_s)^2\frac{\partial\vec{M}}{\partial t}.\end{aligned}\tag{3.57}$$

Taking the last term on the right hand side of equation (3.57) to the left and simplifying the expression, the resulting equation is

$$\frac{\partial\vec{M}}{\partial t}=-\frac{\gamma}{1+(\gamma\eta M_s)^2}\vec{M}\times\vec{\mathcal{H}}-\frac{\gamma^2\eta}{1+(\gamma\eta M_s)^2}\vec{M}\times\Big[\vec{M}\times\vec{\mathcal{H}}\Big].\tag{3.58}$$

The Landau–Lifshitz form of the Gilbert equation is thus

$$\frac{\partial\vec{M}}{\partial t}=-\gamma'\vec{M}\times\vec{\mathcal{H}}-\frac{\lambda'}{M_s}\vec{M}\times\Big[\vec{M}\times\vec{\mathcal{H}}\Big]\tag{3.59}$$

where $\gamma'=\frac{\gamma}{1+\alpha^2}$, $\lambda'=\frac{\gamma\alpha}{1+\alpha^2}$ and $\alpha=\gamma\eta M_s$.

The predictions of equation (3.59) and equation (3.44) are similar if $\alpha^2\ll 1$.

However, for $\alpha^2 \approx 1$, the two equations yield different results, with equation (3.59) indicating that the magnetisation precesses slower than equation (3.44).

A convenient form to solve equation (3.59) is by expressing the magnetisation components in spherical coordinates since the magnitude of magnetisation is constant (Mansuripur, 1988). In this case, equation (3.59) becomes

$$\frac{\partial \theta}{\partial t} = \gamma' \mathcal{H}_\phi + \lambda' \mathcal{H}_\theta \tag{3.60}$$

$$\sin\theta \frac{\partial \phi}{\partial t} = -\gamma' \mathcal{H}_\theta + \lambda' \mathcal{H}_\phi \tag{3.61}$$

where $\mathcal{H}_\theta$ and $\mathcal{H}_\phi$ represent the polar and azimuthal components of the effective field respectively.

3.3.3 Thermal activation

An understanding of thermal effects is necessary since the recording process takes place at finite temperature. These effects become important as ferromagnetic particle sizes reduce. Likewise, this also applies to magnetic islands in BPM due to their expected sizes for areal densities beyond 1 Tb/in^2. Thermal effects determine the thermal stability of the recording medium.

If there is a large number, n, of identical and non–interacting particles at temperature T and applied field H, then the number of particles, n_i, in orientation i vary with time according to (Brown, 1979)

$$\frac{\mathrm{d}n_i}{\mathrm{d}t} = \sum_{j \neq i} (\nu_{ji} n_j - \nu_{ij} n_i) \tag{3.62}$$

where ν_{ij} is the probability per unit time to jump from orientation i to j. For k directions of easy axes, there are k values of equation (3.62) for $i = 1$ to k. However, since $\sum_i \frac{\mathrm{d}n_i}{\mathrm{d}t} = 0$, the total number, n, of particles is constant and hence there are $k - 1$ independent equations.

The probabilities per unit time, ν_{ij}, can be written as

$$\nu_{ij} = \nu_{ij}^0 e^{-v(\mathcal{U}_m - \mathcal{U}_i)/k_B T} \tag{3.63}$$

where v represents the particle volume, $\mathcal{U}_i$ the free energy density for magnetisation in orientation i and $\mathcal{U}_m$ the free energy density at the top of the barrier

separating orientations i and j (Brown, 1979). The inverse, $(\nu_{ij})^{-1}$, is sometimes called the *relaxation time*, which is a measure of the time taken by a particle to jump from orientation i to j. For uniaxial anisotropy, either $i = 1, j = 2$ or $i = 2, j = 1$.

The pre–exponential factor, ν_{ij}^0, referred to as *attempt frequency*, is taken to vary slowly with temperature as compared to the exponential term and is normally assumed to be constant (Brown, 1979). Néel (1949) estimated the attempt frequency to be 10^9 s^{-1} but values of 10^{10} s^{-1} have been used (Aharoni, 2000, p. 94).

According to equation (3.63), the exponential dependence of relaxation time on the volume, v, indicates that if the size of a particle is increased by a small amount, the increase in relaxation time is very large at fixed temperature. Thus the behaviour of ferromagnetic particles depends on particle size. For example, a cobalt sphere whose radius is 4.4 nm has a relaxation time of 6×10^5 s, whereas a 3.6 nm radius cobalt sphere has a relaxation time of 0.1 s at room temperature (Aharoni, 2000, p. 96). Since the relaxation time varies, it is necessary to consider the experimental time, which is the time taken to perform a measurement.

- *Relaxation time much greater than experimental time*
  If this is the case, there are no observable changes in magnetisation within the experimental time and thus the magnetisation does not change with time in the absence of an applied field. This is the *stable ferromagnetism* region and hysteresis is observed (Aharoni, 2000, p. 96). Therefore, for a recording medium to be thermally stable, the thermal energy (k_BT) of each ferromagnetic particle must be very small compared to the energy barriers.

- *Relaxation time much less than experimental time*
  This happens for small particles where the magnetisation jumps from one orientation to another and vice-versa during the experimental time. Thus, in the absence of an applied field, there is no measurable magnetisation. In the presence of the applied field, the magnetisation is determined by an applied field. For a recording medium having such particles and if the interactions between the particles is negligible, the magnetic properties are similar to that of a paramagnetic sample. In this case, the behaviour of such particles is the same as that of paramagnetic particles and have no hysteresis. This phenomenon is known as *superparamagnetism*.

- *Relaxation time comparable to experimental time*
  If the energy barrier is comparable to thermal energy, applying an external field and later changing its magnitude neither causes the sample to remain in one state for a long time nor attain a statistical–mechanical equilibrium in a short time. Here, magnetisation changes are observable within the experimental time and more time is needed for the change to be completed. For the case of an alternating applied field, the change in magnetisation lags behind the field. This phenomenon is referred to as *magnetic aftereffect* or *magnetic viscosity*.

  A large number of experiments have been conducted in the magnetic viscosity region, which lies between stable ferromagnetism and superparamagnetism (Aharoni, 2000, p.101). In this region, the magnetic properties change as they are being measured.

  As an illustration of magnetic viscosity, when an initially present applied field is later removed, the average (remanent) magnetisation decays with time in the timescale of the relaxation time according to

$$M_r(t) = M_r(0)e^{-t/\tau} \tag{3.64}$$

  where τ and t represent the relaxation and observation time respectively (Aharoni, 2000, p. 101). If there is a wide distribution in particle size instead, equation (3.64) can be written as

$$M_r(t) = M_r(0)\int_0^\infty P(\tau)e^{-t/\tau}\mathrm{d}\tau \tag{3.65}$$

  where P is a distribution function (Aharoni, 2000, p.101). The above integration can be carried out analytically if the distribution function is represented by the *gamma distribution function*

$$P(\tau) = \frac{1}{\tau_0\Gamma(p)}\left(\frac{\tau}{\tau_0}\right)^{p-1}e^{-t/\tau_0} \tag{3.66}$$

  where Γ represents the gamma function, p and τ_0 are parameters that can be adjusted to fit the intended distribution function (Aharoni, 2000, p. 103).

From this analysis, it is evident that thermal effects take place at different timescales, from short to long times.

3.3.4 Thermal fluctuations of non–interacting single domain particles

Brown (1979) introduced a dynamic theory that explained all the phenomena from stable ferromagnetism to superparamagnetism. The theory applies to fine ferromagnetic particles and not only describes equilibrium states but also transitions to new states when the external field is changed.

A fine ferromagnetic particle does not possess a domain structure and has a uniform magnetisation $\vec{M}$ of which its magnitude, M_s, is dependent on the material and the temperature. The magnetisation direction is determined by the anisotropy (either crystalline, or shape or both) and the applied field. Thus the theory applies to single domain particles and it is assumed that they are far apart so that interactions are negligible.

As a starting point to the theory, a relevant thermodynamic potential is the *Helmholtz free energy* where temperature is an independent variable. The Helmholtz free energy is expressed mathematically as

$$F = U - TS \tag{3.67}$$

where U is the internal energy, and S the entropy of the system. The free energy is expressed in statistical mechanics as $F = -k_B T \ln Z$, where $Z = \sum_{st} e^{-E/k_B T}$ is the partition function and E represents the energy of a microstate. The partition function can also be written as $Z = e^{-F/k_B T}$.

Brown (1979) pointed out that according to the Brownian motion in one dimension the system is essentially a particle in a viscous fluid which is not in equilibrium. In this case, choosing a coordinate, x, of the center of mass of a particle together with other appropriate coordinates, ξ_i, the subsystem portrayed by ξ_i can be viewed as being in thermal equilibrium at each value of x. The partition function for each x is $Z_1(x) = e^{-F_1(x)/k_B T}$. Here Z_1 only includes the summation over the ξ_i states. The free energy for the entire system in thermodynamic equilibrium is $Z = \sum_x Z_1(x) = \sum_x e^{-F_1(x)/k_B T}$.

For a magnetic system, the coordinate x is represented by angles θ and ϕ which describe orientations of the magnetic moment. In this case, the subsystem free energy analogous to F_1 is $F(\theta, \phi)$. When the system is in equilibrium, the mean values of observable quantities can be obtained by summing over the states with the quantity in each state weighed by a factor $e^{-F(\theta,\phi)/k_B T}$. The time to attain

internal equilibrium at each (θ, ϕ) has been assumed to be very short compared to the time to attain equilibrium values of θ and ϕ (Brown, 1979).

Discrete orientation model

This model works if the energy barriers are large in comparison to thermal energy. In the absence of an applied field, the magnetisation lies along one of the easy axis directions (θ_i, ϕ_i). Only the simplest case of two orientations is considered. This applies to particles that possess uniaxial anisotropy or prolate ellipsoids. For simplicity, it is assumed that the applied field is along the easy axis. Using the notation of Brown (1979), $i = 1$ represents the positive orientation and $i = 2$ the negative. Equation (3.62) simplifies to

$$\frac{\mathrm{d}n_1}{\mathrm{d}t} = -\frac{\mathrm{d}n_2}{\mathrm{d}t} = \nu_{21} n_2 - \nu_{12} n_1. \tag{3.68}$$

Since $n_2 = n - n_1$, this implies that equation (3.68) becomes

$$\frac{\mathrm{d}n_1}{\mathrm{d}t} = \nu_{21}(n - n_1) - \nu_{12} n_1 = \nu_{21} n - (\nu_{12} + \nu_{21}) n_1 \tag{3.69}$$

whose solution is

$$n_1(t) = \frac{\nu_{21}}{\nu_{12} + \nu_{21}} n + \left(n_1(t = 0) - \frac{\nu_{21}}{\nu_{12} + \nu_{21}} n \right) e^{-(\nu_{21} + \nu_{12})t} \tag{3.70}$$

provided ν_{21} and ν_{12} are not functions of time. Similarly,

$$n_2(t) = \frac{\nu_{12}}{\nu_{12} + \nu_{21}} n + \left(n_2(t = 0) - \frac{\nu_{12}}{\nu_{12} + \nu_{21}} n \right) e^{-(\nu_{21} + \nu_{12})t} \tag{3.71}$$

where $1/(\nu_{21} + \nu_{12})$ is a time constant.

In thermodynamic equilibrium, the time derivatives in equation (3.68) vanish and thus $n_1/n_2 = \nu_{21}/\nu_{12}$. According to equation (3.63), assuming the same attempt frequency, $\nu_{21}/\nu_{12} = e^{-v(\mathcal{U}_1 - \mathcal{U}_2)/k_B T}$. However, the dependence of n_i on $e^{-v\mathcal{U}_i/k_B T}$ is not strictly proportional as Brown (1979) pointed out, and attributed this to particles having statistical distributions about the easy axis orientations.

Brown (1979) highlighted the weaknesses of the discrete orientation model. When the energy barriers are not large in comparison to thermal energy, a better model is required that not only evaluates ν_{ij}^0 but also justifies the suitability of the discrete orientation model for large barriers. It is clear that neither does this

model apply when energy barriers are comparable to k_BT nor provides a criterion for choosing a ratio between the energy barrier and k_BT that can be considered large enough for its validity.

Dynamic model with thermal fluctuations

The Landau–Lifshitz–Gilbert (LLG) equation describes the dynamics of magnetisation without thermal fluctuations. This provides a suitable starting point towards a model that incorporates thermal effects. The Landau–Lifshitz equivalent of the LLG equation which appears as equation (3.59) was written by Brown (1979) in a different form by making use of a unit vector parallel to the magnetisation, $\hat{m} = \frac{\vec{M}}{M_s}$. Since the effective field can be expressed as $\vec{\mathcal{H}} = -\frac{\partial \mathcal{U}}{\partial \vec{M}}$, where $\mathcal{U}$ is the free energy per unit volume, this implies that

$$\begin{aligned} \vec{\mathcal{H}} &= -\frac{1}{M_s}\frac{\partial \mathcal{U}}{\partial \hat{m}} \\ &= -\frac{1}{M_s}\nabla \mathcal{U}. \end{aligned} \tag{3.72}$$

In this case, equation (3.59) becomes

$$\frac{\mathrm{d}\hat{m}}{\mathrm{d}t} = a\hat{m} \times \nabla \mathcal{U} + b\hat{m} \times (\hat{m} \times \nabla \mathcal{U}) \tag{3.73}$$

where $a = \frac{\gamma'}{M_s}$ and $b = \frac{\lambda'}{M_s}$.

Brown (1979) indicated that, analogous to Brownian motion where a random force whose time and ensemble averages are zero is added to account for thermal fluctuations, a random term $\vec{h}(t)$ can added to the effective field. Alternatively, a random term $\vec{g}(t) = M_s\vec{h}(t)$ is added to $-\nabla \mathcal{U}$ such that the components of $\vec{g}(t)$ satisfy

$$\big\langle g_i(t) \big\rangle = 0 \qquad \big\langle g_i(t) g_j(t+\tau) \big\rangle = \mu \delta_{ij} \delta(\tau) \tag{3.74}$$

where the first part of equation (3.74) indicates that the ensemble average of $\vec{g}(t)$ is zero and the second part states that for $i \neq j$, different components of $\vec{g}(t)$ are not correlated; for $i = j$, $g_i(t)$ and $g_i(t+\tau)$ are uncorrelated for any $\tau \neq 0$. The quantity μ is a function of temperature, δ_{ij} is the *Kronecker delta* and δ is the *Dirac delta*.

Equation (3.73) thus becomes

$$\frac{\mathrm{d}\hat{m}}{\mathrm{d}t} = a\hat{m} \times \Big[\nabla\mathcal{U} - \vec{g}(t)\Big] + b\hat{m} \times \Big[\hat{m} \times \big(\nabla\mathcal{U} - \vec{g}(t)\big)\Big] \tag{3.75}$$

Equation (3.75) describes the evolution of magnetisation with time and incorporates thermal fluctuations.

It was mentioned earlier in this section that particles have magnetisation orientations which have statistical distributions about the easy axis orientations. In order to include these distributions, Brown (1979) considered a unit sphere representing an instantaneous orientation (θ, ϕ) of the magnetisation. A statistical ensemble of identical particles where $\mathcal{W}(\theta, \phi)\mathrm{d}\Omega$ represent a probability of an ensemble member having an orientation (θ, ϕ) within a solid angle $\mathrm{d}\Omega$ was also considered. Since the summation of all probabilities (which is an integration in this case) is unity, it is seen that $\mathcal{W}(\theta, \phi)$ corresponds to a surface density on the unit sphere. From the equation of continuity, a surface density corresponds to a current density, $\vec{\mathrm{J}}$, according to

$$\frac{\partial\mathcal{W}}{\partial t} = -\nabla \cdot \vec{\mathrm{J}}. \tag{3.76}$$

If there is a large number, n, of non–interacting particles, the statistical properties approximate a statistical ensemble and hence the number of particles having orientations (θ, ϕ) within a solid angle $\mathrm{d}\Omega$ is approximately $n\mathcal{W}(\theta, \phi)\mathrm{d}\Omega$ (Brown, 1979).

An expression for the current density, $\vec{\mathrm{J}}$, in terms of equation (3.75) can be obtained. Without the random field, $\vec{\mathrm{J}} = \mathcal{W}\frac{\mathrm{d}\hat{m}}{\mathrm{d}t}$ whereas with the random field, as argued by Brown (1979), the current density is

$$\vec{\mathrm{J}} = \mathcal{W}\frac{\mathrm{d}\hat{m}}{\mathrm{d}t} - k'\nabla\mathcal{W} \tag{3.77}$$

where k' is a positive constant and depends on temperature.

Substituting the expression for current density from equation (3.77) into equation (3.76), the result is

$$\frac{\partial\mathcal{W}}{\partial t} = -\nabla \cdot \Big[\mathcal{W}\frac{\mathrm{d}\hat{m}}{\mathrm{d}t} - k'\nabla\mathcal{W}\Big] = -\nabla \cdot \Big[\mathcal{W}\frac{\mathrm{d}\hat{m}}{\mathrm{d}t}\Big] + k'\nabla^2\mathcal{W}. \tag{3.78}$$

Using the expression of $\frac{\mathrm{d}\hat{m}}{\mathrm{d}t}$ from equation (3.75), when substituted into equation (3.78), the final expression is

$$\frac{\partial \mathcal{W}}{\partial t} = a\hat{m}\Big[\nabla\mathcal{W} \times \nabla\mathcal{V}\Big] + b\nabla \cdot \Big[\mathcal{W}\nabla\mathcal{V}\Big] + k'\nabla^2\mathcal{W} \tag{3.79}$$

Equation (3.79) is also referred to as the *Fokker–Planck* equation of the problem. The constant k' is obtained by substituting the equilibrium distribution, $W_0 = Ae^{-v\mathcal{U}/k_BT}$, where A is a constant, for $\frac{\partial \mathcal{W}}{\partial t} = 0$. It is found that $k' = \frac{bk_BT}{v}$.

The low energy barrier or high temperature case corresponds to $\frac{v|\mathcal{U}|}{k_BT} \ll 1$. An equilibrium solution of the Fokker–Planck equation for this case, according to Brown (1979) for $\mathcal{V} = \mathcal{U}(\theta)$ only, is $\mathcal{W} =$ constant.

In the high energy barrier approximation and for an axially symmetric free energy per unit volume, $\mathcal{U} = \mathcal{U}(\theta)$, Brown (1963) showed that the attempt frequency can be expressed as

$$f_0 = \frac{\gamma\alpha H_K}{1+\alpha^2}\sqrt{\frac{K_1V}{\pi k_BT}}\left(1-h^2\right)(1+h) \tag{3.80}$$

where γ is the gyromagnetic ratio of an electron spin, α is a phenomenological damping constant, H_K is the effective anisotropy field, V is the volume, $h = H/H_K$, and H is the external field which is applied along the easy axis. For magnetisation initially in a shallower local minimum, h is negative.

The intermediate energy barrier case corresponds to $\frac{v|\mathcal{U}|}{k_BT} \approx 1$. Here numerical methods have to be used to solve the Fokker–Planck equation.

In the above cases, the free energy density, $\mathcal{U}$, was taken as a function of the polar angle θ only. The case $\mathcal{U} = \mathcal{U}(\theta, \phi)$ is more complicated, as Brown (1979) pointed out, and he found some approximate solutions in certain limiting cases. Klik and Gunther (1990) and Coffey *et al.* (1998) have developed a theoretical formalism of determining the attempt frequency for a non-axially symmetric free energy density. Numerical simulations based on the Landau-Lifshitz-Gilbert equation with a random thermal field was carried out by Suh *et al.* (2008) to validate the theoretical formalism which revealed attempt frequencies in good agreement with theory.

The theoretical studies of attempt frequencies depend on the phenomenological damping constant, for example equation (3.80). However, the actual value

of damping constant is not easily measurable. For uniaxial anisotropy, as Aharoni (2000, p. 94) pointed out, treating the attempt frequency as a constant is a sufficiently good approximation provided the chosen value is not drastically different from the predictions of the theory.

3.4 Models of magnetic recording in BPM

The concepts discussed in previous sections are all relevant to the modelling of write errors in BPM. Experimental studies of write errors in BPM showed that this is a practical problem and thus a further investigation of parameters causing write errors is necessary (Grobis *et al.*, 2010). A number of attempts have been made to model BPM write errors, some are purely statistical, others entirely micromagnetic based. Other models combine micromagnetic simulations and statistical concepts.

3.4.1 Richter's model

Richter *et al.* (2006b) proposed an extremely computationally efficient statistical model that considers write errors and the ability of the head field to switch islands when there is a distribution of switching fields. The model predicts error rates as a function of standard deviations of island properties. Richter *et al.* (2006b) assumed that a target island will switch correctly if the head switches within a range of $B/2$ from the expected switching point (where B is the down-track island spacing, or island period). A write error will occur if variations of head position relative to the island lead to a displacement greater than $B/2$.

The effect of variations in island properties on the timing window are incorporated in the model by mapping them onto variations in head switching positions. In the case of island position variations, these are treated as head position variations. Variations in island switching field (ΔH_k) are transformed into variations in position (Δx) by use of the head field gradient at the ideal switching position according to

$$\frac{\mathrm{d}x}{\mathrm{d}H_{\mathrm{eff}}}\Delta H_k = \Delta x, \tag{3.81}$$

where H_{eff} is the effective head field (ratio of field magnitude to normalised switching field), x is the position, and H_k is the switching field of the island. Equation (3.81) shows that all variations in island properties can be mapped into

position variations (jitter).

Considering a timing margin of ±B/2, the probability of a timing error to happen assuming a *Gaussian* distribution of head positions is

$$P_t = 1 - \mathrm{erf}\left(\frac{B/2}{\sigma_x\sqrt{2}}\right) \tag{3.82}$$

where B is the bit length (island period), σ_x is the standard deviation of all distributions combined and erf represents the *error function*.

If σ_1, σ_2, σ_3 denotes the standard deviation of the distribution in parameter 1, 2, 3 respectively which are not correlated, the standard deviation of these distributions combined is

$$\sigma_{\mathrm{tot}} = \sqrt{\sigma_1^2 + \sigma_2^2 + \sigma_3^2}. \tag{3.83}$$

Apart from assuming a timing margin in a calculation of write errors, this approach relies on the assumption of an effective head field that is a symmetric function of position and has a constant gradient within the write-window. This second approximation is not likely to be the case in a practical system with acceptable error rates where errors occur at the extremities of distributions and thus near the edges of the write-window. A realistic head will be designed to have an effective field that attenuates substantially between islands and thus the approximation of a symmetric head field with constant gradient is quite unlikely to be accurate in the regions where errors actually occur.

Richter *et al.* (2006b) also calculated errors due to a writing margin that arose from the island switching field distribution. Since there is a maximum effective field available from the head, and the island switching fields are variable, the probability that an island will have a switching field greater than the maximum available head field can be calculated and included in the overall write error rate. The probability of failing to write high anisotropy islands can be expressed as

$$P_w = \frac{1}{2}\left(1 - \mathrm{erf}\left(\frac{H_{\mathrm{eff,\ max}} - H_{\mathrm{eff,av}}}{\sigma_{H_{\mathrm{eff}}}\sqrt{2}}\right)\right) \tag{3.84}$$

where $H_{\mathrm{eff,\ max}}$ is the maximum effective head field experienced by islands, $H_{\mathrm{eff,\ av}}$ is the mean anisotropy field and $\sigma_{H_{\mathrm{eff}}}$ is the standard deviation in anisotropy field.

The combined error rate is obtained from

$$\mathrm{BER}_{\mathrm{tot}} \approx 0.5(P_t + P_w). \tag{3.85}$$

Middleton (2009) studied the recording potential of imperfect magnetic particles in terms of probabilities of occurence of imperfections. The study indicated that the incidence and size of imperfections should be reduced significantly below currently known values in order to achieve error rates of practical interest in BPM. Middleton and McKirdy (2009) studied perpendicular recording on BPM using a shielded and unshielded head. The study showed that higher recording densities can be achieved for particles displaying non-uniform magnetisation reversal compared to those whose magnetisation reverse coherently. The study also revealed that shielded heads are more favourable for attaining higher recording densities compared to unshielded heads.

3.4.2 Micromagnetic based models

The major limitation of micromagnetic models is the computation times involved in write modelling. Despite being computationally intensive, some work has been carried out to study write errors in BPM.

Fidler *et al.* (2006) carried out full micromagnetic simulations involving many islands to model writing in BPM. Recent work using micromagnetic simulations of a single BPM element was used to determine the region available to switch the target island only for a given head field strength, spacing between islands, and distributions in anisotropy fields in the down-track direction (Livshitz *et al.*, 2009b). In this approach, the switching field of a target island as a function of head switching position is first computed. From this, the switching field curve for the previously written island is obtained by shifting the curve by the island period assuming weak magnetostatic interactions. For a given head field strength, the intersection of the switching field curve for the target, head field strength line, and the previously written island curve provides a region where the head can write the target island and not the previously written one. Livshitz *et al.* (2009b) also presented an expression for the switching probability that depends on the switching field curves and takes into account distributions in island properties. This 1-D model was extended to 2-D in order to study the effect of overwriting adjacent tracks as the head attempts to write the target island (Livshitz *et al.*,

2009a). The results of 1-D and 2-D simulations showed that the distributions have severe impact on the performance of BPM. The model assumes a linear relationship between distributions in switching fields to those of anisotropy fields in a calculation of switching probability. This is true for homogeneous islands (single domain) but not so for heterogeneous (ECC) type which is a weakness of the model.

Schabes (2008) carried out an analysis of design tolerances of BPM using dynamic micromagnetic simulations and statistical models. A larger population of islands was considered to determine the impact of distributions (assumed to be Gaussian) in island magnetic properties on Bit Error Rate (BER) and phase margin during writing. The fabrication tolerances were estimated from statistical analysis. His results predicted narrow timing margins and quite high error rates for one particular design point. It was also shown that a deviation of the separation between the write head and the island from the optimum separation for higher recording densities (> 1 Tb/in^2) leads to a significant BER.

Micromagnetic models have also been used to study the recording performance of BPM by producing switching maps (Greaves *et al.*, 2010). The switching maps are obtained from a range of head switching positions as the head attempts to switch the islands. The write-window was obtained by considering switching maps for two islands, one of which the head intends to write and the other being the previously written island. The results predicted a narrow write-window at higher recording densities.

3.5 Summary and Conclusions

This chapter has reported current models in magnetic recording. The Stoner-Wohlfarth model is the simplest but captures the essential physics of magnetic recording. The limitations of this model lie in not only considering particles that are described by an ellipsoid of revolution but also ignoring magnetisation dynamics. Micromagnetic models avoid the limitations of the Stoner-Wohlfarth model and include all the relevant competing energy terms. Thermal effects can be added to the equation governing the evolution of magnetisation since recording takes place at finite temperature.

Current models of recording in BPM have been discussed and each has its own

weaknesses and strengths. What is desired is a model that avoids the approximations of earlier models without resorting to time consuming micromagnetic simulation of huge populations of islands. The purpose of the next two chapters is to present the development of a realistic but efficient model of write errors in BPM.

Chapter 4

Statistical write model development: Part I

A great deal of my work is just playing with equations and seeing what they give – Paul A. M. Dirac

4.1 Introduction

The purpose of this chapter and the next is to develop a statistical write model. A simple but realistic model of a single island switching in uniform and non-uniform fields is needed because micromagnetic models are too slow. The Stoner-Wohlfarth model is the simplest, in that the island is represented by a single anisotropy. What is required is an expression for the switching field that includes both shape and crystalline anisotropy to enable the study of the effect of variable shape among others. For realistic shaped islands, the switching fields require the volume averaged demagnetising factors but these factors are difficult to calculate.

To begin with, the volume averaged demagnetising factors of a generalised geometry that satisfactorily describes most proposed island shapes are derived. Following this is a derivation of an analytic model of switching in uniform applied fields for islands described by this generalised geometry. In this section, the dependence of switching fields on island geometry is studied. The chapter then extends the model of switching to non-uniform fields.

Some sections of this chapter are taken from the papers included in appendix B. These papers were written by the author of this thesis who carried out all of the model developments and obtained all of the model results described in

those papers.

4.2 Magnetometric demagnetising factors of an arbitrary truncated elliptic cone

An arbitrary truncated elliptic cone which is a generalised geometry that satisfactorily describes most proposed island shapes (Belle *et al.*, 2008, 2007) was selected. Figure 4.1(a) shows the parameters that describe this geometry which covers a range of shapes from truncated elliptic to circular full cones, and from elliptic cylinders to circular cylinders. Figure 4.1(b) shows the Scanning Electron Microscope (SEM) image of real islands for comparison.

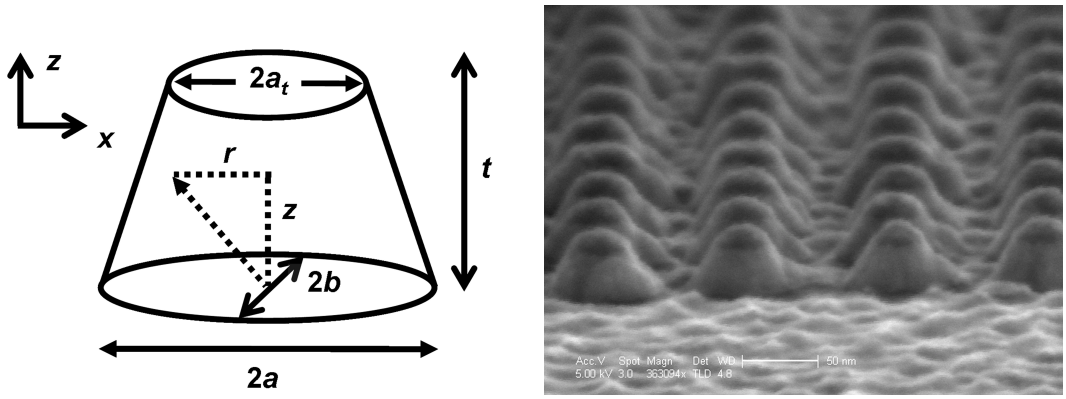

(a) (b)

Figure 4.1: (a) Truncated elliptic cone geometry and associated parameters: a is the semi-major axis, b is the semi-minor axis, $e = b/a$ is the in-plane ellipticity. (b) SEM image of real islands (Belle *et al.*, 2008, 2007) where the lighter shaded material in the shape of truncated cones is magnetic.

The self-demagnetising field of a uniformly magnetised truncated elliptic cone shaped island is non-uniform which implies that the demagnetising field will vary with position. In order to study the magnetostatics of such an object, it is necessary to calculate the volume average of the demagnetising field over the island. The demagnetising field derive the demagnetising factors for the whole body. The volume average of the demagnetising factors are referred to as *magnetometric* demagnetising factors and are used in a calculation of magnetostatic self energy.

The calculation of magnetometric demagnetising factors for an arbitrary truncated elliptic cone can be attempted in real space. A suitable starting point is

the magnetostatic self energy of a ferromagnetic particle which is written in SI units as (Aharoni, 2000, p. 111)

$$\mathcal{E}_d = -(\mu_0/2)\int \vec{M}\cdot\vec{H}_d \mathrm{d}^3\vec{r} \tag{4.1}$$

where μ_0 is the permeability of free space, $\vec{M}$ is the magnetisation and $\vec{H}_d$ is the self-demagnetising field.

The self-demagnetising field is given by (Aharoni, 2000, p. 125)

$$\vec{H}_d = -\nabla U \tag{4.2}$$

where

$$U = \frac{1}{4\pi}\left(-\int \frac{\nabla'\cdot\vec{M}(\vec{r}')}{|\vec{r}-\vec{r}'|}\mathrm{d}^3\vec{r}' + \int \frac{\vec{n}\cdot\vec{M}(\vec{r}')}{|\vec{r}-\vec{r}'|}\mathrm{d}S'\right). \tag{4.3}$$

In equation (4.2), U represents the magnetic scalar potential that is given by equation (4.3). The del operator, ∇', contains derivatives with respect to $\vec{r}'$. The first integral in the magnetic scalar potential is over the ferromagnetic body whereas the second integral is over the surface, $\vec{n}$ is the unit outward normal.

For an arbitrary particle shape, which includes an arbitrary truncated elliptic cone, the evaluation of the surface integral in equation (4.3) is a non-trivial task since the unit outward normal should be known explicitly. This can be avoided by converting the surface integral to a volume integral by applying the divergence theorem. The self-demagnetising field becomes

$$\begin{aligned}\vec{H}_d &= \frac{1}{4\pi}\nabla\left(\int \frac{\nabla'\cdot\vec{M}(\vec{r}')}{|\vec{r}-\vec{r}'|}\mathrm{d}^3\vec{r}' - \int \nabla'\cdot\left[\frac{\vec{M}(\vec{r}')}{|\vec{r}-\vec{r}'|}\right]\mathrm{d}^3\vec{r}'\right)\\ &= -\frac{1}{4\pi}\nabla\int \vec{M}(\vec{r}')\cdot\nabla'\frac{1}{|\vec{r}-\vec{r}'|}\mathrm{d}^3\vec{r}'.\end{aligned} \tag{4.4}$$

The final expression is obtained after expanding the divergence in the second term. For a uniformly magnetised particle, equation (4.4) becomes

$$\vec{H}_d = -\vec{M}\cdot\left[\frac{1}{4\pi}\int \nabla\nabla'\frac{1}{|\vec{r}-\vec{r}'|}\mathrm{d}^3\vec{r}'\right] \tag{4.5}$$

where the integral is over the volume occupied by the particle.

The self-demagnetising field of a uniformly magnetised particle, according to

equation (4.5), can be expressed as

$$H_d = -\vec{N} \cdot \vec{M} \tag{4.6}$$

where $\vec{N}$ is the demagnetising factor tensor which depends on island shape.

Using equation (4.5), the magnetostatic self energy, equation (4.1), for a uniformly magnetised particle becomes

$$\mathcal{E}_d = \frac{\mu_0}{2}\vec{M} \cdot \int \left[\frac{1}{4\pi} \int \nabla\nabla' \frac{1}{|\vec{r} - \vec{r}'|} \mathrm{d}^3\vec{r}' \right] \mathrm{d}^3\vec{r} \cdot \vec{M} \tag{4.7}$$

where the integrals are over the volume occupied by the particle.

Now, using equation (4.6), the magnetostatic self energy can be expressed as

$$\begin{aligned} \mathcal{E}_d &= \frac{\mu_0}{2} \int \vec{M} \cdot \vec{N} \cdot \vec{M} \mathrm{d}^3\vec{r} \\ &= \frac{\mu_0}{2}\vec{M} \cdot \left[\int \vec{N} \mathrm{d}^3\vec{r} \right] \cdot \vec{M}. \end{aligned} \tag{4.8}$$

According to equation (4.8), the magnetostatic self energy can be written as

$$\mathcal{E}_d = \frac{\mu_0}{2} V \vec{M} \cdot \mathcal{N} \cdot \vec{M} \tag{4.9}$$

where V is the particle volume and $\mathcal{N}$ is the volume average of the demagnetising factor tensor also referred to as magnetometric demagnetising factor tensor.

Upon comparing equation (4.9) to equation (4.7), the magnetometric demagnetising factor tensor for an arbitrary shape can be expressed as

$$\mathcal{N} = \frac{1}{4\pi V} \int \left[\nabla \int \nabla' \frac{1}{|\vec{r} - \vec{r}'|} \mathrm{d}^3\vec{r}' \right] \mathrm{d}^3\vec{r}. \tag{4.10}$$

According to equation (4.10), the calculation of magnetometric demagnetising factors for an arbitrary truncated elliptic cone in real space is cumbersome and non-trivial because it involves a sixfold integral with variable limits of integration.

It is convenient to calculate these factors in Fourier space using an approach proposed by Beleggia and Graef (2003). Equation (4.10) can be expressed as

$$\mathcal{N} = \frac{1}{4\pi V} \int \left[\mathscr{F}^{-1} \left\{ \mathscr{F} \left\{ \nabla \int \nabla' \frac{\rho(\vec{r}')}{|\vec{r} - \vec{r}'|} \mathrm{d}^3\vec{r}' \right\} \right\} \right] \mathrm{d}^3\vec{r} \tag{4.11}$$

where $\mathscr{F}$ and $\mathscr{F}^{-1}$ represent the *Fourier transform* and *inverse Fourier transform* operators respectively, $\rho(\vec{r}')$ is a shape function which is one (unity) for any point inside the particle geometry and vanishes outside. This allows the volume integral over $\vec{r}'$ to cover all space. The Fourier transform of the quantity that appears in equation (4.11) can be obtained and the result is

$$\mathscr{F}\left\{\nabla\int\nabla'\frac{\rho(\vec{r}')}{|\vec{r}-\vec{r}'|}\mathrm{d}^3\vec{r}'\right\}=4\pi\frac{\vec{k}\vec{k}\rho(\vec{k})}{k^2} \tag{4.12}$$

where $\vec{k}$ is a wavevector and k the magnitude of the wavevector.

Upon substituting equation (4.12) into equation (4.11) and using an explicit expression for the inverse Fourier transform the result is

$$\begin{aligned}\mathcal{N}&=\frac{1}{(2\pi)^3V}\int_{\vec{r}}\left[\int_{\vec{k}}e^{i\vec{k}\cdot\vec{r}}\frac{\vec{k}\vec{k}\rho(\vec{k})}{k^2}\mathrm{d}^3\vec{k}\right]\mathrm{d}^3\vec{r}\\&=\frac{1}{(2\pi)^3V}\int_{\vec{k}}\left[\int_{\vec{r}}e^{i\vec{k}\cdot\vec{r}}\mathrm{d}^3\vec{r}\right]\frac{\vec{k}\vec{k}\rho(\vec{k})}{k^2}\mathrm{d}^3\vec{k}\\&=\frac{1}{(2\pi)^3V}\int_{\vec{k}}\rho^\star(\vec{k})\frac{\vec{k}\vec{k}\rho(\vec{k})}{k^2}\mathrm{d}^3\vec{k}\\&=\frac{1}{(2\pi)^3V}\int_{\vec{k}}\frac{|\rho(\vec{k})|^2}{k^2}\vec{k}\vec{k}\mathrm{d}^3\vec{k}.\end{aligned} \tag{4.13}$$

The magnetometric demagnetising factors, $\mathcal{N}_{x_ix_j}$, can thus be obtained from the Fourier space integral over the entire $\vec{k}$ space (Beleggia and Graef, 2003) according to

$$\mathcal{N}_{x_ix_j}=\frac{1}{(2\pi)^3V}\int\frac{|\rho(\vec{k})|^2}{k^2}k_ik_j\mathrm{d}^3\vec{k} \tag{4.14}$$

where V is the volume occupied by the particle, $\vec{k}$ is the wave vector, $x_1=x$, $x_2=y$, $x_3=z$, and $\rho(\vec{k})$ is the shape amplitude which has to be obtained from the integral (Beleggia and Graef, 2003; Beleggia *et al.*, 2005; Tandon *et al.*, 2004)

$$\rho(\vec{k})=\int_{\mathcal{R}}e^{-i\vec{k}\cdot\vec{r}}\mathrm{d}^3\vec{r}. \tag{4.15}$$

The region $\mathcal{R}$ in equation (4.15) covers the volume V.

The trace of the magnetometric demagnetising factor tensor, equation (4.13),

is

$$\begin{aligned}
\mathcal{N}_{x_1x_1} + \mathcal{N}_{x_2x_2} + \mathcal{N}_{x_3x_3} &= \frac{1}{(2\pi)^3 V} \int \frac{|\rho(\vec{k})|^2}{k^2} \left(k_x^2 + k_y^2 + k_z^2\right) \mathrm{d}^3\vec{k} \\
&= \frac{1}{(2\pi)^3 V} \int |\rho(\vec{k})|^2 \mathrm{d}^3\vec{k} \\
&= \frac{1}{(2\pi)^3 V} \int_{\vec{k}} \int_{\mathcal{R}} \int_{\mathcal{R}'} e^{i\vec{k}\cdot(\vec{r}-\vec{r}')} \mathrm{d}^3\vec{r}' \mathrm{d}^3\vec{r} \mathrm{d}^3\vec{k} \\
&= \frac{1}{(2\pi)^3 V} \int_{\mathcal{R}} \int_{\mathcal{R}'} (2\pi)^3 \delta\left(\vec{r} - \vec{r}'\right) \mathrm{d}^3\vec{r}' \mathrm{d}^3\vec{r} \\
&= \frac{1}{V} \int_{\mathcal{R}} \mathrm{d}^3\vec{r} \\
&= 1. \qquad (4.16)
\end{aligned}$$

For an arbitrary truncated elliptic cone, the region $\mathcal{R}$ in equation (4.15) is bounded by the planes $z = 0$, $z = t$ and the surface of the cone which is given by the equation

$$\frac{x^2}{a^2} + \frac{y^2}{b^2} = \left(1 - \frac{z}{z_0}\right)^2 \qquad (4.17)$$

where $z_0 = t/(1 - a_t/a)$, $0 \le z \le t$, $-a \le x \le a$, $-b \le y \le b$.

Using cylindrical coordinates (r, ϕ, z) as shown in Figure 4.2, the parametric form of equation (4.17) becomes

$$x_s = a(1 - z/z_0)\cos\phi \qquad y_s = \beta a(1 - z/z_0)\sin\phi \qquad (4.18)$$

where $\beta = b/a$ and ϕ is the azimuthal angle. The parametric equation of a point

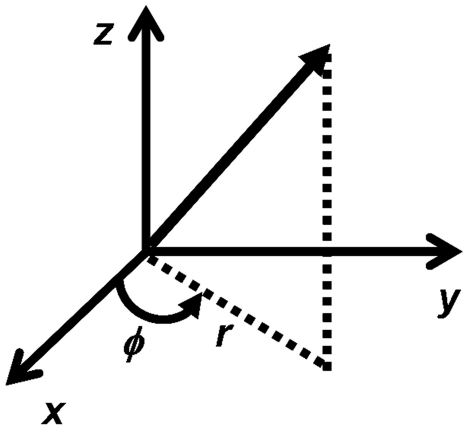

Figure 4.2: Cylindrical coordinates illustration.

inside the arbitrary truncated elliptic cone, according to equation (4.18), is

$$x = r\cos\phi \qquad y = \beta r\sin\phi \qquad z = z \tag{4.19}$$

where $0 \leq r \leq a(1 - z/z_0)$, $0 \leq \phi \leq 2\pi$ and $0 \leq z \leq t$.

In cylindrical coordinates, the volume element, $\mathrm{d}^3\vec{r}$, is $\beta r\mathrm{d}r\mathrm{d}\phi\mathrm{d}z$ and equation (4.15) becomes

$$\rho(\vec{k}) = \int_{\mathcal{R}} \beta r\mathrm{d}r\mathrm{d}\phi\mathrm{d}z e^{-i\vec{k}\cdot r}. \tag{4.20}$$

The phase factor in equation (4.20) can be written as

$$\vec{k}\cdot\vec{r} = k_x x + k_y y + k_z z = r(k_x\cos\phi + \beta k_y\sin\phi) + k_z z. \tag{4.21}$$

Letting $k_x = k_\rho\cos\phi_k$ and $\beta k_y = k_\rho\sin\phi_k$ (Beleggia *et al.*, 2005) implies that $\vec{k}\cdot\vec{r} = rk_\rho\cos(\phi_k - \phi) + k_z z$ and thus

$$\rho(\vec{k}) = \beta\int_{z=0}^{t} e^{-ik_z z}\mathrm{d}z\int_{r=0}^{a(1-z/z_0)} r\mathrm{d}r\int_{\phi=0}^{2\pi} e^{-irk_\rho\cos(\phi_k-\phi)}\mathrm{d}\phi \tag{4.22}$$

$$= \beta\int_{z=0}^{t} e^{-ik_z z}\mathrm{d}z\int_{r=0}^{a(1-z/z_0)} r\mathrm{d}r 2\pi J_0(rk_\rho) \tag{4.23}$$

$$= \beta\int_{z=0}^{t} e^{-ik_z z}\mathrm{d}z\frac{2\pi}{k_\rho}a(1-z/z_0)J_1(k_\rho a(1-z/z_0)). \tag{4.24}$$

The shape amplitude becomes

$$\rho(\vec{k}) = \frac{2\pi b}{k_\rho}\int_{z=0}^{t}(1-z/z_0)J_1(k_\rho a(1-z/z_0))e^{-ik_z z}\mathrm{d}z \tag{4.25}$$

where $J_1(z)$ is a *Bessel function* of the first kind.

The integral in equation (4.25) is an *incomplete Lipshitz–Hankel* type and such integrals are non-trivial to evaluate. This makes the computation of magnetometric demagnetising factors for an arbitrary truncated elliptic cone rather difficult. Closed-form solutions for *incomplete Lipshitz–Hankel* integrals can be expressed in terms of *Kampé de Fériet double hypergeometric functions* (Miller, 1986). The numerical computation of these integrals has been carried out by Dvorak and Kuester (1990). The problem with this approach is that it significantly slows down the computation of the magnetometric demagnetising factors.

However, it is convenient to leave the shape amplitude in integral form when

evaluating the integrals in equation (4.14). In this case, the complexity can be reduced in the manner below.

Expressing equation (4.14) in cylindrical coordinates, this becomes (Beleggia *et al.*, 2005)

$$\mathcal{N}_{x_i x_j} = \frac{1}{(2\pi)^3 V\beta} \int_{k_z=-\infty}^{\infty} \mathrm{d}k_z \int_{k_\rho=0}^{\infty} |\rho(k_\rho, k_z)|^2 k_\rho \mathrm{d}k_\rho \times \int_{\phi_k=0}^{2\pi} \frac{k_i k_j \mathrm{d}\phi_k}{k_\rho^2(\cos^2\phi_k + \beta^{-2}\sin^2\phi_k) + k_z^2} \tag{4.26}$$

$$k_1 = k_x = k_\rho \cos\phi_k$$
$$k_2 = k_y = \beta^{-1} k_\rho \sin\phi_k$$
$$k_3 = k_z.$$

According to equation (4.26), if $i \neq j$, the angular integration vanishes. To verify this, consider the following integral

$$I_{ij} = \int_{\phi_k=0}^{2\pi} \frac{k_i k_j \mathrm{d}\phi_k}{k_\rho^2(\cos^2\phi_k + \beta^{-2}\sin^2\phi_k) + k_z^2}. \tag{4.27}$$

If $i \neq j$, the possible integrals are

$$I_{12} = \frac{1}{\beta} \int_{\phi_k=0}^{2\pi} \frac{k_\rho^2 \cos\phi_k \sin\phi_k \mathrm{d}\phi_k}{k_\rho^2(\cos^2\phi_k + \beta^{-2}\sin^2\phi_k) + k_z^2} \tag{4.28}$$

$$I_{23} = \frac{1}{\beta} \int_{\phi_k=0}^{2\pi} \frac{k_\rho k_z \sin\phi_k \mathrm{d}\phi_k}{k_\rho^2(\cos^2\phi_k + \beta^{-2}\sin^2\phi_k) + k_z^2} \tag{4.29}$$

$$I_{13} = \int_{\phi_k=0}^{2\pi} \frac{k_\rho k_z \cos\phi_k \mathrm{d}\phi_k}{k_\rho^2(\cos^2\phi_k + \beta^{-2}\sin^2\phi_k) + k_z^2} \tag{4.30}$$

which all vanish upon integrating with respect to ϕ_k.

In this case, all cross terms in equation (4.26) vanish leaving only three non-vanishing integrals of the form

$$\mathcal{N}_{x_i x_i} = \frac{1}{(2\pi)^3 V\beta} \int_{k_z=-\infty}^{\infty} \mathrm{d}k_z \int_{k_\rho=0}^{\infty} |\rho(k_\rho, k_z)|^2 k_\rho \mathrm{d}k_\rho \times \int_{\phi_k=0}^{2\pi} \frac{k_i^2 \mathrm{d}\phi_k}{k_\rho^2(\cos^2\phi_k + \beta^{-2}\sin^2\phi_k) + k_z^2} \tag{4.31}$$

where $\mathcal{N}_{x_1 x_1} = \mathcal{N}_{xx}$, $\mathcal{N}_{x_2 x_2} = \mathcal{N}_{yy}$ and $\mathcal{N}_{x_3 x_3} = \mathcal{N}_{zz}$.

The condition for the cross terms to vanish applies to objects that have cylindrical symmetry.

The shape amplitude in equation (4.25) does not depend on the azimuthal angle which implies that the angular integral in equation (4.31) can be evaluated without difficulties. In this case the magnetometric demagnetising factors can be obtained by numerically computing the remaining double integral provided the shape amplitude is known for all values of k_ρ and k_z.

However, an efficient approach is to express the square modulus of the shape amplitude as a double integral shown in equation (4.32)

$$|\rho(k_\rho, k_z)|^2 = \left[\frac{2\pi b}{k_\rho}\right]^2 \int_{z=0}^{t}\int_{z'=0}^{t} \left[1 - \frac{z}{z_0}\right]\left[1 - \frac{z'}{z_0}\right] \times J_1\left[k_\rho a(1 - z/z_0)\right] J_1\left[k_\rho a(1 - z'/z_0)\right] e^{ik_z(z-z')} \mathrm{d}z'\mathrm{d}z. \tag{4.32}$$

Substituting equation (4.32) into equation (4.31) and after some simplifications, the fivefold integral becomes

$$\mathcal{N}_{x_i x_i} = \frac{ab}{2\pi V} \int_{z=0}^{t}\int_{z'=0}^{t} \left[1 - \frac{z}{z_0}\right]\left[1 - \frac{z'}{z_0}\right] \mathrm{d}z'\mathrm{d}z \int_{k_z=-\infty}^{\infty} e^{ik_z(z-z')} \mathrm{d}k_z \times \int_{k_\rho=0}^{\infty} \frac{J_1\left[k_\rho a(1 - z/z_0)\right] J_1\left[k_\rho a(1 - z'/z_0)\right]}{k_\rho} \mathrm{d}k_\rho \times \int_{\phi_k=0}^{2\pi} \frac{k_i^2 \mathrm{d}\phi_k}{k_\rho^2(\cos^2\phi_k + \beta^{-2}\sin^2\phi_k) + k_z^2}. \tag{4.33}$$

Considering $\mathcal{N}_{xx}$ first and reordering the integrals,

$$\mathcal{N}_{xx} = \frac{ab}{2\pi V} \int_{z=0}^{t} \int_{z'=0}^{t} \left[1 - \frac{z}{z_0}\right] \left[1 - \frac{z'}{z_0}\right] \mathrm{d}z' \mathrm{d}z \int_{\phi_k=0}^{2\pi} \cos^2 \phi_k \mathrm{d}\phi_k \int_{k_z=-\infty}^{\infty} e^{ik_z(z-z')} \mathrm{d}k_z \times \int_{k_\rho=0}^{\infty} \frac{k_\rho J_1 \left[k_\rho a(1 - z/z_0)\right] J_1 \left[k_\rho a(1 - z'/z_0)\right]}{k_\rho^2(\cos^2 \phi_k + \beta^{-2} \sin^2 \phi_k) + k_z^2} \mathrm{d}k_\rho. \tag{4.34}$$

The integral over k_ρ can be evaluated using the following standard integral (Gradshteyn and Ryzhik, 1994, p. 703)

$$\int_{x=0}^{\infty} \frac{x J_\nu(ux) J_\nu(wx)}{x^2 + c^2} \mathrm{d}x = \begin{array}{ll} I_\nu(wc) K_\nu(uc) & \text{if } 0 < w < u, \mathrm{Re}\ c > 0 \\ I_\nu(uc) K_\nu(wc) & \text{if } 0 < u < w, \mathrm{Re}\ c > 0. \end{array} \tag{4.35}$$

$I_\nu(x)$ and $K_\nu(x)$ are respectively the *modified Bessel function* of the first and second kind provided $\mathrm{Re}\ \nu > -1$.

After substituting equation (4.35) for the integral over k_ρ, the integral over k_z can then be performed using a standard integral (Gradshteyn and Ryzhik, 1994, p. 752)

$$\int_{x=0}^{\infty} I_\mu(wx) K_\mu(\nu x) \cos(cx) \mathrm{d}x = \frac{1}{2\sqrt{w\nu}} Q_{\mu - \frac{1}{2}} \left[\frac{w^2 + \nu^2 + c^2}{2w\nu}\right] \quad \mathrm{Re}\ w > |\mathrm{Re}\ \nu|, c > 0, \mathrm{Re}\ \mu > -1/2. \tag{4.36}$$

According to Gradshteyn and Ryzhik (1994, p. 1017), in the case $\mu = 1$, the *associated Legendre function*, $Q_{1/2}(z)$, can be expressed as

$$Q_{\frac{1}{2}}(z) = \frac{1}{\sqrt{2}} \int_{x=0}^{\pi} \frac{\cos x}{\sqrt{z - \cos x}} \mathrm{d}x. \tag{4.37}$$

After substituting equation (4.37) for the integral over k_z in equation (4.34),

the resulting expression becomes, after simplifications and rearranging integrals

$$\mathcal{N}_{xx} = \frac{ab}{2\pi V}\int_{x=0}^{\pi}\cos x\mathrm{d}x\int_{\phi_k=0}^{2\pi}\frac{\cos^2\phi_k}{\sqrt{\cos^2\phi_k+\beta^{-2}\sin^2\phi_k}}\mathrm{d}\phi_k \times\int_{z=0}^{t}\int_{z'=0}^{t}\frac{(1-z/z_0)(1-z'/z_0)}{\sqrt{F(z,z',\phi_k,x)}}\mathrm{d}z'\mathrm{d}z \tag{4.38}$$

where

$$\begin{aligned}F(z,z',\phi_k,x) = {}&(z'-z)^2(\cos^2\phi_k+\beta^{-2}\sin^2\phi_k)\\ &+a^2((1-z/z_0)^2+(1-z'/z_0)^2)\\ &-2a^2(1-z/z_0)(1-z'/z_0)\cos x.\end{aligned}$$

Similarly,

$$\mathcal{N}_{yy} = \frac{ab}{2\pi V}\int_{x=0}^{\pi}\cos x\mathrm{d}x\int_{\phi_k=0}^{2\pi}\frac{\sin^2\phi_k}{\sqrt{\cos^2\phi_k+\beta^{-2}\sin^2\phi_k}}\mathrm{d}\phi_k \times\int_{z=0}^{t}\int_{z'=0}^{t}\frac{(1-z/z_0)(1-z'/z_0)}{\sqrt{F(z,z',\phi_k,x)}}\mathrm{d}z'\mathrm{d}z \tag{4.39}$$

and $\mathcal{N}_{zz} = 1-\mathcal{N}_{xx}-\mathcal{N}_{yy}$ according to equation (4.16).

The integrals over z followed by z' in equations (4.38) and (4.39) can be performed easily. The result appears in appendix A.2. For $\beta = 1$, the integral over ϕ_k is trivial otherwise the remaining double integral can then be performed numerically.

The advantage of this approach is that it is computationally efficient compared to a method where the shape amplitude is first computed numerically for any k_ρ and k_z and its square modulus substituted in the integral for the magnetometric demagnetising factors. This is because the shape amplitude involves an integral of a *Bessel function* which can be regarded as another integral. The shape amplitude computation thus amounts to a double integral which has to be substituted into a triple integral to compute magnetometric demagnetising factors. This alternative approach can thus be seen as a fivefold integral which slows down the computation.

To study the dependence of magnetometric demagnetising factors on island shape, it is necessary to keep the volume constant. The volume of a truncated elliptic cone is (see appendix A.1 for a derivation)

$$V = \frac{\pi t a b}{3}\left[\left(\frac{a_t}{a} + \frac{1}{2}\right)^2 + \frac{3}{4}\right] \tag{4.40}$$

where t is the island height and a_t, a, b are defined as shown in Figure 4.1(a).

One way of varying the island shape is by changing the *ellipticity*, $e = b/a$, where the volume (V), height (t) and a_t/a as shown in equation (4.40) are fixed. In this case, equation (4.40) implies that $ab = a_0 b_0$. The parameters a_0 and b_0 were set to be equal to t. The ratio, a_t/a, was set to 1/2 and height, t, was set to 25 nm though the actual value of t does not affect the results. Since $ab = a^2 e$, a value of the parameter a corresponding to $\sqrt{a_0 b_0/e}$ was determined for a given e. The value b was then determined from $b = ea$. With the values of a, b, t and a_t/a, the magnetometric demagnetising factors were then obtained. Figure 4.3 shows the dependence of magnetometric demagnetising factors of a truncated elliptic cone on *ellipticity*, $e = b/a$, with the volume (V), height (t) and a_t/a as shown in equation (4.40) fixed.

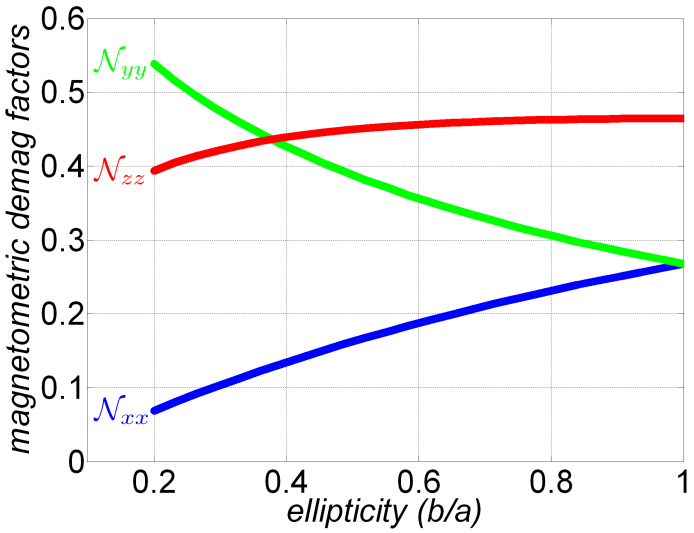

Figure 4.3: The magnetometric demagnetising factors of a truncated elliptic cone as a function of *ellipticity*, $e = b/a$. The volume, height (t = 25 nm) and a_t/a (see Figure 4.1(a)) are fixed. For $e = b/a = 1$, a_t = 12.5 nm.

Another way of varying the island shape is by changing the *sidewall angle* (see

Figure 4.4) where the volume (V), height (t) and ellipticity (e) are fixed. In this case, equation (4.40) implies that

$$a^2\left[\left(\frac{a_t}{a}+\frac{1}{2}\right)^2+\frac{3}{4}\right]=a_0^2\left[\left(\frac{a_{0t}}{a_0}+\frac{1}{2}\right)^2+\frac{3}{4}\right] \tag{4.41}$$

where $a_0 = t$ and $a_{0t} = a_0/2$.

The height, t, was set to 25 nm though the actual value of t does not affect the results. For a given value of a_t/a, a corresponding value of parameter a was obtained according to equation (4.41). With the values of a, b, t and a_t/a, the magnetometric demagnetising factors were then obtained. Figure 4.5 shows the dependence of magnetometric demagnetising factors on *sidewall angle* (see Figure 4.4) with the volume and height fixed. A sidewall angle of 39° corresponds to a cone whereas a sidewall angle of 90° corresponds to a cylinder. Only two magnetometric demagnetising factors are shown since $a = b$ in this case and thus $\mathcal{N}_{xx} = \mathcal{N}_{yy}$.

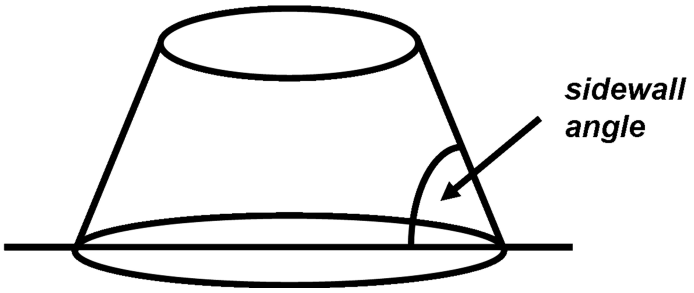

Figure 4.4: Illustration of sidewall angle. A 90° angle corresponds to a cylinder.

4.3 Switching in uniform fields

Having derived the magnetometric demagnetising factors of an arbitrary truncated elliptic cone, the next step was to determine the switching fields of magnetic islands in uniform fields. In order to obtain a sufficiently simple analytic model of switching fields, it is assumed that coherent reversal occurs and that shape is included by magnetometric demagnetising factors. A suitable starting point is the magnetostatic self energy of a ferromagnetic island, equation (4.9). If equation (4.9) is expanded using cartesian coordinates, the resulting expression

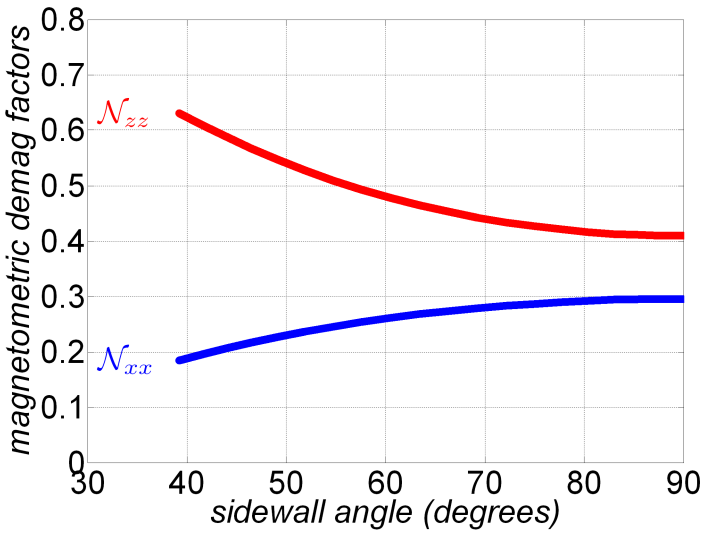

Figure 4.5: The magnetometric demagnetising factors of a truncated elliptic cone as a function of *sidewall angle* in degrees. The volume and height ($t = 25$ nm) are fixed. For a 90° sidewall angle, $a_t = a = 19.1$ nm.

is

$$\begin{aligned}\mathcal{E}_d = \frac{\mu_0 V}{2}&\left[\mathcal{N}_{xx}M_x^2 + \mathcal{N}_{yy}M_y^2 + \mathcal{N}_{zz}M_z^2\right] \\ &+ \mu_0 V\left[\mathcal{N}_{xy}M_xM_y + \mathcal{N}_{xz}M_xM_z + \mathcal{N}_{yz}M_yM_z\right].\end{aligned} \tag{4.42}$$

The cross magnetometric demagnetising factors $\mathcal{N}_{xy}$, $\mathcal{N}_{yz}$, and $\mathcal{N}_{xz}$ for truncated elliptic cones vanish according to equation (4.27). It is convenient to express the magnetisation components in spherical coordinates (M_s, θ, ϕ) and these are obtained from (M_x, M_y, M_z) by

$$M_x = M_s \sin\theta\cos\phi \quad M_y = M_s \sin\theta\sin\phi \quad M_z = M_s\cos\theta \tag{4.43}$$

where M_s is the saturation magnetisation of the island. Substituting equation (4.43) into equation (4.42), the result is

$$\mathcal{E}_d = \frac{\mu_0 M_s^2}{2}\left[\mathcal{N}_{xx}\cos^2\phi + \mathcal{N}_{yy}\sin^2\phi - \mathcal{N}_{zz}\right]V\sin^2\theta + \frac{\mu_0 M_s^2}{2}\mathcal{N}_{zz}V. \tag{4.44}$$

If the energy contribution due to crystalline uniaxial anisotropy K_1 (assumed to be along the z direction) and the external field $\vec{H}$ are included, the total energy

becomes

$$\begin{aligned}\mathcal{E} &= \left[K_1 + \frac{\mu_0 M_s^2}{2}\left[\mathcal{N}_{xx}\cos^2\phi + \mathcal{N}_{yy}\sin^2\phi - \mathcal{N}_{zz}\right]\right] V\sin^2\theta \\ &\quad + \frac{\mu_0 M_s^2}{2}\mathcal{N}_{zz}V - \mu_0 V\vec{M}\cdot\vec{H} \\ &= \left[K_1 + \frac{\mu_0 M_s^2}{2}\left[\mathcal{N}_{xx}\cos^2\phi + \mathcal{N}_{yy}\sin^2\phi - \mathcal{N}_{zz}\right]\right] V\sin^2\theta \\ &\quad - \mu_0 M_s V H(\sin\theta_H\sin\theta\cos(\phi_H-\phi) + \cos\theta_H\cos\theta) + \frac{\mu_0 M_s^2}{2}\mathcal{N}_{zz}V \qquad (4.45)\end{aligned}$$

where θ_H, ϕ_H are the applied field polar and azimuthal angles respectively and H is the applied field magnitude.

Minimisation of equation (4.45) with respect to ϕ implies that

$$M_s\sin^2\theta\left[\mathcal{N}_{yy} - \mathcal{N}_{xx}\right]\sin\phi\cos\phi = H\sin\theta_H\sin\theta\sin\left(\phi_H - \phi\right). \qquad (4.46)$$

Equation (4.46) reveals that if $\sin\theta = 0$, any magnetisation azimuthal, ϕ, is a solution. In the general case, the magnetisation azimuthal, ϕ, is coupled to the magnetisation polar angle, θ, which implies that reversal is not in a plane. This makes the problem of finding the magnetisation directions difficult. However, if $\mathcal{N}_{xx} = \mathcal{N}_{yy}$, or $\phi_H = \pi/2$ or $\phi_H = 0$, then reversal occurs in a plane and $\phi = \phi_H$ as shown below.

If $\mathcal{N}_{xx} = \mathcal{N}_{yy}$, the left hand side of equation (4.46) vanishes. The right hand side vanishes if $\phi = \phi_H$. If $\phi_H = \pi/2$, the right hand side of equation (4.46) becomes $H\sin\theta_H\sin\theta\cos\phi$ and thus $\phi = \phi_H = \pi/2$ ensures that the left and right hand side of equation (4.46) vanish. If $\phi_H = 0$, the right hand side of equation (4.46) becomes $H\sin\theta_H\sin\theta\sin\phi$ and thus $\phi = \phi_H = 0$ ensures that the left and right hand side of equation (4.46) vanish.

For these conditions, the magnetisation always lies in the plane formed by the anisotropy and external field. For reversal in a plane, the total energy simplifies to

$$\begin{aligned}\mathcal{E} &= \left[K_1 + \frac{\mu_0 M_s^2}{2}\left[\mathcal{N}_{xx}\cos^2\phi_H + \mathcal{N}_{yy}\sin^2\phi_H - \mathcal{N}_{zz}\right]\right] V\sin^2\theta \\ &\quad - \mu_0 M_s V H\cos(\theta_H - \theta) + \frac{\mu_0 M_s^2}{2}\mathcal{N}_{zz}V. \qquad (4.47)\end{aligned}$$

It is convenient to work with dimensionless quantities. Let

$$K_1^{\text{eff}} = K_1 + \frac{\mu_0 M_s^2}{2}\left[\mathcal{N}_{xx}\cos^2\phi_H + \mathcal{N}_{yy}\sin^2\phi_H - \mathcal{N}_{zz}\right] \tag{4.48}$$

be the total anisotropy constant including crystalline and shape anisotropy.

Dividing equation (4.47) by $2K_1^{\text{eff}}V$ and ignoring the constant energy term which does not affect the behaviour of the magnetisation, this becomes

$$\begin{aligned}\mathcal{E}' = \frac{\mathcal{E}}{2K_1^{\text{eff}}V} &= \frac{1}{2}\sin^2\theta - \frac{\mu_0 M_s H}{2K_1^{\text{eff}}}\cos\left(\theta_H - \theta\right) \\ &= \frac{1}{2}\sin^2\theta - \frac{H}{H_K^{\text{eff}}(\phi_H)}\cos\left(\theta_H - \theta\right).\end{aligned} \tag{4.49}$$

Letting $h = H/H_K^{\text{eff}}$ be the reduced applied field, where

$$H_K^{\text{eff}}(\phi_H) = \frac{2K_1^{\text{eff}}}{\mu_0 M_s} = \frac{2K_1}{\mu_0 M_s} + M_s\left[\mathcal{N}_{xx}\cos^2\phi_H + \mathcal{N}_{yy}\sin^2\phi_H - \mathcal{N}_{zz}\right] \tag{4.50}$$

is the effective anisotropy field which includes the crystalline intrinsic anisotropy and shape anisotropy, the total reduced energy for reversal in a plane becomes

$$\mathcal{E}' = \frac{1}{2}\sin^2\theta - h\cos(\theta_H - \theta). \tag{4.51}$$

The switching field as a function of applied field angle can be obtained from equation (4.51) by solving the following two equations

$$\begin{aligned}\frac{\partial\mathcal{E}'}{\partial\theta} &= \sin\theta\cos\theta - h\sin(\theta_H - \theta) = 0 \\ \frac{\partial^2\mathcal{E}'}{\partial\theta^2} &= \cos^2\theta - \sin^2\theta + h\cos(\theta_H - \theta) = 0.\end{aligned} \tag{4.52}$$

The result is similar to equation (3.22) derived in section 3.2 except that the effective anisotropy field now includes the crystalline intrinsic anisotropy and shape anisotropy and thus the switching field is

$$H_{\text{sw}}(\theta_H, \phi_H) = H_K^{\text{eff}}(\phi_H)\left[\cos^{2/3}\theta_H + \sin^{2/3}\theta_H\right]^{-3/2}. \tag{4.53}$$

H_K^{eff} is defined according to equation (4.50). A parametric plot of equation (4.53) is a *Stoner–Wohlfarth astroid* which is shown in Figure 3.5. By applying an external field along the perpendicular (z–axis) direction as shown in Figure 4.6, a

lower field as obtained from the astroid can be used to switch the magnetisation direction which is important in recording.

4.3.1 Dependence of switching field on island geometry

The analytic model of switching in uniform fields, equation (4.53), was used to study the dependence of switching field on island geometry which can be either shape or size.

4.3.1.1 Island Sidewall Angle Variations

One way of varying the island shape is by changing the sidewall angle while keeping the volume constant. This was explained in section 4.2 where the dependence of magnetometric demagnetising factors on island sidewall angle was studied. Figure 4.6 shows the sidewall angle.

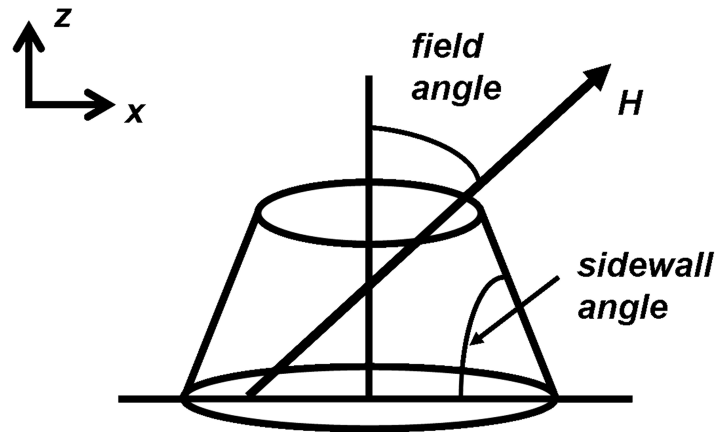

Figure 4.6: Illustration of sidewall angle and field angle. A 90° angle corresponds to a cylinder.

To validate the calculated switching fields of the analytic model, a micromagnetic simulation package, *magpar*, (Scholz *et al.*, 2003), that is an implementation of the micromagnetic model described in chapter 3 was used for comparative simulations, with island geometries generated using *netgen* (Schöberl, 1997). An implementation of an arbitrary truncated elliptic cone was included in *netgen* in order to be able to model this geometry. Figure 4.7 shows an example of the mesh generated by *netgen*. It was not a trivial task to get the desired mesh size and some time was devoted to learn how to use a micromagnetic simulation package. Figure 4.8 shows the z–component of the normalised magnetisation (M_z/M_s) at

an instant before magnetisation reversal for the island geometry shown in Figure 4.7. The visualisation software used was *paraview* (Henderson, 2005). For this particular case, the external field was applied along the long shape axis (major axis) at 10° to the perpendicular (z–axis). As can be seen from Figure 4.8, the magnetisation is not uniform within the island.

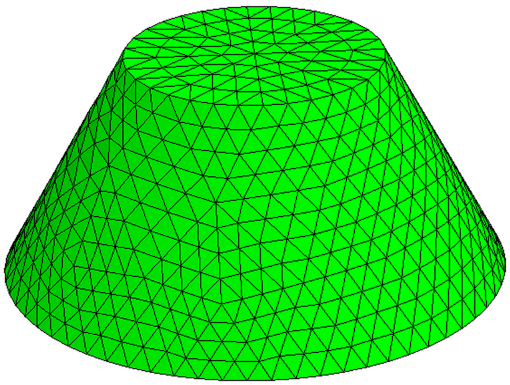

Figure 4.7: Truncated elliptic cone geometry mesh generated using *netgen* (Schöberl, 1997).

The dependence of switching fields on island sidewall angle was studied for applied fields at various angles to the perpendicular (z axis) direction. The saturation magnetisation M_s was 227 kA/m, the uniaxial anisotropy constant, K_1 was 1.134×10^5 J/m^3 (Belle *et al.*, 2008), and the exchange constant, A, used in simulations was 1×10^{-11} J/m. The island volume (height = 25 nm, $a = b = 25$ nm) and ellipticity ($e = b/a = 1$) were kept constant while varying the sidewall angle from 39° (with reference to the $x - y$ plane) to 90°.

Figure 4.9 shows the dependence of switching field on applied field polar angle for different sidewall angles at constant island volume and height. With uniform applied fields, the switching fields of islands were seen to follow the *Stoner-Wohlfarth astroid*, equation (4.53), despite the non-uniform internal fields and non-uniformity in magnetisation reversal as shown in Figure 4.8. The switching fields plotted in Figure 4.9 are normalised by the crystalline intrinsic anisotropy field, $H_K = 2K_1/(\mu_0 M_s)$, which can lead to normalised switching fields, H_{sw}/H_K, that are less than 0.5 for smaller sidewall angles because of the negative contribution of shape anisotropy. The Figure shows little change in switching fields

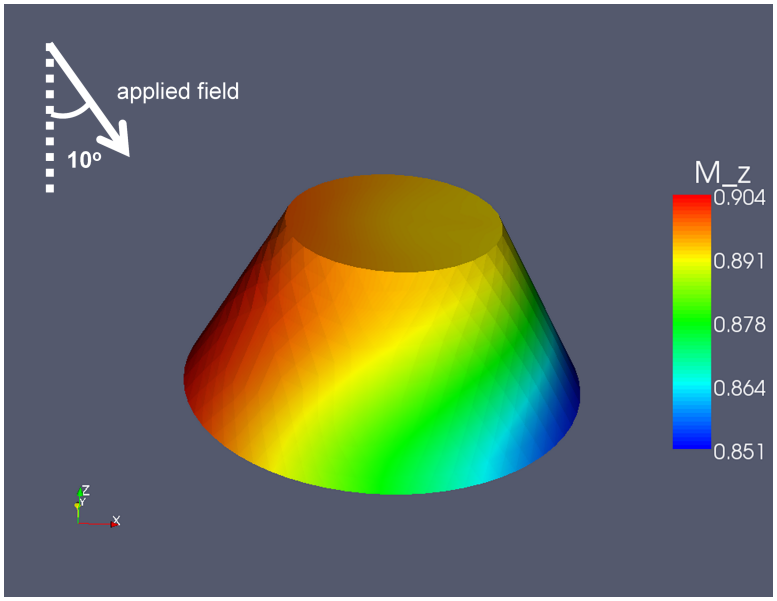

Figure 4.8: Snapshot of the z–component of normalised magnetisation just before reversal showing non-uniformity in magnetisation reversal. The external field was applied at 10° to the perpendicular and along the long shape axis. The visualisation was carried out in *paraview* (Henderson, 2005).

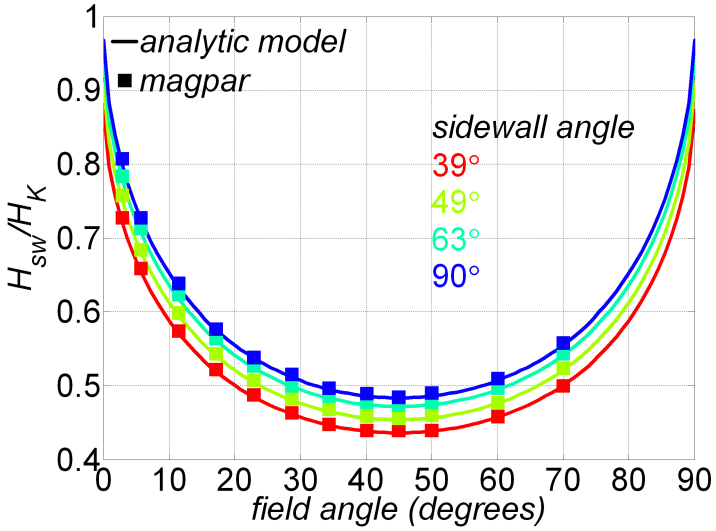

Figure 4.9: Effect on switching field, H_{sw}, of varying applied field polar angle for different sidewall angles. $H_K = 2K_1/(\mu_0 M_s) = 796$ kA/m, $M_s = 227$ kA/m. The largest sidewall angle (90°) corresponds to a cylinder. Continuous lines represent the analytic model and markers, *magpar* results.

from cones to cylinders and this can be attributed to slowly varying magnetometric demagnetising factors at constant volume and aspect ratio according to Figure 4.5.

The agreement between *magpar* and the analytic model shows that although there are non-uniform internal fields that are modelled in *magpar* and non-uniformity in the magnetisation reversal of these islands, a properly constructed single-moment model can accurately predict their switching in a uniform head field.

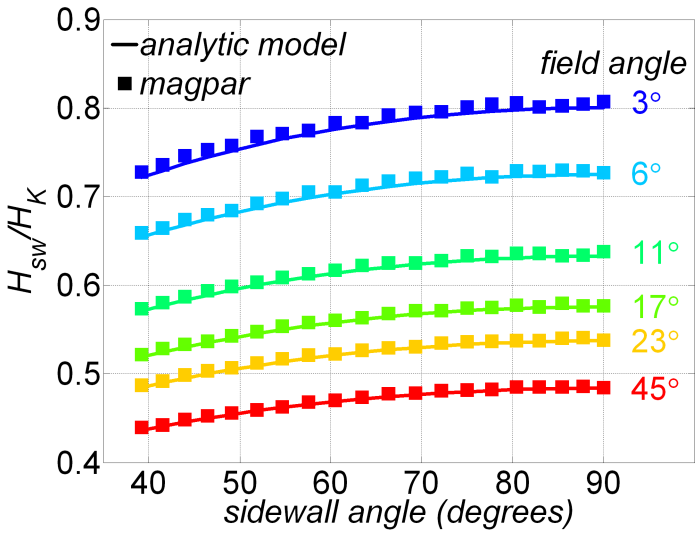

Figure 4.10: Effect on switching field, H_{sw}, of varying sidewall angle for different applied field polar angles. $H_K = 2K_1/(\mu_0 M_s) = 796$ kA/m, $M_s = 227$ kA/m. The largest sidewall angle (90°) corresponds to a cylinder.

Figure 4.10 shows the dependence of switching field on island sidewall angle. For islands of the same volume and height, a truncated cone can be more easily switched than a cylinder. The agreement between the analytic model and the micromagnetic model shows that where islands are small enough that exchange coupling keeps the magnetisation uniform, the effects of the non-uniform fields generated by the shape are captured by a uniform reversal model in which the magnetometric demagnetising factors are correctly computed.

4.3.1.2 Island Aspect Ratio Variations

In this case, the island volume, height and sidewall angle were kept constant as ellipticity, $e = b/a$, was varied to cover aspect ratios in the range 1:1 to 4:1.

This was explained in section 4.2 where the dependence of magnetometric demagnetising factors on ellipticity was studied. The volume, height and magnetic properties were the same as for the sidewall angle calculations. The semi-major axis, a, is aligned to the x-axis whereas the semi-minor axis, b, is aligned to the y-axis.

With uniform applied fields, the switching fields of islands were again seen to follow the *Stoner-Wohlfarth astroid*, equation (4.53), despite the non-uniform internal fields. Figure 4.11 displays the dependence of switching fields on ellipticity for fields applied in the $x-z$ plane (see Figure 4.1(a)). Normalised switching fields, H_{sw}/H_K, that are less than 0.5 arise because of the negative contribution of shape anisotropy. Figure 4.12 displays the ratio of switching field in the $x-z$ plane to that in the $y-z$ plane as a function of ellipticity. The ratio is insensitive to the applied field angle and shows that as ellipticity increases it becomes harder to switch with a field applied across the short axis than down the long-axis, even for out of plane fields, regardless of the angle of the field to the perpendicular.

Thus for Bit Patterned Media with a bit aspect ratio (BAR) > 1 (wider cross-track than down-track) it will become harder to switch down-track and easier to switch cross-track as BAR is increased. This result means that writing the on-track islands will become harder and overwriting islands on adjacent tracks will become more likely as BAR is increased.

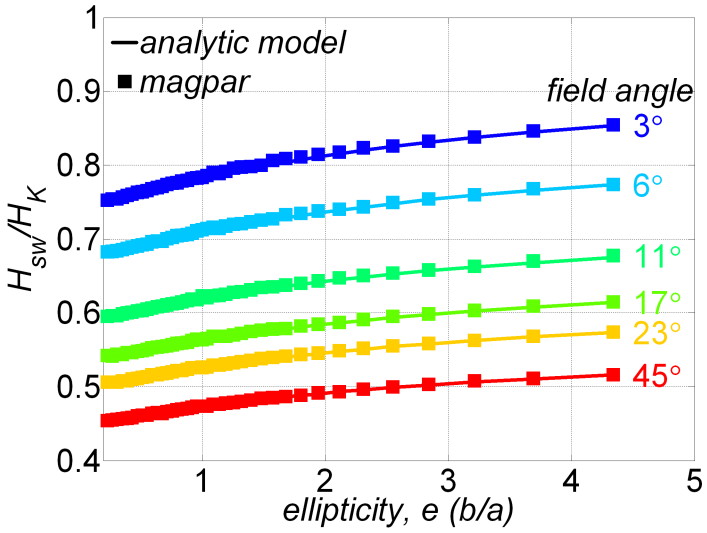

Figure 4.11: Dependence of switching field, H_{sw}, on island ellipticity for applied field polar angles between 3 and 45°. $H_K = 2K_1/(\mu_0 Ms) = 796$ kA/m, $M_s = 227$ kA/m.

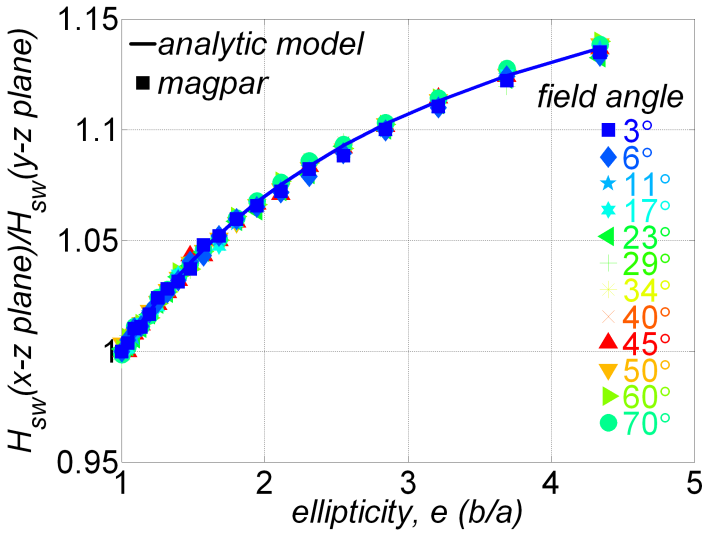

Figure 4.12: Dependence of switching field ratios, $H_{\mathrm{sw}}(x-z \quad \text{plane})/H_{\mathrm{sw}}(y-z \quad \text{plane})$, on island ellipticity for various applied field polar angles. $H_K = 2K_1/(\mu_0 M_s) = 796$ kA/m, $M_s = 227$ kA/m.

4.3.1.3 Island Size Variations

The island geometry can also be altered by varying the island size. This was done by fixing the island shape and scaling the parameters a, b, t, a_t according to Figure 4.1(a) by the same proportion. This keeps the magnetometric demagnetising factors constant. Figure 4.13 displays the dependence of switching fields on various island sizes (represented by a) with shape kept the same (a cone with circular base and sidewall angle of 63°). The magnetic properties for the island were based on experimental results according to Morrison (2008). It is evident that the analytic model predicts a switching field in agreement with micromagnetic models for small islands. When the island diameter increases above 50nm the micromagnetic model predictions diverge from the analytical model, which occurs when non-uniform reversal modes become possible. For islands sizes at which BPM is likely to be used switching fields do not vary much with size and the analytic model is in excellent agreement with the micromagnetic model. In Figure 4.14, the island height (10nm), ellipticity ($a = 2b$), and the ratio of top semi-major axis to bottom semi-major axis, a_t/a, (see Figure 4.1(a)) were kept constant, while size, a, was varied. If the thickness is kept constant as a is increased, the analytic model agrees with simulations even for larger sizes. The

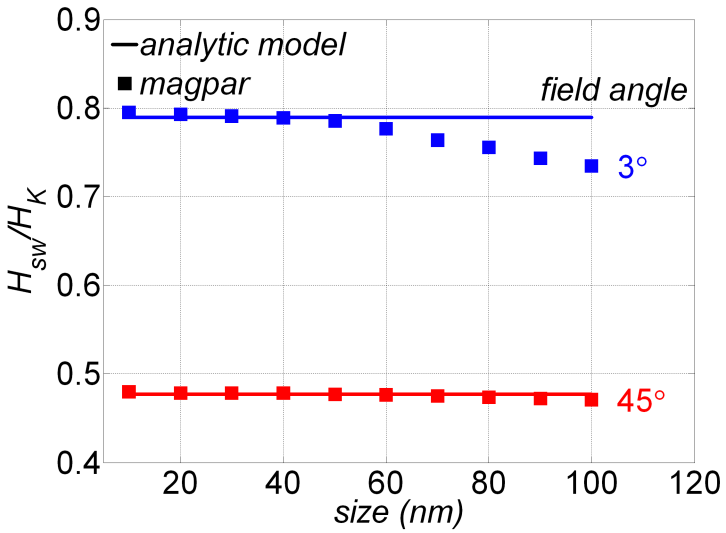

Figure 4.13: Dependence of switching field, H_{sw}, on island size for a cone with circular base and sidewall angle of 63°. The size was represented by island semi-major axis a. $H_K = 2K_1/(\mu_0 M_s) = 1798$ kA/m, $M_s = 413$ kA/m.

magnetic parameters in Figure 4.13 were chosen in order to understand how the model works with different magnetic parameters.

4.3.2 Switching at various field angles in general

According to equation 4.46, reversal occurs in a plane if $\mathcal{N}_{xx} = \mathcal{N}_{yy}$, or $\phi_H = \pi/2$ or $\phi_H = 0$ and $\phi = \phi_H$. In the case where $\mathcal{N}_{xx} \neq \mathcal{N}_{yy}$, the model of switching is exact for field angles along the shape easy ($\phi_H = 0$) or hard ($\phi_H = \pi/2$) axis but not for $0 < \phi < \pi/2$. In practical recording, islands experience head fields at a wide range of angles and it is essential that the model gives correct results for all intermediate angles. Figure 4.15 shows the island geometry considered in this study. The switching field as a function of applied field polar angle for various applied field azimuthal between the easy and hard shape axis is shown in Figure 4.16. The results show that the analytic and micromagnetic models agree for a wide range of field azimuthal and polar angles.

4.4 Switching in non-uniform fields

Practical write heads produce non-uniform fields. To study switching in non-uniform fields, the head was assumed to be an unshielded Karlqvist-type single

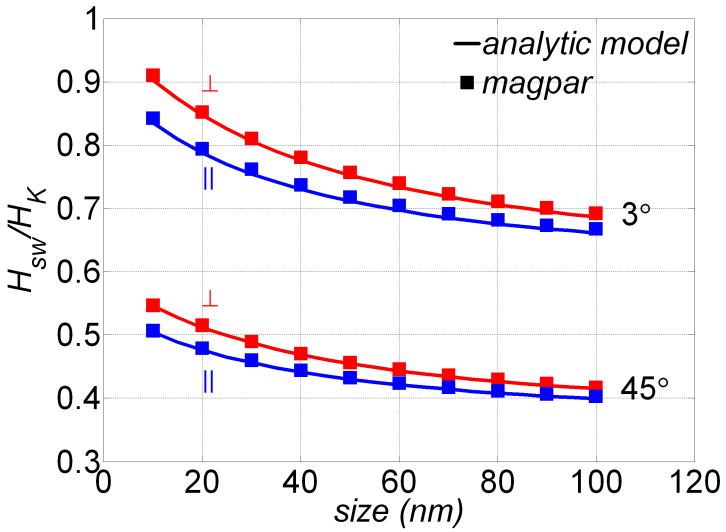

Figure 4.14: Dependence of switching field, H_{sw}, on island size with height, ellipticity, a_t/a fixed and applied field perpendicular ($\perp$) and parallel ($||$) to the $x-z$ plane at field angles 3° and 45° to the perpendicular. $H_K = 2K_1/(\mu_0 M_s) =$ 796 kA/m, $M_s = 227$ kA/m. The island semi-major axis, a, was varied.

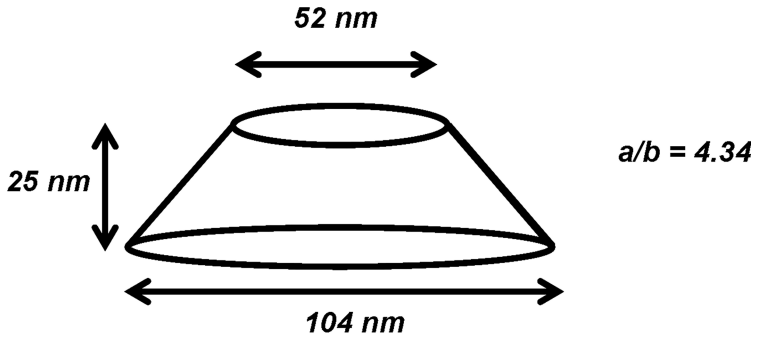

Figure 4.15: Truncated elliptic cone geometry for off-axis switching field study.

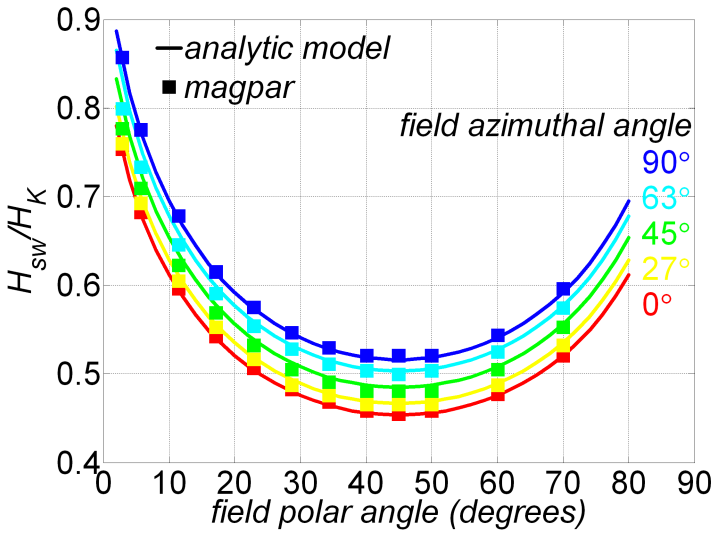

Figure 4.16: Dependence of switching field, H_{sw}, on applied field azimuthal (ϕ_H) and polar angles (θ_H). $H_K = 2K_1/(\mu_0 M_s) = 796$ kA/m, $M_s = 227$ kA/m.

pole head (Karlqvist, 1954) reflected in a soft underlayer as shown in Figure 4.17. This particular write head was chosen because the head field distribution can be expressed using elementary functions. Any realistic write head could be employed but this would complicate the problem as the head field distribution cannot be computed analytically. The islands were assumed to be described by an arbitrary truncated elliptic cone shown in Figure 4.1(a). Magnetic properties used were $M_s = 413$ kA/m (Morrison, 2008), $K_1^{\text{eff}} V/k_B T = 60$ and $T = 300K$, where k_B is the Boltzmann constant, M_s the saturation magnetisation and V the island volume, $K_1^{\text{eff}} = \mu_0 M_s H_K^{\text{eff}}/2$ is the total anisotropy constant including crystalline and shape anisotropy.

By taking into account the contribution of the pole (Karlqvist, 1954) and its image at a point (x, y, z), the horizontal and vertical components of field (H_x, H_z)

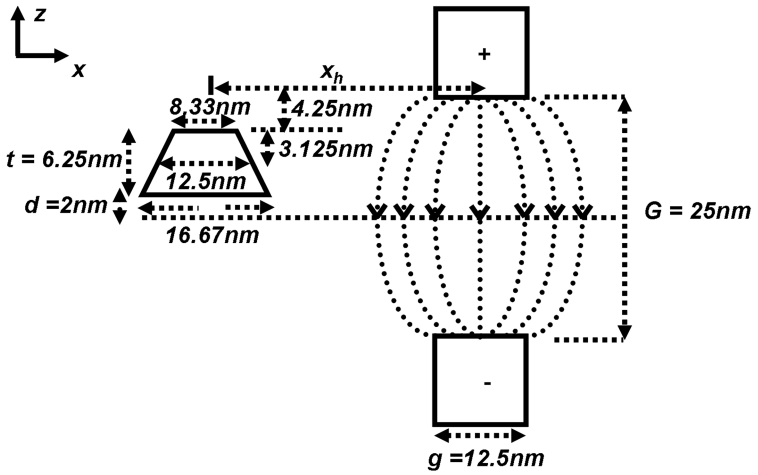

Figure 4.17: Side-view geometry of the truncated elliptic cone and the Karlqvist-type single pole head reflected in a soft underlayer. Also shown is a sketch of a 2-D head field distribution.

can be obtained:

$$H_x = \frac{H_g}{2\pi}\ln\left[\frac{(g/2+x_h-x)^2+(G/2+z+d)^2}{(g/2-x_h+x)^2+(G/2+z+d)^2}\right] - \frac{H_g}{2\pi}\ln\left[\frac{(g/2+x_h-x)^2+(G/2-z-d)^2}{(g/2-x_h+x)^2+(G/2-z-d)^2}\right] \tag{4.54}$$

$$H_z = \frac{H_g}{\pi}\left[\arctan\left(\frac{g/2+x_h-x}{G/2-z-d}\right)+\arctan\left(\frac{g/2-x_h+x}{G/2-z-d}\right)\right] + \frac{H_g}{\pi}\left[\arctan\left(\frac{g/2+x_h-x}{G/2+z+d}\right)+\arctan\left(\frac{g/2-x_h+x}{G/2+z+d}\right)\right] \tag{4.55}$$

where H_g, g, x_h, G, d are respectively the head gap field, pole width, head-island separation, gap width and the separation between island base and mirror plane as shown in Figure 4.17.

In order to incorporate the non-uniform field into a model of coherent reversal, the average of the vector head field over the island volume is required. This was obtained as shown in equations (4.56) and (4.57)

$$H_x^{\mathrm{av}}V = \beta\int_{\phi=0}^{2\pi}\mathrm{d}\phi\int_{z=0}^{t}\mathrm{d}z\int_{r=0}^{a(1-z/z_0)} r\mathrm{d}rH_x(r,\phi,z) \tag{4.56}$$

$$H_z^{\mathrm{av}}V = \beta\int_{\phi=0}^{2\pi}\mathrm{d}\phi\int_{z=0}^{t}\mathrm{d}z\int_{r=0}^{a(1-z/z_0)} r\mathrm{d}rH_z(r,\phi,z) \tag{4.57}$$

where $\beta = b/a = 1$, $x = r\cos\phi$ and V is the island volume. The parameters $z_0 = t/(1 - a_t/a)$, a_t, a, r and z are defined in Figure 4.1(a), and ϕ is the usual azimuthal angle. Though the head field distribution is 2-D, the volume averaging over the island was carried out in 3-D using cylindrical coordinates because these are convenient for this island geometry.

The average head field components in equations (4.56) and (4.57) can be expressed as

$$H_x^{\mathrm{av}}(x_h) = \frac{H_g}{2\pi V} H_1(x_h) \tag{4.58}$$

$$H_z^{\mathrm{av}}(x_h) = \frac{H_g}{\pi V} H_2(x_h) \tag{4.59}$$

where $H_1(x_h)$ and $H_2(x_h)$ represent integrals and were computed numerically. The magnitude and the polar angle of the average head field are

$$H^{\mathrm{av}} = \frac{H_g}{\pi V}\sqrt{(H_1/2)^2 + H_2^2} \tag{4.60}$$

$$\theta_H = \arccos\left(H_z^{\mathrm{av}}/H^{\mathrm{av}}\right) = \arccos\left(H_2/\sqrt{(H_1/2)^2 + H_2^2}\right). \tag{4.61}$$

For coherent reversal of a single-domain uniaxial island, the switching field in terms of the field angle is given by equation (4.53).

The minimum magnitude of the head gap field that will switch the island can be obtained by equating equation (4.60) to equation (4.53) and solving for the head gap field giving

$$H_g^{\mathrm{switch}} = \pi V H_K^{\mathrm{eff}} \left(H_2^{2/3} + (H_1/2)^{2/3}\right)^{-3/2}. \tag{4.62}$$

Figure 4.18 shows the minimum head gap field required to switch the island for various head-island separations. The smallest gap field for switching is around 5 nm because the effective head field which is given by

$$H_{\mathrm{eff}}^{\mathrm{av}} = \frac{H^{\mathrm{av}}}{\left[\cos^{2/3}\theta_H + \sin^{2/3}\theta_H\right]^{-3/2}} \tag{4.63}$$

is a maximum near that point as shown in Figure 4.19.

An implementation of a Karlqvist type head field distribution was included in *magpar* in order to validate the model. The model results were then compared to finite element calculations in *magpar* in which the same island geometry was

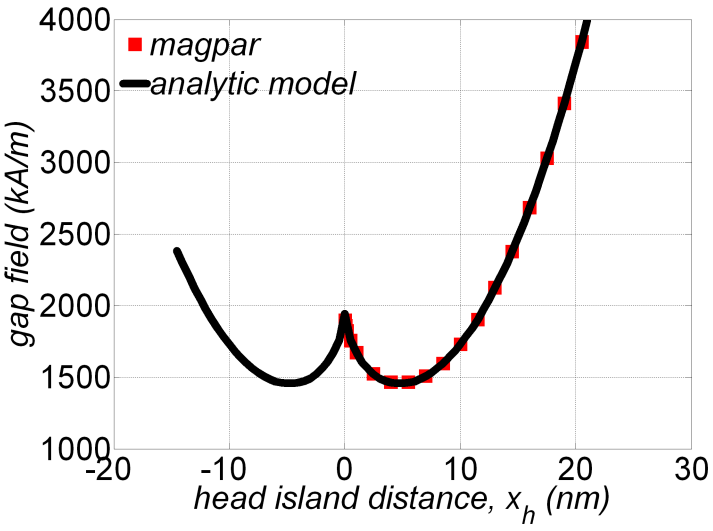

Figure 4.18: Dependence of the minimum head gap field, H_g, that would be required to switch the island at head-island separation x_h.

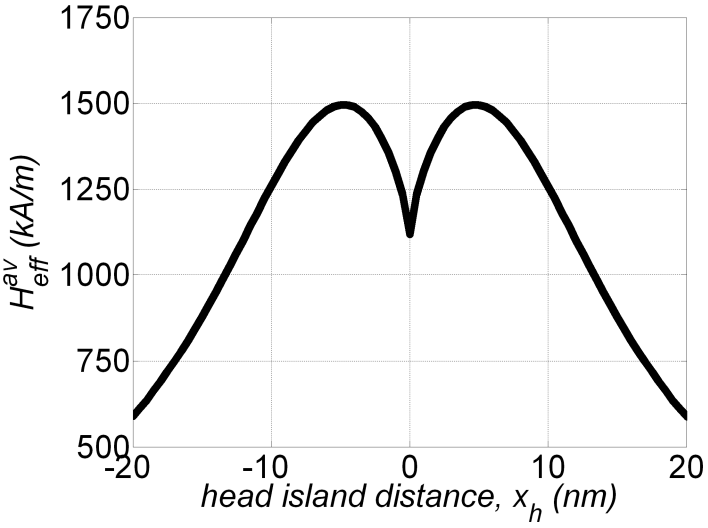

Figure 4.19: Dependence of effective head field (equation (4.63)) on head-island separation x_h. The head gap field, H_g, was 1806.1 kA/m.

subjected to the spatially varying (non-averaged) head field described by equations (4.54) and (4.55). Figure 4.20(a) shows the head field distribution given by equation (4.55) for the head-island separation, x_h (see Figure 4.17), of 12.5 nm. It was observed in *magpar* that magnetisation reversal was not strictly coherent rotation, with the regions that experience the strongest head field having the largest tilt in magnetisation angle as shown in Figure 4.20(b).

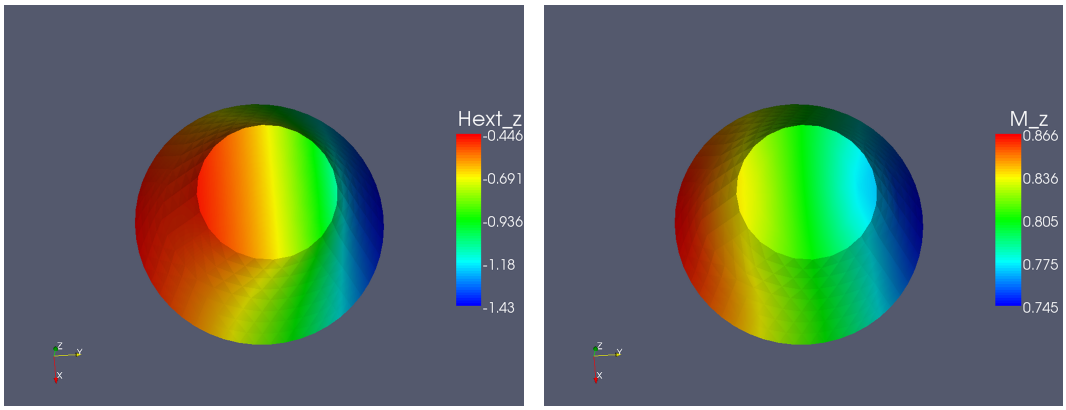

(a) (b)

Figure 4.20: (a) Spatial variation of the vertical component of head field in Tesla. The head-island separation, x_h (see Figure 4.17), was 12.5 nm and (b) normalised magnetisation from *magpar*.

However the deep gap field required to switch an island in the single moment model is in excellent agreement with the deep gap field at which the island magnetisation irreversibly changes direction in the *magpar* simulations as shown in Figure 4.18. This shows that although there is some non-uniformity in the magnetisation reversal of these islands, a properly constructed single-moment model can accurately predict their switching in a non-uniform head field.

4.5 Summary and Conclusions

This chapter has derived components required in the development of the statistical write model. It has been demonstrated that the magnetometric demagnetising factors of a generalised geometry that describe proposed island shapes can be calculated analytically and that switching fields for islands in BPM can thereby be predicted using an analytical model. The results are in excellent agreement with micromagnetic simulations.

The analytic model forms an excellent basis to characterise the statistics of write errors due to its high efficiency compared to micromagnetic simulations (*magpar*). The model was more than a thousand times faster than micromagnetic simulations. The model was validated against *magpar* for a range of sizes, shapes, azimuthal and polar angles including non-uniform fields and it is accurate for sizes of interest. The switching fields of islands in BPM are predicted to vary little with size, but somewhat more with ellipticity and sidewall angle, suggesting that fabrication of vertical sided islands of constant ellipticity is desirable. The model suggests that using islands with a non 1:1 aspect ratio (BAR$>$ 1) may worsen write errors on adjacent tracks, and that cylindrical islands might therefore be optimal.

The next chapter continues the development of a statistical model of write errors where the analytic model plays an important role.

Chapter 5

Statistical write model development: Part II

5.1 Introduction

This chapter derives further components required in the development of the statistical write model. To begin with an analytic expression for the energy barrier of a single domain uniaxial particle for magnetisation rotation confined to a plane is derived. This is followed by a derivation of switching probabilities for identical and non-interacting islands that includes thermal activation. A method of incorporating variations of position, magnetic and geometric properties of islands is then explained. Since islands in BPM interact, a technique to incorporate interactions is explained. This is followed by an extension to two layer structures.

Some sections of this chapter are taken from the papers included in appendix B. These papers were written by the author of this thesis who carried out all of the model developments and obtained all of the model results described in those papers.

5.2 Derivation of energy barrier for a single domain particle

The energy barrier is a quantity of central importance in the statistical model in that it is used to calculate the transition probabilities at finite temperatures. An analytic expression for the energy barrier of a single domain particle as a function

of any applied field polar angle for magnetisation rotation confined to a plane was derived.

The starting point is the total energy expression (see section 4.3)

$$\mathcal{E}' = \frac{1}{2}\sin^2\theta - h\cos(\theta_H - \theta) \tag{5.1}$$

where $\mathcal{E}' = \mathcal{E}/\left(\mu_0 M_s V H_K^{\text{eff}}\right)$ is the reduced total energy, $h = H/H_K^{\text{eff}}$, the reduced applied field, θ is the magnetisation angle and θ_H is the field angle.

To obtain the energy barrier, the critical points of equation (5.1) should be obtained first. These can be obtained by differentiating equation (5.1) with respect to θ and setting to zero. Expressed mathematically,

$$\frac{\mathrm{d}\mathcal{E}'}{\mathrm{d}\theta} = \sin\theta\cos\theta - h\sin(\theta_H - \theta). \tag{5.2}$$

Thus

$$\frac{\mathrm{d}\mathcal{E}'}{\mathrm{d}\theta} = 0 \Rightarrow \sin\theta\cos\theta = h\sin(\theta_H - \theta). \tag{5.3}$$

Despite looking simple, it is a non-trivial task to find solutions of equation (5.3) as mentioned by several authors. Stoner and Wohlfarth (1948) stated

> *The general solution is not only very troublesome to derive, but also, when obtained, not adapted for numerical evaluation.*

Aharoni (2000, p. 107) mentioned that the problem should be solved numerically. It was also indicated by Tannous and Gieraltowski (2008) that for any general field angle, θ_H, equation 5.3 cannot be solved using an analytic approach. Pfeiffer (1990), when looking for analytical solutions for the energy barrier which could only be determined if the analytical solutions for equation (5.3) are known mentioned that for any general field angle, there are no analytic solutions.

Pfeiffer (1990) reported a numerical approximation to the energy barrier which is

$$E_{\text{barrier,approx}} = \frac{\mu_0 V M_s H_a}{2}\left[1 - \frac{h}{h_K(\theta_H)}\right]^{0.86+1.14h_K(\theta_H)} \tag{5.4}$$

where V is the particle volume, M_s the saturation magnetisation, H_a the anisotropy field, h is the reduced applied field, θ_H the applied field angle and $h_K(\theta_H) = \left[\cos^{2/3}\theta_H + \sin^{2/3}\theta_H\right]^{-3/2}$ is the normalised switching field.

In reduced units, equation (5.4) becomes

$$\mathcal{E}_{\text{barrier,approx}} = \frac{1}{2}\left[1 - \frac{h}{h_K(\theta_H)}\right]^{0.86+1.14h_K(\theta_H)} \tag{5.5}$$

where $\mathcal{E}_{\text{barrier,approx}} = \frac{E_{\text{barrier,approx}}}{\mu_0 V M_s H_a}$ is the reduced energy barrier.

Expanding the trigonometric relation, equation (5.3) becomes

$$\sin\theta\cos\theta = h\sin\theta_H\cos\theta - h\cos\theta_H\sin\theta. \tag{5.6}$$

Let $\sin\theta = x$, $\cos\theta = \sqrt{1-x^2}$ (a negative branch, $-\sqrt{1-x^2}$, can also be used), then equation (5.6) takes the form

$$x\sqrt{1-x^2} = h\sin\theta_H\sqrt{1-x^2} - xh\cos\theta_H \tag{5.7}$$

$$\Rightarrow \sqrt{1-x^2}\,(x - h\sin\theta_H) = -xh\cos\theta_H. \tag{5.8}$$

Squaring equation (5.8) and expanding the expression, the result is a quartic

$$x^4 - 2x^3 h\sin\theta_H + x^2(h^2-1) + 2xh\sin\theta_H - h^2\sin^2\theta_H = 0. \tag{5.9}$$

Equation (5.9) can be solved analytically leading to four roots. A derivation of these roots can be found in appendix A.3. The solutions are

$$\begin{aligned}
\sin\theta_1 &= \frac{h\sin\theta_H - s_1 + \sqrt{s_1^2 - 4s_2}}{2} \\
\sin\theta_2 &= \frac{h\sin\theta_H - s_1 - \sqrt{s_1^2 - 4s_2}}{2} \\
\sin\theta_3 &= \frac{h\sin\theta_H + s_1 - \sqrt{s_1^2 - 4s_4}}{2} \\
\sin\theta_4 &= \frac{h\sin\theta_H + s_1 + \sqrt{s_1^2 - 4s_4}}{2}
\end{aligned} \tag{5.10}$$

where

$$
\begin{aligned}
s_2 &= \frac{1}{2}\left[\frac{-3h^2\sin^2\theta_H}{2} + h^2 - 1 + s_1^2 - \frac{h\sin\theta_H(h^2\cos^2\theta_H + 1)}{s_1}\right] \\
s_4 &= \frac{1}{2}\left[\frac{-3h^2\sin^2\theta_H}{2} + h^2 - 1 + s_1^2 + \frac{h\sin\theta_H(h^2\cos^2\theta_H + 1)}{s_1}\right] \\
s_1 &= \sqrt{v^{1/3} + w^{1/3} + h^2\sin^2\theta_H - \frac{2(h^2-1)}{3}} \\
v &= \left[h^2\sin\theta_H\cos\theta_H + \sqrt{\left[h^2\sin\theta_H\cos\theta_H\right]^2 + \left[\frac{h^2-1}{3}\right]^3}\right]^2 \\
w &= \left[h^2\sin\theta_H\cos\theta_H - \sqrt{\left[h^2\sin\theta_H\cos\theta_H\right]^2 + \left[\frac{h^2-1}{3}\right]^3}\right]^2 .
\end{aligned}
$$

Some roots can be complex depending on h. Let $h_k = \left[\cos^{2/3}\theta_H + \sin^{2/3}\theta_H\right]^{-3/2}$ be the reduced switching field and $0 \leq \theta_H \leq \pi/2$.

1. For $h > |h_k|$, there is only one minimum and one maximum, $\sin\theta_3$ and $\sin\theta_4$ are complex whereas $\sin\theta_1$ correspond to a minimum and $\sin\theta_2$ to a maximum.

2. For $-h > |h_k|$, there is only one minimum and one maximum, $\sin\theta_1$ and $\sin\theta_2$ are complex whereas $\sin\theta_3$ correspond to a minimum and $\sin\theta_4$ to a maximum.

3. For $h = 0$, $\sin\theta_1$ and $\sin\theta_2$ correspond to minima whereas $\sin\theta_3$ and $\sin\theta_4$ correspond to maxima. In this case, $\sin\theta_1 = \sin\theta_2 = 0$.

4. For $|h| \leq |h_k|$, all roots are real, there are two minima and two maxima.

5. For $h \geq 0$, $\sin\theta_1$ corresponds to a deeper minimum than $\sin\theta_3$.

6. For $h < 0$, $\sin\theta_3$ corresponds to a deeper minimum than $\sin\theta_1$.

7. For 3, 4, 5 and 6, the minimum in which the system finds itself depends upon its history.

For $\theta_H > \pi/2$, take $\theta_H < \pi/2$ and $h < 0$ (see case 2).

To find a convenient expression for the energy barrier, it is necessary to solve equation (5.6) for $\cos\theta$. Letting $\cos\theta = x$ and following the same analysis as for

$\sin\theta$, the resulting quartic is

$$x^4 + 2x^3 h\cos\theta_H + x^2(h^2-1) - 2xh\cos\theta_H - h^2\cos^2\theta_H = 0. \tag{5.11}$$

Equation (5.11) can be solved analytically leading to four roots. A derivation of these roots can be found in appendix A.3. These are

$$\begin{aligned}
\cos\theta_1 &= \frac{-h\cos\theta_H + c_1 + \sqrt{c_1^2 - 4c_4}}{2} \\
\cos\theta_2 &= \frac{-h\cos\theta_H + c_1 - \sqrt{c_1^2 - 4c_4}}{2} \\
\cos\theta_3 &= \frac{-h\cos\theta_H - c_1 - \sqrt{c_1^2 - 4c_2}}{2} \\
\cos\theta_4 &= \frac{-h\cos\theta_H - c_1 + \sqrt{c_1^2 - 4c_2}}{2}
\end{aligned} \tag{5.12}$$

where

$$\begin{aligned}
c_2 &= \frac{1}{2}\left[\frac{-3h^2\cos^2\theta_H}{2} + h^2 - 1 + c_1^2 + \frac{h\cos\theta_H(h^2\sin^2\theta_H + 1)}{c_1}\right] \\
c_4 &= \frac{1}{2}\left[\frac{-3h^2\cos^2\theta_H}{2} + h^2 - 1 + c_1^2 - \frac{h\cos\theta_H(h^2\sin^2\theta_H + 1)}{c_1}\right] \\
c_1 &= \sqrt{v^{1/3} + w^{1/3} + h^2\cos^2\theta_H - \frac{2(h^2-1)}{3}} \\
v &= \left[h^2\sin\theta_H\cos\theta_H + \sqrt{\left[h^2\sin\theta_H\cos\theta_H\right]^2 + \left[\frac{h^2-1}{3}\right]^3}\right]^2 \\
w &= \left[h^2\sin\theta_H\cos\theta_H - \sqrt{\left[h^2\sin\theta_H\cos\theta_H\right]^2 + \left[\frac{h^2-1}{3}\right]^3}\right]^2 .
\end{aligned}$$

The energy barrier is the difference in energy between a minimum and a maximum. Figure 5.1 shows a schematic of the energy landscape for $h < 0$. To get from θ_1 to θ_3 there are two possible routes, 1 and 1^*. The lower is route 1 which determines the energy barrier. Similarly, to get from θ_3 to θ_1, there are two possible routes. The selected maximum for this case is at θ_2.

Using equation (5.1), the selected reduced energy barriers for $h \leq 0$ are

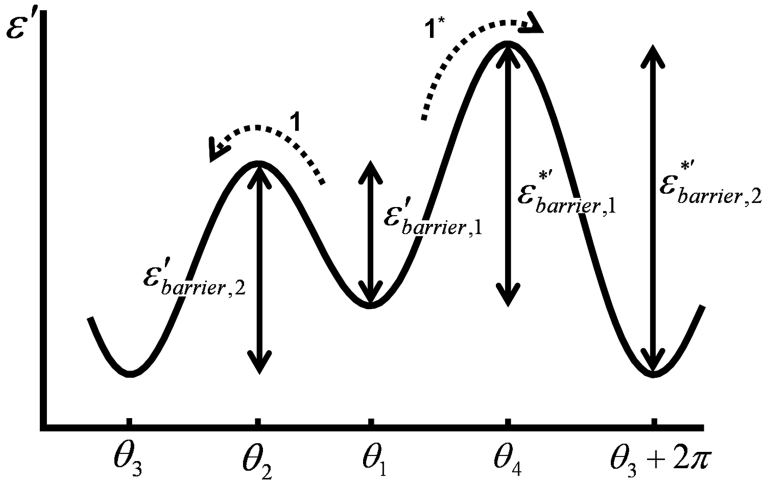

Figure 5.1: Energy landscape schematic for $h < 0$.

$\mathcal{E}'_{\text{barrier},1}$ and $\mathcal{E}'_{\text{barrier},2}$ which are given by

$$\mathcal{E}'_{\text{barrier},1} = \frac{1}{2}\left[\sin^2\theta_2 - \sin^2\theta_1\right] - h\cos\theta_H\left[\cos\theta_2 - \cos\theta_1\right] - h\sin\theta_H\left[\sin\theta_2 - \sin\theta_1\right] \tag{5.13}$$

$$\mathcal{E}'_{\text{barrier},2} = \frac{1}{2}\left[\sin^2\theta_2 - \sin^2\theta_3\right] - h\cos\theta_H\left[\cos\theta_2 - \cos\theta_3\right] - h\sin\theta_H\left[\sin\theta_2 - \sin\theta_3\right]. \tag{5.14}$$

After substituting expressions for angles, the result is

$$\mathcal{E}'_{\text{barrier},1} = \frac{s_1 + h\sin\theta_H}{2}\sqrt{s_1^2 - 4s_2} + h\cos\theta_H\sqrt{c_1^2 - 4c_4} \tag{5.15}$$

$$\begin{aligned}\mathcal{E}'_{\text{barrier},2} = {} & \frac{s_4 - s_2 + s_1 h\sin\theta_H}{2} + \frac{h\sin\theta_H\left[\sqrt{s_1^2 - 4s_2} - \sqrt{s_1^2 - 4s_4}\right]}{4} \\ & + \frac{s_1\left[\sqrt{s_1^2 - 4s_4} + \sqrt{s_1^2 - 4s_2}\right]}{4} \\ & - \frac{h\cos\theta_H\left[2c_1 - \sqrt{c_1^2 - 4c_4} + \sqrt{c_1^2 - 4c_2}\right]}{2}.\end{aligned} \tag{5.16}$$

The other reduced energy barriers are

$$\mathcal{E}^{*\prime}_{\text{barrier},1} = \frac{1}{2}\left[\sin^2\theta_4 - \sin^2\theta_1\right] - h\cos\theta_H\left[\cos\theta_4 - \cos\theta_1\right] - h\sin\theta_H\left[\sin\theta_4 - \sin\theta_1\right] \tag{5.17}$$

$$\mathcal{E}^{*\prime}_{\text{barrier},2} = \frac{1}{2}\left[\sin^2\theta_4 - \sin^2\theta_3\right] - h\cos\theta_H\left[\cos\theta_4 - \cos\theta_3\right] - h\sin\theta_H\left[\sin\theta_4 - \sin\theta_3\right]. \tag{5.18}$$

After substituting expressions for angles, the result is

$$\begin{aligned}\mathcal{E}^{*\prime}_{\text{barrier},1} = {} & \frac{s_2 - s_4 - s_1 h\sin\theta_H}{2} + \frac{h\sin\theta_H\left[\sqrt{s_1^2 - 4s_2} - \sqrt{s_1^2 - 4s_4}\right]}{4} \\ & + \frac{s_1\left[\sqrt{s_1^2 - 4s_4} + \sqrt{s_1^2 - 4s_2}\right]}{4} \\ & - \frac{h\cos\theta_H\left[-2c_1 + \sqrt{c_1^2 - 4c_2} - \sqrt{c_1^2 - 4c_4}\right]}{2}.\end{aligned} \tag{5.19}$$

$$\mathcal{E}^{*\prime}_{\text{barrier},2} = \frac{s_1 - h\sin\theta_H}{2}\sqrt{s_1^2 - 4s_4} - h\cos\theta_H\sqrt{c_1^2 - 4c_2}. \tag{5.20}$$

The terms inside the square roots can be expanded and these are

$$\begin{aligned}s_1^2 - 4s_2 &= 2h^2\sin^2\theta_H - \frac{4\left(h^2-1\right)}{3} - v^{1/3} - w^{1/3} + \frac{2h\sin\theta_H(h^2\cos^2\theta_H + 1)}{s_1} \\ c_1^2 - 4c_4 &= 2h^2\cos^2\theta_H - \frac{4\left(h^2-1\right)}{3} - v^{1/3} - w^{1/3} + \frac{2h\cos\theta_H(h^2\sin^2\theta_H + 1)}{c_1} \\ s_1^2 - 4s_4 &= 2h^2\sin^2\theta_H - \frac{4\left(h^2-1\right)}{3} - v^{1/3} - w^{1/3} - \frac{2h\sin\theta_H(h^2\cos^2\theta_H + 1)}{s_1} \\ c_1^2 - 4c_2 &= 2h^2\cos^2\theta_H - \frac{4\left(h^2-1\right)}{3} - v^{1/3} - w^{1/3} - \frac{2h\cos\theta_H(h^2\sin^2\theta_H + 1)}{c_1}\end{aligned}$$

These expressions imply that the reduced energy barriers are related and in particular

$$\mathcal{E}'_{\text{barrier},1}(h,\theta_H) = \mathcal{E}^{*\prime}_{\text{barrier},2}(-h,\theta_H) \tag{5.21}$$

$$\mathcal{E}'_{\text{barrier},2}(h,\theta_H) = \mathcal{E}^{*\prime}_{\text{barrier},1}(-h,\theta_H). \tag{5.22}$$

Thus for $h \geq 0$, the relevant energy barriers are $\mathcal{E}^{*\prime}_{\text{barrier},2}$ and $\mathcal{E}^{*\prime}_{\text{barrier},1}$.

The reduced energy barrier $\mathcal{E}'_{\text{barrier},1}$ is

$$\mathcal{E}'_{\text{barrier},1} = \frac{s_1 + h\sin\theta_H}{2}\sqrt{2h^2\sin^2\theta_H - \frac{4(h^2-1)}{3} - t + \frac{2h\sin\theta_H(h^2\cos^2\theta_H+1)}{s_1}} + h\cos\theta_H\sqrt{2h^2\cos^2\theta_H - \frac{4(h^2-1)}{3} - t + \frac{2h\cos\theta_H(h^2\sin^2\theta_H+1)}{\sqrt{t + h^2\cos^2\theta_H - \frac{2}{3}(h^2-1)}}} \tag{5.23}$$

where $s_1 = \sqrt{h^2\sin^2\theta_H + t - \frac{2(h^2-1)}{3}}$ and $t = v^{1/3} + w^{1/3}$ with

$$v = \left[h^2\sin\theta_H\cos\theta_H + \sqrt{\left[h^2\sin\theta_H\cos\theta_H\right]^2 + \left[\frac{h^2-1}{3}\right]^3}\right]^2$$

$$w = \left[h^2\sin\theta_H\cos\theta_H - \sqrt{\left[h^2\sin\theta_H\cos\theta_H\right]^2 + \left[\frac{h^2-1}{3}\right]^3}\right]^2.$$

This analytic approach to the energy barrier was also derived independently by Wood (2009). A similar solution to the exact roots of the critical points of the energy and a new approximation of the energy barrier was obtained and published shortly after this expression was obtained.

Figure 5.2 compares the exact calculation of energy barrier using equation (5.23) to the approximation provided by Pfeiffer (1990), equation (5.5), to check the accuracy of the numerical fit. The approximation is in good agreement with the analytic expression except at small off-axis field angles. This is shown in Figure 5.3(a) where the maximum percentage error for any field angle within the astroid is given by

$$\text{error} = \frac{\max\left(|\mathcal{E}_{\text{barrier,approx}} - \mathcal{E}'_{\text{barrier},1}|\right)}{\mathcal{E}'_{\text{barrier},1}} \times 100\%. \tag{5.24}$$

For an applied field equal to the switching field, the energy barrier, $\mathcal{E}'_{\text{barrier},1}$, vanishes and thus equation (5.24) is not a convenient way to express percentage errors. To avoid this, the maximum percentage error was computed according to

$$\text{error} = \frac{\max\left(|\mathcal{E}_{\text{barrier,approx}} - \mathcal{E}'_{\text{barrier},1}|\right)}{0.5} \times 100\%. \tag{5.25}$$

where the denominator in equation (5.25) is the energy barrier in the absence of an applied field. Figure 5.3(b) shows the maximum percentage error within the astroid according to equation (5.25). This shows that Pfeiffer's approximation is least accurate for applied field angles close to 0° or 90°.

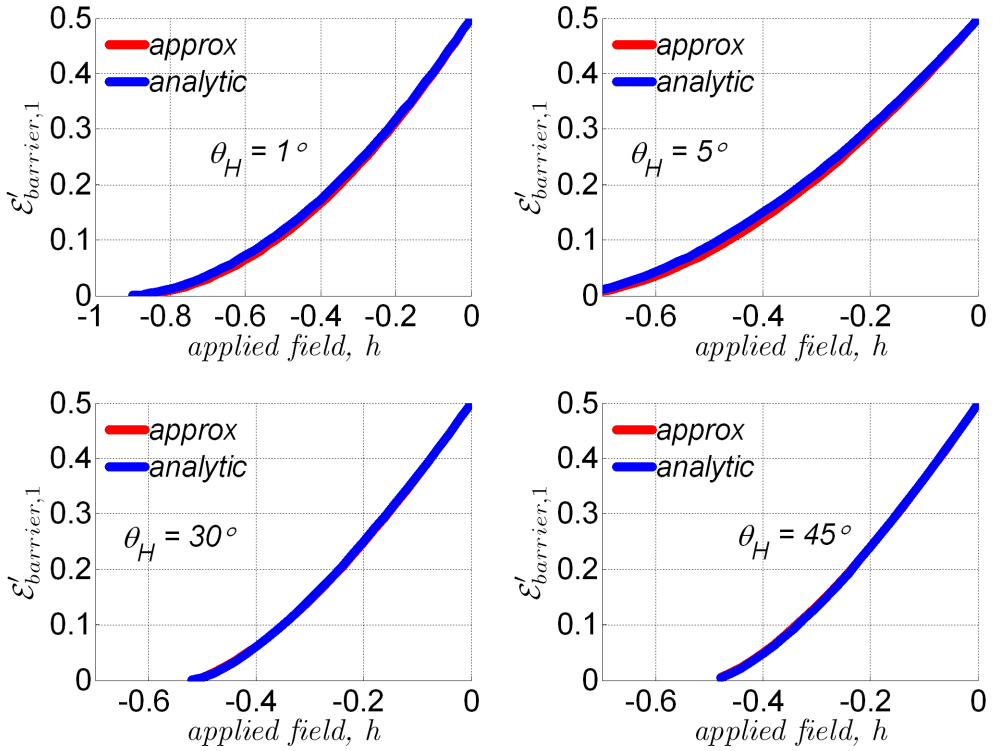

Figure 5.2: Energy barrier comparison for selected applied field angles. The analytic expression is given by equation (5.23) whereas Pfeiffer's approximation is given by equation (5.5).

5.3 Derivation of switching probability

The energy barrier is used in a calculation of switching probabilities where thermal activation is taken into account. In order to derive a statistical model in which the probability of writing or failing to write is calculated and in which reversal depends not only on the statistically variable geometric and magnetic parameters but also on random thermal activation, large numbers of identical and non-interacting islands at the same temperature and external field should be considered (Brown, 1979). In the case of uniaxial anisotropy, there are two

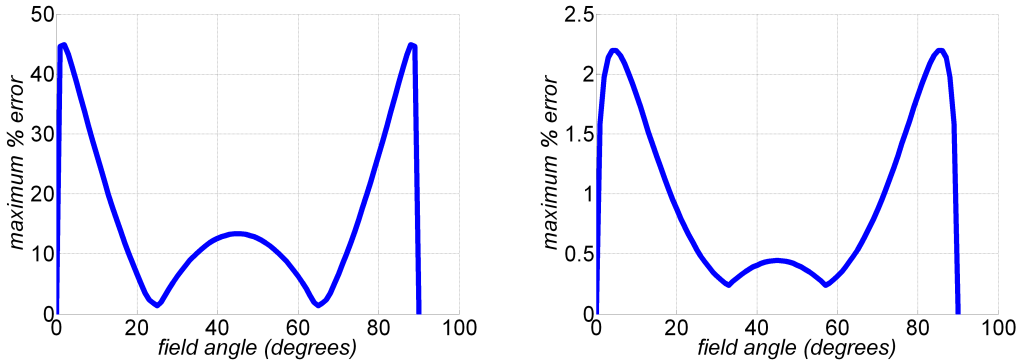

(a) (b)

Figure 5.3: Maximum errors within the astroid according to (a) equation (5.24) and (b) equation (5.25).

possible magnetisation orientations and the time dependence of the number of single domain islands whose magnetisation is in one orientation (n_1), according to (Brown, 1979), can be obtained from

$$\frac{\mathrm{d}n_1}{\mathrm{d}t} + (\nu_{12} + \nu_{21})\, n_1 = \nu_{21} n \tag{5.26}$$

where n represents the total number of islands and n_1 the number of islands whose magnetisation is in orientation 1. The transition rates ν_{12} and ν_{21} represent the probability per unit time of the magnetisation jumping from orientation 1 to 2 and 2 to 1 respectively. These are given by

$$\nu_{12} = f_0 \exp(-E_{\text{barrier},1}/(k_B T)), \quad \nu_{21} = f_0 \exp(-E_{\text{barrier},2}/(k_B T)) \tag{5.27}$$

where f_0 is the attempt frequency, k_B the Boltzmann constant and T the absolute temperature. $E_{\text{barrier},1}$ and $E_{\text{barrier},2}$ represent the energy barrier for the magnetisation escaping from orientations 1 and 2 respectively. For an island being written by a head, the energy barrier (see Figure 5.5(a)) depends on the applied field which in turn varies with time as the head passes over the island (see Figure 5.4(a)). This implies that the transition rates in a recording system are not constant throughout the recording process. The energy barriers were calculated at each position as the head passes over the island using $E_{\text{barrier},1} = \mu_0 M_s V H_K^{\text{eff}} \mathcal{E}'_{\text{barrier},1}$ and $E_{\text{barrier},2} = \mu_0 M_s V H_K^{\text{eff}} \mathcal{E}'_{\text{barrier},2}$ that were derived in section 5.2.

Since large numbers of islands are involved, equation (5.26) can be transformed to describe the probability of not switching by dividing by the total number of islands, n. Taking account of the variation of the transition rates with time, equation (5.26) becomes

$$\frac{\mathrm{d}p_1}{\mathrm{d}t} + (\nu_{12}(t) + \nu_{21}(t))\, p_1 = \nu_{21}(t) \tag{5.28}$$

where $p_1 = n_1/n$, is the probability of remaining in orientation 1.

Since the transition rates are not constant, equation (5.28) can be integrated using the *integrating factor method* of first order linear differential equations. The result is

$$\begin{aligned} p_1(t) = p_1(0) \exp\left(-\int_{t'=0}^{t} \nu(t')\,\mathrm{d}t'\right) \\ + \exp\left(-\int_{t'=0}^{t} \nu(t')\,\mathrm{d}t'\right) \int_{t'=0}^{t} \exp\left(-\int_{t''=0}^{t'} \nu(t'')\,\mathrm{d}t''\right) \nu_{21}(t')\,\mathrm{d}t' \end{aligned} \tag{5.29}$$

where $\nu = \nu_{12} + \nu_{21}$ is the total transition rate and $p_1(0) = 1$.

Orientation 1 is taken to refer to the shallower minimum in the presence of an applied field and orientation 2 to a deeper minimum. This corresponds to the recording situation where the island is initially magnetised in one direction and is reversed by a field in the opposite direction. In the alternate case, the magnetisation is already in the direction of the field and the probability of thermally activated reversal against the field is so low that it can be neglected. During magnetic recording, the energy barrier for reversal against the applied field from orientation 2 to orientation 1 is large ($\approx 60 k_B T$) and it can be seen from equation (5.27) that ν_{21} is extremely small. Thus the second term in equation (5.29) can be ignored and $\nu \approx \nu_{12}$. The switching probability when thermal activation is taken into account in this case becomes

$$p_{switch}(t) = 1 - p_1(t) = 1 - \exp\left(-\int_{t'=0}^{t} \nu(t')\,\mathrm{d}t'\right). \tag{5.30}$$

The total transition rate, ν, depends on the energy barrier between minima, which depends on the position of the island relative to the head and the vector head field averaged over the island volume, which in turn is a function of time. In this case, any head field distribution can be employed provided it is volume

averaged.

Figure 5.4(a) shows a write head traversing over an island. At some time, the head is switched on as it attempts to write an island. The effective volume averaged head field distribution was obtained from

$$H_{\text{eff}} = \frac{H}{\left(\sin^{\frac{2}{3}}\theta_H + \cos^{\frac{2}{3}}\theta_H\right)^{-\frac{3}{2}}} \tag{5.31}$$

where $H = \sqrt{H_x^2 + H_y^2 + H_z^2}$ is the field magnitude, H_x, H_y, H_z, the volume averaged cartesian field components and $\theta_H = \arccos(H_z/H)$ the spherical polar angle.

Figure 5.4(b) shows the volume averaged effective head field distribution for an unshielded Karlqvist-type single pole head (Karlqvist, 1954) reflected in a soft underlayer (see section 4.4) as a function of elapsed time after the head is switched on.

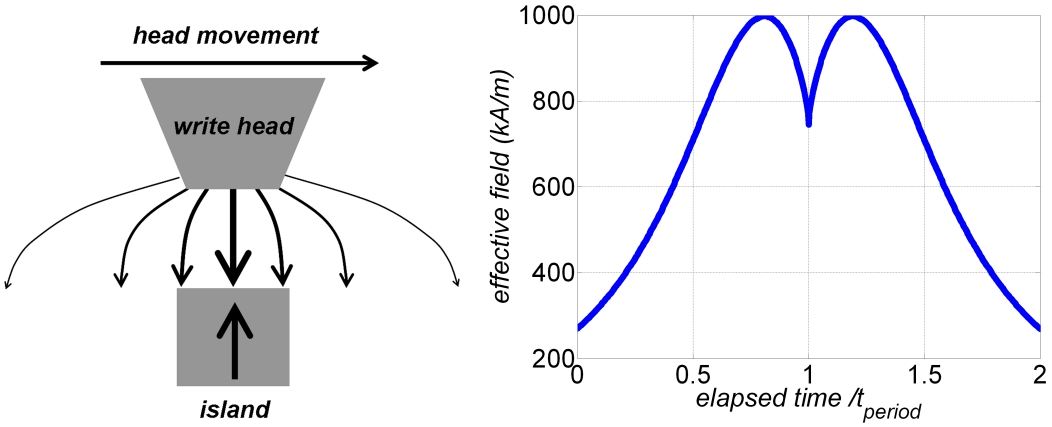

(a) (b)

Figure 5.4: (a) Write head traversing over an island. (b) Volume averaged effective head field distribution in kA/m as a function of elapsed time. Head velocity $= 5\times10^{-6}$ m/s, $f_0 = 1000$ GHz, $M_s = 413$ kA/m, $H_g = -H_K^{\text{eff}} = -1.2\times10^3$ kA/m. The head is directly above the island at elapsed time/$t_{period} = 1$ where $t_{period} = 5 \times 10^{-3}$ s.

Figure 5.5(a) shows the dependence of energy barrier on elapsed time as the head traverses over an island. The assumed island geometry (truncated elliptic cone) and head parameters are shown in Figure 4.17. The head gap field was allowed to vary according to an *error function* of rise time 0.2 ns (Livshitz *et al.*,

2009b). As the head approaches the island after being switched on the energy barrier reduces until a certain position where it takes the minimum value. Beyond that position the energy barrier increases until the head is directly above the island. Further than that the energy barrier reduces to a certain point beyond which the energy barrier starts to increase.

This can be explained using the astroid derived in section 3.2 where the island is more easily switched by the off-axis field at the edge of the head, less easily by the perpendicular field under the centre of the pole and that is reflected in the energy barrier. Figure 5.4(b) also verifies this dependence in terms of the effective field where a larger value of the effective field implies that the island can be switched easily. Figure 5.5(b) shows the dependence of switching probability on elapsed time (t) given by equation (5.30). As can be seen, initially the switching probability is zero, and as time elapses it increases and eventually becomes practically constant.

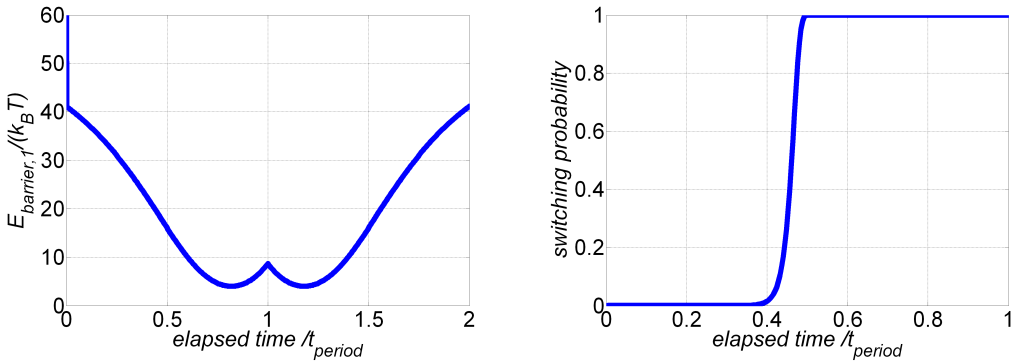

(a) (b)

Figure 5.5: (a) Energy barrier, $E_{\text{barrier},1}/(k_BT)$, as a function of elapsed time, $t_{period} = 5 \times 10^{-3}$ s. (b) Switching probability as a function of elapsed time. Head velocity $= 5 \times 10^{-6}$ m/s, $f_0 = 1000$ GHz, $M_s = 413$ kA/m, $H_g = -H_K^{\text{eff}} = -1.2 \times 10^3$ kA/m.

5.4 Including variations in island parameters

Equation (5.30) applies to the case where islands are identical but in reality islands will not be identical. Due to tolerances during fabrication, islands tend to vary in position, geometric and magnetic properties. It has been established that the written-in error rate of BPM depends upon the distribution of island

parameters (Richter *et al.*, 2006b). In order to include these variations in the statistical model the *probability distribution function* (pdf) of island parameters is required. The switching probability with variations was calculated by convolving the switching probability with the pdf. A *Gaussian* distribution of island position, geometric or magnetic properties has been assumed (Belle *et al.*, 2008). Expressed mathematically, the switching probability with parameter variations is

$$\begin{aligned} p_{\text{switch}}^{\text{var}}(t) &= \frac{\int p\left(a\right) p_{\text{switch}}\left(a,t\right) \mathrm{d}a}{\int p\left(a\right) \mathrm{d}a} \\ &= 1 - \frac{\int p\left(a\right) p_{1}\left(a,t\right) \mathrm{d}a}{\int p\left(a\right) \mathrm{d}a} \end{aligned} \tag{5.32}$$

where p_{switch}^{var} is the switching probability taking into account variations in parameter a, and $p(a)$ is the probability distribution function (pdf) of the parameter a. If the pdf is assumed to be Gaussian then its integral is the error function, *erf*. For parameters with non-zero mean and where the parameter value is always positive (size, shape, crystalline anisotropy), equation (5.32), written explicitly, becomes

$$p_{\text{switch}}^{\text{var}}(\sigma,t) = 1 - \frac{\int_{x=0}^{\infty} \exp\left(-\frac{(x-1)^2}{2\sigma^2}\right) \exp\left(-\int_{t'=0}^{t} \nu\left(x,t'\right) \mathrm{d}t'\right) \mathrm{d}x}{\frac{\sigma\sqrt{2\pi}}{2}\left(1+\operatorname{erf}\left(\frac{1}{\sigma\sqrt{2}}\right)\right)} \tag{5.33}$$

where x is the normalised parameter whose mean is 1, σ is the standard deviation of x and *erf* is the error function. For island position variations (jitter), where the parameter x can be negative, the switching probability with variations is

$$p_{\text{switch}}^{\text{var}}(\sigma,t) = 1 - \frac{\int_{x=-\infty}^{\infty} \exp\left(-\frac{(x-\bar{x})^2}{2\sigma^2}\right) \exp\left(-\int_{t'=0}^{t} \nu\left(x,t'\right) \mathrm{d}t'\right) \mathrm{d}x}{\sigma\sqrt{2\pi}} \tag{5.34}$$

where $\bar{x}$ is the expected position of the island.

5.5 Incorporating magnetostatic interactions

An assumption taken in a derivation of the switching probability is that islands are non-interacting. In BPM at higher recording densities each island is expected to experience interactions from surrounding islands and a mechanism to incorporate

these was devised. An exact calculation of magnetostatic interactions between two particles having arbitrary shapes and at any separation between them using a Fourier space approach was proposed by Beleggia *et al.* (2004). For two particles (1 and 2) having uniform magnetisation, the magnetostatic interaction energy is given by

$$E_{\text{int}}(\vec{R}) = \mu_0 M_{s1} M_{s2} \Re \left[\mathscr{F}^{-1} \left\{ \frac{(\vec{m}_1 \cdot \vec{k})(\vec{m}_2 \cdot \vec{k})}{k^2} \rho_1(\vec{k}) \rho_2^*(\vec{k}) \right\} \right] \tag{5.35}$$

where $\Re$ denotes the real part, $\mathscr{F}^{-1}$ the inverse Fourier transform operator, $\vec{R}$ the separation between particles, $*$ the complex conjugate operator. M_{s1}, M_{s2}, $\vec{m}_1$, $\vec{m}_2$, $\rho_1(\vec{k})$ and $\rho_2(\vec{k})$, represent the saturation magnetisation, unit magnetisation vector, shape amplitude (see section 4.2) of particle 1 and 2 respectively.

The dipole-dipole approximation for the magnetostatic interaction energy, on the other hand, is given by (Beleggia *et al.*, 2004)

$$E_{\text{dipole}}(\vec{r}) = \frac{\mu_0}{4\pi} \left[\frac{\vec{\mu_1} \cdot \vec{\mu_2}}{r^3} - 3 \frac{(\vec{\mu_1} \cdot \vec{r})(\vec{\mu_2} \cdot \vec{r})}{r^5} \right] \tag{5.36}$$

where $\mu_1 = M_{s1} V_1$, $\mu_2 = M_{s2} V_2$, V_1 the volume of particle 1, V_2 the volume of particle 2, $\vec{r}$ the separation between particles and $r = |\vec{r}|$.

Equation (5.36) is equivalent to equation (5.35) if the particles are spherical. In the general case, equation (5.35) converges to equation (5.36) if the separation between particles is much larger than the dimensions of the particles. Figure 5.6 compares an exact calculation of the magnetostatic interaction energy for two islands according to equation (5.35) to a dipole-dipole expression, equation (5.36), for various particle separations. In this calculation, $M_{s1} = M_{s2} = 413$ kA/m. An extreme in-plane aspect ratio of $4:1$ ($a = 4b$) was selected because islands having this geometric property have been considered as candidates for data storage (Richter *et al.*, 2006b). Two different orientations of islands to cover down-track and cross-track spacing as shown in Figure 5.6 were also considered.

The Figure shows that an exact calculation of magnetostatic interactions is needed for small separations, whereas for large separations, the dipole approximation is sufficient. If a normalised separation of $r/a = 4$ in Figure 5.6 is considered, which corresponds roughly to a minimum separation between islands, an error of less than 10% is introduced if a dipole-dipole interaction energy is assumed. Therefore to speed up the computation of interactions, a simple dipole-dipole

expression was considered.

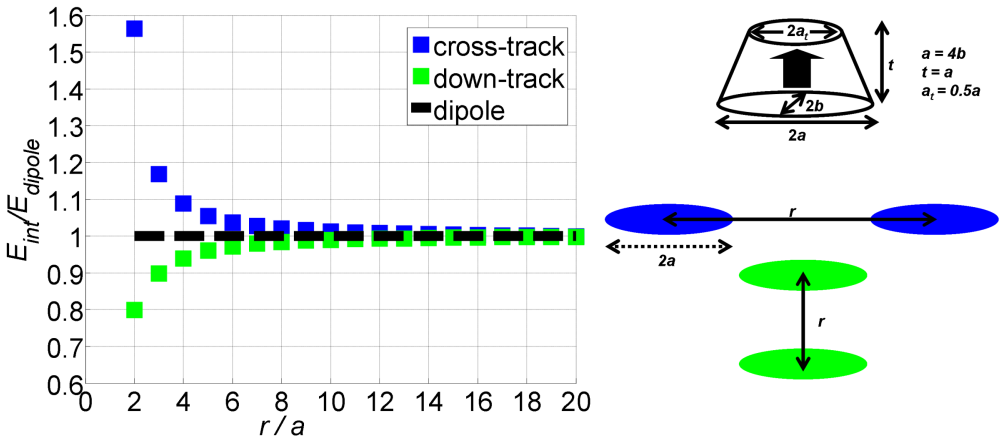

Figure 5.6: Comparison of an exact calculation of magnetostatic interactions to a dipole approximation. $M_{s1} = M_{s2} = 413$ kA/m.

In a recording system, the ideal case is where the magnetisation of surrounding islands is expected to be random. In order to include magnetostatic interactions, a large number of islands on a lattice where each island is randomly magnetised up or down should be considered. This applies if perpendicular anisotropy is assumed and that the final written states of islands are random and uncorrelated with the intended data pattern.

The total dipolar interaction field experienced by a dipole whose magnetic moment is $\mu_i = M_{si}V_i$, located at $\vec{r}_i$ due to other dipoles where each magnetic moment is $\mu_j = M_{sj}V_j$ located at $\vec{r}_j$ can be expressed as

$$\vec{H}_{\text{dipole}}(\vec{r}_{\text{i}}) = \frac{\mu_i}{4\pi} \sum_{j \neq i} \left[3\frac{(\vec{\mu_j} \cdot \vec{r}_{\text{ji}})\vec{r}_{\text{ji}}}{r_{\text{ji}}^5} - \frac{\vec{\mu_j}}{r_{\text{ji}}^3} \right] \tag{5.37}$$

where $\vec{r}_{\text{ji}} = \vec{r}_{\text{j}} - \vec{r}_{\text{i}}$ and $r_{\text{ji}} = |\vec{r}_{\text{ji}}|$.

Equation (5.37) is a convolution and for a large number of dipoles it is convenient to compute the dipolar interaction field using a *Fast Fourier Transform* (FFT) technique to speed up the computation. Figure 5.7 shows a histogram plot of dipolar interaction fields at the centre of a 256×256 square array of islands for several populations computed using an FFT technique. In this calculation, the saturation magnetisation, M_s, was 413 kA/m and the (intrinsic) anisotropy field, H_K, was 133.4 kA/m. The island geometric parameters were as shown in Figure 4.17 and the lattice period was 25 nm. The histogram plot shows that the

interaction fields can reasonably be described by a Gaussian distribution whose mean is 0 and standard deviation is $0.27\%H_K$. This additional field can be considered to be identical in effect to an additional distribution of anisotropy field and would reduce the tolerable anisotropy field distribution accordingly.

If M_s is allowed to vary from island to island according to a *Gaussian* distribution, a calculation of interaction fields at the centre of a square array reveals that for a 10% standard deviation of M_s normalised to the mean (413 kA/m), no change is observed in the interaction fields.

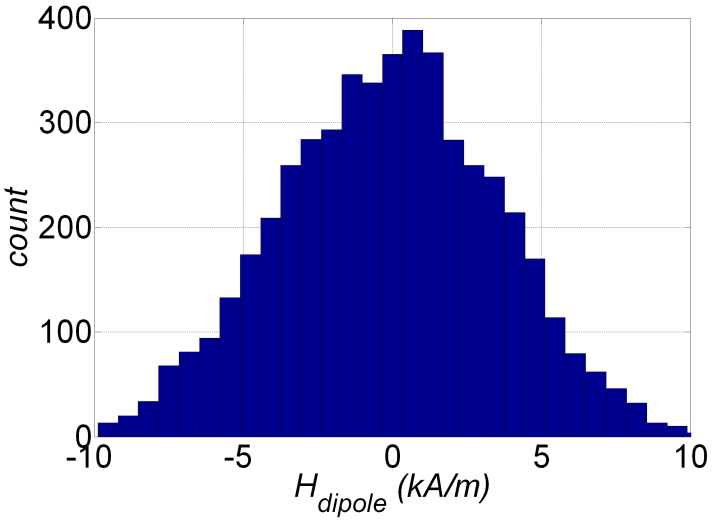

Figure 5.7: Histogram plot of dipolar interaction field at the center of a 256×256 square array of islands.

5.6 Comparison to Richter's model

The statistical write model avoids the approximations of the original statistical model of Richter *et al.* (2006b) (see section 3.4.1) without resorting to micromagnetic simulation of huge populations of islands. In this model, the switching probability is computed from the entire head field profile and thus takes into account the head field asymmetry and non-linearity.

According to the original statistical model of Richter (Richter *et al.*, 2006b) all variations in island properties, (δH_k), can be mapped into position variations (δx) according to

$$\frac{\mathrm{d}x}{\mathrm{d}H_{\mathrm{eff}}}\delta H_k = \delta x, \tag{5.38}$$

where H_{eff} is the effective head field at the write point, x is the position, and H_k is the switching field of the island. Richter's model assumes a constant effective head field gradient at the write point to $\pm B/2$ where B is the bit length. The statistical model avoids this assumption and uses the full effective head field gradient.

According to Richter *et al.* (2006b), the probability of failing to write a target island or overwriting a previously written island, P_t, due to an incorrect timing event, assuming a *Gaussian* distribution, is obtained by considering that any island found more than $B/2$ away from the ideal position will create a write error. By counting the number of islands that fall in this range the result is

$$P_t = 1 - \text{erf}\left(\frac{B/2}{\sigma_x\sqrt{2}}\right) \tag{5.39}$$

where B is the bit length (island period), σ_x is the standard deviation of all distributions combined. The assumption of moving an island $B/2$ from the current position before an error can occur is not necessarily safe if the head field gradient is low.

In addition, the effect of switching field distributions causing some islands to be unwritable is treated separately in Richter's model. In this model, however, the effect of switching field distributions is automatically included in the switching probability calculations and does not need to be computed separately.

5.7 Extension to two layer structures

BPM composed of single domain islands is expected to extend areal densities in a narrow range beyond 1 Tb/in^2 (see chapter 7). In order to further extend areal densities, Exchange Coupled Composite (ECC) BPM described in section 2.5.1 is a likely successor. Figure 5.8(a) shows a two layer island model.

The moment of the low anisotropy layer (soft) rotates easily in a applied field. The high anisotropy layer (hard) provides thermal stability in the absence of an applied field. A lower field than required to switch the hard layer causes the magnetisation in the lower layer to start reversing and thus in addition to the external field there is an exchange field. The interlayer exchange coupling ensures that the reversed top layer helps the bottom layer to switch. These collective features, when optimised, can lead to a system that supports higher recording

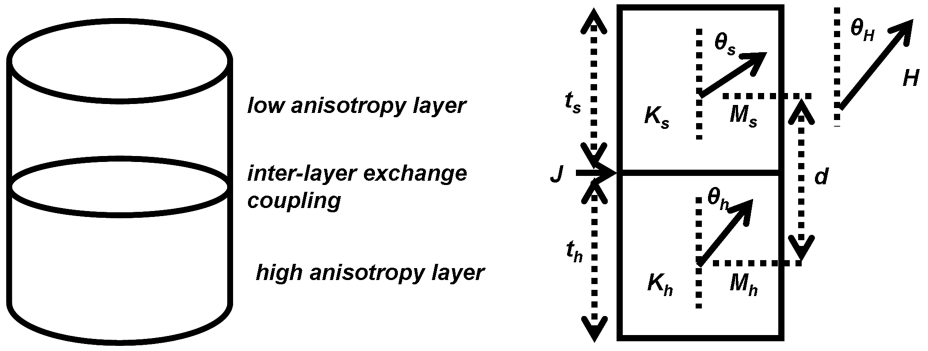

(a) (b)

Figure 5.8: (a) Two layer Exchange Coupled Composite (ECC) island model. (b) Model parameters used in a calculation of the total energy.

densities.

5.7.1 Energy barriers of ECC islands in an applied field

A study of energy barriers for a two spin model in the presence of an applied field using a power law exponent was reported by Bertram and Lengsfield (2007). This required the switching field to be computed first before fitting exponents can be determined. A different approach was carried out to compute energy barriers where a calculation of the switching field is not necessary.

The energy of ECC islands in an applied field must be computed efficiently to enable a write error model to compute error rates. A computationally efficient two spin energy model including the energy of each layer and interlayer exchange energy was developed. This model assumes the change in magnetisation angle occurs entirely at the interface. This works if the exchange coupling is somehow weakened at the interface otherwise there will be a domain wall that will spread into the soft and hard layers. Figure 5.8(b) shows the model parameters used in a calculation of the energy. The total energy assuming in-plane rotation is expressed mathematically as (Bertram and Lengsfield, 2007)

$$\begin{aligned}\mathcal{E} = {} & K_h V_h \sin^2\theta_h + K_s V_s \sin^2\theta_s - JA\cos\left(\theta_s - \theta_h\right) - \mu_0 M_h V_h H \cos\left(\theta_h - \theta_H\right) \\ & - \mu_0 M_s V_s H \cos\left(\theta_s - \theta_H\right) - \frac{\mu_0 M_s V_s M_h V_h}{4\pi d^3}\left[3\cos\theta_s \cos\theta_h - \cos\left(\theta_s - \theta_h\right)\right]\end{aligned} \tag{5.40}$$

where V_s and V_h represent the volume of the soft and hard layer respectively. M_s

and M_h are the saturation magnetisation of the soft and hard layer respectively. K_s and K_h represent the total anisotropy constant that includes crystalline and shape anisotropy of the soft layer and hard layer respectively. θ_s and θ_h are the polar angles of the magnetisation in the soft and hard layer respectively. θ_H is the applied field polar angle. H represents the magnitude of the applied field, J is the interlayer exchange coupling constant and A is the cross-sectional area at the interface. The parameters t_h and t_s represent the hard and soft layer thickness whereas d represents the spacing between centres of the hard and soft layers.

The magnetisation in the hard and soft layers are assumed to lie in a plane formed by the external field and the total anisotropy field of both layers (where the anisotropy field in the soft and hard layer are parallel to each other). Hence the azimuthal angle is constant ($\phi = 0$). In zero or low fields this may not be true but for thermally activated reversal in a moderate to strong field, the applied field should be enough to ensure they are coplanar.

The first and second terms in equation (5.40) represent the anisotropy energy (crystalline and shape) in the hard and soft layers respectively. The third term represents the interface exchange coupling energy. The fourth and fifth terms represent the Zeeman energy in the hard and soft layers respectively. The last term represents the dipolar interaction energy.

If equation (5.40) is divided by $2K_hV_h$ throughout and introducing $H_{kh} = 2K_h/(\mu_0 M_h)$, the resulting reduced total energy is

$$\mathcal{E}' = \frac{1}{2}\sin^2\theta_h + \frac{K_sV_s}{2K_hV_h}\sin^2\theta_s - \frac{JA}{2K_hV_h}\cos\left(\theta_s - \theta_h\right) - \frac{H}{H_{kh}}\cos\left(\theta_h - \theta_H\right) - \frac{M_sV_s}{M_hV_h}\frac{H}{H_{kh}}\cos\left(\theta_s - \theta_H\right) - \frac{M_sV_s}{4\pi d^3 H_{kh}}\left[3\cos\theta_s\cos\theta_h - \cos\left(\theta_s - \theta_h\right)\right] \quad (5.41)$$

where $\mathcal{E}' = \frac{\mathcal{E}}{2K_hV_h}$.

The critical points of equation (5.41) can be obtained by solving the equations

$$\frac{\partial\mathcal{E}'}{\partial\theta_h} = \sin\theta_h\cos\theta_h - \frac{JA}{2K_hV_h}\sin\left(\theta_s - \theta_h\right) + \frac{H}{H_{kh}}\sin\left(\theta_h - \theta_H\right) + \frac{M_sV_s}{4\pi d^3 H_{kh}}\left[3\cos\theta_s\sin\theta_h + \sin\left(\theta_s - \theta_h\right)\right] = 0 \quad (5.42)$$

$$\frac{\partial\mathcal{E}'}{\partial\theta_s} = \frac{K_sV_s}{K_hV_h}\sin\theta_s\cos\theta_s + \frac{JA}{2K_hV_h}\sin\left(\theta_s - \theta_h\right) + \frac{M_sV_s}{M_hV_h}\frac{H}{H_{kh}}\sin\left(\theta_s - \theta_H\right) + \frac{M_sV_s}{4\pi d^3 H_{kh}}\left[3\sin\theta_s\cos\theta_h - \sin\left(\theta_s - \theta_h\right)\right] = 0. \quad (5.43)$$

If the dipole term in equation (5.41) is ignored, the coupled equations (5.42) and (5.43) simplify to

$$\sin\theta_h\cos\theta_h - \frac{JA}{2K_hV_h}\sin\left(\theta_s-\theta_h\right) + \frac{H}{H_{kh}}\sin\left(\theta_h-\theta_H\right) = 0 \tag{5.44}$$

$$\frac{K_sV_s}{K_hV_h}\sin\theta_s\cos\theta_s + \frac{JA}{2K_hV_h}\sin\left(\theta_s-\theta_h\right) + \frac{M_sV_s}{M_hV_h}\frac{H}{H_{kh}}\sin\left(\theta_s-\theta_H\right) = 0. \tag{5.45}$$

Equations (5.44) and (5.45) can be decoupled by introducing an extra parameter, $x = \frac{JA}{2K_hV_h}\sin\left(\theta_s-\theta_h\right)$ in which case they take the form

$$\sin\theta_h\cos\theta_h + \frac{H}{H_{kh}}\left(\sin\theta_h\cos\theta_H - \cos\theta_h\sin\theta_H\right) = x \tag{5.46}$$

$$\frac{K_sV_s}{K_hV_h}\sin\theta_s\cos\theta_s + \frac{M_sV_s}{M_hV_h}\frac{H}{H_{kh}}\left(\sin\theta_s\cos\theta_H - \cos\theta_s\sin\theta_H\right) = -x. \tag{5.47}$$

Equation (5.46) or (5.47) can be expressed as

$$r\sin\theta\cos\theta + h\sin\theta_h\cos\theta_H - h\cos\theta\sin\theta_H = y \tag{5.48}$$

where for the hard layer $r = 1$, $h = \frac{H}{H_{kh}}$, $y = x$ and for the soft layer, $r = \frac{K_sV_s}{K_hV_h}$, $h = \frac{M_sV_s}{M_hV_h}\frac{H}{H_{kh}}$, $y = -x$.

If equation (5.48) is expressed as

$$\cos\theta\left(r\sin\theta - h\sin\theta_H\right) = y - h\cos\theta_H\sin\theta \tag{5.49}$$

and squaring the above equation, the result is

$$r^2\sin^4\theta - 2rh\sin\theta_H\sin^3\theta + \left[h^2-r^2\right]\sin^2\theta + 2h\left[r\sin\theta_H - y\cos\theta_H\right]\sin\theta + y^2 - h^2\sin^2\theta_H = 0 \tag{5.50}$$

which is a quartic.

Equation (5.50) can be solved analytically leading to four expressions for $\sin\theta$. A derivation of these roots can be found in appendix A.3. Since the value of y is unknown, this can be obtained from the non-linear equation

$$y = \frac{JA}{2K_hV_h}\sin\left(\theta_s(y)-\theta_h(y)\right) \quad \text{for the hard layer} \tag{5.51}$$

$$y = -\frac{JA}{2K_hV_h}\sin\left(\theta_s(y)-\theta_h(y)\right) \quad \text{for the soft layer} \tag{5.52}$$

The presence of the dipole term in equation (5.41) implies that the coupled equations (5.42) and (5.43) cannot be decoupled and the equations can be solved numerically. In this case, the critical points of equation (5.41) can be obtained numerically by direct energy optimisation near the point of interest. Equation (5.41) was minimised near $\theta_h = 0, \theta_s = 0$ as a starting point to obtain a local minimum near those points since the limits are known in advance. This local minimum was then used as a starting point in the next minimisation step. The process was done iteratively with a previously obtained local minimum as a new starting point until the solution converged to a local minimum. This minimisation technique was also carried out near $\theta_h = \pi, \theta_s = \pi$ to obtain the local minimum near that point.

The saddle point was obtained by solving numerically equation (5.42) and (5.43) simultaneously with the initial guess near $\theta_h = \pi/2, \theta_s = \pi/2$ and updated after several iterations. The energy barrier is the difference in energy at the saddle point and the minimum. Figure 5.9(a) shows the energy barrier without the dipole term as a function of applied field angle, for various reduced applied fields. The island parameters are shown in Table 5.1 and are suitable for a 4 Tb/in^2 areal density (Greaves *et al.*, 2010). Figure 5.9(b) shows the energy barrier with the dipole term included. The results show that the dipole term increases the energy barrier for any field angle. With these parameters, the energy barrier does not vary much with field angle for a given applied field. This suggests that the speed of computation of energy barriers in this case can be improved by an interpolation scheme. A reduced field between $0.1H_{kh}$ and $0.2H_{kh}$ is sufficient to switch the island at an appropriate field angle.

Figure 5.10 shows the energy landscape for island parameters defined in Table 5.1. The applied field angle, θ_H, was 30° to the perpendicular and the applied field, H, was $-0.05H_{kh}$. Also shown is the minimum energy path required for the magnetisation in both layers to reverse from one orientation to another. This path was computed by setting the path tangent to the ratio of energy gradients as shown in equation (5.53) and numerically integrating the equations

$$\frac{\mathrm{d}\theta_s}{\mathrm{d}\theta_h} = \frac{\frac{\partial \mathcal{E}'}{\partial \theta_s}}{\frac{\partial \mathcal{E}'}{\partial \theta_h}} \tag{5.53}$$

where the starting point is the saddle point and two end points of integration corresponding to the two minima.

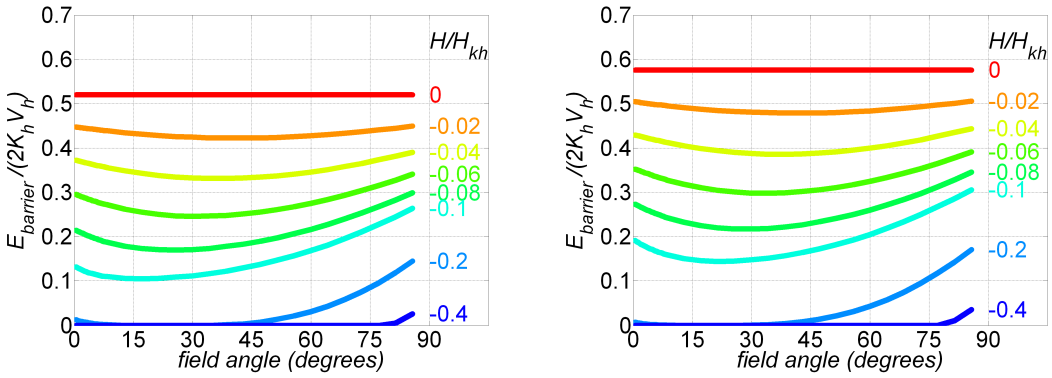

Figure 5.9: (a) Energy barrier, $E_{\text{barrier},1}$, without the dipole term as a function of field angle for various applied field for the island parameters shown in Table 5.1. (b) Energy barrier, $E_{\text{barrier},1}$, with the dipole term as a function of field angle for various applied field values.

Table 5.1: Parameters suitable for a 4 Tb/in^2 recording density

Parameter	Value
M_s	1000 kA/m
M_h	400 kA/m
t_s	5 nm
t_h	5 nm
diameter	6.7 nm
K_h	1.49×10^6 J/m^3
K_s	5.77×10^4 J/m^3
H_{kh}	5.94×10^3 kA/m
J	5×10^{-3} J/m^2

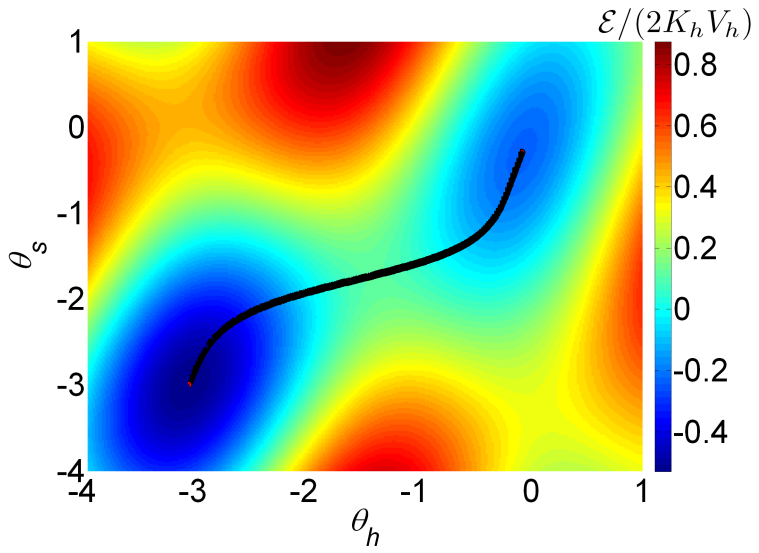

Figure 5.10: Energy landscape and minimum energy path. Island parameters are described in Table 5.1, $\theta_H = 30°$, $H = -0.05H_{kh}$, $H_{kh} = 5.94 \times 10^3$ kA/m.

5.7.2 Switching field versus Coercivity

Apart from the energy barrier, the switching field and coercivity are also quantities of interest. The switching field can be defined as the field magnitude at which the energy barrier vanishes. The coercivity is the field at which the probability of switching at a given temperature and in a given time is 1/2. The switching field was obtained at $T = 0$ K whereas the coercivity was obtained at 300 K.

In order to obtain the coercivity, the starting point is equation (5.30) for the switching probability. Considering constant transition rates, the switching probability becomes

$$p_{\text{switch}} = 1 - \exp(-\nu t) \tag{5.54}$$

where

$$\nu = f_0 \exp(-E_{\text{barrier},1}(h,\theta)/(k_B T)) + f_0 \exp(-E_{\text{barrier},2}(h,\theta)/(k_B T)) \tag{5.55}$$

f_0 is the attempt frequency, k_B is the Boltzmann constant, $E_{barrier,1}$, $E_{barrier,2}$, represent the energy barriers, t is the time elapsed and T is the absolute temperature. Using the definition of coercivity where the switching probability is set to 0.5, the coercivity, h_c, can be obtained from

$$\nu(h_c,\theta) = \frac{\ln 2}{t} \tag{5.56}$$

where $f_0 = 10^9$ Hz, $t = 10$ ns, and $T = 300$ K (Greaves *et al.*, 2010). Equation (5.56) was solved using an iterative scheme starting at a value of $h = 0$ and incrementing h if $\nu(h,\theta) < \frac{\ln 2}{t}$ or decrementing h if $\nu(h,\theta) > \frac{\ln 2}{t}$ until $\nu(h,\theta) = \frac{\ln 2}{t}$.

Figure 5.11 compares the switching field at 0 K to the coercivity at 300 K. The switching field for a given field angle was obtained by computing the field magnitude where the energy barrier vanishes. According to Figure 5.11, the switching field appears to have a sharp increase at small field angles. This can be attributed to the fact that the energy barrier does not completely disappear at small field angles as shown in Figure 5.12 and thus a larger field value is required to completely remove the energy barrier. The energy barrier falls to a low value by $H \approx -0.15 H_{kh}$ but does not reach zero until $H \approx -0.36 H_{kh}$. Thermal activation allows the energy barrier to be jumped and thus $H_c \approx 0.14 H_{kh}$ but the switching field is much higher.

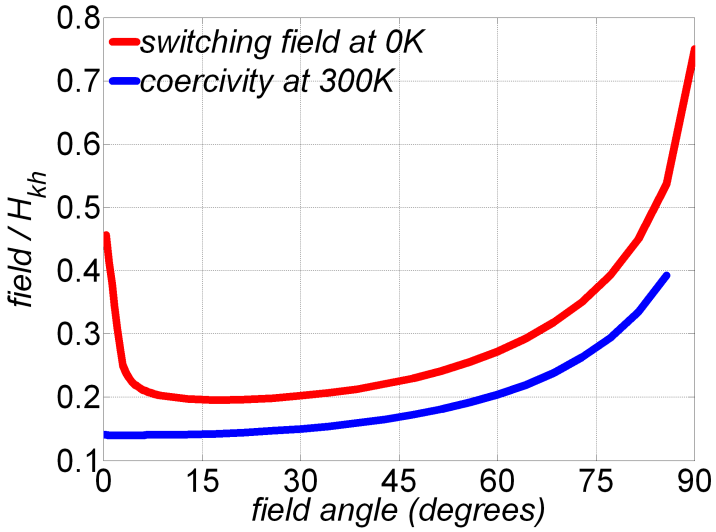

Figure 5.11: Switching field at 0 K and coercivity at 300 K. Island parameters are described in Table 5.1. $H_{kh} = 5.94 \times 10^3$ kA/m.

There are micromagnetic simulation results for coercivity reported by Greaves *et al.* (2010) for an island having the same parameters. Figure 5.13(a) shows the coercivity from Figure 5.11 on a different scale for comparison with micromagnetic simulations in Figure 5.13(b). The agreement in coercivity results between the model and micromagnetic simulations is excellent. This confirms that for this type of ECC island the two-spin model of equation (5.41) is adequate for a

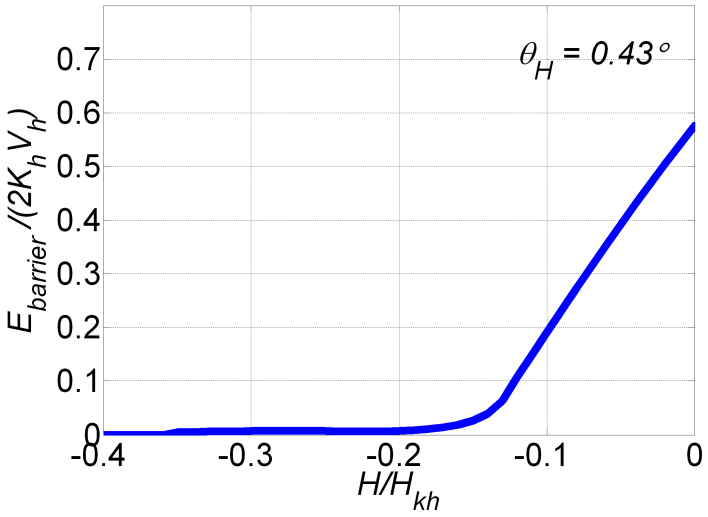

Figure 5.12: Dependence of energy barrier, $E_{\text{barrier},1}$, on applied field values for $\theta_H = 0.43°$.

calculation of the energy barrier.

5.7.3 Energy barriers and switching fields for ECC versus single domain islands

A study of the dependence of energy barrier on field angle for a single domain island and ECC island at various uniform applied fields at 1 Tb/in^2 was carried out. The single domain island (cylindrical) had diameter, $d = 13.4$ nm, thickness, $t = 10$ nm, saturation magnetisation, $M_s = 700$ kA/m, and anisotropy constant (intrinsic), K_1 =3.85 $\times$ 10^5 J/m^3 (see chapter 7). With these parameters, a switching field, $H_{\text{sw}} = 751.31$ kA/m was obtained at a field angle of 1° to the perpendicular. The ECC island had parameters defined in Table 5.2. The hard layer crystalline anisotropy constant, K_{1h}, was varied to obtain the same switching field as the single domain island at a field angle of 1° to the perpendicular. This occurred at K_{1h} =5 $\times$ 10^5 J/m^3.

Figure 5.14(a) shows the dependence of energy barrier on field angle for both islands at various uniform applied fields. Considering the smallest field angle, the results show that ECC islands can be designed to switch at a similar field to single domain islands but retain a significant energy barrier in the presence of an external field.

Figure 5.14(b) shows the dependence of switching fields on field angle for a

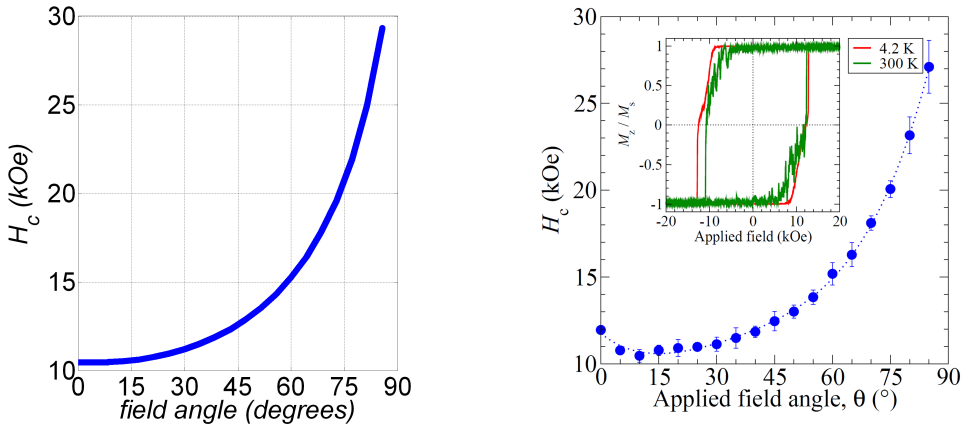

(a) (b)

Figure 5.13: (a) Coercivity at 300 K as predicted by the model. (b) Coercivity at 300 K as obtained from micromagnetic simulations using similar island parameters as described in Table 5.1 (Greaves *et al.*, 2010).

Table 5.2: Parameters suitable for a 1 Tb/in^2 recording density

Parameter	Value
M_s	1000 kA/m
M_h	400 kA/m
t_s	5 nm
t_h	5 nm
diameter	13.4 nm
K_{1s} (crystalline)	1×10^5 J/m^3
K_{1h} (crystalline)	5×10^5 J/m^3

single domain and ECC island. The switching field of an ECC island is higher than that of a single domain island at all field angles except at an angle where the two are set to be equal. This supports the higher energy barriers shown in Figure 5.14(a).

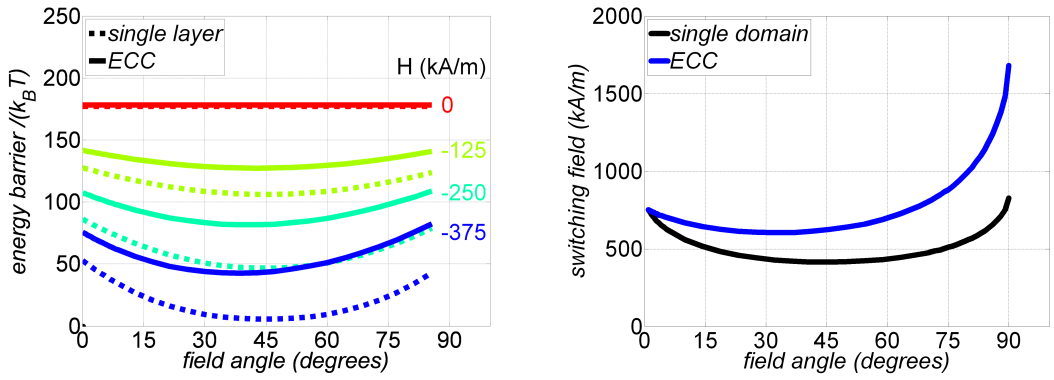

(a) (b)

Figure 5.14: (a) Dependence of energy barrier on field angle for a single domain and ECC island at various uniform applied fields. T = 300 K. (b) Dependence of switching fields on field angle for a single domain and ECC island.

5.8 Summary and Conclusions

This chapter has derived further components required in a development of the statistical write model. It has been demonstrated that the energy barrier of a single domain particle for rotation in a plane given any vector head field can be calculated analytically. This enables the fast computation of transition probabilities in a write error model that includes thermal activation. The switching probabilities for non-interacting and identical islands that take into account thermal activation were derived. Since islands are not expected to be identical, a method to incorporate variations was put forward. A technique to include interactions among islands was introduced.

A computationally efficient but accurate statistical model of write errors has thus been developed to predict switching probabilities of islands in BPM. The model avoids approximations of earlier models without resorting to micromagnetic simulations of huge populations of islands.

Finally, an extension to two layer systems with the aim of further extending

recording densities was provided. The coercivity results obtained using a two-spin model are in excellent agreement with micromagnetic simulations. This confirms that for this type of ECC island, a properly constructed two-spin model is adequate for a calculation of the energy barrier. The results have shown that ECC islands can be designed to switch at a similar field to single domain islands but retain a significant energy barrier in the presence of a destabilising field.

Chapter 6

One-dimensional write simulations

6.1 Introduction

The previous two chapters focused on a development of the statistical write model. In this chapter, one-dimensional write simulations at an areal density of 1Tb/in^2 based on the model are reported. To begin with, the problem of synchronising the write head switching position to a target island that the system intends to write is studied. This is followed by a calculation of the write-window, which determines the range of write head switching positions required to write data on a target island in order to achieve a given required Bit Error Rate (BER). The dependence of the write-window on attempt frequency and various head-medium relative velocities is also studied. The distributions of island position, geometric (size or shape) and magnetic properties are then included and their impact on the write-window studied. Following this is a comparison of the model predictions against other models.

Some sections of this chapter are taken from the papers included in appendix B. These papers were written by the author of this thesis who carried out all of the model developments and obtained all of the model results described in those papers.

6.2 Write head synchronisation

As pointed out in section 2.6.1, a challenge associated with BPM is the difficulty in synchronising the write head current waveform to individual islands as the head traverses over islands. Therefore it is important to predict the timing margin available for synchronising the write head switching position with respect to the target island in order to achieve a required BER (Richter *et al.*, 2006b; Albrecht *et al.*, 2002a,b). This information will be useful to designers in revealing the required values of key parameters in media design and will enable the design parameters of servo systems to be determined.

To study this problem, two islands are considered, the target which is the island the system intends to write and the previously written island. The assumed island geometry (truncated elliptic cone) and head parameters are shown in Figure 4.17. Figure 6.1 shows a schematic of the write head and the two islands. As the write head attempts to write the target island, there is a risk that the previously written island may be overwritten which leads to a write error. The previously written island experiences a finite head field which lowers the energy barrier and thus increases the probability of thermally activated magnetisation reversal. There is a risk that the target island may fail to write if the write head is not switched on at an appropriate location. The write head should be switched on at a position far enough from the previously written island to ensure the probability of writing it is acceptably low but also not too far from the target island. It is important to determine the positions at which the write head should be switched on to keep write errors acceptable. To study this problem quantitatively requires the calculation of the write-window which is explained in a section that follows.

6.3 Write-window with identical islands

If the write head is too near the target island, the previously written island experiences a weak field and thus the probability of write error on the previously written island is negligible. Similarly, if the write head is too near the previously written island, the target island experiences a weak field and thus the probability of write error on the target island is negligible. At these extremes, the probability of write error on both islands is negligible.

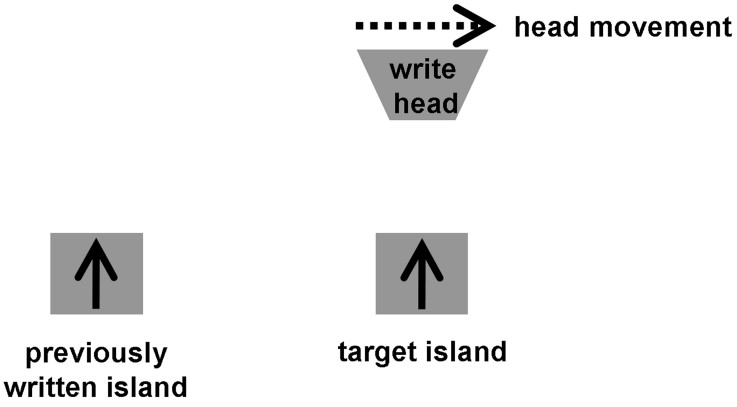

Figure 6.1: Write head attempting to write data on target island. There is a risk of overwriting a previously written island or failing to write the target island which leads to a write error.

A write-window for a given BER, e, is obtained by identifying the head switching positions at which the probability of incorrectly writing the previously written island is e and the head switching position at which the probability of failing to write the target island is $1 - e$. These two head switching positions define the range within which the head must switch in order to achieve the given error rate without assuming any properties of the head field and incorporating thermal activation. The errors e and $1 - e$ define the boundaries of the write-window.

To compute the write-window without island variations, equation (6.1) derived in section 5.3 was used to obtain the switching probabilities for the target or previously written island.

$$p_{switch}\left(t\right) = 1 - \exp\left(-\int_{t'=0}^{t} \nu\left(t'\right) \mathrm{d}t'\right). \tag{6.1}$$

In equation (6.1), $\nu = f_0 \exp(-E_{\mathrm{barrier},1}/(k_B T)) + f_0 \exp(-E_{\mathrm{barrier},2}/(k_B T))$ represents the total transition rate. Though the switching probability in equation (6.1) is a function of elapsed time (t) after the head is switched on, it becomes essentially constant beyond a certain time after the head has moved beyond the intended island as shown in Figure 5.5(b). It is this constant value that is taken as the switching probability.

6.3.1 Write-window for various attempt frequencies

To apply equation (6.1), the attempt frequency, f_0, should be known. As reported in section 3.3.3, Brown (1979) showed that f_0, equation (3.80), depends on a number of parameters which include the phenomenological damping constant and magnetic properties. However, the actual value of damping constant is not easily measurable and thus the correct value of f_0 is debatable (Weller and Moser, 1999; Wernsdorfer *et al.*, 1997). In order to get an estimate of f_0 using Brown's equation, a damping constant of 0.1 (Gilbert, 2004) was chosen.

Magnetic properties used in simulations are $M_s = 413$ kA/m (Morrison, 2008), $K_1^{\text{eff}}V/k_BT = 60$ and $T = 300K$, where k_B is the Boltzmann constant, M_s the saturation magnetisation and V the island volume, K_1^{eff} is the total anisotropy constant including crystalline and shape anisotropy.

In the absence of an applied field and substituting the magnetic properties as described above into equation (3.80), a value of $f_0 = 134$ GHz was obtained. Since this is an estimate, switching probabilities were calculated with values of f_0 ranging from 1 to 1000 GHz.

A Karlqvist type single pole head reflected in a soft underlayer as described in Figure 4.17 was considered. The volume averaged head field distribution from this write head was used for simulations. Since the vector head field varies in the down-track direction only (one-dimensional), the switching probability varies in only one dimension and consequently one-dimensional simulations were carried out. The head gap field, H_g, was chosen to be $1.5H_K^{\text{eff}} = 1807$ kA/m (22.69 kOe), where H_K^{eff} is defined according to equation (4.50). This value exceeds the maximum gap field for a practical Karlqvist head, although it does not exceed the 2.4 T limit (Richter, 2007) of the saturation magnetisation of the pole pieces.

During a single bit write event, the head traverses the islands and at some point is switched on. The head gap field takes a finite time to rise and was varied with time as an *error function* of rise time 0.2 ns (Livshitz *et al.*, 2009b) from 0 to $1.5H_K^{\text{eff}}$ during switching, where the switching position is taken as the location of the centre of the head at the moment that the gap field is zero. The probability of each island switching was obtained by numerically carrying out the integration in equation (6.1) for a range of head gap field switching positions.

The separation between islands (island period) was 25 nm since this value can support a recording density of 1 Tb/in^2 if islands are arranged on a square lattice. The island geometric parameters are shown in Figure 4.17. Magnetostatic

interactions between these islands are relatively small because the saturation magnetisation is relatively low and the islands are well separated and thus were not included. To verify this, the standard deviation of the interaction field was found to be $0.27\%H_K$ where $H_K = 1.33 \times 10^3$ kA/m using the approach described in section 5.5.

Figure 6.2 shows the switching probability for previously written and target islands as a function of head switching position for a velocity of 5×10^{-6} m/s (the speed of a high resolution drag tester). The location of these islands is also shown for clarity. The write-window can be obtained by identifying the head switching position at which the probability of inadvertently writing the previously written island is e, and the position at which the probability of failing to write the target island is $1 - e$. This is shown in Figure 6.3. The timing window is the separation between these two head field switching positions.

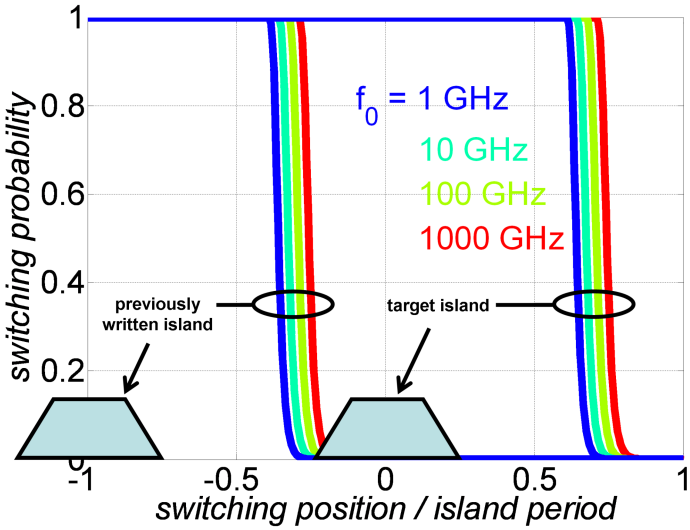

Figure 6.2: Switching probability for target and previously written islands as a function of head switching position for various attempt frequencies f_0. Island period = 25 nm, head velocity = 5×10^{-6} m/s. The head dimensions appear in Figure 4.17.

Figure 6.4 shows the calculated write-window as a function of $\log_{10}$(BER) for a range of attempt frequencies. The BER in this case is defined to be half the probability of switching a previously written island. At this very low (dragtester) velocity, for BER $\geq 10^{-6}$, the write-window does not vary significantly as a function of attempt frequency. At higher drive velocities, thermal activation would be expected to have substantially less effect because there is less time for

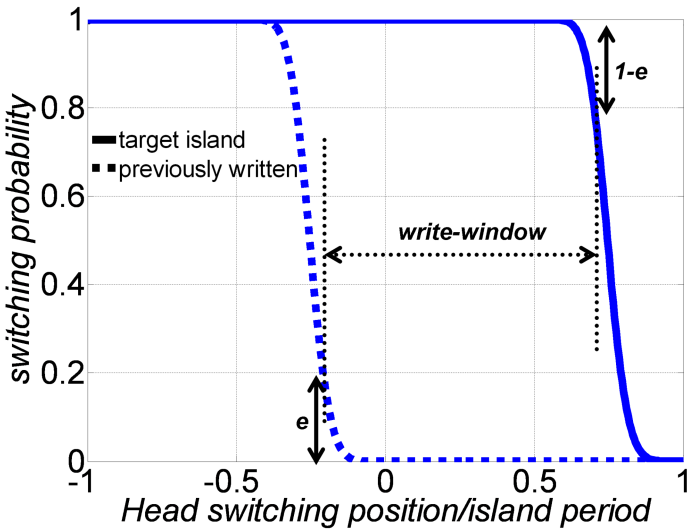

Figure 6.3: Write-window illustration.

each write event and thus fewer attempts per bit. The largest attainable write-window is obtained for a BER of 0.5, which is the error rate that would result if the final written states of islands were random and uncorrelated with the intended data pattern.

The write-window calculated in this manner is significantly different in meaning from the timing window assumed by Richter *et al.* (2006b) (see section 6.5 where this is fully discussed). In that model, the timing window was effectively defined to be the island spacing or bit spacing. Therefore where Richter's model provides a means of calculating the error rate as a function of island period, this model reveals how the system timing tolerance depends upon the required write error rate for a given island period.

6.3.2 Write-window for different head velocities

Different head velocities were considered in order to understand their impact on the write-window. Head velocities ranging from 5×10^{-6} m/s (the speed of a high resolution drag tester) to 25 m/s (the head-medium speed in a disk drive) were considered. Figure 6.5 shows that at any given BER the write-window deteriorates with decreasing head velocity. This is due to increased thermal activation as the head takes a longer time to travel between islands. For BER $= 10^{-5}$ or worse, the write-window does not vary significantly with head velocity.

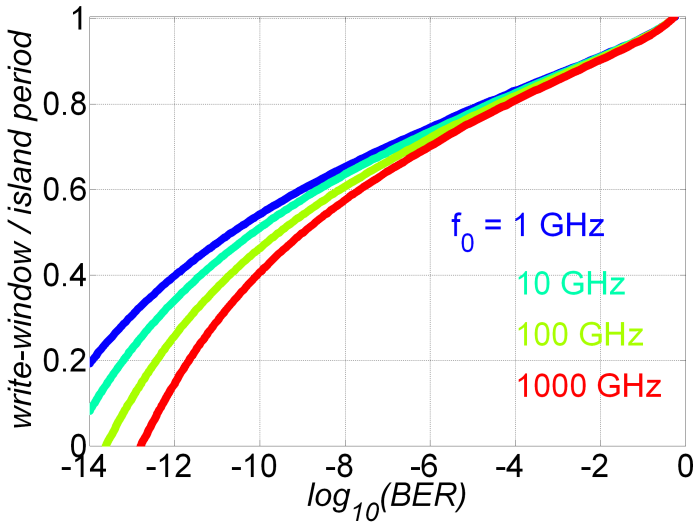

Figure 6.4: Dependence of write-window on $\log_{10}$(BER) for various attempt frequencies f_0, head velocity $= 5 \times 10^{-6}$ m/s.

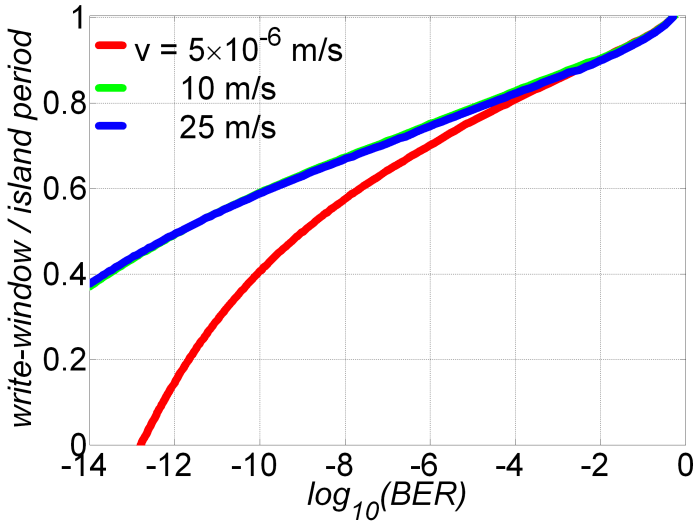

Figure 6.5: Dependence of write-window on $\log_{10}$(BER) for different head velocities.

6.4 Write-window with island variations

As pointed out in section 5.4, islands tend to vary in position, geometric and magnetic properties. To study the impact of variations on the write-window, a Gaussian probability distribution function was used to describe the variation of parameters (Belle *et al.*, 2008). The variations of island position, magnetic and geometric properties of islands were studied and the results are reported in this section.

6.4.1 Position variations

Islands in BPM tend to deviate from their expected positions (jitter). The calculation of switching probabilities in media with position variations was based upon calculation of equation (5.34) where the island geometry (shape or size) was fixed. In order to speed up the computation, a precomputed switching probability curve (for example Figure 6.6 with $\sigma = 0$) was used. The switching probability with position variations was then obtained by observing that if an island is shifted from its expected position by an amount δ, the switching probability curve is identical to that in its expected position but shifted by an amount δ along the down-track dimension. Hence, the switching probability curve for the distribution can be obtained by a weighted sum of shifted curves, where the weight for each shift value is the corresponding value of the Gaussian pdf of the position distribution according to

$$p^{\text{var}}_{\text{switch}}\left(\sigma_{\text{position}}, x_s\right) = \frac{\int_{x=-\infty}^{\infty} \exp\left(-\frac{(x-\bar{x})^2}{2\sigma^2_{\text{position}}}\right) p_{\text{switch}}\left(x-\bar{x}, x_s\right) \mathrm{d}x}{\sigma_{\text{position}}\sqrt{2\pi}}. \tag{6.2}$$

In equation (6.2), $\bar{x}$ is the expected position of the island, x_s is the head switching position and σ_{position} the standard deviation in position. The denominator normalises the switching probability.

Figure 6.6 shows the switching probabilities for various distributions of position while Figure 6.7 shows the calculated write-window. Increasing the variations reduces the write-window for a given BER.

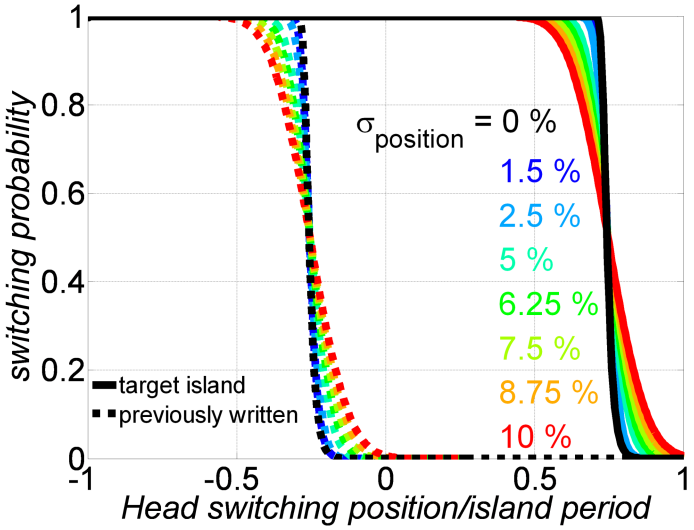

Figure 6.6: Switching probability for target and previously written islands as a function of head switching position for various distributions of island position. Standard deviation of island position is expressed as a percentage of island period. Head velocity $= 5 \times 10^{-6}$ m/s, $f_0 = 1000$ GHz.

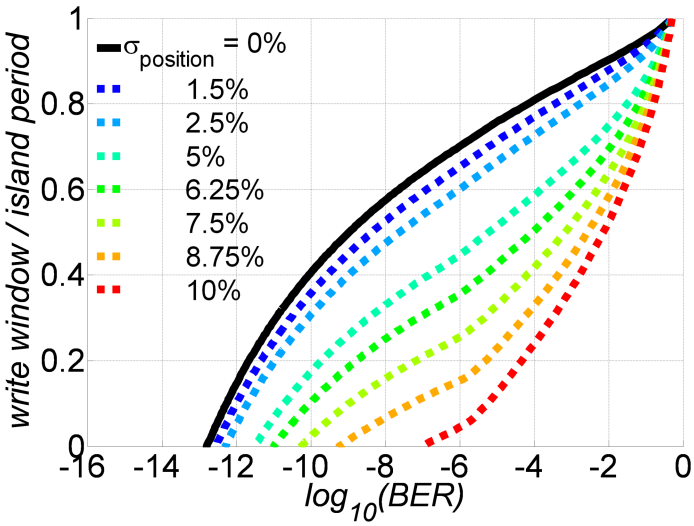

Figure 6.7: Dependence of write-window on $\log_{10}$(BER) for various distributions of island position. Standard deviation of island position is expressed as a percentage of island period. Head velocity $= 5 \times 10^{-6}$ m/s, $f_0 = 1000$ GHz.

6.4.2 Shape variations

To determine the effect of island shape upon write-window, a population of islands of varying shape was considered. Shape variation was assumed to arise from a finite variance of the in-plane ellipticity (semi-minor axis (b)/semi-major axis (a)) of the islands with the thickness remaining constant. The island size (volume) was assumed to be constant (to exclude the effect of size) as the in-plane ellipticity varies from island to island. The varying magnetometric demagnetising factors for this shape were computed using the approach described in section 4.2.

The switching probabilities in media with shape variations were calculated using equation (5.33). To speed up the computation of switching probabilities, the volume averaged head fields were precomputed for various head-island separations and island shapes. The volume averaged head field for any given head position and island shape was then computed by a two-dimensional polynomial interpolation of the precomputed table of values.

Several standard deviations of ellipticity between 0 and 10% of the mean (1.0) were considered. The dependence of write-window on $\log_{10}$(BER) is shown in Figure 6.8. Very little difference can be observed, showing that the write-window is not very sensitive to shape.

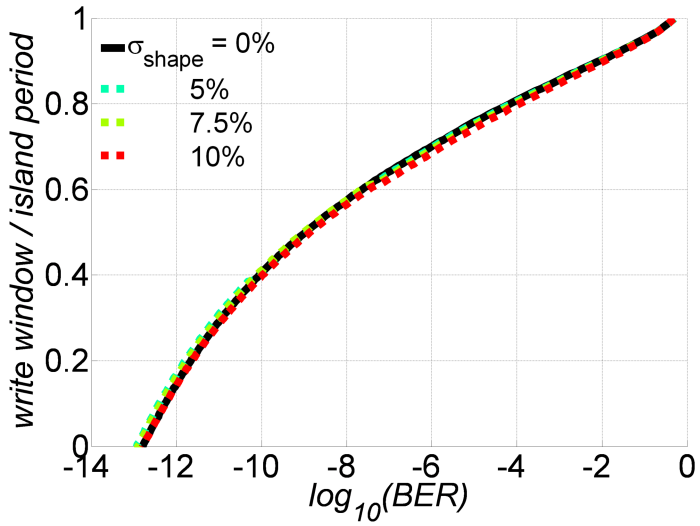

Figure 6.8: Dependence of write-window on $\log_{10}$(BER) for various populations of island in-plane ellipticity (b/a). Standard deviation of in-plane ellipticity is expressed as a percentage of mean ellipticity = 1. Head velocity = 5×10^{-6} m/s, f_0 = 1000 GHz.

6.4.3 Size variations

To study size variations, the island thickness and in-plane ellipticity were fixed ($b/a = 1$) while the radius was varied. The switching probabilities were calculated using the same method as for the shape distributions described above.

Several standard deviations between 0 and 10% of the mean radius were considered. Figure 6.9 shows the dependence of write-window on $\log_{10}$(BER) for these distributions of size. Analysis of Figures 6.8 and 6.9 shows that shape vari-

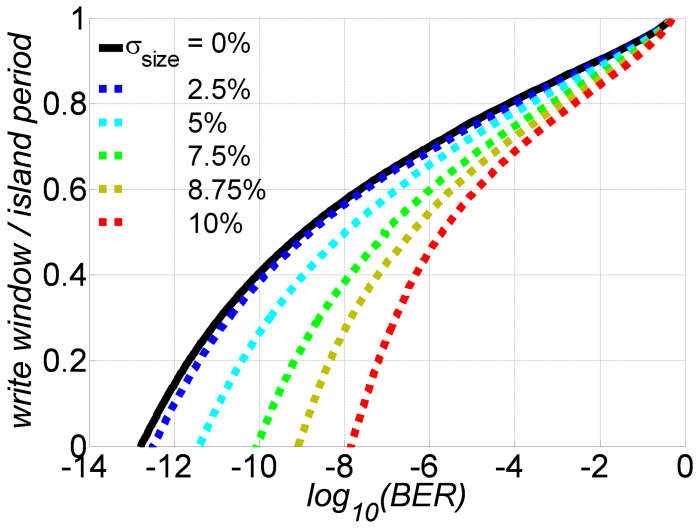

Figure 6.9: Dependence of write-window on $\log_{10}$(BER) for various populations of island radius. Standard deviation of radius is expressed as a percentage of mean radius. Head velocity $= 5 \times 10^{-6}$ m/s, $f_0 = 1000$ GHz.

ation has little effect on the write-window at almost all values of BER. However variation in island size has a severe impact upon write-window. Assuming a BER of 10^{-6} to be acceptable, with no size variation in the islands, the write-window is 0.7P (where P is the island period = 25 nm), while 5% and 10% standard deviations in size reduce the write-window to 0.65P and 0.46P, respectively. Thus island size distributions arising during fabrication will have a significant impact upon write-window and thus upon the servo tolerances required for a viable system. Position variations have a more severe impact upon write-window than size variations.

6.4.4 Crystalline anisotropy variations

Islands in BPM tend to vary in their magnetic properties (Thomson *et al.*, 2006). In this analysis, the island geometry was fixed while distributions in magnetic properties were introduced by varying the crystalline anisotropy, K_1. Equation (5.33) was used to obtain switching probabilities in the presence of K_1 variations. Figure 6.10 shows the write-window for various distributions in K_1. As shown in Figure 6.10, for these islands, there is no write-window for a standard deviation of 10% at a BER $= 10^{-6}$ which indicates the detrimental effect of K_1 variations.

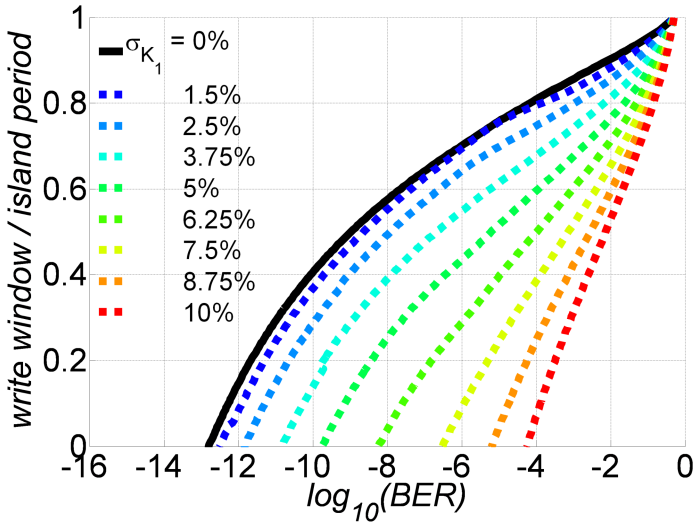

Figure 6.10: Dependence of write-window on $\log_{10}$(BER) for various populations of island K_1. Standard deviation of K_1 is expressed as a percentage of the mean. Head velocity $= 5 \times 10^{-6}$ m/s, $f_0 = 1000$ GHz.

6.4.5 Combining parameters

Position and K_1 variations were seen to have a more significant effect on BER than geometry variations. The impact of a combination of both variations was studied to determine whether the effect of varying both simultaneously is worse than would be expected from each individually. In principle a double integral taking into account both distributions should be evaluated. To speed up the calculations, the precomputed switching probability curve for K_1 variations only was used. Position variations were then included by using a technique similar to

one employed for position variations described by equation (6.3).

$$p^{\text{var}}_{\text{switch}}\left(\sigma_{\text{position}}, \sigma_{K_1}, x_s\right) = \frac{\int_{x=-\infty}^{\infty} \exp\left(-\frac{(x-\bar{x})^2}{2\sigma^2_{\text{position}}}\right) p^{\text{var}}_{\text{switch}}\left(\sigma_{K_1}, x-\bar{x}, x_s\right) \mathrm{d}x}{\sigma_{\text{position}}\sqrt{2\pi}} \tag{6.3}$$

where $\bar{x}$ is the expected position of the island, x_s is the head switching position and σ_{position} the standard deviation in position.

Figure 6.11 shows the write-window for these distributions. Combining distributions worsens the performance of the system significantly. For these islands, there is no write-window for a standard deviation of 7.5% and above at a BER $= 10^{-6}$.

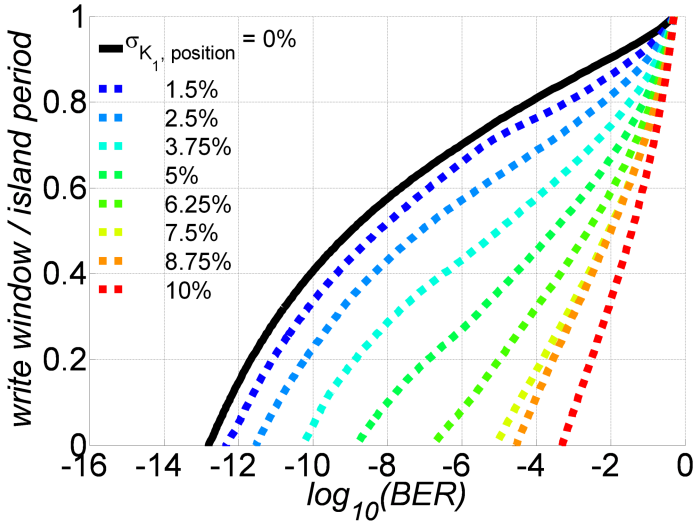

Figure 6.11: Dependence of write-window on $\log_{10}$(BER) for various populations of island position and K_1 combined. Head velocity $= 5 \times 10^{-6}$ m/s, $f_0 = 1000$ GHz.

6.4.6 Write-window – standard deviation plots for fixed BER

The write-window was determined as a function of standard deviation of island properties at selected BER values in order to easily identify the impact of parameter variations on the write-window. These values were obtained from the write-window – BER plots. Figures 6.12, 6.13 and 6.14 show the dependence of write-window on standard deviation for the selected parameters at BER values of

10^{-6}, 10^{-5} and 10^{-4} respectively. As can be seen, variations in island geometry (shape or size) have a less impact on the write-window compared to position or magnetic property variations. Combining parameters worsens the performance of the system significantly.

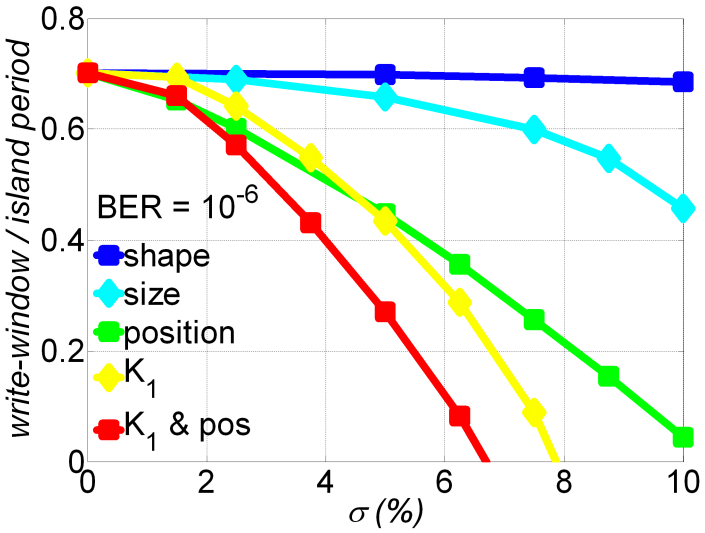

Figure 6.12: Dependence of write-window on standard deviation for various populations of islands for a BER = 10^{-6}.

6.5 Comparison with other models

The results of this model were compared with those of earlier models. The original statistical model of Richter (Richter *et al.*, 2006b) was used to calculate error rates for the same system as shown in Figure 6.11. For the 1 Tb/in^2 islands considered in this study, a 5% standard deviation of island position (jitter) gives rise to a $0.05 \times 25 = 1.25$ nm standard deviation of island position (jitter). The mean anisotropy field is 1.204×10^3 kA/m (15.13 kOe) and the gradient of the write head field at the write point is 77.465 kA/m/nm (973 Oe/nm). Using Richter *et al.* (2006b) analysis, all variations in island properties (ΔH_k) can be mapped into position variations (Δx) according to

$$\frac{\mathrm{d}x}{\mathrm{d}H_{\mathrm{eff}}} \Delta H_k = \Delta x \tag{6.4}$$

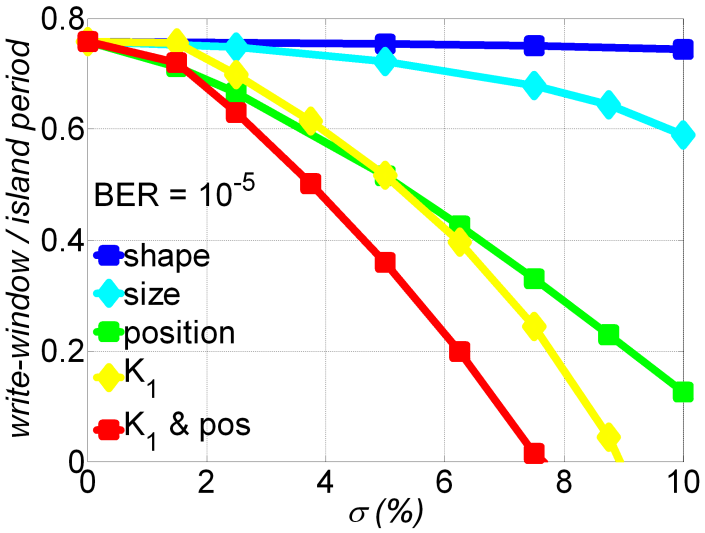

Figure 6.13: Dependence of write-window on standard deviation for various populations of islands for a BER = 10^{-5}.

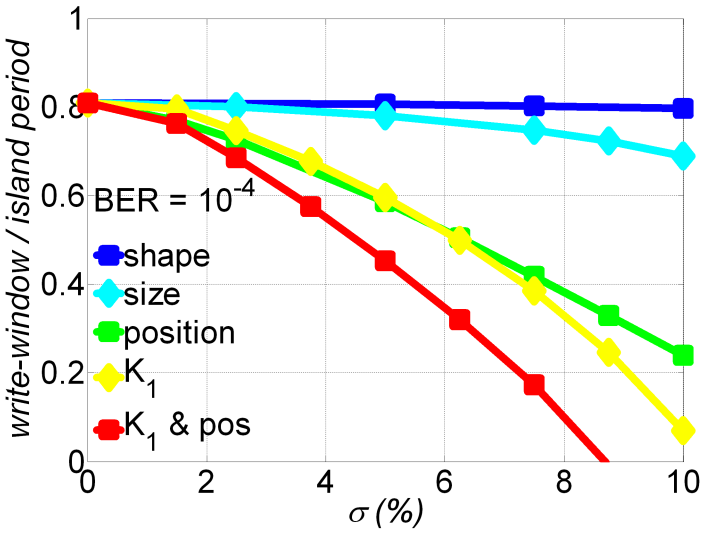

Figure 6.14: Dependence of write-window on standard deviation for various populations of islands for a BER = 10^{-4}.

where H_{eff} is the effective head field, x is the position and H_k is the switching field of the island. From equation (6.4), a 5% standard deviation of anisotropy field corresponds to a position jitter of $\frac{1}{77.465} \times 0.05 \times 1.204 \times 10^3 = 0.772$ nm. Combining the island position jitter and the equivalent jitter arising from anisotropy variation leads to a total jitter of $\sqrt{0.772^2 + 1.25^2} = 1.472$ nm.

According to Richter *et al.* (2006b), the probability of a timing error to occur, P_t, assuming a *Gaussian* distribution is obtained by considering that any island found more than $B/2$ away from the ideal position will create a write error and is

$$P_t = 1 - \text{erf}\left(\frac{B/2}{\sigma_x\sqrt{2}}\right) \tag{6.5}$$

where B is the bit length (island period), σ_x is the standard deviation of all distributions combined. The assumption that any island found more than $B/2$ from the correct position leads to a write error is not necessarily safe if the head field gradient is low.

If $B = 25$ nm, $\sigma_x = 1.472$ nm, a write error rate, $P_t/2$, of 1.012×10^{-17} would be predicted. For a write-window corresponding to the island period, this model predicts a BER= 0.5 which is higher.

The model of Richter *et al.* (2006b) also considers errors arising from islands with such high anisotropy that the head field is unable to write them. The probability of failing to write high anisotropy islands is given by

$$P_w = \frac{1}{2}\left(1 - \text{erf}\left(\frac{H_{\text{eff, max}} - H_{\text{eff,av}}}{\sigma_{H_{\text{eff}}}\sqrt{2}}\right)\right) \tag{6.6}$$

where $H_{\text{eff, max}}$ is the maximum effective head field experienced by islands, $H_{\text{eff, av}}$ is the mean anisotropy field and $\sigma_{H_{\text{eff}}}$ is the standard deviation in anisotropy field. For the system modelled in this study the maximum effective head field experienced by islands is 1.496×10^3 kA/m (18.80 kOe). In a population of islands with mean anisotropy field of 1.204×10^3 kA/m (15.13 kOe) and a 5% standard deviation, the probability of write error according to equation (6.6) is 3.85×10^{-3} giving a total write error probability of $1.012 \times 10^{-17} + 3.85 \times 10^{-3} = 3.85 \times 10^{-3}$ ($\log_{10}(\text{BER}) = -2.415$).

The model of Richter *et al.* (2006b) assumes that any island found within $B/2$ of the write position is correctly written, which could be thought to relate to a timing window equal to the island period. The results shown in Figure 6.11 predict a BER = 0.5 ($\log_{10}(\text{BER}) = -0.301$) for 5% variation in island position

and anisotropy and a timing window equal to the island period, indicating that a more accurate treatment of the head field profile predicts a higher error rate.

If equation (6.5) is modified to assume an error for any island found more than $B/4$ away from the ideal position (which could be thought to relate to a write-window of 50% of the island period), an error rate of 1.087×10^{-5} is predicted. Combining this error rate with the errors due to unwritably high anisotropy islands, Richter's model predicts a total write error rate of 3.861×10^{-3} ($\log_{10}(\text{BER}) = -2.413$) while the prediction of this model from Figure 6.11 is $\log_{10}(\text{BER}) = -3.524$ for a 50% timing window which is a lower error rate.

These two models describe different behaviour. According to Richter *et al.* (2006b), errors arise if islands are moved either physically or by virtue of anisotropy variation beyond $B/2$ from their ideal position, and thus in that model as B is reduced BER increases. In this model the bit length is fixed and timing window is the calculated accuracy that needs to be maintained in write head position (that is down-track servo accuracy) to achieve a given BER, and as timing window narrows (servo accuracy improves), BER decreases. The two error rates computed by these models cannot meaningfully be compared and any similarity between the two error rates calculated above is therefore fortuitous.

Previous work using micromagnetic simulations (Schabes, 2008) considered parallelepiped shaped islands with a 15 nm period along track. The target areal density was 1.3 Tb/in^2. For these islands, with $\sigma_{K_1} = 4\%$, a BER of $10^{-2.5}$ gave a phase margin of ± 3.5 nm. This amounts to a write-window of 7 nm, which is 0.47 of the period. Computation using the statistical write model, with island magnetic and geometric properties similar to those reported by Schabes (2008) but with a different head (Karlqvist type single pole) gave a write-window of 0.60 of the period, which is larger than the value predicted by Schabes (2008). Though the difference in the write-window is only 0.13 of the island period, this arise from a number of factors, primarily the lower head field gradient used by Schabes (2008) and also neglecting magnetostatic interactions in the statistical write model. With the smaller down-track bit separation and the particularly large saturation magnetisation used by Schabes (2008), interactions have a more significant effect than the medium used in this work. In the study by Schabes (2008), variations in saturation magnetisation, exchange constant, and damping were also included but these would have a lesser effect than head field gradient and interaction fields.

6.6 Summary and Conclusions

A computationally efficient statistical write model has been employed to predict the on-track write-window for a given BER in patterned media. The model uses the full head field distribution and thus allows for head field asymmetry and non-linearity in a calculation of write errors without recourse to micromagnetic modelling. This contrasts Richter's model which considers the value and gradient at the write point which effectively assumes the head field to be linear to $\pm B/2$ where B is the bit length. The model predicts the write-error performance of BPM composed of populations of islands with distributions of position, geometric and magnetic parameters, and can be used to calculate the write-window or down-track servo tolerance for given BER.

The model has shown that the smallest attempt frequency gives rise to the largest write-window, although for BER = 10^{-6} or worse the write-window does not depend significantly on attempt frequency or velocity. The model has also predicted that the error rates observed in a drag tester will be similar to a disk drive for error rates greater than about 10^{-6}. The effects of distributions of island position, geometry (shape or size) and magnetic properties have been investigated, and it has been shown that island position/anisotropy distributions have a much more significant effect upon BER than geometric variations.

In the next chapter, two dimensional write simulations are reported where a finite track-width head that varies in two dimensions is employed. This enables a study of Adjacent Track Erasure (ATE) in addition to on-track write errors.

Chapter 7

Two-dimensional write simulations

7.1 Introduction

This chapter presents two-dimensional simulation results based on the model developed in chapters 4 and 5. Finite track-width write heads have a head field distribution that localises the field onto a single track, but the cross-track head field gradient is finite which implies that adjacent tracks experience a finite field. Thus apart from studying write errors that arise if the head is perfectly on-track, it is important to study errors that arise on adjacent tracks as the head deviates off-track.

In order to carry out this analysis, this chapter begins by extending the model to two dimensions. This is followed by a study of on-track errors arising from inadvertently overwriting the previously written island and failing to write the target island as the head deviates off-track. Following this is a study of errors arising from accidentally overwriting islands on adjacent tracks. The combination of on-track and adjacent track errors leads to a total error probability. The impact of distributions of island position and magnetic properties on total errors is also studied.

Some sections of this chapter are taken from the papers included in appendix B. These papers were written by the author of this thesis who carried out all of the model developments and obtained all of the model results described in those papers.

7.2 Extension to two dimensions (2-D)

One-dimensional simulations showed that in order to write a specific target island at an acceptable error rate, there is an optimal down-track head location at which the head field switches the island and a deviation from that position will cause an increase in errors. Similarly, even if the head is perfectly positioned on-track there is a finite probability of accidentally writing islands on adjacent tracks and as the head position deviates off-track, Adjacent Track Erasure (ATE) and the on-track probability of write errors will rise. By modelling these effects the accuracy of two-dimensional servo control that is required in order to achieve a required error rate can be established. Experimental studies of the off-track margin in BPM (Moser *et al.*, 2007) have shown that this is a practical problem and thus a further investigation of parameters limiting this margin is necessary.

A number of theoretical studies on the available timing margin in BPM based on micromagnetic simulations and incorporating distributions in island properties have been reported (Livshitz *et al.*, 2009a,b; Schabes, 2008). Error rates of practical interest are 10^{-4} or below, and to predict timing margins for such low error rates, high precision is required in the down-track direction, which requires many switching calculations. If a micromagnetic model of single island switching is used this will be very slow, the more efficient statistical model developed in chapters 4 and 5 enables timing margins to be more easily calculated for realistic error rates. Thermal activation is included in this model which is missing in the previous literature (Richter *et al.*, 2006b; Livshitz *et al.*, 2009a,b; Schabes, 2008). This is important in ATE where in a realistic system the head field should never be sufficient to switch islands on neighbouring tracks, but where thermal activation may cause infrequent random errors.

The model was thus extended to 2-D in order to include ATE in addition to errors on the main track, and to study the effect of the head position deviating off-track from its ideal location over the island locations. If the head moves slightly off-track due to imperfect head position servo control, the head field experienced by one of the adjacent tracks and the associated probability of errors will rise, but for the other adjacent track the head field and the associated probability of errors will fall. The on-track probability of write errors will also rise. To calculate the error probability, the switching probability of islands was computed as a function of head-island separation in the down-track and cross-track dimensions in the same manner as for the 1-D model but for the two adjacent tracks as well as

on-track islands.

In this study, a finite track-width write head was used with media suitable for 1 Tb/in^2 areal density. The head (see Figure 7.1) was designed for a 4 Tb/in^2 square lattice BPM system. The head had a rectangular main pole of 13 by 40 nm (cross-track × down-track) with pole trailing shield gap of 5 nm and pole side shield gap of 10 nm. The distance from the pole to the top surface of the medium was 5 nm, the medium was 10 nm thick and there was a 2 nm interlayer between the soft underlayer (SUL) and the medium, making a total SUL to pole spacing of 17 nm. The peak perpendicular head field gradients were 34.2 kA/m/nm (430 Oe/nm) down-track and 24.1 kA/m/nm (303 Oe/nm) cross-track (Jinbo and Greaves, 2010). Although the practical fabrication of a head with the dimensions and structure described would be very challenging, a larger pole could not confine the head field sufficiently for recording at this density.

A way to alleviate some head manufacturing challenges is to use a wider pole in staggered BPM where islands are located on a hexagonal lattice. This would require doubling the down-track field gradient but would present severe design problems in down-track pole-shield spacing. An optimal value of the crystalline anisotropy field, $H_K = 875.35$ kA/m (11 kOe), was selected to maximise the effective field gradient from the write head at the write point.

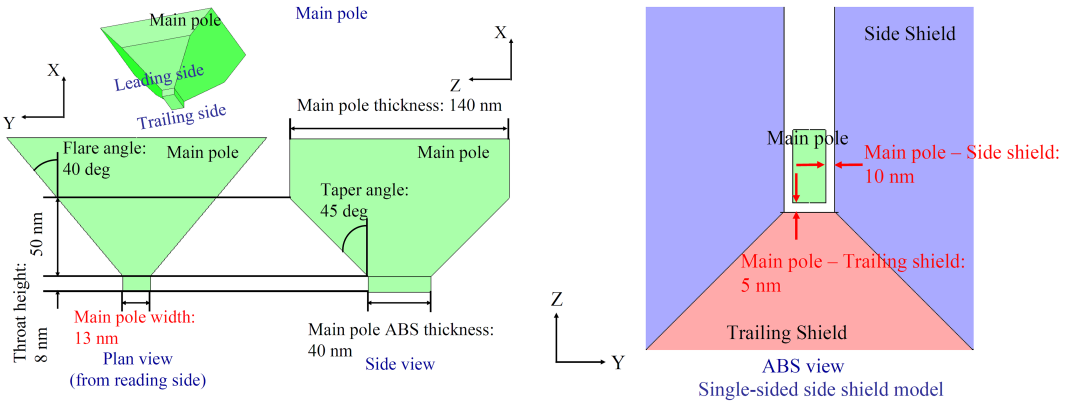

(a) (b)

Figure 7.1: (a) Plan and side view of the design of a 13 by 40 nm rectangular main pole. (b) Air Bearing Surface (ABS) view of the main pole (Jinbo and Greaves, 2010).

A 3-D finite element method (FEM) model of the head field was used in the simulations. The 3-D head field distribution (Jinbo and Greaves, 2010) was

averaged over the island volume to obtain a 2-D field distribution that varies in down and cross-track directions. This 2-D field distribution can be used in the model to obtain the volume averaged field at any island position. A technique to speed up the computation of volume averaging was devised. A normalised 3-D shape function of the island geometry was first generated in *matlab*. For each position along the z-axis (perpendicular), corresponding values of head fields were obtained and a 1-D convolution taken. In principle this is equivalent to averaging the field over the island along the z-axis. Following this, a 2-D convolution of the island cross-section shape function and the previously obtained head field distribution was taken. The result was a volume averaged head field distribution that varies in 2-D. This method is computationally faster than a direct numerical integration of the head field distribution over the island volume for each island position in a plane.

The effective volume averaged head field distribution was obtained as

$$H_{\text{eff}} = \frac{H}{\left(\sin^{\frac{2}{3}}\theta_H + \cos^{\frac{2}{3}}\theta_H\right)^{-\frac{3}{2}}} \tag{7.1}$$

where $H = \sqrt{H_x^2 + H_y^2 + H_z^2}$ is the field magnitude, H_x, H_y, H_z, the volume averaged cartesian field components and $\theta_H = \arccos(H_z/H)$ the polar angle in spherical polar coordinates. Figure 7.2 shows the 2-D effective volume averaged field distribution of this head as obtained from equation (7.1). The centre of the main pole is located at $(300, 300)$. The islands were cylindrical each having a thickness of 10nm and diameter of 13.4 nm.

Single-layer, single-domain islands were assumed, located on a square lattice of 25.4 nm period (1 Tb/in^2) and with $M_s = 700$ kA/m (700 emu/cc) (Greaves *et al.*, 2010), $H_K = 875.35$ kA/m (11 kOe), T =300 K, head velocity =25 m/s and head field rise time = 0.06 ns (Schabes, 2008) where M_s is the saturation magnetisation, H_K is the crystalline anisotropy field and T is the absolute temperature. Using the island dimensions appropriate for 1 Tb/in^2 (cylindrical in shape with height = 10 nm, diameter = 13.4 nm) and the crystalline anisotropy constant, $K_1 = \mu_0 M_s H_K/2 = 3.85 \times 10^5$ J/m^3 (3.85×10^6 erg/cc), this gives a high stability ratio, $K_1 V/k_B T = 131$ where V is the island volume and k_B is the Boltzmann constant.

The volume averaged shape demagnetising factors were computed using a Fourier space method described in section 4.2. The attempt frequency estimated using equation 3.80 for the above magnetic properties and a damping constant

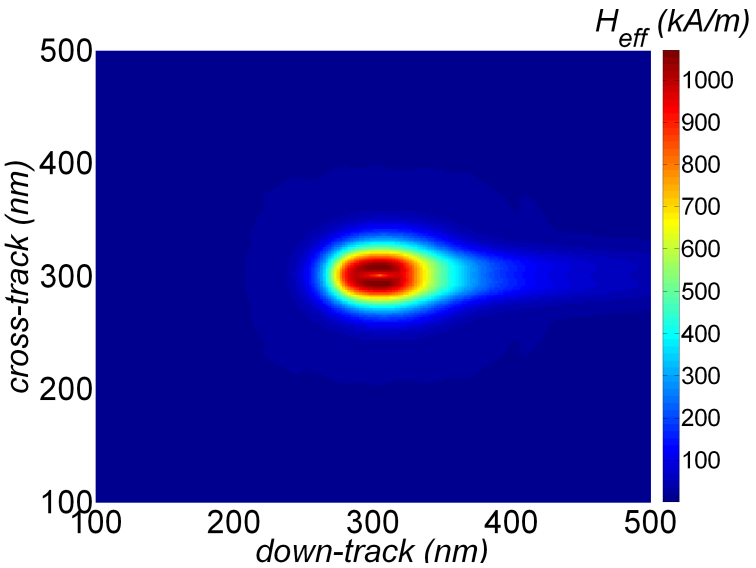

Figure 7.2: Volume averaged 2-D effective head field distribution in kA/m. The centre of the main pole is located at $(300, 300)$.

of 0.1 (Gilbert, 2004) in the absence of an applied field was about 100 GHz.

The interaction fields were calculated using a dipole approximation for a 512×512 array of islands whose magnetisation was randomly up or down. This process was repeated 5000 times for different populations of islands. An exact calculation of magnetostatic interactions (see section 5.5) showed that for island spacing greater than 2 times the island diameter (minimum spacing) the dipole-dipole approximation for the interaction field that was used introduced an error of less than 10%. A histogram plot of the interactions revealed that the interaction field at the centre can be approximated as a Gaussian distribution with a mean of zero and a standard deviation of $1.18\% H_K$. This additional random field was not explicitly included but could be considered to be identical in effect to an additional distribution of anisotropy field (see section 5.5) and would reduce the tolerable anisotropy field distribution accordingly. A study of reversal in non-uniform fields as described in section 4.4 showed that the field required to reverse the island magnetisation in a single spin approximation agreed with micromagnetic simulation results.

7.3 On-track errors

On-track write errors were studied in the same manner as for the 1-D simulations described in chapter 6, where the switching probability of the previously written and target island on the main track was computed for various head switching positions. This process was repeated for a range of off-track head positions to obtain a 2-D switching probability map. Since the head field profile was symmetric in the cross-track direction it was assumed that the resultant error probability map was also symmetric and only half the map was computed to reduce the calculation time. Figure 7.3(a) and 7.3(b) show the 2-D switching probability map on a logarithmic scale for the previously written and target island respectively. The previously written island is located at $(0, 0)$ and the target island is located at $(1, 0)$. The head field is assumed to switch on at the given down-track position and then remain on until $x = \infty$ in the manner of chapter 6.

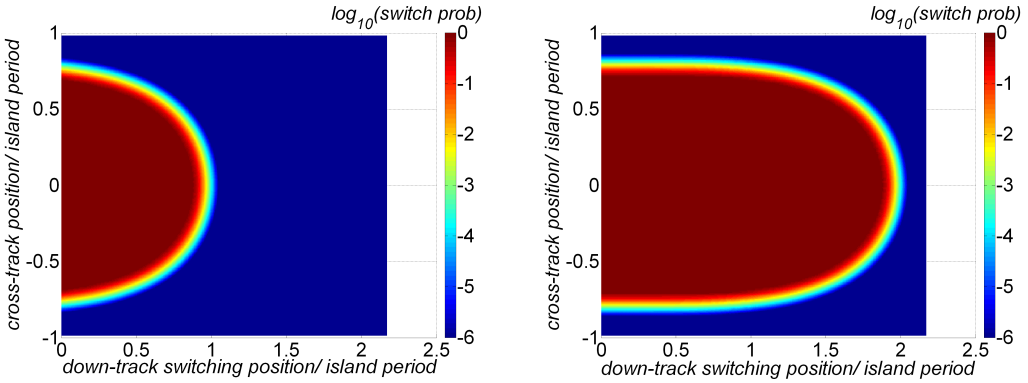

(a) (b)

Figure 7.3: $\log_{10}$(switching probability) as a function of 2-D head field switching position of (a) previously written island located at $(0, 0)$ and (b) target island located at $(1, 0)$.

If the final written states of islands were random and uncorrelated with the intended data pattern, the bit error rate (BER) arising from overwriting the previously written island would be $\text{BER}_{\text{written}} = 0.5p_{\text{written}}$ where p_{written} is the switching probability of previously written island since half the time the island would be overwritten in the correct sense. The BER arising from failing to write the target island is $\text{BER}_{\text{target}} = 0.5(1 - p_{\text{target}})$ where p_{target} is the switching probability of the target island. Figure 7.4(a) and 7.4(b) show the 2-D error rate map for the previously written ($\text{BER}_{\text{written}}$) and target island ($\text{BER}_{\text{target}}$)

respectively. In Figure 7.4(b), the region which appears empty is where the switching probability is unity and so $\mathrm{BER}_{\mathrm{target}} = 0$ and $\log_{10}(0) = -\infty$.

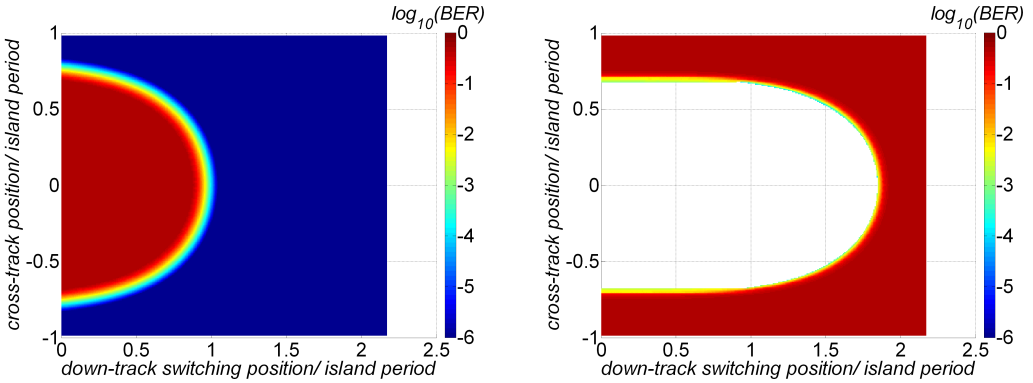

Figure 7.4: $\log_{10}(\mathrm{BER})$ as a function of 2-D head field switching position of (a) previously written island and (b) target island.

The on-track error rate was obtained by summing errors arising from failing to write the target island and errors arising from accidentally writing the previously written island ($\mathrm{BER}_{\text{on-track}} = \mathrm{BER}_{\text{written}} + \mathrm{BER}_{\text{target}}$). Figure 7.5 shows the combined on-track error rate as a 2-D map of the down-track head field switching position and the cross-track position of the head.

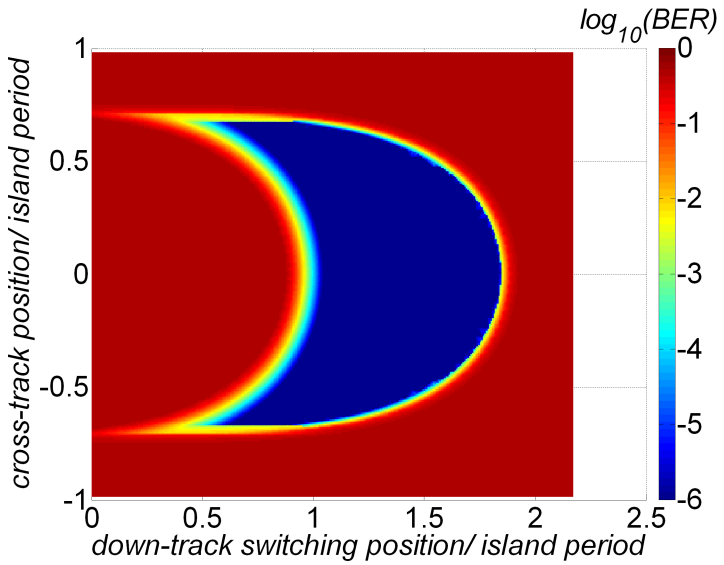

Figure 7.5: $\log_{10}(\mathrm{BER})$ as a function of 2-D head field switching position for on-track errors.

7.4 Adjacent track errors

The study of accidentally overwriting adjacent tracks was carried out by a similar technique to the 1-D model, except that the head field was assumed to be constantly on since the island of interest could be accidentally overwritten by an attempt to write any island on the target track.

If t_N represents the total elapsed time corresponding to N write events, the switching probability, equation (6.1), can be written by splitting the integral into several integrals each representing one write attempt as

$$\begin{aligned} p_{switch}\left(t_N\right) &= 1-\exp\left(-\int_{t'=0}^{t_N}\nu\left(t'\right)\mathrm{d}t'\right) \\ &= 1-\exp\left(-\int_{t'=0}^{t_1}\nu\left(t'\right)\mathrm{d}t'+\int_{t'=t_1}^{t_2}\nu\left(t'\right)\mathrm{d}t'+\ldots+\int_{t'=t_{N-1}}^{t_N}\nu\left(t'\right)\mathrm{d}t'\right). \end{aligned} \tag{7.2}$$

If all single write events in equation (7.2) are identical, the switching probability becomes

$$p_{switch}\left(t_N\right) = 1-\exp\left(-N\int_{t'=0}^{t_1}\nu\left(t'\right)\mathrm{d}t'\right). \tag{7.3}$$

Since the total transition rate, ν, is proportional to the attempt frequency, f_0, equation 7.3 indicates multiple writes can be accommodated by multiplying f_0 by the number of write attempts, N.

In the 1-D model the switching probability involves an integral from the head field switching position to $+\infty$ in the down-track direction, in the 2-D model the integral is from $-\infty$ to $+\infty$. In a real system it could be that the target track is written many times while the data on the adjacent track must be retained.

The probability of inadvertently overwriting any island on either of the adjacent tracks was modelled by assuming that an adjacent track must survive 10^4 writes to the target track, which is obtained by multiplying f_0 by the number of write attempts as shown in equation (7.3). A 2-D probability of switching islands on adjacent tracks was obtained by calculating the probability for a range of cross-track head positions. Because down-track switching position does not affect ATE the probability of error varies only with cross-track head position. Figure 7.6 shows the 2-D probability of inadvertently overwriting adjacent tracks.

The BER associated with accidentally overwriting islands on adjacent tracks was obtained in a manner similar to previously written island, that is $\mathrm{BER}_{\mathrm{ATE}} =$

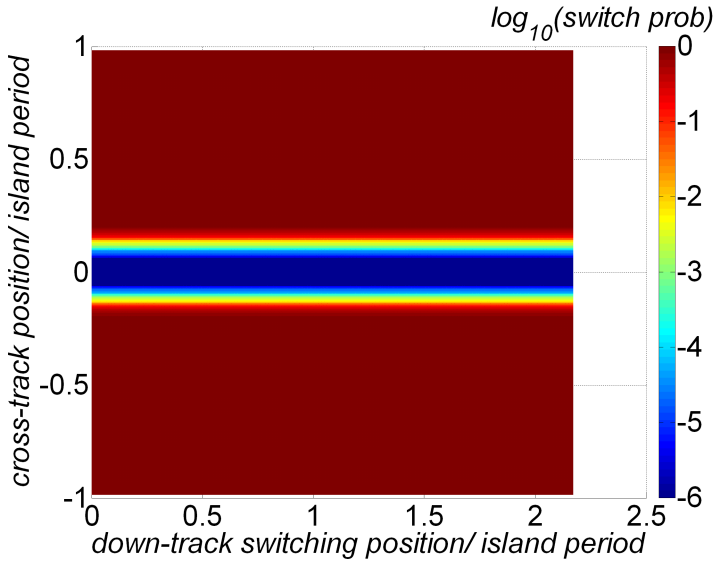

Figure 7.6: $\log_{10}$(switching probability) as a function of 2-D head field switching position for inadvertently overwriting adjacent tracks.

$0.5p_{\mathrm{ATE}}$ where p_{ATE} is the probability of accidentally overwriting islands on the adjacent tracks. This is to account for the fact that the bits can only be 0 or 1 and overwriting may be in the same direction as the intended data for that island with a probability of 0.5.

Figure 7.7 shows a 2-D error rate map of errors arising from ATE for 10^4 write attempts on the target track when any adjacent island can be switched at any down-track head position. Although the cross-track and down-track head field gradients are similar, the cross-track width of the low-error region in the ATE plot (Figure 7.7) is considerably smaller than the down-track length of the low-error region in the on-track error plot (Figure 7.5). This is because there is only one write attempt that may accidentally overwrite the previous island on-track while the adjacent track may be subjected to many writes of the target track. This indicates that for islands on a square lattice, cross-track head field gradient is more important than down-track.

7.5 Total errors

Figure 7.8 shows a 2-D error rate map of total errors. This was obtained from $\mathrm{BER_{total}} = \mathrm{BER_{on\text{-}track}} + \mathrm{BER_{ATE}}$. For a BER of 10^{-4}, Figure 7.8 predicts a down-track margin of 0.85P and a cross-track margin of 0.2P where P=25.4 nm. This

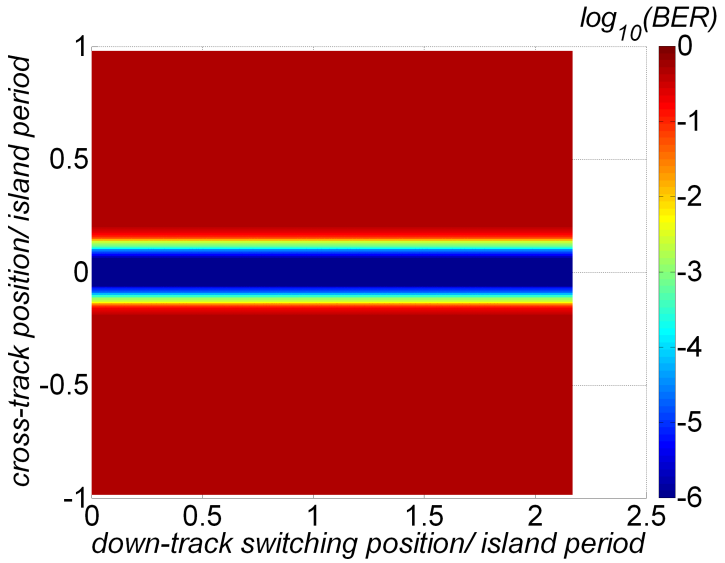

Figure 7.7: $\log_{10}$(BER) as a function of 2-D head field switching position for adjacent track errors.

shows that with this head design, perfectly manufactured single layer BPM at 1Tb/in^2 could give a reasonable down and cross-track servo margin at acceptable error rates.

7.6 Position variations

Islands in BPM may have variations in geometry. A study of island geometry variations described in chapter 6 showed that size and shape variations were less important than position variations. The 2-D switching probability with position variations according to equation (5.32) and assuming a *Gaussian* distribution is given by

$$p^{\text{var}}_{\text{switch}}(\sigma_x, \sigma_y, t) = \frac{\int_{x=-\infty}^{\infty} \int_{y=-\infty}^{\infty} \exp\left(-\frac{(x-\bar{x})^2}{2\sigma_x^2} - \frac{(y-\bar{y})^2}{2\sigma_y^2}\right) p_{\text{switch}}(x, y, t)\text{d}y\text{d}x}{2\pi\sigma_x\sigma_y} \tag{7.4}$$

where x, $\bar{x}$, σ_x represent the island position, expected position and standard deviation in the cross-track direction respectively whereas y, $\bar{y}$, σ_y represent the island position, expected position and standard deviation in the down-track direction. The 2-D switching probability without variations in island properties,

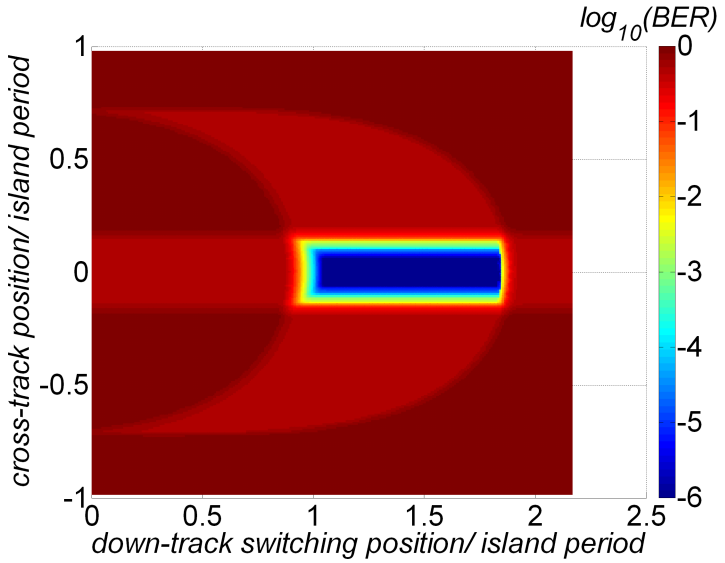

Figure 7.8: $\log_{10}$(BER) as a function of 2-D head field switching position for total errors.

$p_{\text{switch}}(x, y, t)$, is given by

$$p_{\text{switch}}(x, y, t) = 1 - \exp\left(-\int_{t'=0}^{t} \nu\,(x, y, t')\,\mathrm{d}t'\right) \tag{7.5}$$

where t, ν are defined in section 5.3.

In order to speed up the calculation of equation 7.4, the switching probability with down-track position variations for a given head cross-track position and several down-track switching positions were calculated by performing the integral with respect to y in a manner described in section 6.4.1. Cross-track position variations were included by computing the remaining integral numerically.

On-track errors were obtained using a method described in section 7.3 where the switching probabilities with position variations were calculated using equation 7.4. Adjacent track errors were obtained using a method described in section 7.4 where position variations were included. Figure 7.9(a) and 7.9(b) show the 2-D error rate map for on-track errors and adjacent track errors respectively for a 5% standard deviation of both down-track and cross-track position (normalised to the island period of 25.4 nm).

Figure 7.10 shows the combined error rate for the medium studied above, with a 5% standard deviation of both down-track and cross-track position. The performance of the system is significantly degraded compared to Figure 7.8 and

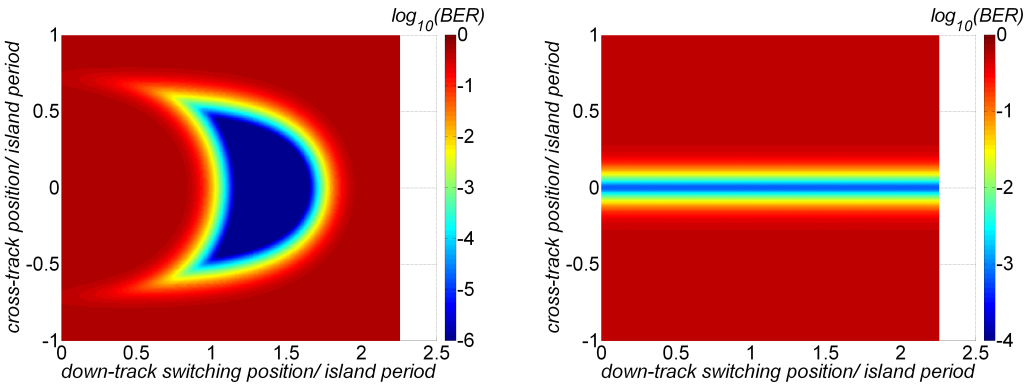

Figure 7.9: $\log_{10}$(BER) as a function of 2D head field switching position of (a) on-track errors and (b) Adjacent track errors. A 5% standard deviation of island position normalised to island period (25.4 nm) in both down and cross-track was applied.

the smallest BER achievable even with perfect positioning is 6.75×10^{-4}.

Although island position variations are random from island to island while servo position errors are (on this length scale) constant, the effects of the two are comparable and to some extent interchangeable so that tighter island position control allows greater position servo tolerance.

7.7 K_1 variations

Islands in BPM also tend to vary in their magnetic properties (Thomson *et al.*, 2006). The switching probabilities with K_1 variations were computed using equation (5.33). On-track errors were obtained using a method described in section 7.3. Adjacent track errors were obtained using a method described in section 7.4 where K_1 variations were included. Figure 7.11(a) and 7.11(b) show the 2-D error rate map for on-track errors and adjacent track errors respectively for a 5% standard deviation of intrinsic (crystalline) anisotropy.

Figure 7.12 shows the combined error rate with a 5% standard deviation in intrinsic (crystalline) anisotropy (K_1). K_1 variations degrade the performance of the system significantly compared to Figure 7.8. However, the impact of K_1 variations is not as severe as that of island position variations at the same fractional standard deviation. For these islands and with this write head, the smallest BER is 8.5×10^{-5}.

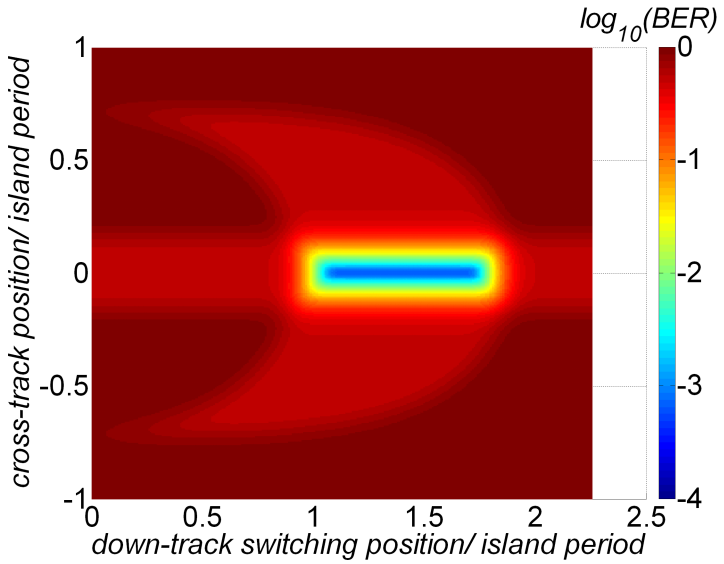

Figure 7.10: $\log_{10}$(BER) as a function of 2D head field switching position (total error). A 5% standard deviation of island position normalised to island period (25.4 nm) in both down and cross-track was applied.

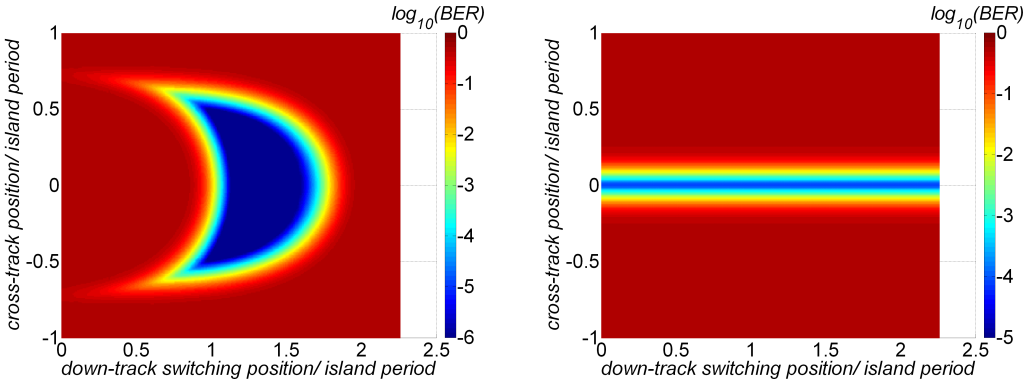

(a) (b)

Figure 7.11: $\log_{10}$(BER) as a function of 2D head field switching position of (a) on-track errors and (b) Adjacent track errors. A 5% standard deviation of intrinsic (crystalline) anisotropy was applied.

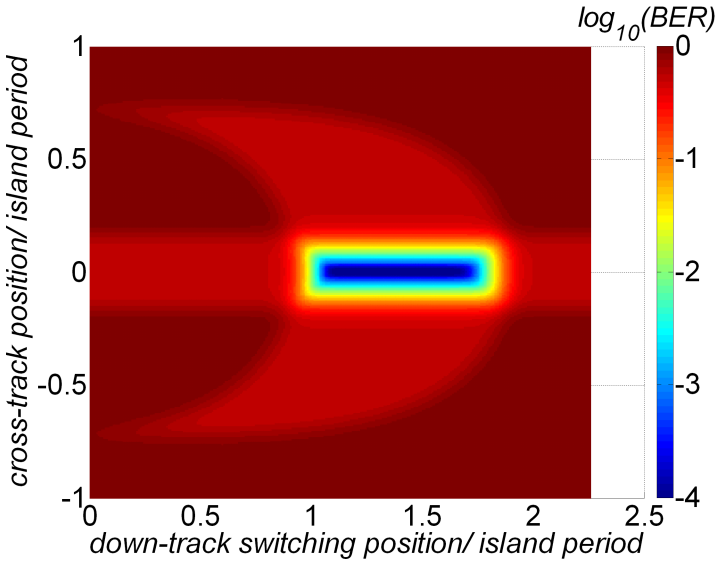

Figure 7.12: $\log_{10}$(BER) as a function of 2D head field switching position (total error). A 5% standard deviation of intrinsic (crystalline) anisotropy was applied.

7.8 Simulations at 4 Tb/in^2

Simulations in 1-D with the same write head were carried out at 4 Tb/in^2 with single-layer, single-domain islands located on a square lattice of 12.7 nm period with medium properties identical to the 1 Tb/in^2 medium above except for island diameter which was reduced to 6.7 nm. Consequently K_1V/k_BT reduced to 32.77 because the volume reduced by a factor of 4. Ideally K_1 would increase as island volume falls, but that requires a larger head field to write and the head used was designed to maximise head field for the given pole area. Higher field (and thus higher K_1) can only be obtained by using a larger pole which will not sufficiently confine the field.

Magnetostatic interactions were computed for randomly (up or down) magnetised islands. Histogram plots for several populations of islands showed that the interaction fields can be approximated by a *Gaussian* distribution having a standard deviation of about 2.5%H_{K} where H_{K} =875.35kA/m (11 kOe). These were neglected in the calculations but would have an effect comparable to anisotropy field distributions of the same magnitude, that is, 2.5%K_1 in Figure 7.13(a). Figure 7.13(a) shows the on-track write-window for various distributions of crystalline anisotropy. Figure 7.13(b) shows the on-track write-window for various distributions of island position.

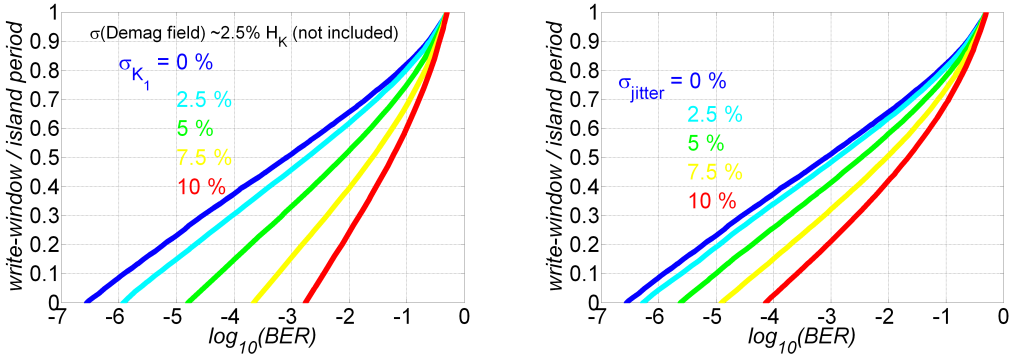

(a) (b)

Figure 7.13: Dependence of write-window on $\log_{10}$(BER) for various standard deviations of (a) K_1 expressed as a percentage of the mean and (b) island position expressed as a percentage of island period.

Figure 7.13(a) shows that at a BER=10^{-4} and 5%K_1 variation a write-window amounting to 15% of island period is obtained. Figure 7.13(b) shows that at a BER=10^{-4} and 5% position variation a write-window amounting to 25% of island period is obtained. The 1-D results suggest that with tight distributions of island parameters, a finite write-window at a BER of 10^{-4} might the achievable. However Figure 7.14 shows the 2-D error rate map arising from ATE for 10^4 write attempts on the target track which shows that with single domain islands written by this head, acceptable error rates could not be achieved at 4 Tb/in^2.

7.9 Summary and Conclusions

A statistical model of write errors in BPM has been applied to calculate the 2-D positional accuracy required to achieve a given error rate. The extension of the model to 2-D enabled a calculation of off-track errors that arise when the head is not perfectly aligned on-track. This also required the study of ATE. The effect of off-track position of the head on on-track and adjacent track errors was studied and it was shown that distributions of island position and anisotropy have a significant impact on the cross-track margin. In a study of ATE, the attempt frequency was shown to play an important role in that the effect of multiple writes on an adjacent track can be accommodated by multiplying the attempt frequency by the number of write attempts.

The inclusion of thermal activation in the model shows that ATE is expected

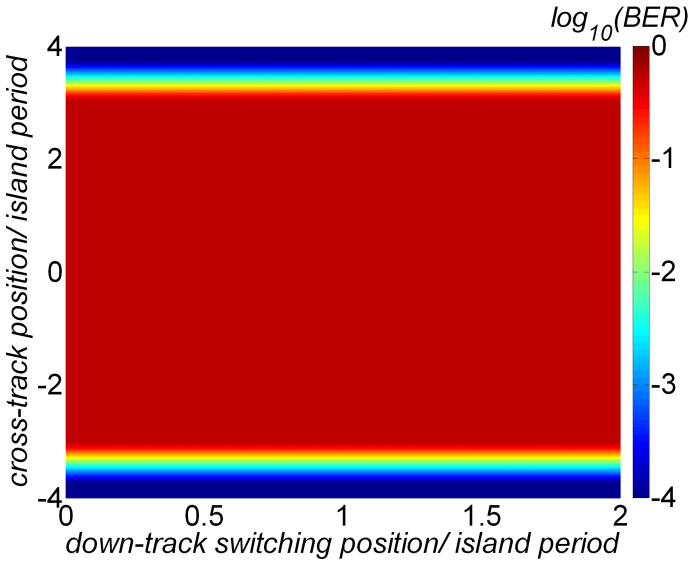

Figure 7.14: $\log_{10}$(BER) as a function of 2-D head field switching position for adjacent track errors at 4Tb/in^2.

to be a severe problem and the risk of large numbers of adjacent track writes implies that cross-track head field gradients need to be very tightly controlled. The results have indicated that with the head design used, a 1 Tb/in^2 system could be possible, provided that the medium had position and switching field distributions of less than 5%. Simulations at 4 Tb/in^2 indicate that BPM with single domain islands could not yield acceptable error rates and at these densities different media types will be required. One likely possibility is Exchange Coupled Composite (ECC) media that was studied in section 5.7.1 which could provide greater thermal stability at the same switching field and thus thermally activated ATE would be reduced.

Chapter 8

Conclusions and Future Work

Life goes on and we will continue muddling through
– Andre K. Geim

This chapter reports the main findings of the research project and possible directions for future work.

8.1 Conclusions

Bit Patterned Media (BPM) is one of the promising approaches to extend magnetic recording densities beyond 1 Tb/in^2 (Albrecht *et al.*, 2009) in that it provides thermal stability (Weller and Moser, 1999; Hughes, 2000) and thereby delays the onset of superparamagnetism (White *et al.*, 1997). In order to study the overall reliability of BPM, simulations of very large numbers of islands would be required. However, this is not practical using normal micromagnetic simulation models because they are time consuming whereas Richter's model (Richter *et al.*, 2006b) is very fast but simple and consequently limited.

A computationally efficient statistical write model that captures the essential features of data storage was therefore developed to study write errors in BPM systems. The model enables realistic servo requirements for practical disk drives using BPM to be established for a given raw BER. The model avoids assumptions of simpler models without resorting to micromagnetic simulations of huge populations of islands. The model uses the full head field distribution and thus allows for head field asymmetry and non-linearity in a calculation of write errors. Distributions of island position, geometric and magnetic parameters that

are thought to be sources of write errors (Richter *et al.*, 2006a,b) were incorporated in the model. This was achieved by convolving the switching probability with a probability distribution function. A method to incorporate magnetostatic interactions was also devised.

In order to study the impact of island geometry variations on the recording performance of BPM systems, the demagnetising factors for a truncated elliptic cone, a generalised geometry that reasonably describe most proposed island shapes, were derived. It was thus demonstrated that the magnetometric demagnetising factors of truncated elliptic cones can be calculated analytically. This enabled a derivation of an analytic model for switching fields for islands having this geometry. The predictions of the analytic model were in excellent agreement with micromagnetic simulation results for island sizes of interest. The model showed that switching fields of islands in BPM are expected to vary less with size but somewhat more with ellipticity and sidewall angle. This suggested that fabrication of vertical sided islands of constant ellipticity is desirable. The model also suggested that using islands with a non 1:1 aspect ratio (BAR $>$ 1) may worsen write errors on adjacent tracks, and that cylindrical islands might therefore be optimal. A method to predict switching fields for non-uniform applied fields was devised and the results were in excellent agreement with micromagnetic simulations.

An analytic expression for the energy barrier of a single domain uniaxial island for magnetisation rotation confined to a plane at any applied field angle was derived. This showed that the energy barrier of a single domain particle for rotation in a plane can be calculated analytically given any vector head field. A method to compute the energy barrier for Exchange Coupled Composite (ECC) media in a two-spin approximation that does not rely on switching fields was also developed. The coercivity results obtained using a two-spin model are in excellent agreement with micromagnetic simulations. This confirms that for this type of ECC island a properly constructed two-spin model is adequate for a calculation of the energy barrier. The results also showed that ECC islands can be designed to switch at a similar field to single domain islands but retain a significant energy barrier in the presence of an external field.

The energy barrier for single domain islands was used in a calculation of transition rates and this led to a derivation of the switching probability that takes into account thermal activation at a given head position. This eventually

developed into an accurate and computationally efficient error model for down-track write errors.

The statistical model was used to study the write-error performance of BPM composed of populations of islands with distributions of position, geometric (shape or size) and magnetic parameters. This was achieved by calculating the write-window or down-track servo tolerance for a given BER. For the 1 Tb/in^2 case considered, at BER = 10^{-6} or worse, the model showed that the write-window does not depend significantly on attempt frequency or velocity. Simulation results also showed that island geometric variations have a less impact than position and anisotropy variations on the write-error performance of a BPM system.

The model was then extended to 2-D in order to calculate off-track errors that arise when the head is not perfectly aligned on-track. This also required the study of Adjacent Track Erasure (ATE). A study of the head off-track position on on-track and adjacent track errors showed that distributions of island position and anisotropy have a significant impact on the cross-track margin. A study of ATE showed that the attempt frequency plays an important role in that the effect of multiple writes on an adjacent track can be accommodated by multiplying the attempt frequency by the number of write attempts. The results also showed that ATE is expected to be a severe problem and to avoid the risk of large numbers of adjacent track writes, cross-track head field gradients need to be more tightly controlled than down-track. Simulation results showed that with the head design used, a 1 Tb/in^2 system could be feasible, provided that the medium had position and switching field distributions of less than 5%. Simulations at 4 Tb/in^2 indicated that BPM with single domain islands could not yield acceptable error rates and at these densities different media types will be required. ECC materials are candidate media which could provide greater thermal stability at the same switching field and thus less thermally activated ATE.

A model of write errors in BPM has thus been developed that avoids the limitations of previous statistical models without requiring the excessive computation of micromagnetic models. This new model has been shown to be capable of determining the 2-D write-window available at a given error rate taking the relevant parameters into account.

8.2 Future work

In order to attain higher recording densities using BPM, one possibility would be to use composite media such as ECC media or exchange spring media. ECC media could provide greater thermal stability at the same switching field compared to single domain islands and thus thermally activated ATE would be reduced. It would be of interest to extend the statistical model in order to study the write-error performance of BPM using ECC type media.

The first step would involve optimising the numerical computation of the energy barriers. This improves the efficiency of computing the switching probabilities. The next task would involve carrying out simulations taking into account variations in position, magnetic properties, and combinations of these at a higher recording density of 4 Tb/in^2. It would be of interest to undertake a comparison of the model predictions to micromagnetic simulation results and experiments.

It would be worth studying the effect of exchange length or domain wall width in ECC to validate the two-spin model. Furthermore, since the model requires an attempt frequency to obtain transition rates, this should be known for ECC islands. The angular dependence of switching fields for ECC looks more like domain wall propagation than Stoner–Wohlfarth astroid and thus it is worth verifying the validity of Brown's model.

In addition, it would be would be of interest if magnetostatic interactions are included explicitly. To first order, these have a similar effect to σ_{H_K} but in practice the actual sequences of binary digits affect the field and thus certain bit patterns will be more or less susceptible to errors.

The magnetostatic interactions should be modified by the effect of the head pole and shields which divert flux away from islands during the write event. In reality a few islands only will contribute but the effect will depend on head position.

Appendix A

Derivations

A.1 Volume of a truncated elliptic cone

The volume of a truncated elliptic cone can be obtained from

$$\begin{aligned} V &= \beta \int_{z=0}^{t} \mathrm{d}z \int_{r=0}^{a(1-z/z_0)} r\mathrm{d}r \int_{\phi=0}^{2\pi} \mathrm{d}\phi \\ &= 2\pi\beta \int_{z=0}^{t} \mathrm{d}z \int_{r=0}^{a(1-z/z_0)} r\mathrm{d}r \\ &= \pi ab \int_{z=0}^{t} (1 - z/z_0)^2 \, \mathrm{d}z \\ &= \frac{\pi abz_0}{3} \left[1 - \left(1 - \frac{t}{z_0} \right)^3 \right] \\ &= \frac{\pi abz_0}{3} \left[1 - \left(\frac{a_t}{a} \right)^3 \right] \\ &= \frac{\pi abt}{3(1 - a_t/a)} \left[1 - \left(\frac{a_t}{a} \right)^3 \right] \\ &= \frac{\pi tab}{3} \left[\left(\frac{a_t}{a} + \frac{1}{2} \right)^2 + \frac{3}{4} \right] \end{aligned} \tag{A.1}$$

where t is the island height and a_t, a, b are defined as shown in Figure 4.1(a).

A.2 Demagnetising factors integrals

Consider the following double integral that appears in equation (4.38)

$$I = \int_{z=0}^{t} \int_{z'=0}^{t} \frac{(1 - z/z_0)(1 - z'/z_0)}{\sqrt{F(z, z', \phi_k, x)}} \mathrm{d}z' \mathrm{d}z \tag{A.2}$$

where

$$\begin{aligned} F(z, z', \phi_k, x) = (z' - z)^2 (\cos^2 \phi_k + \beta^{-2} \sin^2 \phi_k) \\ + a^2((1 - z/z_0)^2 + (1 - z'/z_0)^2) \\ - 2a^2(1 - z/z_0)(1 - z'/z_0) \cos x. \end{aligned}$$

Performing the double integral the result is

$$I = I_1 + I_2 + I_3 + I_4 \tag{A.3}$$

where

$$\begin{aligned} I_1 &= \frac{B}{18A^{3/2}} \left(I_{11} + I_{12} + I_{13}\right) \\ I_2 &= -\frac{B}{18A^{3/2}} \left(I_{21} + I_{22} + I_{23} + I_{24} + I_{25} + I_{26}\right) \\ I_3 &= \frac{1}{6A^{7/2}} \left(I_{31} + I_{32} + I_{33}\right) \\ I_4 &= -\frac{1}{6A^{7/2}} \left(I_{41} + I_{42} + I_{43} + I_{44}\right). \end{aligned}$$

$$\begin{aligned} I_{11} &= 6 \log \left(A + \sqrt{2(A - B)}\sqrt{A} - B\right) \\ &\quad - 6 \log \left(A + \sqrt{A}\sqrt{Ac^2 - 2Bc + A} - Bc\right) c^3 \\ I_{12} &= -2 + 2c^3 - 3(1 - 3(B/A)^2) \log \left(-B + A + \sqrt{A}\sqrt{2(A - B)}\right) \\ &\quad + 3\left(1 - 3(B/A)^2\right) \log \left(-B + Ac + \sqrt{A}\sqrt{Ac^2 - 2Bc + A}\right) \\ I_{13} &= 3(3B + A)\frac{\sqrt{2(A - B)}}{A^{3/2}} - 3(3B + Ac)\frac{\sqrt{Ac^2 - 2Bc + A}}{A^{3/2}} \end{aligned}$$

$$
\begin{aligned}
I_{21} &= -3(1-3(B/A)^2)\log\left(-Bc+A+\sqrt{A}\sqrt{A(c^2+1)-2Bc}\right)c^3\\
I_{22} &= 3(1-3(B/A)^2)\log\left(-Bc+Ac+\sqrt{A}\sqrt{2Ac^2-2Bc^2}\right)c^3\\
I_{23} &= 3(3Bc+A)\frac{c\sqrt{A(c^2+1)-2Bc}}{A^{3/2}}-2\\
I_{24} &= -3(3Bc+Ac)\frac{c\sqrt{2(A-B)c^2}}{A^{3/2}}+2c^3\\
I_{25} &= 6\log\left(Ac-B+\sqrt{A}\sqrt{A(c^2+1)-2Bc}\right)\\
I_{26} &= -6c^3\log\left((A-B)c+\sqrt{A}\sqrt{2(A-B)c^2}\right)
\end{aligned}
$$

$$
\begin{aligned}
I_{31} &= \sqrt{A}\sqrt{2(A-B)}\left(4A^2-BA-3B^2\right)\\
&\quad +3B(A^2-B^2)\log\left(-B+A+\sqrt{A}\sqrt{2(A-B)}\right)\\
I_{32} &= -\sqrt{A}\sqrt{Ac^2-2Bc+A}\left(2(c^2+1)A^2-BAc-3B^2\right)\\
I_{33} &= -3B(A^2-B^2)\log\left(-B+Ac+\sqrt{A}\sqrt{Ac^2-2Bc+A}\right)
\end{aligned}
$$

$$
\begin{aligned}
I_{41} &= 3B(A^2-B^2)\log\left(-Bc+A+\sqrt{A}\sqrt{A(c^2+1)-2Bc}\right)c^3\\
I_{42} &= -3B(A^2-B^2)\log\left((A-B)c+\sqrt{A}\sqrt{2(A-B)c^2}\right)c^3\\
I_{43} &= \sqrt{A}\sqrt{A(c^2+1)-2Bc}\left(2(c^2+1)A^2-BAc-3B^2c^2\right)\\
I_{44} &= -\sqrt{A}\sqrt{2(A-B)c^2}\left(4c^2A^2-BAc^2-3B^2c^2\right)
\end{aligned}
$$

$$
\begin{aligned}
c &= 1-t/z_0\\
A &= (a/z_0)^2+\cos^2\phi_k+\beta^{-2}\sin^2\phi_k\\
B &= (a/z_0)^2\cos x+\cos^2\phi_k+\beta^{-2}\sin^2\phi_k.
\end{aligned}
$$

A.3 Solutions of a quartic equation

Consider a monic quartic

$$x^4+bx^3+cx^2+dx+e=0. \tag{A.4}$$

Equation (A.4) can be cast into a depressed quartic

$$u^4 + \alpha u^2 + \beta u + \gamma = 0 \tag{A.5}$$

provided $x = u - \frac{b}{4}$, $\alpha = -\frac{3b^2}{8} + c$, $\beta = \frac{b^3}{8} - \frac{bc}{2} + d$ and $\gamma = -\frac{3b^4}{256} + \frac{cb^2}{16} - \frac{bd}{4} + e$. To find the roots of equation (A.5) assume

$$u^4 + \alpha u^2 + \beta u + \gamma = \left(u^2 + c_1 u + c_2\right)\left(u^2 + c_3 u + c_4\right). \tag{A.6}$$

Upon expanding the right hand side and equating coefficients of identical powers of u, we observe that

$$c_3 = -c_1 \tag{A.7}$$

$$c_4 = \frac{1}{2}\left[\alpha + c_1^2 + \frac{\beta}{c_1}\right] \tag{A.8}$$

$$c_2 = \frac{1}{2}\left[\alpha + c_1^2 - \frac{\beta}{c_1}\right] \tag{A.9}$$

$$c_2 c_4 = \gamma. \tag{A.10}$$

The coefficients c_2, c_3 and c_4 depend on c_1 and thus c_1 is determined first. Upon equating the product of equation (A.8) and (A.9) to (A.10) and solving for c_1, the result is

$$k^3 + 2\alpha k^2 + \left(\alpha^2 - 4\gamma\right)k - \beta^2 = 0. \tag{A.11}$$

where $k = c_1^2$.

Let $a' = 2\alpha$, $b' = (\alpha^2 - 4\gamma)$, $c' = -\beta^2$, equation (A.11) takes the form

$$k^3 + a'k^2 + b'k + c' = 0. \tag{A.12}$$

Equation (A.12) can be cast into

$$t^3 + pt + q = 0. \tag{A.13}$$

where $k = t - \frac{a'}{3}$, $p = b' - \frac{(a')^2}{3}$ and $q = c' + \frac{2(a')^3 - 9a'b'}{27}$.

Now equation (A.13) has a solution

$$t = v^{1/3} + w^{1/3} \tag{A.14}$$

where $v = -\frac{q}{2} + \sqrt{\frac{q^2}{4} + \frac{p^3}{27}}$ and $w = -\frac{q}{2} - \sqrt{\frac{q^2}{4} + \frac{p^3}{27}}$

This implies that

$$\begin{aligned} k &= t - \frac{a'}{3} \\ &= v^{1/3} + w^{1/3} - \frac{a'}{3} \\ &= \left[-\frac{q}{2} + \sqrt{\frac{q^2}{4} + \frac{p^3}{27}}\right]^{1/3} + \left[-\frac{q}{2} - \sqrt{\frac{q^2}{4} + \frac{p^3}{27}}\right]^{1/3} - \frac{a'}{3} \end{aligned} \tag{A.15}$$

Now, $c_1^2 = k \Rightarrow c_1 = \sqrt{k}$. A negative square root can also be used; the final result is not affected.

From equation (A.6), $(u^2 + c_1 u + c_2)(u^2 - c_1 u + c_4) = 0$ implies that

$$u = \frac{-c_1 \pm \sqrt{c_1^2 - 4c_2}}{2} \qquad \text{or} \qquad u = \frac{c_1 \pm \sqrt{c_1^2 - 4c_4}}{2} \tag{A.16}$$

Therefore, the roots of $x^4 + bx^3 + cx^2 + dx + e = 0$ are

$$x = -\frac{b}{4} + \frac{-c_1 \pm \sqrt{c_1^2 - 4c_2}}{2} \qquad \text{or} \qquad x = -\frac{b}{4} + \frac{c_1 \pm \sqrt{c_1^2 - 4c_4}}{2} \tag{A.17}$$

where

$$\begin{aligned} c_2 &= \frac{1}{2}\left[\alpha + c_1^2 - \frac{\beta}{c_1}\right] \\ c_4 &= \frac{1}{2}\left[\alpha + c_1^2 + \frac{\beta}{c_1}\right] \\ c_1 &= \sqrt{\left[-\frac{q}{2} + \sqrt{\frac{q^2}{4} + \frac{p^3}{27}}\right]^{1/3} + \left[-\frac{q}{2} - \sqrt{\frac{q^2}{4} + \frac{p^3}{27}}\right]^{1/3} - \frac{2\alpha}{3}} \\ p &= \alpha^2 - 4\gamma - \frac{4\alpha^2}{3} \\ q &= -\beta^2 + \frac{16\alpha^3 - 18\alpha(\alpha^2 - 4\gamma)}{27} \\ \alpha &= -\frac{3b^2}{8} + c \\ \beta &= \frac{b^3}{8} - \frac{bc}{2} + d \\ \gamma &= -\frac{3b^4}{256} + \frac{cb^2}{16} - \frac{bd}{4} + e. \end{aligned}$$

Appendix B

Publications

- Poster presentation *Dependence of Switching Fields on Island Shape in Bit Patterned Media* at InterMag conference in Sacramento, California, USA in May 2009
- Poster presentation *Dependence of Write-Window on Write Error Rates in Bit Patterned Media* at InterMag/MMM joint conference in Washington, DC, USA in January 2010
- Poster presentation *Analysis of write-head synchronization and Adjacent Track Erasure in Bit Patterned Media using a Statistical Model* at MMM joint conference in Atlanta, Georgia, USA in November 2010
- Paper titled *Dependence of Switching Fields on Island Shape in Bit Patterned Media* was published as a Journal paper in IEEE Transactions on Magnetics in October 2009
- Paper titled *Dependence of Write-Window on Write Error Rates in Bit Patterned Media* was published as a regular Journal paper in IEEE Transactions on Magnetics in October 2010
- Paper titled *Analysis of write-head synchronization and Adjacent Track Erasure in Bit Patterned Media using a Statistical Model* was published as a Journal paper in Journal of Applied Physics in April 2011

IEEE TRANSACTIONS ON MAGNETICS, VOL. 45, NO. 10, OCTOBER 2009 3531

Dependence of Switching Fields on Island Shape in Bit Patterned Media

Josephat Kalezhi[1,2], Jim J. Miles[1], and Branson D. Belle[1]

[1]School of Computer Science,University of Manchester, Manchester M13 9PL, U.K.
[2]Computer Science Department, School of Technology, Copperbelt University, Kitwe 10101, Zambia

Nanofabricated islands in bit patterned media (BPM) for magnetic data storage tend to vary in shape, size, and material properties which leads to variations in switching fields, causing write errors. In a working system, write errors will be rare, and therefore, an efficient analytic model is preferable to a micromagnetic model. An analytic model has been developed that calculates magnetometric (volume averaged) demagnetizing factors and predicts switching fields for different island shapes, particularly islands that can be described as truncated elliptic cones, since variants of this geometry can represent real islands. The model has been shown to agree well with micromagnetic simulations for various island shapes with fields at various angles to the perpendicular. Switching field calculations reveal that 4 : 1 aspect ratio islands may be more prone to adjacent track erasure compared to those with lower aspect ratios and that islands with slanted side walls were easier to reverse compared to cylindrical ones.

Index Terms—**Bit patterned media (BPM), magnetic recording, magnetometric demagnetizing factors, shape demagnetizing factors, switching field distribution (SFD).**

I. Introduction

BIT PATTERNED MEDIA (BPM), in which the medium is patterned into nanometer-sized magnetic islands where each stores one bit, is a promising candidate for areal densities beyond 1 Tb/in^2 [1], [2]. Due to the tolerances associated with fabrication, islands vary in shape, size, position, and material properties. These variations will have a detrimental effect on the replay performance of the read channel [3] and the resulting switching field distribution (SFD) will cause write errors [2]. An understanding of the origins of the SFD is required to minimize write errors. If write errors are relatively rare events, their prediction requires the simulation of very large numbers of write events using necessarily simple but realistic models. An analytic model has been developed that efficiently calculates magnetometric (shape) demagnetizing factors for realistic island geometries, and thus, generates switching fields. This analytic model enables the distribution of switching fields due to size, shape, and position to be calculated and will enable write error rates to be predicted. In order to validate the analytic model, a micromagnetic simulation package, *magpar* [4], was used for comparative simulations, with island geometries generated using *netgen* [5].

II. Analytic Model

A. Magnetometric Demagnetizing Factors of an Arbitrary Truncated Elliptic Cone

An arbitrary truncated elliptic cone geometry was selected because it resembles the CoPt multilayer islands described in [6] and [7], and as a generalized geometry it will satisfactorily describe most proposed island shapes. Fig. 1 shows the parameters that describe this geometry. This covers shapes from elliptic cones through elliptic cylinders to circular cylinders.

Manuscript received March 06, 2009. Current version published September 18, 2009. Corresponding author: J. Kalezhi (e-mail: kalezhij@cs.man.ac.uk).
Digital Object Identifier 10.1109/TMAG.2009.2022407

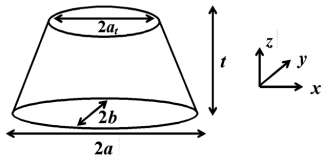

Fig. 1. Geometry of the truncated elliptic cone with parameters that describe it.

To calculate the magnetometric (volume averaged) demagnetizing factors, the magnetization has been assumed to be uniform throughout the island.

The demagnetizing field of a uniformly magnetized truncated elliptic cone is nonuniform implying that the demagnetizing factors vary with position. Therefore, it is necessary to calculate the volume average of these factors over the island in order to determine the magnetostatic self energy.

The computation of magnetometric demagnetizing factors for arbitrary truncated elliptic cones has not been previously published, so integral equations to compute them for this particular shape were determined using the Fourier transform approach. This approach was proposed by Beleggia *et al.* [8] and their method was adopted. According to [8], the magnetometric demagnetizing factors N can be obtained from the integral

$$N_{x_i x_j} = \frac{1}{(2\pi)^3 V} \int \frac{|\rho(\vec{k})|^2}{k^2} k_i k_j d^3\vec{k} \tag{1}$$

which is carried out in Fourier space where $\vec{k}$ is the wave vector, V is the volume, $x_1 = x, x_2 = y, x_3 = z$, and ρ is the shape amplitude to be determined [8]–[10] from the integral

$$\rho(\vec{k}) = \int_{\text{body}} e^{-i\vec{k}\bullet\vec{r}} d^3\vec{r}. \tag{2}$$

The equation describing the surface of the arbitrary truncated elliptic cone of Fig. 1 is

$$x^2/a^2 + y^2/b^2 = (1 - z/z_0)^2 \tag{3}$$

where $z_0 = t/(1 - a_t/a), 0 \leq z \leq t, t \leq z_0, -a \leq x \leq a, -b \leq y \leq b, \beta = b/a$.

Using cylindrical coordinates as indicated in [9], the shape amplitude takes the form

$$\rho(\vec{k}) = \beta \int_{z=0}^{t} e^{-ik_z z} dz \int_{r=0}^{a(1-z/z_0)} r dr \times \int_{\phi=0}^{2\pi} e^{-irk_\rho \cos(\phi_k - \phi)} d\phi. \quad (4)$$

Upon performing the angular followed by radial integration, (4) evaluates to

$$\rho(\vec{k}) = \frac{2\pi b}{k_\rho} \int_{z=0}^{t} (1 - z/z_0) J_1(k_\rho a(1 - z/z_0)) e^{-ik_z z} dz \quad (5)$$

where $J_1(z)$ is a *Bessel* function of the first kind.

The integral in (5) is an *incomplete Lipschitz–Hankel* type which is nontrivial to evaluate. Closed-form solutions for *Lipschitz–Hankel* integrals can be expressed in terms of *Kampe de Feriet double hypergeometric* functions [11]. The numerical computation of these integrals can be found in [12].

Equation (1) has to be expressed in cylindrical coordinates before inserting the square modulus of the shape amplitude. According to [9], this becomes

$$N_{x_i x_j} = \frac{1}{(2\pi)^3 V\beta} \int_{k_z=-\infty}^{\infty} dk_z \int_{k_\rho=0}^{\infty} |\rho(k_\rho, k_z)|^2 k_\rho dk_\rho \times \int_{\phi_k=0}^{2\pi} \frac{k_i k_j d\phi_k}{k_\rho^2(\cos^2\phi_k + \beta^{-2}\sin^2\phi_k) + k_z^2} \quad (6)$$

$$k_1 = k_x = k_\rho \cos\phi_k$$
$$k_2 = k_y = \beta^{-1} k_\rho \sin\phi_k$$
$$k_3 = k_z.$$

From (6), it can be shown, without difficulty, that if $i \neq j$, the angular integration vanishes. This being the case, we are only left with $Nx_1x_1 = N_{xx}$, $Nx_2x_2 = N_{yy}$, and $Nx_3x_3 = N_{zz}$. Therefore

$$N_{x_i x_i} = \frac{1}{(2\pi)^3 V\beta} \int_{k_z=-\infty}^{\infty} dk_z \int_{k_\rho=0}^{\infty} |\rho(k_\rho, k_z)|^2 k_\rho dk_\rho \times \int_{\phi_k=0}^{2\pi} \frac{k_i^2 d\phi_k}{k_\rho^2(\cos^2\phi_k + \beta^{-2}\sin^2\phi_k) + k_z^2}. \quad (7)$$

As can be seen from (5), since the shape amplitude does not depend on the azimuthal angle, the angular integral in (7) can be evaluated analytically. The magnetometric demagnetizing factors can then be obtained by numerically performing the remaining double integral provided the value for the shape amplitude at all values of k_ρ and k_z is known.

The approach taken in this paper was not to evaluate the angular integral but instead express the square modulus of the shape amplitude as a double integral as shown in

$$|\rho(k_\rho, k_z)|^2 = \left[\frac{2\pi b}{k_\rho}\right]^2 \int_{z=0}^{t} \int_{z'=0}^{t} \left[1 - \frac{z}{z_0}\right] \left[1 - \frac{z'}{z_0}\right] \times J_1[k_\rho a(1 - z/z_0)] J_1 \times [k_\rho a(1 - z'/z_0)] e^{ik_z(z-z')} dz dz'. \quad (8)$$

Substituting (8) for square modulus of shape amplitude into (7) and after some simplifications, the result is

$$N_{x_i x_i} = \frac{ab}{2\pi V} \int_{z=0}^{t} \int_{z'=0}^{t} \left[1 - \frac{z}{z_0}\right] \left[1 - \frac{z'}{z_0}\right] dz dz' \times \int_{k_z=-\infty}^{\infty} e^{ik_z(z-z')} dk_z \times \int_{k_\rho=0}^{\infty} \frac{J_1[k_\rho a(1 - z/z_0)] J_1[k_\rho a(1 - z'/z_0)]}{k_\rho} k_\rho dk_\rho \times \int_{\phi_k=0}^{2\pi} \frac{k_i^2 d\phi_k}{k_\rho^2(\cos^2\phi_k + \beta^{-2}\sin^2\phi_k) + k_z^2}. \quad (9)$$

Considering N_{xx} first and reordering the integrals

$$N_{xx} = \frac{ab}{2\pi V} \int_{z=0}^{t} \int_{z'=0}^{t} \left[1 - \frac{z}{z_0}\right] \left[1 - \frac{z'}{z_0}\right] dz dz' \times \int_{\phi_k=0}^{2\pi} \cos^2\phi_k d\phi_k \int_{k_z=-\infty}^{\infty} e^{ik_z(z-z')} dk_z \times \int_{k_\rho=0}^{\infty} \frac{k_\rho J_1[k_\rho a(1 - z/z_0)] J_1[k_\rho a(1 - z'/z_0)]}{k_\rho^2(\cos^2\phi_k + \beta^{-2}\sin^2\phi_k) + k_z^2} dk_\rho. \quad (10)$$

The integral over k_ρ which involves a product of two *Bessel* functions of the first kind can be evaluated using the standard integral [13] to yield a product of *modified Bessel* functions of first and second kind. After substituting the expression for this integral, the integral over k_z can then be performed using another standard integral [13] to yield an *associated Legendre* polynomial. Substituting an integral form for the *associated Legendre* polynomial [13], and after simplifications, (10) becomes

$$N_{xx} = \frac{ab}{2\pi V} \int_{x=0}^{\pi} \cos x dx \int_{\phi_k=0}^{2\pi} \frac{\cos^2\phi_k}{\sqrt{\cos^2\phi_k + \beta^{-2}\sin^2\phi_k}} d\phi_k \times \int_{z=0}^{t} \int_{z'=0}^{t} \frac{(1 - z/z_0)(1 - z'/z_0) dz dz'}{\sqrt{F(z, z', \phi_k, x)}} \quad (11)$$

where

$$F(z, z', \phi_k, x) = (z' - z)^2(\cos^2\phi_k + \beta^{-2}\sin^2\phi_k) + a^2((1 - z/z_0)^2 + (1 - z'/z_0)^2) - 2a^2(1 - z/z_0)(1 - z'/z_0)\cos x.$$

Similarly

$$N_{yy} = \frac{ab}{2\pi V\beta^2} \int_{x=0}^{\pi} \cos x dx \int_{\phi_k=0}^{2\pi} \frac{\sin^2\phi_k}{\sqrt{\cos^2\phi_k + \beta^{-2}\sin^2\phi_k}} d\phi_k \times \int_{z=0}^{t} \int_{z'=0}^{t} \frac{(1 - z/z_0)(1 - z'/z_0) dz dz'}{\sqrt{F(z, z', \phi_k, x)}} \quad (12)$$

and $N_{zz} = 1 - N_{xx} - N_{yy}$.

The integrals over z followed by z' can be performed easily. For $\beta = 1$, the integral over the azimuthal is trivial, otherwise the remaining double integral can be computed numerically. The advantage of this approach is that it is computationally faster than a method where the shape amplitude is first computed for any wave vector and the square modulus substituted in the integrals as explained previously.

B. Switching Field for an Arbitrary Truncated Elliptic Cone

The analytic model for switching fields assumes coherent reversal and incorporates magnetometric demagnetizing factors. The starting point is the magnetostatic self energy of a ferromagnetic particle. This is expressed as [14]

$$E_d = -(\mu_0/2)\int \vec{M}\cdot\vec{H}_d d\tau \tag{13}$$

where $\vec{M}$ is the magnetization and $\vec{H}_d$ the self-demagnetizing field. The self-demagnetizing field can be written as

$$\vec{H}_d = -\vec{N}\cdot\vec{M} \tag{14}$$

where $\vec{N}$ is the demagnetizing factor tensor which depends on particle shape. The magnetometric demagnetizing factors are the volume average of the demagnetizing factors.

The magnetization components expressed in spherical polar coordinates are

$$\begin{aligned} M_x &= M_s\sin\theta\cos\phi, M_y = M_s\sin\theta\sin\phi \\ M_z &= M_s\cos\theta \end{aligned} \tag{15}$$

where M_s is the saturation magnetization of the particle.

Substituting (14) into the magnetostatic self energy, (13) and using (15), the energy takes the form

$$E_d = \frac{\mu_0 V M_s^2}{2}[N_1(\phi)\sin^2\theta + N_2(\phi)\sin\theta\cos\theta + N_{zz}] \tag{16}$$

where V is the volume

$$\begin{aligned} N_1(\phi) &= N_{xx}\cos^2\phi + N_{yy}\sin^2\phi + 2N_{xy}\sin\phi\cos\phi - N_{zz} \\ N_2(\phi) &= 2(N_{yz}\sin\phi + 2N_{xz}\cos\phi). \end{aligned}$$

The cross terms N_{xy}, N_{yz} and N_{xz} vanish for arbitrary truncated elliptic cones according to (6). In this case, the contribution to the total energy due to shape anisotropy, crystalline uniaxial anisotropy K_1 (assumed to be along the z direction), and the external field H ignoring constant terms becomes

$$\begin{aligned} E_{\rm tot} = &\left[K_1 + \frac{\mu_0 M_s^2}{2}N_1(\phi)\right] V\sin^2\theta \\ &- \mu_0 M_s V H(\sin\theta_H\sin\theta\cos(\phi_H - \phi) + \cos\theta_H\cos\theta) \end{aligned} \tag{17}$$

where θ_H, ϕ_H are the applied field polar and azimuthal angles, respectively. Minimization of (17) with respect to ϕ reveals that $\phi = \phi_H$ when $N_{xx} = N_{yy}$, or $\phi_H = \pi/2$ or $\phi_H = 0$. For these cases, the magnetization always lies in the plane formed by the anisotropy and external field. In the general case, the magnetization azimuthal angle is coupled to its polar angle which implies that the rotation is not confined to a plane.

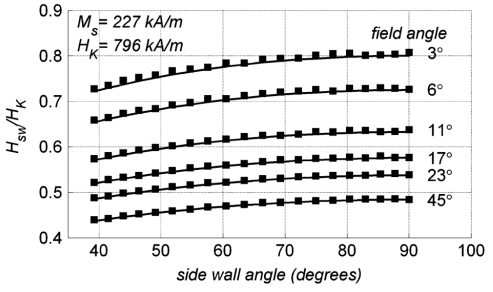

Fig. 2. Effect on switching field $H_{\rm sw}$ of a varying sidewall angle for different applied field angles. $H_K = 2\ {\rm K}_1/\mu_0 M_s$. The largest sidewall angle (90°) corresponds to a cylinder. Continuous lines in all diagrams represent the analytic model and markers, *magpar* results.

For reversal in a plane, the dependence of the switching field on island shape can be deduced from (17) and is given by

$$H_{\rm sw} = H_K^{\rm eff}[\cos^{2/3}\theta_H + \sin^{2/3}\theta_H]^{-3/2} \tag{18}$$

where

$$H_K^{\rm eff} = \frac{2K_1}{\mu_0 M_s} + M_s[N_{xx}(1+\cos^2\phi_H) + N_{yy}(1+\sin^2\phi_H) - 1].$$

III. Results

A. Island Sidewall Angle Variations

The dependence of switching field on island sidewall angle was studied for applied fields at various angles to the perpendicular. The saturation magnetization M_s was 227 kA/m, the uniaxial anisotropy constant K_1 was 1.134×10^5 J/m^3 [6], and the exchange constant A was 1×10^{-11} J/m. The island volume (height = 25 nm, $a = b = 25$ nm), ellipticity ($e = b/a = 1$) were kept constant with initial side wall angle of 39° reference to the x–y plane as sidewall angle was varied to 90°.

Fig. 2 shows the dependence of switching field on island sidewall angle.

For islands of the same volume and height, a truncated cone can be more easily switched than a cylinder. The agreement between the analytic model and the micromagnetic model shows that where islands are small enough that exchange coupling keeps the magnetization uniform, the effects of the nonuniform fields generated by the shape are captured by a uniform rotation model in which the magnetometric demagnetization factors are correctly computed.

B. Island Aspect Ratio Variations

The island volume, height, and sidewall angle were kept constant as ellipticity was varied to cover aspect ratios in the range 1 : 1 to 4 : 1. The volume, height, and magnetic properties were the same as for the sidewall angle calculations. The islands were elongated in the x-axis so that $a >= b$ always, but fields were applied in the x–z or the y–z plane. For fields in the x–z plane ellipticity was defined as $e = b/a$, while for fields in the y–z plane the ellipticity was defined as a/b. With uniform applied fields, the switching fields of islands were seen to follow the

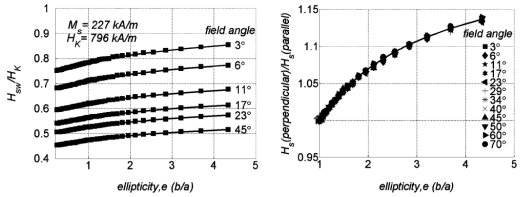

Fig. 3. (a) Dependence of switching field $H_{\rm sw}$ on island ellipticity for applied field polar angles between 3° and 45°. (b) Dependence of switching field ratios on island ellipticity for various field angles.

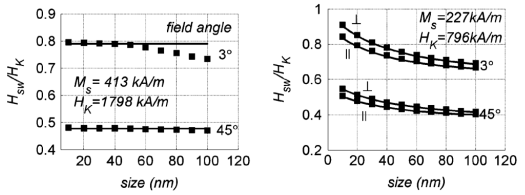

Fig. 4. (a) Dependence of switching field on island size (circular base). (b) Dependence of switching field on island size with height, ellipticity, a_t/a fixed, and applied field perpendicular ($\perp$) and parallel ($\|$) to the z–x plane at field angles 3° and 45° to the perpendicular.

Stoner–Wohlfarth astroid despite the nonuniform internal fields. Fig. 3(a) displays the dependence of switching fields on e. A larger applied field is required to switch the island in the y–z plane compared to x–z plane. Fig. 3(b) displays the ratio of switching field in the y–z plane to that in the x–z plane as a function of e. The ratio is insensitive to the applied field angle and shows that as ellipticity increases it becomes harder to switch with a field applied across the short axis than down the long axis, even for out of plane fields, regardless of the angle of the field to the perpendicular. Thus, for BPM with a bit aspect ratio (BAR) of >1 (wider cross-track than down-track) it will become harder to switch down-track and easier to switch cross-track as BAR is increased. This result means that writing the on-track islands will become harder and overwriting islands on adjacent tracks will become more likely as BAR is increased.

C. Island Size Variations

Fig. 4(a) displays the dependence of switching fields for various island sizes with shape kept the same (an elliptic cone with circular base and sidewall angle of 63°).

It is evident that the analytic model predicts a switching field in agreement with micromagnetic models for small islands. When the island diameter increases above 50 nm, the micromagnetic model predictions diverge from the analytical model, which occurs when nonuniform reversal modes become possible. For island sizes at which BPM is likely to be used, switching fields do not vary much with size and the analytic model is in excellent agreement with the micromagnetic model. In Fig. 4(b), the island thickness (10 nm), ellipticity ($a = 2b$), and a_t/a was kept constant, while size a was varied. However, with constant thickness, the analytic model agrees with simulations even for larger sizes.

IV. Conclusion

We have demonstrated that magnetometric demagnetizing factors of arbitrary truncated elliptic cones can be calculated analytically and that switching fields for islands in BPM can thereby be predicted using an analytic model, with results that are in excellent agreement with micromagnetic simulations. The switching fields of islands in BPM are predicted to vary little with size, but somewhat more with ellipticity and sidewall angle, suggesting that fabrication of vertical sided islands of constant ellipticity is desirable. The model suggests that using islands with a non $1:1$ aspect ratio (BAR $>$ 1) may worsen write errors on adjacent tracks, and that cylindrical islands might therefore be optimal. The analytic model forms an excellent basis for future work to characterize the statistics of write errors due to its high efficiency compared to micromagnetic simulations.

Acknowledgment

This work was supported by EPSRC under Grant EP/E017657/1.

References

[1] D. Weller and A. Moser, "Thermal effect limits in ultrahigh-density magnetic recording," *IEEE Trans. Magn.*, vol. 35, pp. 4423–4439, Nov. 1999.

[2] H. J. Richter, A. Y. Dobin, O. Heinonen, K. Z. Gao, R. J. M. v. d. Veerdonk, R. T. Lynch, J. Xue, D. Weller, P. Asselin, M. F. Erden, and R. M. Brockie, "Recording on BPM at densities of 1 Tb/in^2 and beyond," *IEEE Trans. Magn.*, vol. 42, pp. 2255–2260, Oct. 2006.

[3] P. W. Nutter, S. Yuanjing, B. D. Belle, and J. J. Miles, "Understanding sources of errors in BPM to improve read channel performance," *IEEE Trans. Magn.*, vol. 44, pp. 3797–3800, Nov. 2008.

[4] W. Scholz, J. Fidler, T. Schrefl, D. Suess, R. Dittrich, H. Forster, and V. Tsiantos, "Scalable parallel micromagnetic solvers for magnetic nanostructures," *Comput. Mater. Sci.*, vol. 28, pp. 366–383, Oct. 2003.

[5] J. Schöberl, "NETGEN An advancing front 2D/3D-mesh generator based on abstract rules," *Comput. Visual. Sci.*, vol. 1, pp. 41–52, July 1997.

[6] B. D. Belle, F. Schedin, T. V. Ashworth, P. W. Nutter, E. W. Hill, H. J. Hug, and J. J. Miles, "Temperature dependent remanence loops of ion-milled BPM," *IEEE Trans. Magn.*, vol. 44, pp. 3468–3471, Nov. 2008.

[7] B. D. Belle, F. Schedin, N. Pilet, T. V. Ashworth, E. W. Hill, P. W. Nutter, H. J. Hug, and J. J. Miles, "High resolution magnetic force microscopy study of e-beam lithography patterned Co/Pt nanodots," *J. Appl. Phys.*, vol. 101, May 2007, 09F517.

[8] M. Beleggia and M. De Graef, "On the computation of the demagnetization tensor field for an arbitrary particle shape using a Fourier space approach," *J. Magn. Magn. Mater.*, vol. 263, pp. L1–L9, Jul. 2003.

[9] M. Beleggia, M. De Graef, Y. T. Millev, D. A. Goode, and G. Rowlands, "Demagnetization factors for elliptic cylinders," *J. Phys. D, Appl. Phys.*, vol. 38, pp. 3333–3342, Sep. 2005.

[10] S. Tandon, M. Beleggia, Y. Zhu, and M. De Graef, "On the computation of the demagnetization tensor for uniformly magnetized particles of arbitrary shape. Part I: Analytical approach," *J. Magn. Magn. Mater.*, vol. 271, pp. 9–26, Apr. 2004.

[11] A. R. Miller, *An Incomplete Lipschitz-Hankel Integral of K0. Part 1*. Washington, DC: Naval Research Laboratory, 1986.

[12] S. L. Dvorak and E. F. Kuester, "Numerical computation of the incomplete Lipschitz-Hankel integral Je$_0$ (a, z)," *J. Comput. Phys.*, vol. 87, pp. 301–327, Apr. 1990.

[13] I. S. Gradshteyn and I. M. Ryzhik, *Tables of Integrals, Series and Products*, 5th ed. New York: Academic, 1994.

[14] A. Aharoni, *Introduction to the Theory of Ferromagnetism*, J. Birman, Ed. *et al.* Oxford, U.K.: Oxford Univ. Press, 2000, pp. 109–132.

3752 IEEE TRANSACTIONS ON MAGNETICS, VOL. 46, NO. 10, OCTOBER 2010

Dependence of Write-Window on Write Error Rates in Bit Patterned Media

Josephat Kalezhi[1,2], Branson D. Belle[1], and Jim J. Miles[1]

[1]School of Computer Science, The University of Manchester, Manchester M13 9PL, U.K.
[2]Computer Science Department, School of Technology, Copperbelt University, Kitwe 10101, Zambia

In bit patterned media (BPM), the medium is patterned into nanometer-sized magnetic islands where each island stores one bit. Although BPM samples of credible densities have been made, many problems remain, one of which is the synchronization of the write head switching position with respect to the targeted island. An accurate but efficient model has been developed to calculate the timing margin available for a given required write bit error rate (BER). The model predicts the write-error performance of BPM composed of populations of islands with distributions of magnetic, position, and geometric parameters, and can be used to calculate the write-window for a given BER. The effect of distributions of island position, geometric and magnetic properties has been investigated, and it has been shown that island position and magnetic properties have a much more significant effect upon BER than geometric (shape/size) variations. This model enables the relationship between servo requirements and raw BER to be established for disk drives using BPM.

Index Terms—**Bit error rate (BER), bit patterned media (BPM), magnetic recording, write-window.**

I. Introduction

In bit patterned media (BPM), the medium is patterned into nanometer-sized magnetic islands where each island stores one bit. Although BPM samples of credible densities have been made, many problems remain, one of which is to predict the timing margin available for synchronizing the write head switching position with respect to the targeted island in order to achieve a required bit error rate (BER) [1]. This will inform media designers of the key parameters in media design, and will enable the design parameters of servo systems to be determined.

It has been established that the written-in error rate of BPM depends upon the distribution of island parameters [1]. More recent work using micromagnetic simulations of a single BPM element was used to determine the write-window available for a given head field strength, spacing between islands, and distributions in anisotropy fields and showed that the distributions have severe impact on the writing window [2]. Micromagnetic simulations of larger populations of islands have been used to determine the impact of distributions in island magnetic properties on BER and phase margin during writing [3], which predicted narrow timing margins and quite high error rates for one particular design point. The simulations also showed that a deviation of the phase from the optimum phase for Tb/in^2 areal densities leads to a significant BER.

In a working system, error events leading to write errors should be rare and thus to model these, large numbers of islands are required. However, the computational times involved in micromagnetic simulations [2], [3] render them infeasible for modeling large enough numbers of islands to enable the optimization of design parameters. Therefore, a more efficient model that captures the essential features of the system is required to enable the behaviors of systems to be studied.

The original statistical model of Richter *et al.* [1] is an extremely efficient model that considers timing errors and the ability of the head field to write all islands when there is a distribution of switching fields. The model enables a range of system configurations to be compared so that error rates can be computed for different standard deviations of island properties. In [1], it is assumed that if the head switches within a range of B/2 from the expected switching point then the targeted island will switch correctly (where B is the downtrack island spacing, or island period). Any variations of head position relative to the island that lead to a displacement greater than B/2 will result in an error. The effect of variations in island properties on the timing window are determined by mapping them onto variations in the switching location. For island position jitter the island position and head position are treated interchangeably, while variations in island switching field are transformed into variations in position by use of the head field gradient at the ideal switching position using the relationship

$$\frac{dx}{dH_{\text{eff}}}\delta H_k = \delta x \tag{1}$$

where H_{eff} is the effective head field taking account of the angular variation of medium switching field, x is the position, and H_k is the switching field of the island. In this manner, all variations in island properties can be mapped into position variations (jitter) and, by assuming a timing margin of $\pm \text{B}/2$, the number of islands that will fall outside the timing window and result in errors can be readily calculated. This approach to calculating timing errors relies upon an assumed timing window and the approximation that the effective head field has constant gradient and is a symmetric function of position within the timing window. In a practical system with acceptable error rates, errors will occur at the extremities of distributions and thus near the edges of the timing window. Given that the head will have to be designed to ensure that the magnitude of the effective field attenuates substantially between islands, the approximation of a symmetric head field with constant gradient is quite unlikely to be accurate in the regions where errors actually occur.

Richter *et al.* also calculated errors due to a writing margin that arose from the island switching field distribution. Since there is a maximum effective field available from the head, and the island switching fields are variable, the probability that an island will have a switching field greater than the maximum

Manuscript received March 09, 2010; revised June 02, 2010; accepted June 03, 2010. Date of publication June 14, 2010; date of current version September 22, 2010. Corresponding author: J. Kalezhi (e-mail: kalezhij@cs.man.ac.uk).
Digital Object Identifier 10.1109/TMAG.2010.2052626

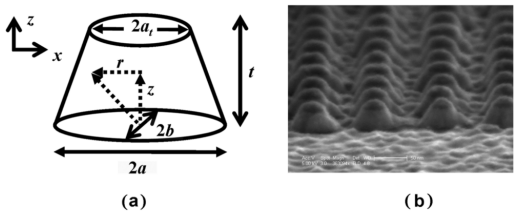

Fig. 1. (a) Geometry of the truncated elliptic cone. (b) SEM images of real islands, the lighter shaded material in the shape of truncated cones is magnetic.

available head field can be calculated and included in the overall write-error rate.

In this paper, we seek to develop a model that avoids the approximations of earlier models without resorting to micromagnetic simulation of huge populations of islands. We propose a model in which the switching probability curve for a targeted island and the previously written island are computed from the head field profile, by determining the probability of thermally activated hopping of the energy barrier. The timing margin or write window for a given BER, e, can then be obtained by identifying the head switching position at which the probability of inadvertantly writing the previously written island is e and that at which the probability of failing to write the target island is $1-e$. These two head positions define the range within which the head must switch in order to achieve the stated error rate, without assuming any properties of the head field and incorporating thermal activation. The effect of switching field distributions causing some islands to be unwritable are automatically included in the switching probability calculation and do not need to be computed separately. The model enables the timing tolerance of the write-head switching waveform to be established for any required BER. The model can be extended to determine thermally activated adjacent track erasures, which will provide a platform for specifying cross-track position tolerances and servo requirements for practical systems.

II. Switching of Islands in Nonuniform Head Fields

To approach this problem, a model of islands switching in a nonuniform field was derived. The assumed island geometry was a truncated elliptic cone shown in Fig. 1(a), which is similar to the shape of the Co/Pt multilayer islands [Fig. 1(b)] described in [4]. Magnetic properties suitable for 1 Tb/in^2 were used: $M_s = 413$ kA/m, $\mathrm{k_{1eff}}V/\mathrm{k}_B T = 60$ and $T = 300$ K (where k_B is Boltzmann's constant, M_s the saturation magnetization and V the island volume, $\mathrm{k_{1eff}}$ is the total anisotropy constant including crystalline and shape anisotropy). The switching fields were calculated using the method described in [5], in which the crystalline and shape anisotropy are assumed to be uniaxial with coincident axes. The shape demagnetising tensor was calculated accurately using the method of [6], which provides an accurate calculation of the switching fields for islands of this shape [5].

The head was assumed to be an unshielded *Karlqvist*-type single pole head reflected in a soft underlayer as shown in Fig. 2.

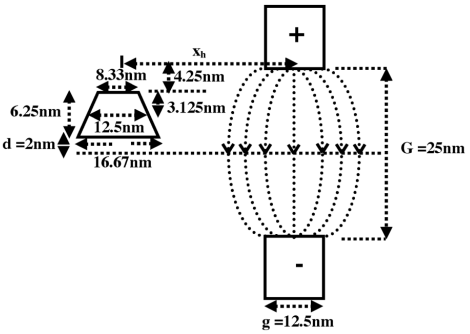

Fig. 2. Side-view geometry of the truncated elliptic cone and the Karlqvist-type single pole head reflected in a soft underlayer.

By taking into account the contribution of the pole and its image at a point (x, y, z), the horizontal and vertical components of field (H_x, H_z) can be obtained:

$$H_x = \frac{H_g}{2\pi}\ln\left(\frac{(g/2+x_h-x)^2+(G/2+z+d)^2}{(g/2-x_h+x)^2+(G/2+z+d)^2}\right) - \frac{H_g}{2\pi}\ln\left(\frac{(g/2+x_h-x)^2+(G/2-z-d)^2}{(g/2-x_h+x)^2+(G/2-z-d)^2}\right) \quad (2)$$

$$H_z = \frac{H_g}{\pi}\left(\tan^{-1}\left(\frac{g/2+x_h-x}{G/2-z-d}\right)+\tan^{-1}\left(\frac{g/2-x_h+x}{G/2-z-d}\right)\right) + \frac{H_g}{\pi}\left(\tan^{-1}\left(\frac{g/2+x_h-x}{G/2+z+d}\right)+\tan^{-1}\left(\frac{g/2-x_h+x}{G/2+z+d}\right)\right) \quad (3)$$

where H_g, g, x_h, G, d are respectively the head gap field, pole width, head-island separation, gap width, and the separation between island base and mirror plane as shown in Fig. 2, x and z are defined as in Fig. 1(a).

In order to incorporate the nonuniform field into a simplified single-moment model of island switching, the average of the vector head field over the island volume was used to calculate the head gap field required to switch the island.

The volume average of the head field over the island was obtained as shown in (4)–(5), where $\beta = b/a = 1, x = r\cos\phi$

$$H_x^{\mathrm{av}}V = \beta\int_{\phi=0}^{2\pi}d\phi\int_{z=0}^{t}dz\int_{r=0}^{a(1-z/z_0)}rdrH_x(r,\phi,z) \quad (4)$$

$$H_z^{\mathrm{av}}V = \beta\int_{\phi=0}^{2\pi}d\phi\int_{z=0}^{t}dz\int_{r=0}^{a(1-z/z_0)}rdrH_z(r,\phi,z) \quad (5)$$

and V is the island volume. $z_0 = t/(1-a_t/a), a_t, a$ are defined in Fig. 1(a), and ϕ is the usual azimuthal angle (not shown).

The average head field components in (4) and (5) can be expressed as

$$H_x^{\mathrm{av}}(x_h) = (H_g/(2\pi V))H_1(x_h) \quad (6)$$

$$H_z^{\mathrm{av}}(x_h) = (H_g/(\pi V))H_2(x_h) \quad (7)$$

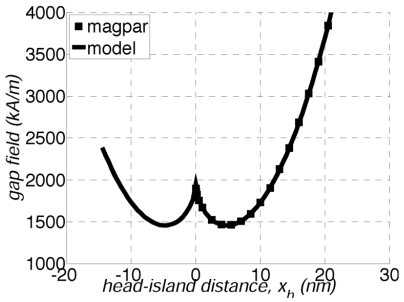

Fig. 3. Dependence of the minimum head gap field, H_g, that would be required to switch the island on head-island separation x_h.

where $H_1(x_h)$ and $H_2(x_h)$ represent integrals and were computed numerically. The magnitude and the polar angle of the average head field are

$$\begin{aligned} H^{\rm av} &= (H_g/(\pi V))\sqrt{(H_1/2)^2 + H_2^2} \\ \theta_H &= \cos^{-1}(H_z^{\rm av}/H^{\rm av}) \\ &= \cos^{-1}(H_2/\sqrt{(H_1/2)^2 + H_2^2}). \end{aligned} \tag{8}$$

For coherent reversal of a single-domain uniaxial island, the switching field in terms of the field angle, θ_H, is [7]

$$H_{\rm sw} = H_{\rm Keff}(\cos^{2/3}\theta_H + \sin^{2/3}\theta_H)^{-3/2} \tag{9}$$

where the effective anisotropy field $H_{\rm keff}$ includes the intrinsic (crystalline) anisotropy and shape anisotropy. In the case where the azimuthal angle of the average field, ϕ_H, is 0 or $\pi/2$, the effective anisotropy field is

$$\begin{aligned} H_{\rm Keff} &= 2K_1/(\mu_0 M_s) \\ &\quad + M_s(N_{xx}\cos^2\phi_H + N_{yy}\sin^2\phi_H - N_{zz}) \end{aligned} \tag{10}$$

where K_1 is the crystalline anisotropy constant, M_s the saturation magnetization, and N_{xx}, N_{yy}, and N_{zz} represent the magnetometric demagnetizing factors.

The minimum magnitude of the head gap field that will switch the island can be obtained by comparing (8) with (9) giving

$$H_g^{\rm switch} = \pi V H_{\rm Keff}(H_2^{2/3} + (H_1/2)^{2/3})^{-3/2}. \tag{11}$$

Fig. 3 shows the minimum head gap field required to switch the island for various head-island separations. These results were compared to finite element calculations in *magpar* [8] in which the same island geometry was subjected to the spatially varying (nonaveraged) head field described by (2) and (3). It was observed in magpar that magnetization reversal was not strictly coherent rotation, with the regions that experience the strongest head field having the largest tilt in magnetization angle. However the deep gap field required to switch an island in the single moment model is in excellent agreement with the deep gap field at which the island magnetization irreversibly changes direction in the *magpar* simulations as shown in Fig. 3. This shows that although there is some nonuniformity in the magnetization reversal of these islands, a properly constructed single-moment model can accurately predict their switching in a nonuniform head field.

III. Thermal Effects

Having verified the model for switching in nonuniform fields, thermal effects were then included to enable switching probabilities to be predicted.

To take thermal activation into account, large numbers of identical and noninteracting islands at the same temperature and external field should be considered [9]. In the case of two possible magnetization orientations (uniaxial anisotropy), the number of islands whose magnetization is in one orientation (n_1) varies with time according to [9]

$$\frac{dn_1}{dt} + (v_{12} + v_{21})n_1 = v_{21}n \tag{12}$$

where n represents the total number of islands and n_1 the number of islands whose magnetization is in orientation 1. The transition rates ν_{12} and ν_{21} represent the probability per unit time of the magnetization jumping from orientation 1 to 2 and 2 to 1, respectively. These are given by

$$\begin{aligned} v_{12} &= f_0\exp(-E_{\rm barrier,1}/(k_BT)), \\ v_{21} &= f_0\exp(-E_{\rm barrier,2}/(k_BT)) \end{aligned} \tag{13}$$

where f_0 is the attempt frequency, k_B the Boltzmann constant, and T the absolute temperature. $E_{\rm barrier,1}$ and $E_{\rm barrier,2}$ represent the energy barrier for the magnetization escaping from orientations 1 and 2, respectively. For an island being written by a head, the energy barrier is a function of the applied field, which varies with time as the island passes under the head and the head field direction reverses, and so the transition rates in a recording system are not constant throughout the recording process.

Energy barriers were calculated at each position as the island passes beneath the head by first finding the roots (four in general) corresponding to the stationary points of the total energy [10]. The energy barrier was then obtained by taking the difference between the minimum and the maximum energy for a given pair of roots.

Since large numbers of islands are involved, (12) can be transformed to describe the probability of not switching by dividing by the total number of islands, n. Taking account of the variation of the transition rates with time, (12) then becomes

$$\frac{dp_1}{dt} + (v_{12}(t) + v_{21}(t))p_1 = v_{21}(t) \tag{14}$$

where $p_1 = n_1/n$, which is the probability of remaining in orientation 1.

Since the transition rates are not constant, (14) cannot be integrated in the normal manner and the overall probability of not switching must be expressed as

$$\begin{aligned} p_1(t) &= p_1(0)\exp(-\int_{t'=0}^{t} v(t')dt') \\ &\quad + \exp\left(-\int_{t'=0}^{t} v(t')dt'\right) \\ &\quad \times \int_{t'=0}^{t}\exp(-\int_{t''=0}^{t'} v(t'')dt'')v_{21}(t')dt' \end{aligned} \tag{15}$$

where $\nu = \nu_{12} + \nu_{21}, p_1(0) = 1$.

Orientation 1 is taken to refer to the shallower minimum in the presence of an applied field and orientation 2 to a deeper minimum. During magnetic recording, the energy barrier for reversal against the applied field, from orientation 2 to orientation 1, is large ($\geq 60 k_B T$) and it can be seen that ν_{21} is extremely small. Thus, the second term in (15) can be ignored and $\nu \sim \nu_{12}$.

The switching probability then becomes

$$p_{\text{switch}}(t) = 1 - p_1(t) = 1 - \exp(-\int_{t'=0}^{t} v(t')dt'). \quad (16)$$

The function ν depends on the energy barrier between minima, which depends on the position of the island relative to the head and the vector head field averaged over the island volume, which in turn is a function of time. This time dependence of the probability of an island switching can be used to determine the write window for a given probability of writing (or not writing).

IV. Write Window With Identical Islands

The correct value of the attempt frequency f_0 is a matter of some debate [11], [12]. In order to determine the effect of the assumed value of f_0, switching probabilities were calculated using (16) with values of f_0 ranging from 1 to 1000 GHz. The head gap field, H_g, was chosen to be $1.5 H_{\text{Keff}} = 1807$ kA/m (22.69 kOe), where H_{Keff} is defined according to (10). This value exceeds the maximum gap field for a Karlqvist head. Although it does not exceed the 2.4 T limit of the saturation magnetization of the pole pieces, achieving such a field in a finite dimension perpendicular recording head with shields would be a significant challenge. During a single bit write event, two islands were considered, the target island (i.e., the island that the system intends to write) and the previously written one. The head traverses the islands, and at some point the direction of the head gap field reverses. Reversal is not assumed to be instantaneous. The head gap field was varied with time as an error function of time constant 0.2 ns [2] during switching, where the switching position is taken as the location of the centre of the head at the moment that the gap field crosses zero. The probability of each island switching was calculated by integrating the probability of switching (16) along the head path with $\nu(t)$ varying with time according to the head field, which reverses as described above. This was performed for a range of head gap field switching positions. Magnetostatic interactions between these islands are relatively small because M_s is relatively low and the islands are quite well separated, and so interactions were not included. Head velocities ranging from 5×10^{-6} m/s (the speed of a high resolution drag tester) to 25 m/s (the head-medium speed in a disk drive) were considered.

Fig. 4 shows the dependence of the switching probability for the previously written and target islands as a function of head switching position for a velocity of 5×10^{-6} m/s (the speed of our drag tester, which was chosen to enable comparison with experiment) and various values of the attempt frequency, f_0.

We define the write window to be the range of head positions within which the head field must change polarity in order to write the required data with an error rate equal to or better

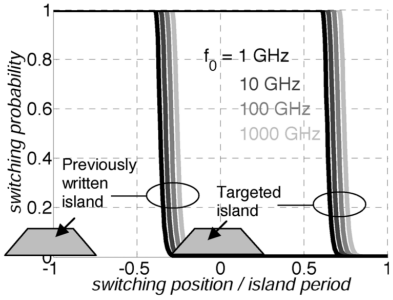

Fig. 4. Switching probability for targeted and previously written islands as a function of head switching position for various attempt frequencies f_0. Island period $= 25$ nm, head velocity $= 5 \times 10^{-6}$ m/s.

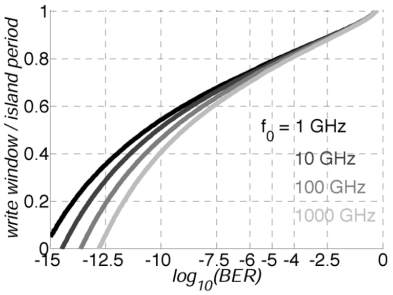

Fig. 5. Dependence of write-window on log(BER), head velocity $= 5 \times 10^{-6}$ m/s.

than a specified value e. This can be obtained by identifying the head switching position at which the probability of inadvertently writing the previously written island is e, and the position at which the probability of failing to write the target island is $1-e$, the timing window being the separation between these two head field switching positions. Fig. 5 shows calculated timing window as a function of BER for a range of attempt frequencies. At this very low (dragtester) velocity, for BER $\geq 10^{-6}$, the write window does not vary significantly as a function of attempt frequency. At drive velocities thermal activation would be expected to have substantially less effect. The largest attainable write-window is obtained for a BER of 0.5, which is the error rate that would result if the final written states of the islands were random and uncorrelated with the intended data pattern.

The write window calculated in this manner is significantly different in meaning from the timing window assumed by Richter *et al.* [1], in whose model the timing window was effectively defined to be the island period or bit spacing. Thus where Richter's model provides a means of calculating the error rate as a function of island period, our model reveals how the system timing tolerance depends upon the required write-error rate for a given island period.

V. Velocity Variations

Different head velocities were considered in order to understand their impact on the write-window.

Fig. 6 shows that at any given BER the write window deteriorates with decreasing head velocity. This is due to increased

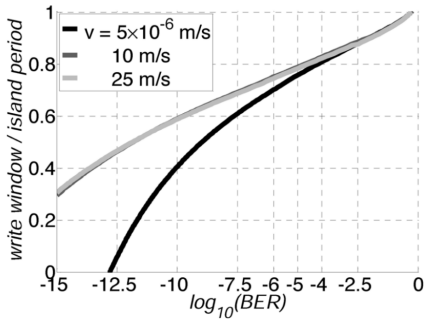

Fig. 6. Dependence of write-window on log(BER) for different head velocities.

thermal activation at lower velocities as the head takes a longer time to travel between islands. For $\mathrm{BER} = 10^{-5}$ or worse, the write window does not vary significantly with head velocity.

VI. Write Window With Island Variations

In order to include variations, a Gaussian distribution of island geometric/position/magnetic properties was assumed [4]. The switching probability with variations was then calculated according to (17)

$$p_{\mathrm{switch}}^{\mathrm{var}}(t) = 1 - \left(\int p(a) p_1(a,t) da \right) / \int p(a) da \qquad (17)$$

where $p_{\mathrm{switch}}^{\mathrm{var}}$ is the switching probability taking into account variations in parameter a, and $p\,(a)$ is the probability distribution function (pdf) of the parameter a. If the pdf is assumed to be a Gaussian then its integral is the error function, *erf*. For parameters with nonzero mean and where the parameter value is always positive (size, shape, crystalline anisotropy) (17), written explicitly, takes the form

$$p_{\mathrm{switch}}^{\mathrm{var}}(\sigma,t) = 1 - \frac{\int_{x=x_0}^{x_1} \exp\left(-\frac{(x-1)^2}{2\sigma^2}\right) \exp\left(-\int_{t'=0}^{t} v(x,t')dt'\right) dx}{\frac{\sigma\sqrt{2\pi}}{2}\left(1+\mathrm{erf}\left(\frac{1}{\sigma\sqrt{2}}\right)\right)} \qquad (18)$$

where x is the normalized parameter whose mean is 1, σ is the standard deviation of x, and erf is the error function. For island position variations (jitter), where the parameter x can be negative, the switching probability is

$$p_{\mathrm{switch}}^{\mathrm{var}}(\sigma,t) = 1 - \frac{\int_{x=x_0}^{x_1} \exp\left(-\frac{(x-\bar{x})^2}{2\sigma^2}\right) \exp\left(-\int_{t'=0}^{t} v(x,t')dt'\right) dx}{\sigma\sqrt{2\pi}} \qquad (19)$$

where $\bar{x}$ is the expected position of the island. The limits of integrations in the numerator were chosen such that the effect of the limits on the value of the computed integrand is negligible.

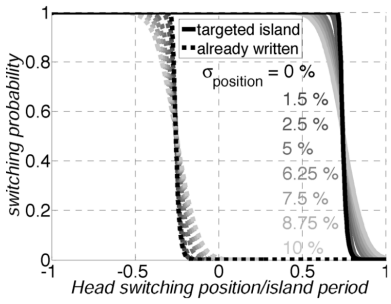

Fig. 7. Switching probability for targeted and previously written islands as a function of head switching position for populations of islands with various standard deviations of position expressed as a percentage of island period. Head velocity $= 5 \times 10^{-6}$ m/s, $f_0 = 1000$ GHz.

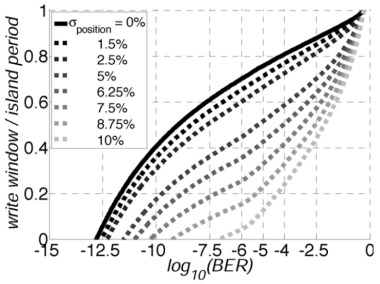

Fig. 8. Dependence of write-window on log(BER) for various distributions of island position. Standard deviation of island position expressed as a percentage of island period. Head velocity $= 5 \times 10^{-6}$ m/s, $f_0 = 1000$ GHz.

A. Position Variations

Islands in BPM tend to deviate from their expected positions (jitter) in addition to having geometric variations. The switching probabilities in media with position variations were calculated using (19) and where the island geometry (shape/size) was fixed. In order to speed up the computation, the previously computed switching probability as a function of switching position (e.g., from Fig. 7 with $\sigma = 0$) was used. The switching probability with position variations was then obtained by noting that if an island is shifted from its expected position by an amount δ, the switching probability curve is identical to that of the island in its expected position but shifted by an amount δ along the x-axis. Hence, the switching probability curve for the distribution can be obtained by a weighted sum of shifted curves, where the weight for each shift value is the corresponding value of the Gaussian pdf of the position distribution as shown in (20)

$$p_{\mathrm{switch}}^{\mathrm{var}}(\sigma_{\mathrm{position}},t) = \frac{\int_{x=x_0}^{x_1} \exp\left(-\frac{(x-\bar{x})^2}{2\sigma_{\mathrm{position}}^2}\right) p_{\mathrm{switch}}(x-\bar{x},t)dx}{\sigma\sqrt{2\pi}}. \qquad (20)$$

Fig. 7 shows the switching probabilities for various distributions of position while Fig. 8 shows the write window. Increasing the variations reduces the write-window.

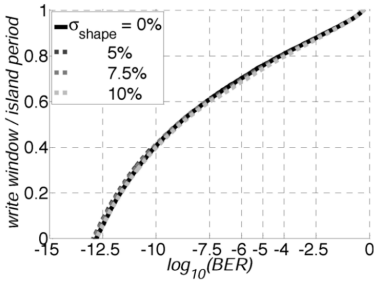

Fig. 9. Dependence of write-window on log(BER) for various populations of island ellipticity standard deviation of ellipticity expressed as a percentage of mean ellipticity $= 1.0$. Head velocity $= 5 \times 10^{-6}$ m/s, $f_0 = 1000$ GH$_z$.

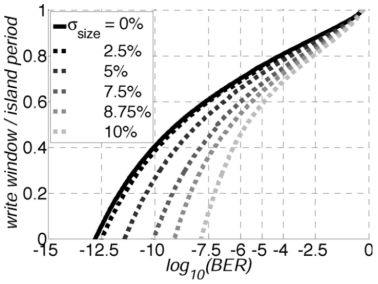

Fig. 10. Dependence of write-window on log(BER) for various populations of island radius, standard deviation of radius expressed as a percentage of mean radius. Head velocity $= 5 \times 10^{-6}$ m/s, $f_0 = 1000$ GH$_z$.

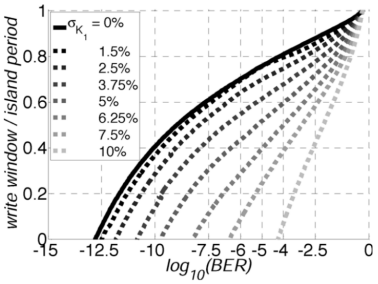

Fig. 11. Dependence of write-window on log(BER) for various populations of island K_1, standard deviation of K_1 expressed as a percentage of the mean. Head velocity $= 5 \times 10^{-6}$ m/s, $f_0 = 1000$ GH$_z$.

B. Shape Variations

To determine the effect of island shape upon timing window, a population of islands of varying shape was considered. Shape variation was assumed to arise from a finite variance of the ellipticity of the islands. The island size (volume) was assumed to be constant as the in-plane ellipticity (semi-minor axis (b)/semi-major axis (a)) varies from island to island. The varying magnetometric demagnetizing factors for this shape were computed using the approach described in [5].

To speed up the computation of (18), the volume averaged head-fields were precomputed for various head-island separations and island shapes. The volume averaged head field for any given head position and island shape was then computed by a two-dimensional polynomial interpolation of the precomputed table of values.

Several standard deviations of ellipticity between 0 and 10% of the mean (1.0) were considered. The dependence of write-window on $\log_{10}$ (BER) is shown in Fig. 9. Very little difference can be observed, showing that the write-window is not very sensitive to shape.

C. Size Variations

In this case, the island thickness and cross-section aspect ratio (in-plane ellipticity) was fixed $(b/a = 1)$ while the radius was varied. The switching probabilities were calculated using the same method as for the shape distributions described above.

Several standard deviations between 0 and 10% of the mean radius were considered. Fig. 10 shows the dependence of write-window on $\log_{10}$ (BER) for these distributions of size.

Analysis of Figs. 9 and 10 shows that shape variation has little effect on the timing window at almost all values of BER. However variation in island size has a severe impact upon timing window. Assuming a BER of 10^{-6} to be acceptable, with no size variation in the islands the timing window is 0.7P (where P is the island period $= 25$ nm), while 5% and 10% standard deviations in size reduce the timing window to 0.65P and 0.46P, respectively. Thus size distribution arising during fabrication will have a significant impact upon timing window and thus upon the servo tolerances required for a viable system. Position variations have a severe impact upon timing window compared to size.

D. Crystalline Anisotropy Variations

Islands in BPM tend to vary in their magnetic properties [13]. In this analysis, the island geometry was fixed while distributions in magnetic properties were introduced by varying the crystalline anisotropy, K_1. Equation (18) was used to obtain switching probabilities in the presence of K_1 variations. Fig. 11 shows the write window for various distributions in K_1. As shown in Fig. 11, for these islands, there is no write window for a standard deviation of 10% at a $\mathrm{BER} = 10^{-6}$.

VII. Combining Parameters

Position and K_1 variations were seen to have a more significant effect on BER than geometry (shape/size) variations. The impact of a combination of both variations was studied to determine whether the effect of both simultaneously is worse than would be expected from each individually. In principle a double integral taking into account both distributions should be evaluated. To speed up the calculations, the precomputed switching probability curve for K_1 variations only was used. Position variations were then included by using a technique similar to one employed for position variations described by (21)

$$p^{\mathrm{var}}_{\mathrm{switch}}(\sigma_{\mathrm{position}}, \sigma_{K1}, t) = \frac{\int_{x=x_0}^{x_1} \exp\left(-\frac{(x-\bar{x})^2}{2\sigma^2_{\mathrm{position}}}\right) p^{\mathrm{var}}_{\mathrm{switch}}(\sigma_{K1}, x-\bar{x}, t)dx}{\sigma\sqrt{2\pi}}. \quad (21)$$

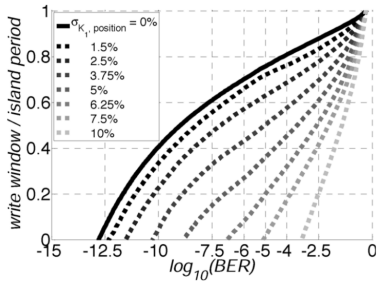

Fig. 12. Dependence of write-window on log(BER) for various populations of island position and K_1 combined. Head velocity $= 5 \times 10^{-6}$ m/s, $f_0 = 1000$ GH$_z$.

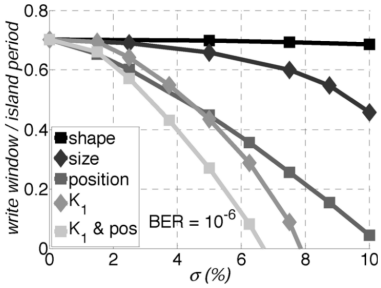

Fig. 13. Dependence of write-window on standard deviation for various populations of islands for a BER $= 10^{-6}$.

Fig. 12 shows the write window for these distributions. As shown in Fig. 12, combining distributions worsens the performance of the system significantly. For these islands, there is no write window for a standard deviation of 7.5% and above at a BER $= 10^{-6}$.

VIII. Write Window—Standard Deviation Plots for Fixed BER

In order to easily identify the impact of parameter variations on the write window, write window was determined as a function of standard deviation of island properties at selected BER values. These values were obtained from the write window—BER plots. Figs. 13, 14, and 15 show the dependence of write window on standard deviation for the selected parameters at BER values of $10^{-6}, 10^{-5}$, and 10^{-4}, respectively. As can be seen, combining parameters worsens the performance of the system significantly.

IX. Comparison With Previous Models

The results of this model were compared with those of earlier models. The statistical model of Richter *et al.* [1] was used to calculate error rates for the same system as shown in Fig. 12. For the 1 Tb/in^2 islands considered in this paper, a standard deviation of island position (jitter) of 5% gives rise to a 1.25 nm standard deviation of island position (jitter). The mean anisotropy field is 1.204×10^3 kA/m (15.13 kOe) and the gradient of the write head field at the write point is 77.465 kA/m/nm (973 Oe/nm). Using (1), a 5% standard deviation of anisotropy field corresponds to a position jitter of 0.772 nm.

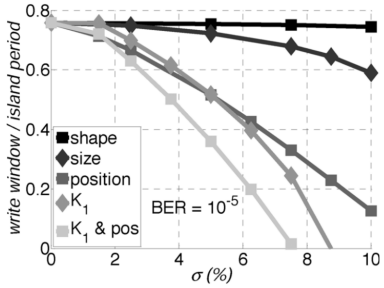

Fig. 14. Dependence of write-window on standard deviation for various populations of islands for a BER $= 10^{-5}$.

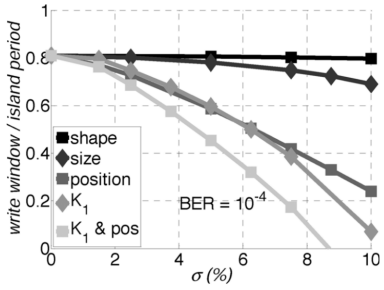

Fig. 15. Dependence of write-window on standard deviation for various populations of islands for a BER $= 10^{-4}$.

Combining the island position jitter and the equivalent jitter arising from anisotropy variation leads to a total jitter of 1.472 nm. Using (3) of [1], in which it is assumed that any island found more than B/2 away from the ideal position will create a write error, a write error rate of 1.012×10^{-17} would be predicted.

The model of [1] also considers errors arising from islands with such high anisotropy that the head field is unable to write them. For the system modeled in this paper the maximum effective head field experienced by islands is 1.496×10^3 kA/m (18.80 kOe). In a population of islands with mean anisotropy field of 1.204×10^3 kA/m (15.13 kOe) and a 5% standard deviation, the probability of write error is 3.85×10^{-3} giving a total write error probability of $1.012 \times 10^{-17} + 3.85 \times 10^{-3} = 3.85 \times 10^{-3}, (\log_{10}(\mathrm{BER}) = -2.415)$. The model of [1] assumes that any island found within B/2 of the write position is correctly written, which could be thought to relate to a timing window equal to the island period. The results shown in Fig. 12 predict a BER $= 0.5$ $(\log_{10}(\mathrm{BER}) = -0.301)$ for 5% variation in island position and anisotropy and a timing window equal to the island period, indicating that a more accurate treatment of the head field profile predicts a higher error rate.

If (3) of [1] is modified to assume an error for any island found more than B/4 away from the ideal position (which could be thought to relate to a write window of 50% of the island period), an error rate of 1.087×10^{-5} is predicted which, when combined with the errors due to unwritably high anisotropy islands, leads to a total write error rate of 3.861×10^{-3} $(\log_{10}(\mathrm{BER}) = -2.413)$ while the prediction of our model from Fig. 12 is $\log_{10}(\mathrm{BER}) = -3.524$ for a

APPENDIX B. PUBLICATIONS

50% timing window, i.e., a lower error rate. These two models describe different behavior. In [1] errors arise if islands are moved either physically or by virtue of anisotropy variation beyond B/2 from their ideal position, and thus in that model as B is reduced BER increases. In our model the timing window is the calculated accuracy that needs to be maintained in write field position (i.e., down-track servo accuracy) to achieve a given BER, and in our model as timing window narrows (servo accuracy improves), BER decreases. The two error rates computed by these models cannot meaningfully be compared and any similarity between the two error rates calculated above is therefore fortuitous.

Previous work using micromagnetic simulations [3] considered parallelepiped shaped islands with a 15 nm period along track. For these islands, with $\sigma_{\mathrm{K1}} = 4\%$, a BER of $10^{-2.5}$ gave a phase margin of ± 3.5 nm. This amounts to a window of 7 nm, which is 0.47 of the period. Computation using the model described in this paper, with island magnetic and geometric properties similar to those reported in [3] but with a different head (Karlqvist type single pole) gave a write window of 0.60 of the period, which is larger than predicted in [3]. The differences between these results arise from a number of factors, primarily the lower head field gradient used in [3] and also neglecting magnetostatic interactions in the model described in this paper. With the smaller down-track bit separation and the particularly large $\mathrm{M_s}$ used in [3], interactions have a more significant effect than in the medium used in this paper. In [3] variations in saturation magnetization, exchange constant, and damping were also included but these would have a lesser effect than head field gradient and interaction fields.

X. Conclusion

A computationally efficient but accurate model has been developed to predict the write-window for a given BER in patterned media. The model uses the full head field distribution rather than the value and gradient at the write point and thus allows for head field asymmetry without recourse to micromagnetic modeling. The model predicts the write-error performance of Bit Patterned Media composed of populations of islands with distributions of magnetic and geometric parameters, and can be used to calculate the write-window or down-track servo tolerance for given BER. The model shows that the smallest attempt frequency gives rise to the largest write window, although for $\mathrm{BER} = 10^{-6}$ or worse the write window does not depend significantly on attempt frequency or velocity. The model also predicts that the error rates observed in a drag tester will be similar to a disk drive for error rates greater than about 10^{-6}. The effect of distributions of island geometry (shape/size), position and magnetic properties has been investigated, and it has been shown that island position/magnetic property distributions have a much more significant effect upon BER than geometric variations.

This model could be used to determine realistic servo requirements for practical disk drives using BPM for a given raw BER as specified by the requirements of the replay channel. The methodology can be extended to predict accidental adjacent track writing using finite track-width heads, which will enable track positioning servo requirements to be established in a similar way. Magnetostatic interactions can be readily incorporated, which will provide a comprehensive and realistic model for BPM system design.

Acknowledgment

This work was supported by EPSRC under Grant EP/E017657/1 and by the Information Storage Industry Consortium (INSIC) EHDR Program.

References

[1] H. J. Richter, A. Y. Dobin, O. Heinonen, K. Z. Gao, R. J. M. V. D. Veerdonk, R. T. Lynch, J. Xue, D. Weller, P. Asselin, M. F. Erden, and R. M. Brockie, "Recording on BPM at densities of 1 Tb/in^2 and beyond," *IEEE Trans. Magn.*, vol. 42, no. 10, pp. 2255–2260, Oct. 2006.

[2] B. Livshitz, A. Inomata, H. N. Bertram, and V. Lomakin, "Analysis of recording in bit patterned media with parameter distributions," *J. Appl. Phys.*, vol. 105, pp. 07C111–3, Mar. 2009.

[3] M. E. Schabes, "Micromagnetic simulations for terabit/in^2 head/media systems," *J. Magn. Magn. Mater.*, vol. 320, pp. 2880–2884, Nov. 2008.

[4] B. D. Belle, F. Schedin, T. V. Ashworth, P. W. Nutter, E. W. Hill, H. J. Hug, and J. J. Miles, "Temperature dependent remanence loops of ion-milled BPM," *IEEE Trans. Magn.*, vol. 44, no. 11, pp. 3468–3471, Nov. 2008.

[5] J. Kalezhi, J. Miles, and B. D. Belle, "Dependence of switching fields on island shape in bit patterned media," *IEEE Trans. Magn.*, vol. 45, no. 10, pp. 3531–3534, Oct. 2009.

[6] M. Beleggia and M. De Graef, "On the computation of the demagnetization tensor field for an arbitrary particle shape using a Fourier space approach," *J. Magn. Magn. Mater.*, vol. 263, pp. L1–L9, Jul. 2003.

[7] E. C. Stoner E. C. and E. P. Wohlfarth, "A mechanism of magnetic hysteresis in heterogeneous alloys," *Phil. Trans. Roy. Soc. A*, vol. 240, pp. 599–642, May 1948, Reprint in *IEEE Trans. Magn.*, vol. 27, pp. 3475–3518, Jul. 1991.

[8] W. Scholz, J. Fidler, T. Schrefl, D. Suess, R. Dittrich, H. Forster, and V. Tsiantos, "Scalable parallel micromagnetic solvers for magnetic nanostructures," *Comput. Mater. Sci.*, vol. 28, pp. 366–383, Oct. 2003.

[9] W. F. Brown, "Thermal fluctuations of fine ferromagnetic particles," *IEEE Trans. Magn.*, vol. MAG-15, pp. 1196–1208, Sep. 1979.

[10] R. Wood, "Exact solution for a Stoner-Wohlfarth particle in an applied field and a new approximation for the energy barrier," *IEEE Trans. Magn.*, vol. 45, no. 1, pp. 100–103, Jan. 2009.

[11] D. Weller and A. Moser, "Thermal effect limits in ultrahigh-density magnetic recording," *IEEE Trans. Magn.*, vol. 35, no. 6, pp. 4423–4439, Nov. 1999.

[12] W. Wernsdorfer, E. B. Orozco, K. Hasselbach, A. Benoit, B. Barbara, N. Demoncy, A. Loiseau, H. Pascard, and D. Mailly, "Experimental evidence of the Neel-Brown model of magnetization reversal," *Phys. Rev. Lett.*, vol. 78, pp. 1791–1794, Mar. 1997.

[13] T. Thomson, G. Hu, and B. D. Terris, "Intrinsic distribution of magnetic anisotropy in thin films probed by patterned nanostructures," *Phys. Rev. Lett.*, vol. 96, pp. 257204-1–257204-4, Jun. 2006.

JOURNAL OF APPLIED PHYSICS **109**, 07B755 (2011)

Analysis of write-head synchronization and adjacent track erasure in bit patterned media using a statistical model

Josephat Kalezhi[1,2,a] and Jim J. Miles[2]
[1]*School of Computer Science, The University of Manchester, Oxford Road, Manchester M13 9PL, United Kingdom*
[2]*Computer Science Department, School of Technology, Copperbelt University, Kitwe 10101, Zambia*

(Presented 17 November 2010; received 24 September 2010; accepted 13 December 2010; published online 7 April 2011)

An analysis of the performance of a bit patterned media data storage system composed of nanoscale islands with variations in position and magnetic properties has been carried out. The statistical model of write errors includes adjacent track erasure and error rates are computed according to the down-track synchronization of the write head switching position and cross-track head position variations. Two-dimensional maps of bit error rates reveal that distributions of position and anisotropy have a severe impact on the performance of the system. Results show that head field cross-track gradients needs to be tightly controlled to minimize the effects of adjacent track erasure. © *2011 American Institute of Physics*. [doi:10.1063/1.3562869]

I. INTRODUCTION

In bit patterned media (BPM), the medium is patterned into nanometer-sized magnetic islands where each island stores one bit. To write a specific 'target' island in such a system there is an optimal down-track head location at which the head field switches, and deviation from that position will cause an increase in errors. Similarly, even if the head is perfectly positioned on track there will be write errors due to adjacent track erasure (ATE), and as the head position deviates off track, ATE and the on-track probability of write errors will rise. By modeling these effects the accuracy of two-dimensional servo control that is required in order to achieve a required error rate can be established. Experimental studies of the off-track margin in BPM[1] have shown that this is a practical problem. A number of theoretical studies on the available timing margin in BPM based on micromagnetic simulations and incorporating distributions in island properties have been reported.[2–4] Error rates of practical interest are 10^{-4} or below, and to accurately predict timing margins for such low error rates requires too many switching calculations for a micromagnetic model. An efficient statistical model of write errors has been previously developed that includes the spatial distribution of the head field, the variations in the magnetic and geometric properties of islands and thermal activation in a calculation of switching probability as a 1-D function of down-track head field switching position.[5] This model improves upon the original extremely efficient statistical model of Richter *et al.*[6] and provides a better resolution of error rates in the down-track position compared to micromagnetic models. Thermal activation is included in this model which is missing in the previous literature. This is important in ATE where in a realistic system the head field should never be sufficient to switch islands on neighboring tracks, but where thermal activation may cause infrequent random errors.

A 1-D model has been described previously that determines the energy barrier to reversal at each head position.[5] The probabilities of thermally activated switching of the target island and the previously written island were calculated for all head field switching positions x_h. A 1-D write window, or region within which the error rate is less than e, was obtained as the separation between the values of x_h at which the probability of correctly writing the target island was 1-e and the probability of inadvertently overwriting the previously written island was e. The distributions of island geometry (shape/size), position and magnetic properties such as anisotropy were included.

This 1-D model of on-track errors has now been extended to study the case when the head is not aligned on track. To calculate the error probability, the switching probability of islands was computed as a function of head-island separation in the down-track (x_h) and cross-track (z_h) dimensions in the same manner as for the 1-D model but for the two adjacent tracks as well as on-track islands.

On-track write errors were studied in the same manner as for the 1-D simulations described above, repeating the process for a range of z_h values to obtain a 2-D error map. The study

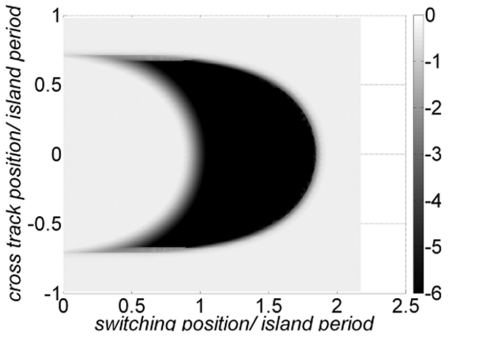

FIG. 1. Log_{10} (BER) as a function of 2-D head field switching position for on track errors.

[a]Electronic mail: kalezhij@cs.man.ac.uk.

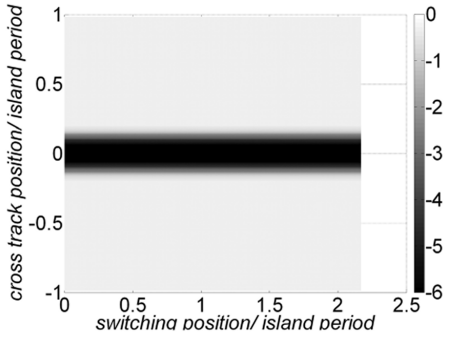

FIG. 2. Log_{10} (BER) as a function of 2-D head field switching position for adjacent-track errors.

of ATE was carried out by a similar technique to the 1-D model, except that the island experienced the head field from $-\infty$ to $+\infty$ in the down-track direction since a specific island on the adjacent track could be accidentally overwritten by an attempt to write any island on the target track. In a real system it could be that the target track is written many times while the data on the adjacent track must be retained. This was modeled by assuming that the adjacent track must survive 10^4 writes to the target track and adjusting the calculation of switching probability accordingly for each z_h value.

II. RESULTS

In this study, a finite track width write head was used with media suitable for 1Tb/in^2 areal density. The head had a rectangular main pole of 13 by 40 nm (cross track × down track) with pole-trailing shield gap of 5 nm and pole-side-shield gap of 10 nm.[7] The distance from the pole to the top surface of the medium was 5 nm, the medium was 10 nm thick and there was a 2 nm interlayer between the soft underlayer (SUL) and the medium. The peak perpendicular head field gradients were 430 Oe/nm down-track and 303 Oe/nm cross track.[7] Although the practical fabrication of a head with the dimensions and structure described would be very challenging, a larger pole could not confine the head field sufficiently for recording at this density. Staggered BPM with a wider pole could alleviate some head manufacturing challenges, but this would require double the down-track field gradient and that would present severe design problems in down-track pole-shield spacing. The optimal value of the anisotropy, $H_K = 875.35$ kA/m (11 kOe) was selected to maximize the effective field gradient from the write head at the write point.

Initially, single-layer, single-domain islands were assumed, located on a square lattice of 25.4 nm period (1 Tb/in^2) and with saturation magnetization (M_s) = 700 kA/m (700 emu/cc). The temperature was T = 300 K, head velocity = 25 m/s, head field rise time = 0.06 ns. Using the island dimensions appropriate for 1 Tb/in^2 (cylindrical in shape with height = 10 nm, diameter = 13.4 nm) and the crystalline anisotropy constant, $K_I = \mu_0 M_s H_K/2 = 3.85 \times 10^5$ J/m^3 (3.85×10^6 erg/cc), this gives a high stability ratio, $K_I V/K_B T = 131$ where V is the island volume and K_B is the Boltzmann constant.

The attempt frequency calculated by Brown's method[8] for a single domain particle in the absence of an applied field was 124 GHz which is higher than commonly used value in recording models, a value of 100 GHz was therefore used to estimate error rates. The magnetostatic interaction fields were

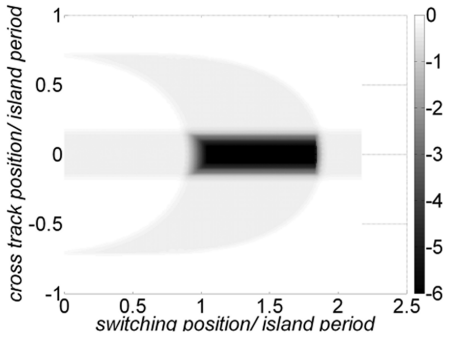

FIG. 3. Log_{10} (BER) as a function of 2-D head field switching position for total errors.

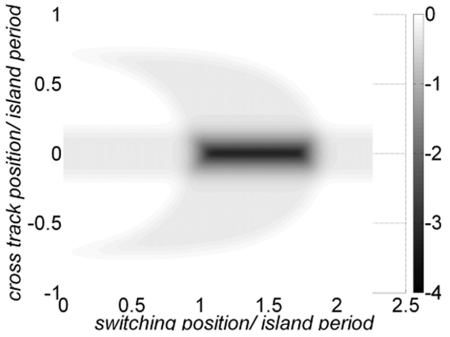

FIG. 4. Log_{10} (BER) as a function of 2D head field switching position (total error). A 5% 2-D standard deviation of island position normalized to island period (25.4 nm) was applied. The minimum BER is 6.75×10^{-4}.

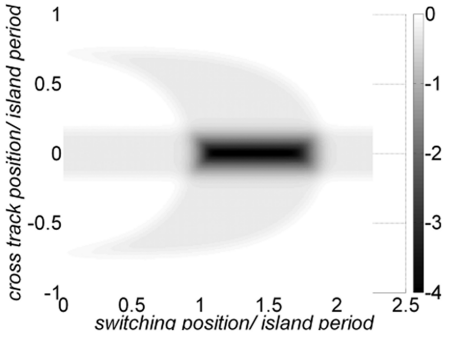

FIG. 5. Log_{10} (BER) as a function of 2D head field switching position (total error). A 5% standard deviation of intrinsic (crystalline) anisotropy was applied. The minimum BER is 8.5×10^{-5}.

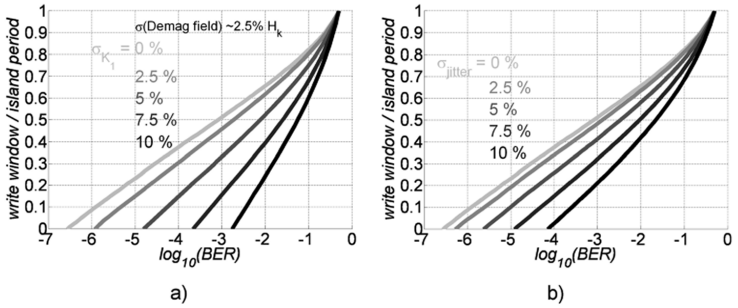

FIG. 6. Dependence of write-window on $\log_{10}$ (BER) for various (a) standard deviations of K_1 expressed as a percentage of the mean and (b) standard deviations of island position expressed as a percentage of island period.

estimated using a dipole approximation for a 512×512 array of islands whose magnetization was randomly up or down.

The resulting interaction field at the center can be approximated as a Gaussian distribution with a mean of zero and a standard deviation of 1.18% of H_K. This additional random field was not explicitly included but could be considered to be identical in effect to an additional distribution of anisotropy field and would reduce the tolerable anisotropy field distribution accordingly.

Figure 1 shows the on-track error rate computed as a function of (x_h,z_h). The target island is located at (1,0) and the previously written island is located at (0,0). Figure 2 shows the 2-D map of error rate arising from ATE for 10^4 write attempts on the target track. The cross-track width of the low-error region in the ATE plot (Fig. 2) is considerably smaller than the down-track length of the low-error region in the on-track error plot (Fig. 1). This is because the cross-track field gradient is somewhat lower than down track and because there is only one write attempt that may result in errors on track while the adjacent track islands may be subjected to many writes of the target track. Cross-track head field gradient is therefore particularly important.

Figure 3 shows the combined error rate of on-track and off-track errors. This shows that with this head design, perfectly manufactured single layer BPM at 1 Tb/in^2 could have a viable down- and cross-track servo margin at acceptable error rates.

Islands in BPM may have variations in geometry. Figure 4 shows the combined error rate for the medium studied above, but with a zero mean, 5% standard deviation variation of both down-track and cross-track island position (normalized to the island period of 25.4 nm).

Figure 5 shows the combined error rate with a 5% standard deviation in intrinsic (crystalline) anisotropy (K_1). K_1 variations degrade the performance of the system significantly but the impact is not as severe as that of island position variations at the same standard deviation. In the 1-D model the effect of 5% variations in position and K_1 were found to be similar to each other. In 2-D the effect of position variations is more severe and this is attributed to the importance of ATE and cross-track head field gradient.

1-D simulations with the same write head were carried out at 4 Tb/in^2 with single-layer, single-domain islands located on a square lattice of 12.7 nm period with medium properties identical to the 1 Tb/in^2 medium above except for the island diameter which was reduced to 6.7 nm, and consequently K_1V/K_BT was reduced to 33 since the volume reduced by a factor of four. Magnetostatic interaction fields for randomly (up or down) magnetized islands had a standard deviation of about 2.5% of H_K. These were neglected in the calculations but would have an effect comparable to anisotropy field distributions of the same percentage.

The 1-D results shown in Fig. 6 suggest that with tight distributions of island parameters a finite write window at a BER of 10^{-4} might be achievable. However calculation of ATE for 10^4 write attempts with the head perfectly centered on the target track resulted in all islands on the adjacent track being overwritten with random data (BER = 0.5). Moving the head off-track results in larger fields on the adjacent track and consequently this error rate occurred for all off-track head positions. Therefore acceptable error rates could not be achieved at 4 Tb/in^2 with this head design and a single layer medium so more advanced media designs such as Exchange Coupled Composite (ECC) would be required.

III. CONCLUSIONS

A statistical model of write errors in BPM has been constructed that calculates the 2-D positional accuracy required to achieve a given error rate. The inclusion of thermal activation in the model shows that ATE is expected to be a severe problem and the risk of large numbers of adjacent track writes implies that cross-track head field gradients need to be very tightly controlled. The results have indicated that with the head design used, a 1 Tb/in^2 system could be possible with a single layer medium, provided that the islands had tightly controlled position and switching field distributions. Simulations at 4 Tb/in^2 indicate that BPM with single domain islands could not yield acceptable error rates with this head design and that different media types will be required. One likely possibility is ECC media which could provide greater thermal stability at the same switching field and thus less thermally activated ATE.

[1]A. Moser *et al.*, Appl. Phys. Lett. **91**, 162502 (2007).
[2]B. Livshitz *et al.*, J. Appl. Phys. **105**, 07C111 (2009).
[3]B. Livshitz *et al.*, IEEE Trans. Magn. **45**, 3519 (2009).
[4]M. E. Schabes, J. Magn. Magn. Mats. **320**(**22**), 2880 (2008).
[5]J. Kalezhi *et al.*, IEEE Trans. Magn. **46**, 3752 (2010).
[6]H. J. Richter *et al.*, IEEE Trans. Magn. **42**, 2255 (2006).
[7]Y. Jinbo and S. Greaves, private communication (2010).
[8]W. F. Brown, Phys. Rev. **130**, 1677 (1963).

References

Aharoni, A. (2000) *Introduction to the Theory of Ferromagnetism*, 2nd edn., no. 109 in International series of monographs on physics, Oxford University Press.

Albrecht, M., Moser, A., Rettner, C.T., Anders, S., Thomson, T. and Terris, B.D. (2002a) 'Writing of high-density patterned perpendicular media with a conventional longitudinal recording head', *Applied Physics Letters*, vol. 80, no. 18, pp. 3409–3411.

Albrecht, M., Rettner, C.T., Moser, A., Best, M.E. and Terris, B.D. (2002b) 'Recording performance of high-density patterned perpendicular magnetic media', *Applied Physics Letters*, vol. 81, no. 15, pp. 2875–2877.

Albrecht, T.R., Hellwing, O., Ruiz, R., Schabes, M.E., Terris, B.D. and Wu, X.Z. (2009) 'Bit-Patterned Magnetic Recording: Nanoscale Magnetic Islands for Data Storage', in: J.P. Liu, E. Fullerton, O. Gutfleisch and D. Sellmyer (eds.) *Nanoscale Magnetic Materials and Applications*, Springer US, pp. 237–274.

Beleggia, M. and Graef, M.D. (2003) 'On the computation of the demagnetization tensor field for an arbitrary particle shape using a Fourier space approach', *Journal of Magnetism and Magnetic Materials*, vol. 263, no. 1-2, pp. L1 – L9.

Beleggia, M., Graef, M.D., Millev, Y.T., Goode, D.A. and Rowlands, G. (2005) 'Demagnetization factors for elliptic cylinders', *Journal of Physics D: Applied Physics*, vol. 38, no. 18, p. 3333.

Beleggia, M., Tandon, S., Zhu, Y. and Graef, M.D. (2004) 'On the magnetostatic interactions between nanoparticles of arbitrary shape', *Journal of Magnetism and Magnetic Materials*, vol. 278, no. 1-2, pp. 270 – 284.

Belle, B.D., Schedin, F., Pilet, N., Ashworth, T.V., Hill, E.W., Nutter, P.W., Hug,

H.J. and Miles, J.J. (2007) 'High resolution magnetic force microscopy study of e-beam lithography patterned Co/Pt nanodots', vol. 101, AIP, p. 09F517.

Belle, B., Schedin, F., Ashworth, T., Nutter, P., Hill, E., Hug, H. and Miles, J. (2008) 'Temperature Dependent Remanence Loops of Ion-Milled Bit Patterned Media', *Magnetics, IEEE Transactions on*, vol. 44, no. 11, pp. 3468 –3471.

Bertram, H. and Lengsfield, B. (2007) 'Energy Barriers in Composite Media Grains', *Magnetics, IEEE Transactions on*, vol. 43, no. 6, pp. 2145 –2147.

Bertram, H. and Williams, M. (2000) 'SNR and density limit estimates: a comparison of longitudinal and perpendicular recording', *Magnetics, IEEE Transactions on*, vol. 36, no. 1, pp. 4 –9.

Brown, W., J. (1979) 'Thermal fluctuation of fine ferromagnetic particles', *Magnetics, IEEE Transactions on*, vol. 15, no. 5, pp. 1196 – 1208.

Brown, W.F. (1963) 'Thermal Fluctuations of a Single-Domain Particle', *Phys Rev*, vol. 130, no. 5, pp. 1677–1686.

Brown, W.F. (1962) *Magnetostatic Principles in Ferromagnetism*, vol. 1, North–Holand Publishing Company.

Brown, W.F. (1978) *Micromagnetics*, 2nd edn., New York: R.E. Krieger.

Chikazumi, S. (1994) *Physics of Magnetism*, Wiley series on the science and technology of materials, John Wiley and Sons Inc.

Chou, S.Y., Krauss, P.R. and Renstrom, P.J. (1996) 'Nanoimprint lithography', vol. 14, AVS, pp. 4129–4133.

Coffey, W.T., Crothers, D.S.F., Dormann, J.L., Geoghegan, L.J. and Kennedy, E.C. (1998) 'Effect of an oblique magnetic field on the superparamagnetic relaxation time. II. Influence of the gyromagnetic term', *Phys Rev B*, vol. 58, no. 6, pp. 3249–3266.

Craik, D.J. (1995) *Magnetism:Principles and Applications*, Chichester: John Wiley and Sons.

Daniel, E., Mee, C. and Clark, M. (1998) *Magnetic Recording: The First 100 Years*, New York: IEEE Press.

Dvorak, S.L. and Kuester, E.F. (1990) 'Numerical computation of the incomplete Lipschitz-Hankel integral $Je_0(a,z)$', *Journal of Computational Physics*, vol. 87, no. 2, pp. 301 – 327.

Fidler, J., Schrefl, T., Suess, D., Ertl, O., Kirschner, M. and Hrkac, G. (2006) 'Full micromagnetics of recording on patterned media', *Physica B: Condensed Matter*, vol. 372, no. 1-2, pp. 312 – 315, proceedings of the Fifth International Symposium on Hysteresis and Micromagnetic Modeling.

Fullerton, E.E., Jiang, J.S., Grimsditch, M., Sowers, C.H. and Bader, S.D. (1998) 'Exchange-spring behavior in epitaxial hard/soft magnetic bilayers', *Phys Rev B*, vol. 58, no. 18, pp. 12193–12200.

Gilbert, T. (2004) 'A phenomenological theory of damping in ferromagnetic materials', *Magnetics, IEEE Transactions on*, vol. 40, no. 6, pp. 3443 – 3449.

Gradshteyn, I.S. and Ryzhik, I.M. (1994) *Tables of Integrals, Series and Products*, 5th edn., New York: Academic.

Greaves, S.J., Kanai, Y. and Muraoka, H. (2010) *System Modelling of Bit Patterned Media*, Tech. Rep. INSIC May Meeting, Research Institute of Electrical Communications Tohoku University, Sendai, Dept. of Information and Electronics Engineering Niigata Institute of Technology, Kashiwazaki.

Grobis, M., Dobisz, E., Hellwig, O., Schabes, M.E., Zeltzer, G., Hauet, T. and Albrecht, T.R. (2010) 'Measurements of the write error rate in bit patterned magnetic recording at 100–320 Gb/in^2', *Applied Physics Letters*, vol. 96, no. 5, 052509.

Henderson, A. (2005.) *ParaView Guide, A Parallel Visualization Application*, Kitware Inc.

Hoagland, A.S. (2005) 'Early History & a 50 Year Perspective on Magnetic Disk Storage', Report, Magnetic Disk Heritage Center.

Hughes, G. (1999) 'Read channels for patterned media', *Magnetics, IEEE Transactions on*, vol. 35, no. 5, pp. 2310 –2312.

Hughes, G. (2000) 'Patterned media write designs', *Magnetics, IEEE Transactions on*, vol. 36, no. 2, pp. 521 –527.

Iwasaki, S. (1980) 'Perpendicular magnetic recording', *Magnetics, IEEE Transactions on*, vol. 16, no. 1, pp. 71 – 76.

Jakubovics, J.P. (1994) *Magnetism and Magnetic Materials*, 2nd edn., The Institute of Materials.

Jinbo, Y. and Greaves, S. (2010) Private communication.

Karlqvist, O. (1954) 'Calculation of the Magnetic Field in the Ferromagnetic Layer of a Magnetic Drum', *Transactions of the Royal Institute of Technology, Stockholm, Sweden*, vol. 86, no. 3.

Klik, I. and Gunther, L. (1990) 'First-passage-time approach to overbarrier relaxation of magnetization', *Journal of Statistical Physics*, vol. 60, pp. 473–484, 10.1007/BF01314931.

Kneller, E. and Hawig, R. (1991) 'The exchange-spring magnet: a new material principle for permanent magnets', *Magnetics, IEEE Transactions on*, vol. 27, no. 4, pp. 3588 – 3560.

Kryder, M.H. and Gustafson, R.W. (2005) 'High-density perpendicular recording–advances, issues, and extensibility', *Journal of Magnetism and Magnetic Materials*, vol. 287, pp. 449 – 458, selected papers from the seventh Perpendicular Magnetic Recording Conference (PMRC 2004).

Landau, L.D. and Lifshitz, E.M. (1935) 'On the theory of the dispersion of magnetic permeability in ferromagnetic bodies', *Soviet Physics Z*, vol. 8, pp. 153–169.

Livshitz, B., Inomata, A., Bertram, H. and Lomakin, V. (2009a) 'Semi-Analytical Approach for Analysis of BER in Conventional and Staggered Bit Patterned Media', *Magnetics, IEEE Transactions on*, vol. 45, no. 10, pp. 3519 –3522.

Livshitz, B., Inomata, A., Bertram, H.N. and Lomakin, V. (2009b) 'Analysis of recording in bit patterned media with parameter distributions', *Journal of Applied Physics*, vol. 105, no. 7, 07C111.

Mallinson, J. (1996) 'Scaling in magnetic recording', *Magnetics, IEEE Transactions on*, vol. 32, no. 2, pp. 599 –600.

Mansuripur, M. (1988) 'Magnetization reversal dynamics in the media of magneto-optical recording', *Journal of Applied Physics*, vol. 63, no. 12, pp. 5809–5823.

Middleton, B.K. and McKirdy, D.M. (2009) 'Perpendicular recording on magnetic particles using probe heads', *Journal of Physics D: Applied Physics*, vol. 42, no. 22, p. 225004.

Middleton, B. (2009) 'Magnetic memory using imperfect magnetic particles', *Electronics Letters*, vol. 45, no. 14, pp. 743 –744.

Miller, A.R. (1986) 'An Incomplete Lipschitz-Hankel Integral of K_0. Part 1', *Naval Research Laboratory*.

Morrison, C. (2008) Private communication.

Moser, A., Hellwig, O., Kercher, D. and Dobisz, E. (2007) 'Off-track margin in bit patterned media', *Applied Physics Letters*, vol. 91, no. 16, 162502.

Moser, A., Takano, K., Margulies, D.T., Albrecht, M., Sonobe, Y., Ikeda, Y., Sun, S. and Fullerton, E.E. (2002) 'Magnetic recording: advancing into the future', *Journal of Physics D: Applied Physics*, vol. 35, no. 19, p. R157.

Néel, L. (1949) 'Théorie du trainage magnétique', *Annales Geophysicae*, vol. 5, p. 99.

O'Grady, K. and Laidler, H. (1999) 'The limits to magnetic recording – media considerations', *Journal of Magnetism and Magnetic Materials*, vol. 200, no. 1-3, pp. 616 – 633.

Pan, L. and Bogy, D.B. (2009) 'Data storage: heat-assisted magnetic recording', *Nature Photonics*, vol. 3, no. 4, p. 189.

Pfeiffer, H. (1990) 'Determination of the anisotropy field distribution in particle assemblies taking into account thermal fluctuations', *Physica Status Solidi (a)*, vol. A118, pp. 295–306.

Richter, H.J. (2007) 'The transition from longitudinal to perpendicular recording', *Journal of Physics D: Applied Physics*, vol. 40, no. 9, pp. R149–R177.

Richter, H.J., Dobin, A.Y., Lynch, R.T., Weller, D., Brockie, R.M., Heinonen, O., Gao, K.Z., Xue, J., v. d. Veerdonk, R.J.M., Asselin, P. and Erden, M.F. (2006a) 'Recording potential of bit-patterned media', *Applied Physics Letters*, vol. 88, no. 22, 222512.

Richter, H.J. (1999) 'Recent advances in the recording physics of thin-film media', *Journal of Physics D: Applied Physics*, vol. 32, no. 21, p. R147.

Richter, H., Dobin, A., Heinonen, O., Gao, K., Veerdonk, R., Lynch, R., Xue, J., Weller, D., Asselin, P., Erden, M. and Brockie, R. (2006b) 'Recording on Bit-Patterned Media at Densities of 1 Tb/in^2 and Beyond', *Magnetics, IEEE Transactions on*, vol. 42, no. 10, pp. 2255 –2260.

Ruigrok, J.J.M., Coehoorn, R., Cumpson, S.R. and Kesteren, H.W. (2000) 'Disk recording beyond 100 Gb/in^2: Hybrid recording? (invited)', *Journal of Applied Physics*, vol. 87, no. 9, pp. 5398–5403.

Schabes, M.E. (2008) 'Micromagnetic simulations for terabit/in^2 head/media systems', *Journal of Magnetism and Magnetic Materials*, vol. 320, no. 22, pp. 2880 – 2884, eighth Perpendicular Magnetic Recording Conference.

Schöberl, J. (1997) 'NETGEN An advancing front 2D/3D-mesh generator based on abstract rules', *Computing and Visualization in Science*, vol. 1, no. 1, pp. 41 – 52.

Scholz, W., Fidler, J., Schrefl, T., Suess, D., Dittrich, R., Forster, H. and Tsiantos, V. (2003) 'Scalable parallel micromagnetic solvers for magnetic nanostructures', *Computational Materials Science*, vol. 28, no. 2, pp. 366 – 383.

Schrefl, T. (1999) 'Finite elements in numerical micromagnetics – Part I: granular hard magnets', *Journal of Magnetism and Magnetic Materials*, vol. 207, pp. 45–65.

Shiroishi, Y., Fukuda, K., Tagawa, I., Iwasaki, H., Takenoiri, S., Tanaka, H., Mutoh, H. and Yoshikawa, N. (2009) 'Future Options for HDD Storage', *Magnetics, IEEE Transactions on*, vol. 45, no. 10, pp. 3816 –3822.

Stoner, E.C. and Wohlfarth, E.P. (1948) 'A Mechanism of Magnetic Hysteresis in Heterogeneous Alloys', *Philosophical Transactions of the Royal Society A*, vol. 240, pp. 599–642.

Suess, D., Schrefl, T., Dittrich, R., Kirschner, M., Dorfbauer, F., Hrkac, G. and Fidler, J. (2005) 'Exchange spring recording media for areal densities up to 10Tb/in^2', *Journal of Magnetism and Magnetic Materials*, vol. 290-291, no. 1, pp. 551–554.

Suh, H.J., Heo, C., You, C.Y., Kim, W., Lee, T.D. and Lee, K.J. (2008) 'Attempt frequency of magnetization in nanomagnets with thin-film geometry', *Phys Rev B*, vol. 78, no. 6, p. 064430.

Tandon, S., Beleggia, M., Zhu, Y. and Graef, M.D. (2004) 'On the computation of the demagnetization tensor for uniformly magnetized particles of arbitrary shape. Part I: Analytical approach', *Journal of Magnetism and Magnetic Materials*, vol. 271, no. 1, pp. 9 – 26.

Tannous, C. and Gieraltowski, J. (2008) 'The Stoner–Wohlfarth model of ferromagnetism', *European Journal of Physics*, vol. 29, no. 3, pp. 475–487.

Thomson, T., Hu, G. and Terris, B.D. (2006) 'Intrinsic Distribution of Magnetic Anisotropy in Thin Films Probed by Patterned Nanostructures', *Phys Rev Lett*, vol. 96, no. 25, p. 257204.

Victora, R.H. and Shen, X. (2005) 'Composite media for perpendicular magnetic recording', *IEEE Transactions on Magnetics*, vol. 41, no. 2, pp. 537–542.

Wang, J.P., Shen, W. and Bai, J. (2005) 'Exchange coupled composite media for perpendicular magnetic recording', *Magnetics, IEEE Transactions on*, vol. 41, no. 10, pp. 3181 – 3186.

Weller, D. and Moser, A. (1999) 'Thermal effect limits in ultrahigh-density magnetic recording', *Magnetics, IEEE Transactions on*, vol. 35, no. 6, pp. 4423 –4439.

Wernsdorfer, W., Orozco, E.B., Hasselbach, K., Benoit, A., Barbara, B., Demoncy, N., Loiseau, A., Pascard, H. and Mailly, D. (1997) 'Experimental Evidence of the Néel-Brown Model of Magnetization Reversal', *Phys Rev Lett*, vol. 78, no. 9, pp. 1791–1794.

White, R., Newt, R. and Pease, R. (1997) 'Patterned media: a viable route to 50 Gbit/in2 and up for magnetic recording?', *Magnetics, IEEE Transactions on*, vol. 33, no. 1, pp. 990 –995.

White, R.L. (2000) 'The physical boundaries to high-density magnetic recording', *Journal of Magnetism and Magnetic Materials*, vol. 209, no. 1-3, pp. 1 – 5.

Winkler, G., Suess, D., Lee, J., Fidler, J., Bashir, M.A., Dean, J., Goncharov, A., Hrkac, G., Bance, S. and Schrefl, T. (2009) 'Microwave-assisted three-dimensional multilayer magnetic recording', *Applied Physics Letters*, vol. 94, no. 23, 232501.

Wood, R. (2000) 'The feasibility of magnetic recording at 1 Terabit per square inch', *Magnetics, IEEE Transactions on*, vol. 36, no. 1, pp. 36 –42.

Wood, R. (2009) 'Exact Solution for a Stoner–Wohlfarth Particle in an Applied Field and a New Approximation for the Energy Barrier', *Magnetics, IEEE Transactions on*, vol. 45, no. 1, pp. 100 –103.

Wood, R., Hsu, Y. and Schultz, M. (2007) 'Perpendicular Magnetic Recording Technology', White paper, Hitachi Global Storage Technologies.

Wood, R., Williams, M., Kavcic, A. and Miles, J. (2009) 'The Feasibility of Magnetic Recording at 10 Terabits Per Square Inch on Conventional Media', *Magnetics, IEEE Transactions on*, vol. 45, no. 2, pp. 917 –923.

Wood, R., Miles, J. and Olson, T. (2002) 'Recording technologies for terabit per square inch systems', *Magnetics, IEEE Transactions on*, vol. 38, no. 4, pp. 1711 –1718.

Wood, R. and Takano, H. (2006) *Prospects for Magnetic Recording over the next 10 years*, Tech. rep., Hitachi Global Storage Technologies.

Zhu, J.G., Zhu, X. and Tang, Y. (2008) 'Microwave Assisted Magnetic Recording', *Magnetics, IEEE Transactions on*, vol. 44, no. 1, pp. 125 –131.